Nanostructured Nickel Catalysts for Sustainable (De-)Hydrogenation Reactions

DISSERTATION

zur Erlangung des akademischen Grades einer

Doktorin der Naturwissenschaften (Dr. rer. nat.)

an der Fakultät für Biologie, Chemie und Geowissenschaften

der Universität Bayreuth

vorgelegt von

M. Sc. Mara Klarner

geboren in Amberg

Bayreuth, 2021

Die vorliegende Arbeit wurde in der Zeit von Februar 2018 bis Juni 2021 in Bayreuth am Lehrstuhl Anorganische Chemie II unter Betreuung von Herrn Professor Dr. Rhett Kempe angefertigt.

Vollständiger Abdruck der von der Fakultät für Biologie, Chemie und Geowissenschaften der Universität Bayreuth genehmigten Dissertation zur Erlangung des akademischen Grades einer Doktorin der Naturwissenschaften (Dr. rer. nat.).

Dissertation eingereicht am: 25.06.2021
Zulassung durch die Promotionskommission: 07.07.2021
Wissenschaftliches Kolloquium: 28.10.2021

Amtierender Dekan: Prof. Dr. Benedikt Westermann

Prüfungsausschuss:

Prof. Dr. Rhett Kempe   (Gutachter)
Prof. Dr. Birgit Weber   (Gutachterin)
Jun.-Prof. Dr. Anna Schenk   (Vorsitz)
Prof. Dr. Rainer Schobert

Für meine großartige Familie,
die meine Neugier und Begeisterung für das Unbekannte geweckt hat.

Table of Contents

Abbreviations

a.u.	arbitrary units
Cp	cyclopentadienyl
BET	Brunauer Emmett Teller
bpy	2,2'-bipyridine
CB	conduction band
CUS	coordinative unsaturated sites
CV	cyclic voltammetry
DFT	density functional theory
DMSO	dimethyl sulfoxide
DOS	density of states
DRIFTS	diffuse reflectance infrared Fourier transform spectroscopy
DRS	diffuse reflectance ultraviolet-visible spectroscopy
dtbbpy	4,4'-di-*tert*-butyl-2,2'-bipyridine
EDX	energy dispersive X-ray spectroscopy
EELS	electron energy loss spectroscopy
EtOH	ethanol
FD-FLIM	frequency domain – fluorescence lifetime imaging microscopy
FT-IR	Fourier transform infrared spectroscopy
g-C_3N_4	graphitic carbon nitride
GC	gas chromatography
GC-MS	gas chromatography - mass spectrometry
GC-TDC	gas chromatography - thermal conductivity detector
HAADF-STEM	high-angle annular dark-field scanning TEM
ICP-OES	inductively coupled plasma optical emission spectrometry
LED	light-emitting diode
M_{13}	13 atom metal cluster (metals: Ni, Pd, Pt)
M@MOF	MOF supported metal nanoparticles
MeCN	acetonitrile
MeOH	methanol
MIL	material of Institute Lavoisier (e.g., MIL-101)
MNP	metal nanoparticle
MOCVD	metal-organic chemical vapor deposition
MOF	metal-organic framework
mol%	mole fraction
NHE	normal hydrogen electrode
Ni/Al_2O_3	γ-Al_2O_3 supported nickel nanoparticles

Ni/C	activated char coal supported nickel nanoparticles
NMR	nuclear magnetic resonance
NP	nanoparticle
PL	photoluminescence
POM	polyoxometalate
ppm	parts per million
ppy	2-phenylpyridine
PS	polystyrene
PXRD	powder X-ray diffraction
rpm	rounds per minute
SBU	secondary building unit
SEM	scanning electron microscopy
ssNMR	solid state nuclear magnetic resonance
TD	time dependent
TEM	transmission electron microscopy
TGA	thermogravimetric analysis
THF	tetrahydrofuran
UiO	Universitetet i Oslo (MOF, e.g., UiO-67)
UV	ultraviolet
VB	valence band
Vis	visible
wt.%	weight percent
XPS	X-ray photoelectron spectroscopy
XRD	X-ray diffraction
ZIF	zeolitic imidazolate framework

1 Summary / Zusammenfassung

1.1 Summary

This thesis mainly focuses on the earth-abundant metal nickel as a nanoparticulate (co-)catalyst in thermal hydrogenation reactions and photocatalytic dehydrogenation reactions.

The first part of this thesis focuses on the design of nanostructured nickel hydrogenation catalysts based on commercial porous support materials. For a fundamental understanding of the synthesis process of Ni/Al_2O_3 catalysts, the influence of the nickel precursor on the hydrogenation activity was investigated. Starting from six Ni-salen complexes with varying steric demand and carbon and nitrogen content, a catalyst library was prepared by wet impregnation followed by pyrolysis and reduction. In the reductive amination of acetophenone with ammonia and hydrogen as the reducing agent, a clear dependence of the catalytic activity on the particular salen precursor was found. Neither the nickel content nor the nickel particle size provided a compelling evidence for these activity differences. Moreover, the key functions of the metal precursor during the catalyst synthesis were identified: the volatility of the Ni-salen complexes enables their vapor deposition on the Al_2O_3 support during pyrolysis to generate catalytically active nickel sites. The subsequent decomposition of the salen ligand forms a nitrogen-doped carbon shell that covers and stabilizes the nickel particles. The embedding process of the nanoparticles is influenced by specific pyrolysis parameters, preventing the formation of carbon nanotubes due to excessive carbon supply.
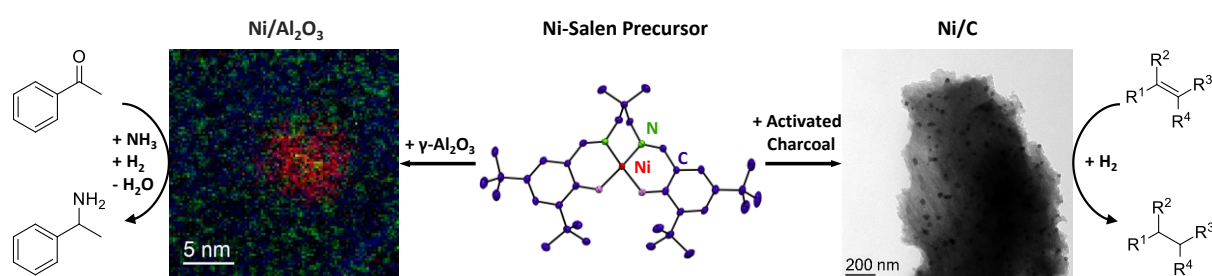
Figure 1.1. Synthesis of nanostructured nickel catalysts starting from a specific Ni-salen precursor. Left: Ni/Al_2O_3 catalyst for the reductive amination of acetophenone. Right: Ni/C catalyst for the chemoselective hydrogenation of olefins.

The selective hydrogenation of C-C double bonds is a challenging reaction and of high interest for the production of industrially relevant chemicals and pharmaceuticals. For this purpose, a novel nanostructured Ni/C catalyst was developed in a two-step process starting from inexpensive charcoal as support material. The catalytically active nickel nanoparticles were generated by the controlled decomposition of a specific Ni-salen complex during the sequence of wet impregnation, pyrolysis and reduction. The surface-oxidized nickel particles with metallic core had an average diameter of 19.5 nm

and were homogeneously distributed on the carbon support. Detailed analysis of a single nanoparticle revealed the coverage with a thin layer, apparently of nitrogen-doped carbon, as a minor nitrogen content was detected in the catalyst material. The Ni/C catalyst was utilized for the chemoselective hydrogenation of pure aliphatic/aromatic and also functionalized olefins. The combination of Ni salen precursor and activated charcoal was crucial for the high catalyst activity, as shown by comparison with oxidic support materials. Several styrene derivatives were converted at mild conditions (0.2 MPa H_2, 40 °C, 1.35 mol% Ni) and 28 examples of more challenging olefins were hydrogenated at slightly harsher conditions (1 MPa H_2, 80 °C, 1.35 mol% Ni). Various functional groups such as carbonyl compounds, esters, ethers and nitriles were tolerated with high selectivity.

The second part of this thesis deals with multicomponent photocatalysts supported on the metal-organic framework MIL-101. The first example of a photocatalyzed, additive-free and acceptorless dehydrogenation of benzylamine was described. By absorbing visible light, Ni/CdS@MIL-101 catalyzed the concerted imine formation and equimolar release of hydrogen. Additionally, a synthesis concept for asymmetric imines was presented by using a second amine acting as a coupling partner, which is not photocatalytically dehydrogenated. MIL-101 enabled the stepwise synthesis of semiconductor and co-catalyst and defined the overall size of the recyclable core-shell photocatalyst. CdS was used as semiconducting material, in which free charge carriers are generated by visible light photoexcitation. Fluorescence lifetime studies revealed a faster electron transfer from the conduction band of CdS across the semiconductor/metal interface to metallic nickel nanoparticles than to noble metals such as palladium and platinum. This directional electron transfer reduced the probability of charge recombination, so that the activity of the catalyst was increased by the spatial separation of the redox half-reactions. Interestingly, the modification with co-catalytic nickel nanoparticles not only promoted the reductive hydrogen evolution, but moreover stabilized the CdS component against photooxidation.
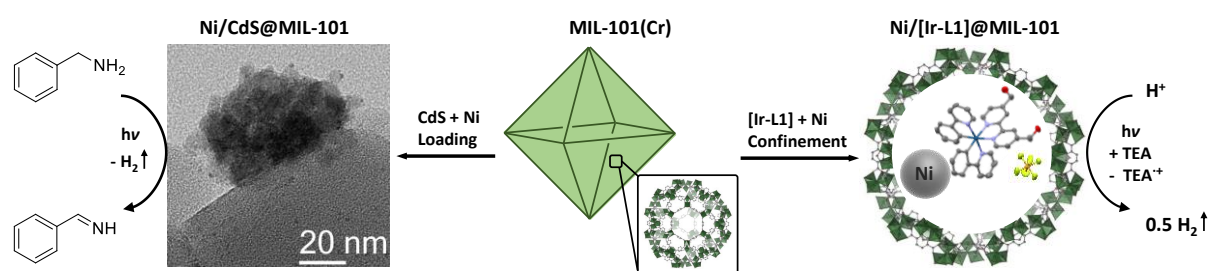
Figure 1.2. Synthesis of metal-organic framework MIL-101 supported photocatalysts for visible light driven dehydrogenation reactions. Left: Ni/CdS@MIL-101 for the acceptorless dehydrogenation of benzylamine. Right: Ni/[Ir-L1]@MIL-101 for the proton reduction in water.

Furthermore, the mesoporous MIL-101 provided a platform to study the influence of metal nanoparticles on the activity of an iridium photosensitizer with $[Ir(bpy)(ppy)_2]^+$ motif in photocatalytic proton reduction. A multistep synthesis of the two components within MIL-101 pores ensured the spatial

proximity and interaction between them. First, the modified bipyridyl ligand L1 was anchored at unsaturated coordination sites in the MOF. This step and the subsequent on-site formation of the photosensitizer [Ir-L1] were monitored by spectroscopic methods. The additional metal loading of [Ir-L1]@MIL-101 with either nickel, palladium or platinum affected the hydrogen evolution rate in proton reduction. While co-catalytic nickel nanoparticles were found to promote the hydrogen evolution, platinum nanoparticles acted as inhibitors. Theoretical simulations on model systems consisting of the respective 13-atom metal cluster and [Ir-L1] demonstrated a pronounced electronic interaction. The highest binding affinity was found between the nickel cluster and [Ir-L1], followed by palladium and platinum. The presence of a metal cluster significantly changed the photoabsorption of [Ir-L1] and resulted in a denser excitation spectrum. In a broad energy range, charge transfer from all three metal clusters to the photosensitizer occurred upon optical excitation.

1.2 Zusammenfassung

Der Fokus dieser Dissertation liegt auf der Verwendung des 3d-Metalls Nickel als nanopartikulärer (Co-)Katalysator in thermischen Hydrierreaktionen und photokatalytischen Dehydrierreaktionen.

Der erste Teil der Dissertation konzentriert sich auf das Design nanostrukturierter Nickel-Hydrierkatalysatoren auf der Basis kommerzieller, poröser Trägermaterialien. Für ein grundlegendes Verständnis des Syntheseprozesses von Ni/Al_2O_3-Katalysatoren wurde der Einfluss des Nickel-Präkursors auf die Hydrieraktivität untersucht. Ausgehend von sechs Ni-Salen-Komplexen mit Variationen hinsichtlich des sterischen Anspruchs, sowie des Kohlenstoff- und Stickstoffgehalts wurde durch Nassimprägnierung und anschließende Pyrolyse und Reduktion eine Katalysatorbibliothek erstellt. In der reduktiven Aminierung von Acetophenon mit Ammoniak und Wasserstoff als Reduktionsmittel wurde eine deutliche Abhängigkeit der katalytischen Aktivität vom jeweiligen Salen-Präkursor festgestellt. Weder der Nickelgehalt noch die Nickelpartikelgröße lieferten eine stringente Erklärung dieser Aktivitätsunterschiede. Zudem konnten die Schlüsselfunktionen des Metallpräkursors während der Katalysatorsynthese identifiziert werden: Die Flüchtigkeit der Ni-Salen-Komplexe ermöglicht während der Pyrolysephase eine Gasphasenabscheidung auf dem Al_2O_3-Träger, um katalytisch aktive Nickelzentren zu erzeugen. Die anschließende Zersetzung des Salen-Liganden bildet eine Stickstoff-dotierte Kohlenstoffhülle, welche die Nickelpartikel bedeckt und stabilisiert. Der Einbettungsprozess der Nanopartikel wird durch spezifische Pyrolyseparameter beeinflusst, wobei unter anderem die Entstehung von Kohlenstoffnanoröhren durch eine zu hohe Kohlenstoffzufuhr verhindert werden muss.
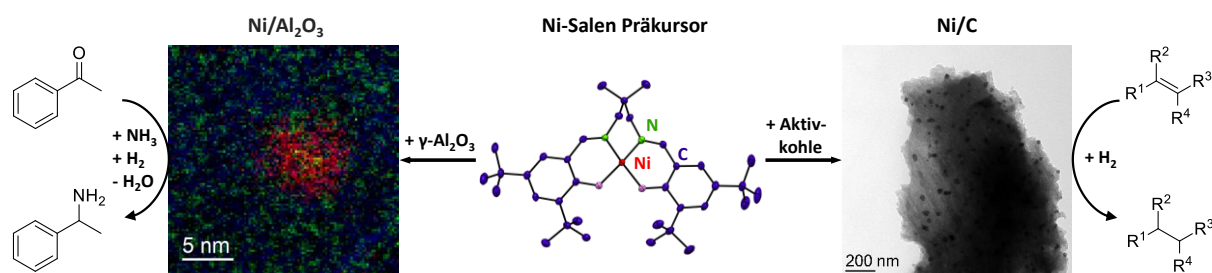

Abbildung 1.1. Synthese von nanostrukturierten Nickelkatalysatoren ausgehend von einem spezifischen Ni-Salen-Präkursor. Links: Ni/Al_2O_3 Katalysator für die reduktive Aminierung von Acetophenon. Rechts: Ni/C Katalysator für die chemoselektive Hydrierung von Olefinen.

Die selektive Hydrierung von C-C Doppelbindungen ist eine anspruchsvolle Reaktion und von hohem Interesse für die Herstellung industriell relevanter Chemikalien und Pharmazeutika. Hierfür wurde ein neuartiger nanostrukturierter Ni/C Katalysator in einem zweistufigen Prozess ausgehend von kostengünstiger Aktivkohle als Trägermaterial entwickelt. Die katalytisch aktiven Nickelnanopartikel wurden durch die kontrollierte Zersetzung eines spezifischen Ni-Salen-Komplexes während der Prozessabfolge von Nassimprägnierung, Pyrolyse und Reduktion erzeugt. Die oberflächenoxidierten Nickelpartikel mit metallischem Kern hatten einen mittleren Durchmesser von 19,5 nm und waren

homogen auf dem Kohlenstoffträger verteilt. Die detaillierte Analyse eines einzelnen Nanopartikels zeigte die Bedeckung mit einer dünnen Schicht, vermutlich aus stickstoffdotiertem Kohlenstoff, da ein geringer Stickstoffgehalt im Katalysatormaterial nachgewiesen wurde. Der Ni/C Katalysator wurde für die chemoselektive Hydrierung von rein aliphatischen/aromatischen und auch funktionalisierten Olefinen eingesetzt. Die Kombination aus Ni-Salen-Präkursor und Aktivkohle war entscheidend für eine hohe Katalysatoraktivität, wie der Vergleich mit oxidischen Trägermaterialien zeigte. Mehrere Styrolderivate wurden bei milden Bedingungen (0,2 MPa H_2; 40 °C; 1,35 mol% Ni) umgesetzt und 28 Beispiele anspruchsvollerer Olefine wurden bei etwas harscheren Bedingungen (1 MPa H_2; 80 °C; 1,35 mol% Ni) hydriert. Verschiedene funktionelle Gruppen wie Carbonylverbindungen, Ester, Ether und Nitrile wurden mit hoher Selektivität toleriert.

Der zweite Teil der Dissertation befasst sich mit Mehrkomponenten-Photokatalysatoren geträgert auf der metallorganischen Gerüstverbindung MIL-101. Erstmals wurde eine photokatalysierte, additiv-freie und akzeptorlose Dehydrierung von Benzylamin beschrieben. Durch Absorption von sichtbarem Licht katalysierte Ni/CdS@MIL-101 die konzertierte Iminbildung und äquimolare Freisetzung von Wasserstoff. Zudem wurde ein Synthesekonzept für asymmetrische Imine vorgestellt, indem ein zweites Amin als Kopplungspartner agiert, welches photokatalytisch nicht dehydriert wird. MIL-101 ermöglichte die stufenweise Synthese von Halbleiter und Co-Katalysator und definierte die Partikelgröße des rezyklisierbaren Kern-Schale-Photokatalysators. Als halbleitendes Material wurde CdS verwendet, in welchem durch die Photoanregung mit sichtbarem Licht freie Ladungsträger erzeugt werden. Studien zur Fluoreszenzlebensdauer zeigten einen schnelleren Elektronentransfer vom Leitungsband des CdS über die Halbleiter/Metall-Grenzfläche zu metallischen Nickelnanopartikeln als zu Edelmetallen wie Palladium und Platin. Dieser gerichtete Elektronentransfer verringerte die Wahrscheinlichkeit der Ladungsträgerrekombination, sodass die Aktivität des Katalysators durch die räumliche Trennung der Redoxhalbreaktionen gesteigert werden konnte. Interessanterweise förderte die Modifikation mit co-katalytischen Nickelnanopartikeln nicht nur die reduktive Wasserstoffentwicklung, sondern stabilisierte zudem die CdS Komponente gegen Photooxidation.
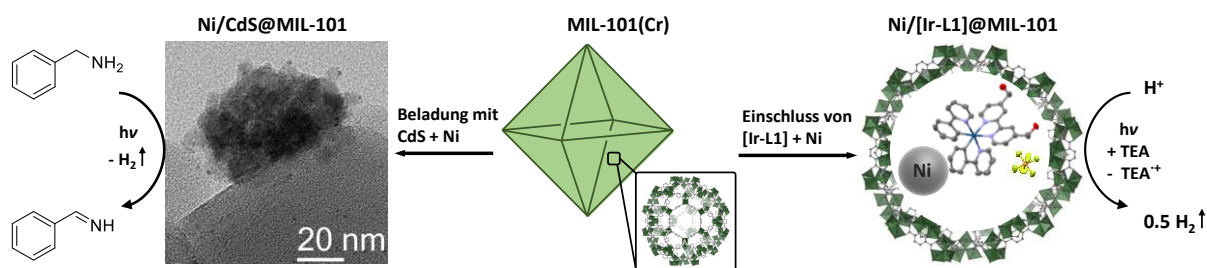

Abbildung 1.2. Synthese von Photokatalysatoren, geträgert auf dem metallorganischen Netzwerk MIL-101, für Dehydrierreaktionen bei Bestrahlung mit sichtbarem Licht. Links: Ni/CdS@MIL-101 für die akzeptorlose Dehydrierung von Benzylamin. Rechts: Ni/[Ir-L1]@MIL-101 für die Protonenreduktion in Wasser.

Weiterhin bot das mesoporöse MIL-101 eine Plattform, um den Einfluss von Metallnanopartikeln auf die Aktivität eines Iridium-Photosensibilisators mit $[Ir(bpy)(ppy)_2]^+$-Motiv in der photokatalytischen Protonenreduktion zu untersuchen. Die räumliche Nähe zur Interaktion der zwei Komponenten wurde durch eine mehrstufige Synthese innerhalb der Poren von MIL-101 erzeugt. Zunächst wurde der modifizierte Bipyridyl-Ligand L1 an ungesättigten Koordinationsstellen im MOF verankert. Dieser Schritt, ebenso wie die anschließende in-situ Synthese des Photosensibilisators [Ir-L1], wurde mit spektroskopischen Methoden verfolgt. Die zusätzliche Metallbeladung von [Ir-L1]@MIL-101 mit Nickel, Palladium oder Platin beeinflusste die Wasserstoffentwicklungsrate in der photokatalytischen Protonenreduktion. Während sich co-katalytische Nickelnanopartikel als Promotor der Wasserstofffreisetzung herausstellten, wirkten Platinnanopartikel als Inhibitor. Theoretische Simulationen an Modellsystemen, bestehend aus dem jeweiligen 13-atomigen Metallcluster und [Ir-L1], zeigten eine ausgeprägte elektronische Wechselwirkung. Die höchste Bindungsaffinität wurde zwischen dem Nickelcluster und [Ir-L1] gefunden, gefolgt von Palladium und Platin. Die Anwesenheit eines Metallclusters veränderte die Photoabsorption von [Ir-L1] signifikant und führte zu einem dichteren Anregungsspektrum. In einem breiten Energiebereich trat bei optischer Anregung ein Ladungstransfer von allen drei Metallclustern zum Photosensibilisator auf.

2   Introduction

2.1 Sustainable and Green Chemistry

In the society of the 21st century, the consequences of climate change and industrial pollution are omnipresent, which has resulted in a profound environmental awareness. Research is also shifting its focus to a science-based approach to environmental protection.[1] By developing a sustainable concept for the chemical industry, society could enjoy everyday products such as pharmaceuticals and polymer-based materials while conserving fossil resources. As early as 1998, P. Anastas and J. Warner presented the 12 principles of *green chemistry* to address the sustainability aspect of chemical research.[2] These include the design, development and implementation of chemical processes and products to reduce or eliminate substances that are hazardous to human health and the environment.[3] A chemical reaction has to meet the 12 principles to be classified as *green* which was later simplified by translating it into the acronym *PRODUCTIVELY*.[4] Special attention is paid to *C: catalytic reagents* and *R: renewable materials* as these two principles have a significant impact on the sustainability of an industrial manufacturing process.

Catalysis plays a central role in *green chemistry*, as it is linked to reduced energy requirements, catalytic rather than stoichiometric amounts of substances, increased selectivity and the use of less toxic materials.[5] More specifically, the catalytic conversion of biomass into fuels and industrial relevant chemicals contributes decisively to the substitution of fossil resources. Crude oil and gas are the primary feedstocks that need to be replaced by renewable materials for a reduced CO_2 footprint.[6] In this context, lignocellulose - consisting of hemicellulose, cellulose and lignin - is the most promising biomass fraction because it is abundant and does not interfere with human food supply. Different heterogeneously catalyzed pathways were developed to convert this renewable carbon source into bio-oil, furfural, hydroxymethylfurfural and levulinic acid.[7] After depolymerization by thermochemical or hydrolytic methods[8], the resulting platform molecules are further used as building blocks to synthesize intermediates and fine chemicals.[9] For these processes, catalysts based on rare noble metals such as Ru, Rh, Ir and Pt are frequently used. In basic research on homogeneous catalysis, acceptorless dehydrogenative condensation and borrowing hydrogen/ hydrogen autotransfer are established concepts for the activation of bio-derived substrates.[10] A central challenge of modern catalysis is the replacement of noble metals with earth-abundant transition metals such as Mn, Fe, Co and Ni to conserve the earth's finite resources.[11] The advantages lie in the generation of new selectivity patterns for an extended reaction scope, high activities and reduced costs.[12] The same trend is evident for Fe[13], Co[14] and Ni[15] catalysts in heterogeneous catalysis as they are applied in selective hydrogenation reactions such as nitroarene hydrogenation[16] and reductive amination.[17] Large-scale industrial processes are mainly

heterogeneously catalyzed due to the easy separation of the catalyst from the reaction product and the recyclability over several cycles.[18] Moreover, photocatalysis is regarded as another pillar of sustainable and *green chemistry*. The exploration of alternative energy sources developed in the 1970s during the oil crisis.[19] Nature was imitated to convert sunlight as a perennial energy source into chemical energy that is easier to store and use. For example, H_2 as clean fuel is accessible through photocatalytic water reduction. Since about 3 % of the solar energy reaching the earth's surface is UV light and 44 % is light in the visible spectrum[20], the development of photocatalysts driven by visible light is consequently focused.[21] Most of the published catalyst systems for water reduction and oxidation involve Ru, Ir or Rh photosensitizers; however, 3d metal catalysts based on Ni, Fe and Co receive growing attention.[22] The second application of photocatalysis evolved in the field of pollutant degradation to stem the ongoing pollution of water and air with toxic chemicals. The third area of photocatalysis covers organic chemical synthesis.[23] Considering the superordinate context, the conversion of renewable energy on the one hand was combined with the synthesis of base chemicals from renewable carbon sources on the other hand. Upon irradiation with visible light, both Ni/CdS and a Co-thioporphyrazine on g-C_3N_4 catalyzed the valorization of biomass intermediates with a simultaneous release of H_2.[24]

2.2 Heterogeneous Nickel Catalysis

The history of heterogeneous nickel catalysis began in 1897 when the French chemists P. Sabatier and J. B. Senderens discovered the hydrogenation of unsaturated hydrocarbons at atmospheric pressure.[25] Sabatier was awarded the Nobel Prize in Chemistry in 1912 for his *Method of hydrogenating organic compounds in the presence of finely disintegrated metals.*[26] The unique activity of the Pt group in hydrogenation reactions, and especially that of Ni, was the basis for the development of the petrochemical industry. The breakthrough of modern Ni catalysis took place in 1927 when M. Raney patented the preparation of a highly active Ni hydrogenation catalyst.[27]
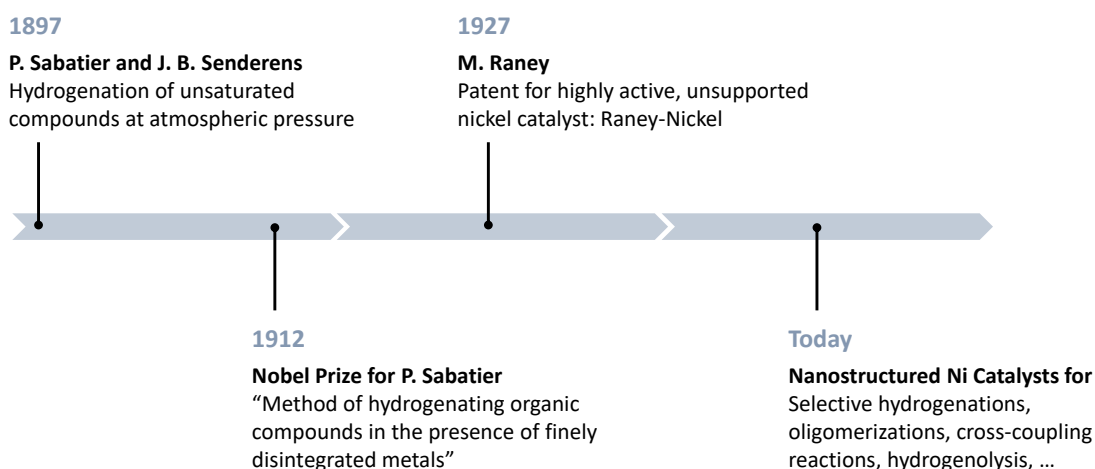

1897

P. Sabatier and J. B. Senderens
Hydrogenation of unsaturated compounds at atmospheric pressure

1927

M. Raney
Patent for highly active, unsupported nickel catalyst: Raney-Nickel

1912

Nobel Prize for P. Sabatier
"Method of hydrogenating organic compounds in the presence of finely disintegrated metals"

Today

Nanostructured Ni Catalysts for
Selective hydrogenations, oligomerizations, cross-coupling reactions, hydrogenolysis, …

Figure 2.1 The history of heterogeneous nickel catalysis.

Raney nickel is a Ni-Al alloy whose Al component has been leached with an alkaline solution to produce the active Ni species as porous material. It is still used today as a state-of-the-art industrial hydrogenation catalyst[28], such as in bulk-scale chemical processes to reduce glucose to sorbitol, benzene to cyclohexane and the hardening of vegetable oils.[29] Despite its high catalytic activity and low cost, Raney Ni has a decisive disadvantage: it is pyrophoric due to its large metal surface area and, therefore, difficult to handle. For this reason, there is an ongoing academic and industrial demand for the development of inexpensive, stable, and easy-to-use Ni catalysts as a substitute for Raney Ni with broad application potential and comparably high hydrogenation activity.

In recent years, numerous nanostructured Ni catalysts have been investigated in hydrogenolysis[30], C-C and C-N cross-couplings[31] and olefin oligomerization.[32] In addition, the selective hydrogenation of unsaturated compounds is of high interest, as demonstrated by *Beller and coworkers* using a Ni-phen@SiO$_2$ catalyst.[33] A specific Ni-phenanthroline complex impregnated on SiO$_2$ was pyrolyzed at 1000 °C to form the active nickel silicide phase. Various chemoselective hydrogenations such as the hydrogenation of nitroarenes, aldehydes and ketones, nitriles, alkenes and alkynes as well as N-heterocycles were catalyzed by adjusting the reaction conditions.

2.2.1 Reductive Amination of Carbonyl Compounds

Primary amines represent a highly relevant substrate class in industry, as the structural motif is present in many pharmaceuticals, agrochemicals and polymer materials. One synthetic route is catalytic nitroarene hydrogenation, which has been intensively studied with heterogeneous Ni catalysts.[15a+15b] Another elegant method is the reductive amination of carbonyl compounds with liquid ammonia, first described 100 years ago by Mignonac using a Ni powder.[34] Mechanistically, the reaction proceeds via a Schiff base condensation of a carbonyl compound with ammonia. In the second reaction step, the intermediate imine is reduced to the corresponding primary amine, for example, by catalytic hydrogenation with molecular H$_2$. The main challenge of this application is the selectivity of the reaction by avoiding multiple alkylation. Many applications using Raney Ni have been reported.[35] However, research in recent years has focused on the development of nanostructured, reusable and easy-to-handle catalysts based on transition metals. In 2019, *Kempe and coworkers* demonstrated reductive amination with Ni/Al$_2$O$_3$ using aqueous NH$_3$ and H$_2$ as reducing agent.[15c] The nanostructured Ni catalyst was prepared via a simple two-step route: The γ-Al$_2$O$_3$ support material was wet impregnated with a specific Ni-salen complex as the metal precursor, then pyrolyzed at 700 °C in constant N$_2$ flow and reduced at 550 °C in forming gas. A broad substrate scope with a high tolerance of functional groups, including hydrogenation-sensitive ones, was obtained at 80 °C, 1 MPa H$_2$ and 1.2 mol% Ni. The combination of ligand, metal and support material proved to be essential for the high hydrogenation activity. The decomposition of the salen ligand to form a N-doped carbon layer was identified as a key step in which the Ni nanoparticles were embedded on the acidic Al$_2$O$_3$ support. In the same year, another Ni catalyst

was obtained by the pyrolysis of an in situ generated Ni-tartaric acid complex on SiO_2 and applied in the reductive amination of aldehydes and ketones at 120 °C, 0.5-0.7 MPa NH_3, 2 MPa H_2 and 6 mol% Ni.[36] Benzylic, heterocyclic and aliphatic amines were obtained in high yields, as were amine-substituted pharmaceuticals and steroid derivatives. The synthesis of biologically active molecules by reductive amination is of particular interest because amines are ubiquitously present among biologically active compounds.[37] Furthermore, Ni nanoparticles on N-doped mesoporous carbon were utilized for the conversion of nine carbonyl derivatives at 80 °C and 0.1 MPa H_2 employing aqueous NH_3. The catalyst was prepared by ion exchange of a pre-synthesized polymer with a Ni ammine complex followed by pyrolysis at 500 °C under H_2 atmosphere.[38]

2.2.2 Selective Hydrogenation of Olefins

The selective hydrogenation of carbon double bonds is a challenging reaction and of high interest in producing industrially relevant chemicals. For example, the synthesis of vitamins and drugs as well as the hardening of natural oils involve a chemoselective hydrogenation step. Most industrially relevant catalysts are based on expensive noble metals or on difficult-to-handle Raney Ni.[39] Therefore, the selective hydrogenation of α-β-unsaturated carbonyls, internal and terminal olefins has been addressed in recent years with various nanostructured Ni catalysts. Different supported catalyst systems, including Ni/TiO_2[40], a Ni-Ir alloy on SiO_2[41] and Ni nanoparticles encapsulated in zeolite materials[42] were investigated. The intermetallic Ni-silicide catalyst Ni-phen@SiO_2, discussed earlier in this chapter, allowed the conversion of unfunctionalized alkenes and those with hydrogenation-sensitive functional groups to the corresponding unsaturated compounds.[33] Aliphatic nitriles, conjugated systems, ketones and, remarkably, one benzaldehyde derivative remained inert at 40 °C, 1 MPa H_2 and 4 mol% Ni. Unsupported Ni nanoparticles were typically synthesized by reduction of a Ni salt and subsequent stabilization with either stearic acid (SA)[43] or carboxymethyl cellulose (CMC).[44] The corresponding catalysts enabled the selective hydrogenation of α-β-unsaturated carbonyls at room temperature and 4 MPa H_2 using Ni-SA colloids and at 60 °C, 0.4 MPa H_2 using Ni-CMC colloids, respectively.

2.3 Photocatalysts based on Metal-Organic Frameworks

Metal-organic frameworks (MOFs), also known as coordination polymers, are considered as an attractive class of porous compounds with broad application potential.[45] These three-dimensional hybrid materials are composed of inorganic metal clusters, the secondary building unit (SBU), and organic bridging ligands. The tunable chemical and physical properties of the active metal centers and the functional linkers, together with the permanent porosity, opens numerous possibilities for the design of heterogeneous photocatalysts. MOFs are classified as (1) photocatalysts, (2) co-catalysts, and (3) host materials for photoredox catalysts depending on their function in the respective photocatalyst system.
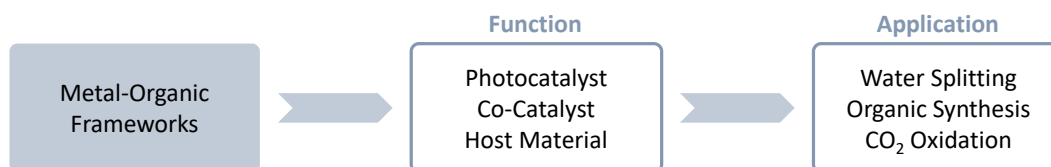
Figure 2.2 Overview of photocatalytic applications and the possible functions of MOFs.

(1) A MOF is defined as active photocatalyst when light absorption by the MOF itself generates free charge carriers for subsequent photoredox reactions. Upon irradiation of NH_2-Ti-MOF with visible light, the amino-functionalized terephthalate linker is excited so that photogenerated electrons are transferred to the titanium-oxo clusters of the SBU via linker-to-cluster charge transfer.[46] Co-catalytic Pt nanoparticles enhance this charge-separated state and drive the proton reduction to H_2. The Zr-based MOF Pt/NH_2-UiO-66 operates by a similar photocatalytic mechanism, highlighting that the choice of appropriate linkers can control the optical absorption properties of MOFs.[47] (2) MOFs are referred to as co-catalysts when a dye or semiconductor harvests the light while the MOF promotes the charge separation and catalytic reaction. Precisely, the zeolitic imidazolate frameworks (ZIFs) are suitable co-catalysts due to the catalytically active transition metal nodes (e.g., Co, Zn, Mn) and functional organic linkers.[48] Co-ZIF-9 was used in combination with both a molecular Ru photosensitizer and semiconducting CdS particles for the photocatalytic reduction of CO_2.[49] The ZIF promotes the visible light-driven charge separation and CO_2 enrichment within the porous catalyst through its adsorption ability. (3) Photocatalytically inactive MOFs are host materials and provide a platform for anchoring and encapsulating photoactive components within their porous structure. The functionalization with photoredox components or semiconductor materials can be performed either during the MOF synthesis or by post-synthetic modifications.[50] For example, a molecular Mn-terpyridine photosensitizer was encapsulated in the pores of the Cr-MOF MIL-101 for photocatalytic water oxidation. The pores of MIL-101 provide sufficient reaction volume and at the same time, the migration of the Mn complex is prevented due to its dimensions compared to the pore windows. The catalytic activity of the Mn catalyst was increased by a factor of 20 by encapsulation.[51] MIL-101 crystallites were also used as an inert structure-directing support material for the modification with a photoactive Au/TiO_2 shell.[52] This colloidal photocatalyst absorbs visible light due to a localized surface plasmon resonance of the

Au nanoparticles, ultimately transferring excited electrons into the conduction band of the TiO$_2$ semiconductor. This MOF-based photocatalyst enabled water reduction and wastewater purification with higher activities than Au-modified commercial TiO$_2$.

2.3.1 Combining Semiconductors and Metal Nanoparticles: Ni/CdS

The combination of metal nanoparticles and semiconductor materials is widely used in heterogeneous photocatalysis to increase the quantum yield of the catalyst system, which corresponds to an increased efficiency.[53] The photoexcitation of a semiconductor generates an electron-hole pair, whose lifetime is increased by a directional electron transfer to a neighboring metal particle. Due to the built-in electrical potential across the semiconductor/metal interface, the nanoparticle acts as an efficient electron trap and significantly decreases the charge carrier recombination rate. Thereafter, spatially separated redox reactions are catalyzed where the metal particle can additionally serve as an active reduction co-catalyst for the electron transfer to a substrate. Frequently, the noble metal Pt, also known for its suitability as an H$_2$-evolution co-catalyst[54], has been applied as an electron trap in combination with the UV-semiconductor TiO$_2$. The combination of the 3d metal Ni and CdS, a semiconductor absorbing in the visible spectral range, also operates according to this principle since the Fermi levels of the two solids are appropriately aligned.[24a+55] The upgrading of biomass-based organic compounds and the simultaneous release of molecular H$_2$ as a clean fuel is of great interest in heterogeneous photocatalysis. The acceptorless alcohol splitting with Ni/CdS represents such a process since the alcohol is split into the corresponding carbonyl compound and one equivalent H$_2$ without the requirement of sacrificial agents.[56] The activated carbonyl functionality can then be used in follow-up reactions, such as C-N bond formation. The acceptorless amine dehydrogenation accompanied by the formation of the homocoupled imine is likewise possible with Ni/CdS as a photocatalyst supported on MIL-101 in an inert gas atmosphere.[57]

2.3.2 Doping MOFs with Molecular Iridium Photosensitizers

Many homogeneous photosensitizers are based on the heteroleptic [Ir(bpy)(ppy)$_2$]$^+$ motif (bpy: 2,2'-bipyridine, ppy: 2-phenylpyridine) with Ir(III) as the central metal atom.[58] These Ir complexes are characterized by a long-living triplet state, which can be accessed by intersystem crossing after optical excitation. Proceeding from this state, redox reactions can be catalyzed by oxidative or reductive quenching. The photocatalytic H$_2$ evolution from water via the reductive quenching pathway was studied in detail using triethylamine (TEA) as the sacrificial agent.[59] As electron relay or water reduction catalyst - typically used to facilitate the electron transfer to the substrate - a wide variety of compounds including methyl viologen and Fe, Co, and Ni complexes were applied.[60] *Lin and coworkers* doped UiO-67 with the [Ir(bpy)(ppy)$_2$]$^+$ photosensitizer by partially replacing the linker of the pristine MOF with a bpy-modified dicarboxylate to match the ligand backbone of the

complex. The photo-functionalized MOF was used for the aza-Henry reaction, the oxidation of water and the reduction of CO_2.[61] Furthermore, MOFs provide a unique platform for the hierarchical integration of multiple components to target synergistic effects that cannot be achieved in solution. A Zr-carboxylate MOF was built from $[Ir(ppy)_2(bpy)]^+$-derived dicarboxylate and additionally loaded with Pt nanoparticles in situ.[54a] The photoinjection of electrons from the phosphorescent MOF onto the metal nanoparticles enhanced the H_2 evolution rate via TEA-mediated reduction of protons. Ni-containing polyoxometalates (POM, $[Ni_4(H_2O)_2(PW_9O_{34})_2]^{10-}$) were also encapsulated in a phosphorescent $[Ir(bpy)(ppy)_2]$@MOF so that the proximity between POM and Ir photosensitizers allowed a rapid electron transfer for H_2 evolution from water.[62] Quenching the phosphorescence of the Ir complex in solution with varying amounts of POM confirmed the directional electron transfer in the catalytic cycle.

2.4 References

[1]   M. Poliakoff, J. M. Fitzpatrick, T. R. Farren, P. T. Anastas, *Science* **2002**, *297*, 807-810.

[2]   P. T. Anastas, J. C. Warner, *Green Chemistry: Theory and Practice*, Oxford University Press: New York, **1998**.

[3]   P. T. Anastas, M. M. Kirchhoff, T. C. Williamson, *Appl. Catal. A Gen.* **2001**, *221*, 3-13.

[4]   S. L. Y. Tang, R. L. Smith, M. Poliakoff, *Green Chem.* **2005**, *7*, 761-762.

[5]   P. T. Anastas, L. B. Bartlett, M. M. Kirchhoff, T. C. Williamson, *Catal. Today* **2000**, *55*, 11-22.

[6]   a) P. Gallezot, *Chem. Soc. Rev.* **2012**, *41*, 1538-1558; b) B. Voss, S. I. Andersen, E. Taarning, C. H. Christensen, *ChemSusChem* **2009**, *2*, 1152-1162.

[7]   a) C. E. Wyman, B. E. Dale, R. T. Elander, M. Holtzapple, M. R. Ladisch, Y. Y. Lee, *Bioresour. Technol.* **2005**, *96*, 1959-1966; b) R. J. Evans, T. A. Milne, M. N. Soltys, *J. Anal. Appl. Pyrolysis* **1986**, *9*, 207-236; c) A. S. Mamman, *Biofuels, Bioprod. Biorefin*. **2008**, *2*, 438-454; d) R. Rinaldi, F. Schüth, *ChemSusChem* **2009**, *2*, 1096-1107; e) R. Rinaldi, F. Schüth, *Energy Environ. Sci.* **2009**, 2, 610-626.

[8]   D. M. Alonso, J. Q. Bond. J. A. Dumesic, *Green Chem.* **2010**, *12*, 1493-1513.

[9]   a) P. Gallezot, *Top. Catal*. **2010**, *53*, 1209-1213; b) P. Gallezot, *Catal. Today* **2011**, *167*, 31-36; c) R. Carrasquillo-Flores, M. Kälderström, F. Schüth, J. A. Dumesic, R. Rinaldi, *ACS Catal.* **2013**, *3*, 993-997; d) T. P. Vispute, H. Zhang, A. Sanna, R. Xiao, G. W. Huber, *Science* **2010**, *330*, 1222-1227.

[10]   a) C. Gunanathan, D. Milstein, *Science* **2013**, *341*, 1229712; b) S. Michlik; R. Kempe, *Nat. Chem.* **2013**, *5*, 140-144; c) S. Michlik, R. Kempe, *Angew. Chem. Int. Ed.* **2013**, *52*, 6326-6329; d) S. Ruch, T. Irrgang, R. Kempe, *Chem. Eur. J.* **2014**, *20*, 13279-13285; e) T. Hille, T. Irrgang, R. Kempe, *Chem. Eur. J.* **2014**, *20*, 5569-5572; f) N. Deibl, K. Ament, R. Kempe, *J. Am. Chem. Soc.* **2015**, *137*, 12804-12807; g) T. Hille, T. Irrgang, R. Kempe, *Angew. Chem. Int. Ed.* **2017**, *56*, 371-374.

[11]   a) G. A. Filonenko, R. van Putten, E. J. M. Hensen, E. A. Pidko, *Chem. Soc. Rev.* **2018**, *47*, 1459-1483; b) N. Gorgas, B. Stöger, L. F. Veiros, E. Pittenhauer, G. Allmaier, K. Kirchner, *Organometallics* **2014**, *33*, 6132-6140; c) S. Rösler, M. Ertl, T. Irrgang, R. Kempe, *Angew. Chem. Int. Ed.* **2015**, *54*, 15046-15050; d) S. Rösler, J. Obenauf, R. Kempe, *J. Am. Chem. Soc.* **2015**, *137*, 7998-8001; e) N. Gorgas, B. Stöger, L. F. Veiros, K. Kirchner, *ACS Catal.* **2016**, *6*, 2664-2672; f) M. Mastalir, M. Glatz, E. Pittenauer, G. Allmaier, K. Kirchner, *J. Am. Chem. Soc.* **2016**, *138*, 15543-15546; g) P. Daw, S. Chakraborty, J. A. Garg, Y. Ben-David, D. Milstein, *Angew. Chem. Int. Ed.* **2016**, *55*, 14373-14377; h) N. Deibl, R. Kempe, *J. Am. Chem. Soc.* **2016**, *138*, 10786-10789; i) N. Deibl, R. Kempe, *Angew. Chem. Int. Ed.* **2017**, *56*, 1663-1666; j) F. Kallmeier, R. Kempe, *Angew. Chem. Int. Ed.* **2017**, *56*, 7261-7265; k) F. Kallmeier, R. Kempe, *Angew. Chem. Int. Ed.* **2018**, *130*, 46-60; l) R. Fertig, T. Irrgang, F. Freitag, J. Zander, R. Kempe, *ACS Catal.* **2018**, *8*, 8525-8530.

[12]   R. Bullock, *Science* **2013**, *342*, 1054-1055.

[13]   a) R. V. Jagadeesh, A.-E. Surkus, H. Junge, M.-M. Pohl, J. Radnik, J. Rabeah, H. Huan, V. Schünemann, A. Brückner, M. Beller, *Science* **2013**, *342*, 1073-1076; b) C. Bäumler, R. Kempe, *Chem. Eur. J.* **2018**, *24*, 8989-8993; c) C. Bäumler, C. Bauer, R. Kempe, *ChemSusChem* **2020**, *13*, 3110-3114.

[14]   a) F. A. Westerhaus, R. V. Jagadeesh, G. Wienhöfer, M.-M. Pohl, J. Radnik, A.-E. Surkus, J. Rabeah, K. Junge, H. Junge, M. Nielsen, A. Brückner, M. Beller, *Nat. Chem.* **2012**, *5*, 537-543; b) T. Schwob, R. Kempe, *Angew. Chem. Int. Ed.* **2016**, *48*, 15175-15179; c) R. V. Jagadeesh, K. Murugesan, A. S. Alshammari, H. Neumann, M.-M. Pohl, J. Radnik, M. Beller, *Science* **2017**, *358*, 326-332; d) T. Senthamarai, V. G. Chandrashekhar, M. B. Gawande, N. V. Kalevaru, R. Zboril, P. C. J. Kamer, R. V. Jagadeesh, M. Beller, *Chem. Sci.* **2020**, *11*, 2973-2981; e) M. Elfinger, T. Schönauer, S. Thomä, R. Stäglich, M. Zobel, J. Senker, M. Drechsler, R. Kempe, *ChemSusChem* **2021**, 10.1002/cssc.202100553.

[15]   a) A. Corma, P. Serna, P. Concepción, J. J. Calvino, *J. Am. Chem. Soc.* **2008**, *130*, 8748-8753; b) G. Hahn, J.-K. Ewert, C. Denner, D. Tilgner, R. Kempe, *ChemCatChem* **2016**, *8*, 2461-2465; c) G. Hahn. P. Kunnas, N. de Jonge, R. Kempe, *Nat. Catal.* **2019**, *2*, 71-77; d) Y. Zhang, H. Yang, Q. Chi, Z. Zhang, *ChemSusChem* **2019**, *12*, 1246-1255.

[16]   D. Formenti, F. Ferretti, F. K. Scharnagl, M. Beller, *Chem. Rev.* **2019**, *119*, 2611-2680.

[17]   a) T. Irrgang, R. Kempe, *Chem. Rev.* **2020**, *120*, 9583-9674; b) K. Murugesan, T. Senthamarai, V. G. Chandrashekhar, K. Natte, P. C. J. Kamer, M. Beller, R. V. Jagadeesh, *Chem. Soc. Rev.* **2020**, *49*, 6273-6328.

[18]   C. Judson King, *Ullmann's Encyclopedia of Industrial Chemistry*, Wiley-VCH: Weinheim, **2007**.

[19]   D. Ravelli, D. Dondi, M. Fagnoni, A. Albini, *Chem. Soc. Rev.* **2009**, *38*, 1999-2011.

[20]   D. M. Schultz, T. P. Yoon, *Science* **2014**, *343*, 1239176.

[21]   a) A. Fujishima, K. Honda, *Nature* **1972**, *238*, 37-38; b) J. A. Turner, *Science* **2004**, *305*, 972-974.

[22]   P. Du, R. Eisenberg, *Energy Environ. Sci.* **2012**, *5*, 6012-6021.

[23]   X. Lang, X. Chen, J. Zhao, *Chem. Soc. Rev.* **2014**, *43*, 473-486.

[24]   a) G. Han, Y.-H. Jin, R. A. Burgess, N. E. Dickenson, X.-M. Cao, Y. Sun, *J. Am. Chem. Soc.* **2017**, *139*, 15584-15587; b) S. Xu, P. Zhou, Z. Zhang, C. Yang, B. Zhang, K. Deng, S. Bottle, H. Zhu, *J. Am. Chem. Soc.* **2017**, *139*, 14775-14782.

[25]   a) P. Sabatier, J. B. Senderens, *Comptes Rendus Acad. Sci.* **1897**, *124*, 1358-1361; b) P. Sabatier, *Librairie Polytechnique*: Paris, **1913**.

[26]   https://www.nobelprize.org/prizes/chemistry/1912/summary/, accessed on 03.06.2021.

[27]   M. Raney, *U.S. Patent* **1927**, 1628190.

[28]   a) L. K. Keefer,G. Lunn, *Chem. Rev.* **1989**, *89*, 459-502; b) Y. Gao, Y. Dinh, *Chem. Eur. J.* **2020**, *26*, 8845-8856.

[29]   a) T. Osawa, Y. Tamaru, *Modern Organonickel Chemistry*, Wiley-VCH: Weinheim, **2005**; b) K. Weissermel, H.-J. Arpe, *Industrial Organic Chemistry*, Wiley-VCH: Weinheim, **2003**.

[30]   a) Q. Sing, F. Wang, J. Xu, *Chem. Commun.* **2012**, *48*, 7019-7021; b) M. Zaheer, J. Hermannsdörfer, W. Kretschmer, G. Motz, R. Kempe, *ChemCatChem* **2013**, *6*, 91-95.

[31]   B. Lipshutz, *Adv. Synth. Catal.* **2001**, *343*, 313-326.

[32]   a) A. Finiels, F. Fajula, V. Hulea, *Catal. Sci. Technol*, **2014**, *4*, 2412-2426; b) S. Forget, H. Olivier-Bourbigou, D. Delcroix, *ChemCatChem* **2017**, *9*, 2408-2417.

[33]   P. Ryabchuk, G. Agostini, M.-M. Pohl, H. Lund, A. Agapova, H. Junge, K. Junge, M. Beller, *Sci. Adv.* **2018**, *4*: eaat0761.

[34]   G. Mignonac, *Compt. Rend.* **1921**, *172*, 223-226.

[35]   a) C. F. Winans, *J. Am. Chem. Soc.* **1939**, *61*, 3566–3567; b) E. J. Schwoegler, H. Adkins, *J. Am. Chem. Soc.* **1939**, *61*, 3499–3502; c) A. S. C. Chan, C.-c. Chen, Y.-c. Lin, *Appl. Catal. A* **1994**, *119*, L1-L5.

[36]   K. Murugesan, M. Beller, R. Jagadeesh, *Angew. Chem. Int. Ed.* **2019**, *58*, 5064-5068.

[37]   O. I. Afanasyev, E. Kuchuk, D. L. Usanov, D. Chusov, *Chem. Rev.* **2019**, *119*, 11857-11911.

[38]   Y. Zhang, H. Yang, Q. Chi, Z. Zhang, *ChemSusChem* **2019**, *12*, 1246-1255.

[39]   a) M. Guerrero, N. T. Than Chau, S. Noel, A. Denicourt-Nowicki, F. Hapiot, A. Roucoux, E. Monflier, K. Philippot, *Curr. Org. Chem.* **2013**, *17*, 364-399; b) B. L. Albuquerque, A. Denicourt-Nowicki, C. Mériadec, J. B. Domingos, A. Roucoux, *J. Catal.* **2016**, *340*, 144-153; c) M. Tamura, K. Tokonami, Y. Nakagawa, K. Tomishige, *ACS Catal.* **2016**, *6*, 3600-3609; d) H. Adkins, H. R. Billica, *J. Am. Chem. Soc.* **1948**, *70*, 695-698; e) A. F. Barrero, E. J. Alvarez-Manzaneda, R. Chahboun, R. Meneses, *Synlett.* **1999**, *10*, 1663-1666.

[40]   M. G. Prakash, R. Mahalakshmy, K. R. Krishnamurthy, B. Viswanathan, *Catal. Sci. Technol.* **2015**, *5*, 3313-3321.

[41]   J.-q. Bai, M. Tamura, Y. Nakagawa, K. Tomishige, *Chem. Commun*. **2019**, *55*, 10519-10522.

[42]   a) K. O. Sebakhy, G. Vitale, P. Pereira- Almao, *Ind. Eng. Chem. Res*. **2019**, *58*, 8597-8611; b) M. Li, J. Fu, S. Xing, L. Yang, X. Zhang, P. Lv, Z. Wang, Z. Yuan, *Appl. Catal. B* **2020**, *260*, 118114-118119.

[43]   L. Zaramello, B. L. Albuquerque, J. B. Domingos, *Dalton Trans*. **2017**, *46*, 5082-5090.

[44]   M. A. Harrad, P. Valerga, M. C. Puerta, I. Houssini, M. A. Ali, L. El Firdoussi, A. Karim, *Molecules* **2011**, *16*, 367-372.

[45]   S. Kitagawa, R. Kitaura, S.-i. Noro, *Angew. Chem. Int. Ed*. **2004**, *43*, 2334-2375.

[46]   Y. Horiuchi, T. Toyao, M. Saito, K. Mochizuki, M. Iwata, H. Higashimura, M. Anpo, M. Matsuoka, *J. Phys. Chem. C* **2012**, *116*, 20848.

[47]   C. G. Silva, I. Luz, F. X. Llabrés i Xamena, A. Corma , H. García , *Chem. Eur. J.* **2010**, *16*, 11133-11138.

[48]   K. S. Park, Z. Ni, A. P. Côté, J. Y. Choi, R. Huang, F. J. Uribe-Romo, H. K. Chae, M. O'Keeffe, O. M. Yaghi, *Proc. Natl. Acad. Sci. USA* **2006**, *103*, 10186-10191.

[49]   a) S. Wang, W. Yao, J. Lin, Z. Ding, X. Wang, *Angew. Chem. Int. Ed.* **2014**, *126*, 1052-1056; b) S. Wang, X. Wang, *Appl. Catal. B: Environ*. **2015**, *162*, 494-500.

[50]   a) M. O'Keeffe, O. M. Yaghi, *Chem. Rev*. **2012**, *112*, 675-702; b) S. M. Cohen, *Chem. Rev*. **2012**, 112, 970-1000.

[51]   B. Nepal, S. Das, *Angew. Chem. Int. Ed*. **2013**, *52*, 7224-7368.

[52]   D. Tilgner, R. Kempe, *Chem. Eur. J.* **2017**, *23*, 3184-3190.

[53]   a) Y. Z. Yang, C.-H. Chang, H. Idriss, *Appl. Catal. B* **2006**, *67*, 217-222; b) Y. Shiraishi, Y. Sugano, S. Tanaka, T. Hirai, *Angew. Chem. Int. Ed.* **2010**, *49*, 1656-1660.

[54]   a) C. Wang, K. E. deKrafft, W. Lin, *J. Am. Chem. Soc*. **2012**, *134*, 7211-7214; b) M. Wen, K. Mori, T. Kamegawa, H. Yamashita, *Chem. Commun*. **2014**, *50*, 11645-11648.

[55]   a) M. Luo, Y. Liu, J. Hu, H. Liu, J. Li, *ACS Appl. Mater. Interfaces* **2012**, *4*, 1813-1821; b) T. Simon, N. Bouchonville, M. J. Berr, A. Vaneski, A. Adrovic, D. Volbers, R. Wyrwich, M. Döblinger, A. S. Susha, A. L. Rogach, F. Jäckel, J. K. Stolarczyk, J. Feldmann, *Nat. Mater*. **2014**, *13*, 1013–1018; c) Y. Xu, R. Xu, *Appl. Surf. Sci*. **2015**, *351*, 779–793; d) S. Cao, C.-J. Wang, X.-J. Lv, Y. Chen, W.-F. Fu, *Appl. Catal. B Environ*. **2015**, *162*, 381-391; e) O. Quiroz-Cardoso, S. Oros-Ruiz, A. Solis-Gomez, R. Lopez, R. Gomez, *Fuel* **2019**, *237*, 227-235.

[56]   a) Z. Chai, T.-T. Zeng, Q. Li, L.-Q- Lu, W.-J. Xiao, D. Xu, *J. Am. Chem. Soc*. **2016**, *138*, 10128-10131; b) D. Tilgner, M. Klarner, S. Hammon, M. Friedrich, A. Verch, N. de Jonge, S. Kümmel, R. Kempe, *Aust. J. Chem*. **2019**, *72*, 842-847; c) R. Wu, S. Wang, Y. Zhou, J. Long, F. Dong, W. Zhang, *ACS Appl. Nano Mater*. **2019**, *2*, 6818-6827.

[57]   a) M. Klarner, S. Hammon, S. Feulner, S. Kümmel, L. Kador, R. Kempe, *ChemCatChem* **2020**, *12*, 4593-4599; b) Y. Huang, C. Liu, M. Li, H. Li, Y. Li, R. Su, B. Zhang, *ACS Catal*. **2020**, *10*, 3904-3910.

[58]   a) J. D. Slinker, A. A. Gorodetsky, M. S. Lowry, J. Wang, S. Parker, R. Rohl, S. Bernhard, G. G. Malliaras, *J. Am. Chem. Soc*. **2004**, *126*, 2763-2767; b) F. Petronijevic, M. Nappi, D. W. C. MacMillan, *J. Am. Chem. Soc*. **2013**, *135*, 18323-18326; c) Z. Zuo, D. T. Ahneman, L. Chu, J. A. Terrett, A. G. Dolye, D. W. C. MacMillan, *Science* **2014**, *345*, 437-440; d) T. Kim, S. J. McCarver, C. Lee, D. W. C. MacMillan, *Angew. Chem. Int. Ed*. **2018**, *130*, 3546-3550.

[59]   S. I. Bokarev, D. Hollmann, A. Pazidis, A. Neubauer, J. Radnik, O. Kühn, S. Lochbrunner, H. Junge, M. Beller, A. Brückner, *Phys. Chem. Chem. Phys*. **2014**, *16*, 4789-4796.

[60]   L. L. Tinker, N. D. McDaniel, P. N. Curtin, C. K. Smith, M. J. Ireland, S. Bernhard, *Chem. Eur. J.* **2007**, *13*, 8726-8732.

[61]   C. Wang, Z. Xie, K. E. deKrafft, W. Lin, *J. Am. Chem. Soc.* **2011**, *133*, 13445-13454.

[62]   X.-J. Kong, Z. Lin, Z.-M. Zhang, T. Zhang, W. Lin, *Angew. Chem. Int. Ed.* **2016**, *55*, 6411-6416.

3 Overview of Thesis Results

The thesis consists of four publications, which are presented in chapter 4 to 7. Chapter 3.1 gives an overview of the individual publications of this thesis and discusses them in an overall context. The individual contributions to joint publications are detailed in chapter 3.2.

3.1 Synopsis

Heterogeneous catalysis is considered as a key technology of the chemical industry. Replacing noble metals with base metals in catalyst materials makes a decisive contribution to sustainability and also opens up new selectivity patterns in heterogeneously catalyzed reactions. In recent years, *Kempe and coworkers* have successfully focused their research on earth-abundant metal catalysts for hydrogenation and dehydrogenation reactions. Certain nanostructured catalysts based on porous support materials were developed for chemoselective hydrogenations and consecutive organic follow-up reactions. Transition metal-salen complexes were successfully used as precursors to generate small, catalytically active nanoparticles. In the field of photocatalysis, several systems have been developed based on the porous metal organic framework MIL-101 as support material. For example, the degradation of pollutants from wastewater and the proton reduction in water were catalyzed upon irradiation with visible light. In particular, nickel proved to be a promising (co-)catalyst in both thermal hydrogenation reactions and photocatalytic dehydrogenation reactions. This dissertation is motivated to discuss nickel nanoparticles as catalyst constituent in these two areas of catalysis and to highlight the outstanding catalytic performance of this earth-abundant transition metal in (de-)hydrogenations.

In recent years, the *Kempe group* has focused on selective hydrogenation reactions using monometallic catalyst systems based on the elements iron, cobalt and nickel. Of particular note is the work of *Hahn et al.* who described a Ni/Al_2O_3 catalyst for the reductive amination of carbonyl compounds using aqueous ammonia and hydrogen as reducing agent. The catalyst operated at mild reaction conditions, was reusable, and showed an exceptional tolerance to functional groups. The combination of the γ-Al_2O_3 support material and a specific nickel precursor, namely a Ni-salen complex, was crucial to achieve a high catalyst activity. At this time, we did not understand the role of the salen complex during the active catalyst formation and were interested in whether the activity of the catalyst could be enhanced by the appropriate choice of the nickel precursor. For this purpose, we developed a library of six Ni-salen complexes, which were used as precursors for six Ni/Al_2O_3 catalysts. As outlined in Figure 3.1, the Ni-salen complexes C1 to C6 were obtained by fine-tuning the steric properties and carbon and nitrogen content by selecting suitable amine precursors and ring substituents.
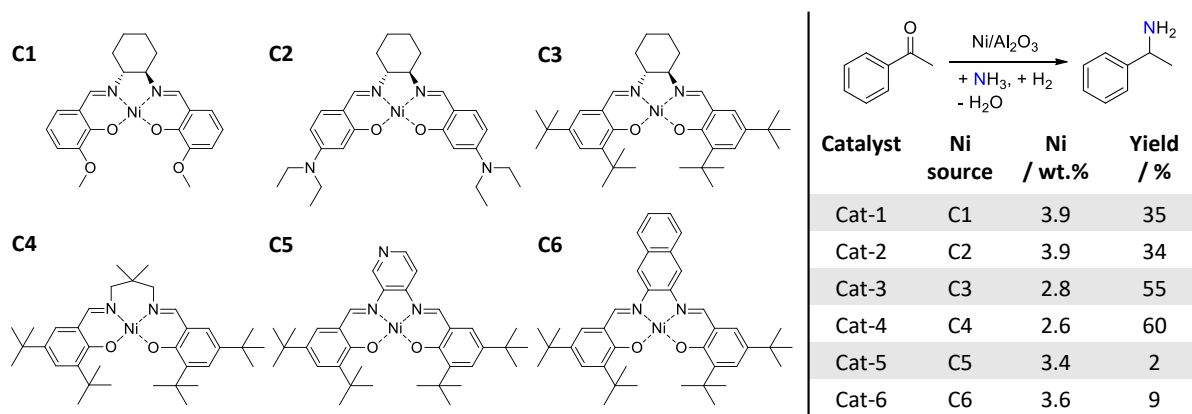
Figure 3.1. A library of six Ni-salen complex precursors (left). The catalytic activity of Ni/Al$_2$O$_3$ catalysts was studied in the reductive amination of acetophenone depending on the Ni source (right). 1.2 mol% Ni/Al$_2$O$_3$ catalyst (0.006 mmol Ni, 0.35 mg Ni), 0.5 mmol acetophenone, 0.5 mL aq. NH$_3$ (25 %, 6.7 mmol), 2 mL H$_2$O, 80 °C, 0.5 MPa H$_2$, 20 h. Yields were determined by gas chromatography using *n*-dodecane as an internal standard. The Ni content was analyzed by ICP-OES.

The catalysts Cat-1 to Cat-6 were prepared by wet-impregnation of the Al$_2$O$_3$ support with 4 wt.% Ni in form of the respective Ni-salen precursor, followed by a pyrolysis step in N$_2$ flow at 700 °C and a reduction step at 550 °C in forming gas. The catalyst activity was investigated in the reductive amination of acetophenone as a catalytic benchmark test. For comparability, we chose the reaction conditions such that complete conversion of the reactant did not occur: 1.2 mol% Ni, 0.5 MPa H$_2$ pressure and 80 °C. In terms of activity, the Ni/Al$_2$O$_3$ catalysts could be classified as highly active (Cat-3 and Cat-4), moderately active (Cat-1 and Cat-2), and nearly inactive (Cat-5 and Cat-6). The Ni content of the systems was determined by ICP-OES analysis to be less than the targeted 4 wt.%. This could be explained by the volatility of the salen complexes above 400 °C during the pyrolysis step in the catalyst preparation.
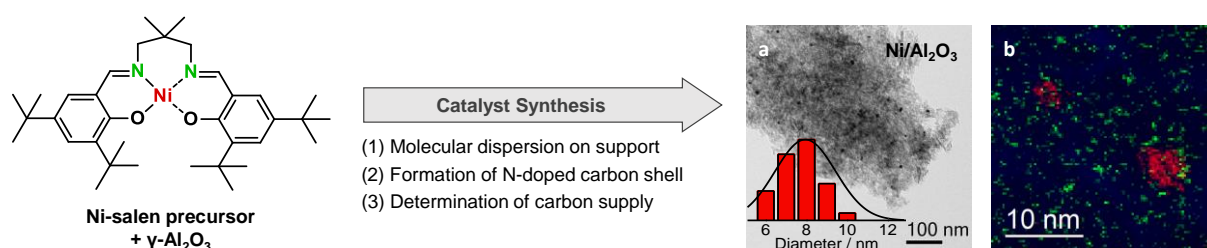
Figure 3.2. The key role of Ni-salen(prop)(di-*tert*-butyl) as metal precursor during the catalyst synthesis. (a) TEM image of the Ni/Al$_2$O$_3$ catalyst with size distribution of nickel particles. (b) Overlayed EELS element maps of nickel (red), carbon (blue) and nitrogen (green) demonstrated the embedding of nickel particles in a nitrogen-doped carbon matrix.

We discovered a clear dependence of the performance of Ni/Al$_2$O$_3$ catalysts on the Ni complex precursor. Neither the Ni content, nor the Ni particle size determined by TEM allowed us to conclude the cause of the activity differences in the reductive amination. Therefore, we aimed at least at the identification of the key properties of the Ni-salen complex during the catalyst formation taking the most active Ni/Al$_2$O$_3$ catalyst Cat-4 and its precursor compound C4 Ni-salen(prop)(di-*tert*-butyl) as an

example. The following three key properties were identified: (1) Molecular dispersion of the metal precursor on the support material. Initial TEM analysis of C4/Al_2O_3 showed that the applied wet-impregnation method did not result in a molecular dispersion of the Ni-salen complex on the Al_2O_3 support. Rather, needles of C4 crystallized starting from Al_2O_3 agglomerates as crystallization nuclei. Accordingly, the volatility of C4 during the pyrolysis step was crucial, favoring a high dispersion on the support by deposition from the gas phase. The subsequent decomposition led to small Ni nanoparticles with an average size of 8 nm (Figure 3.2 a). As already mentioned, we found a reduced Ni content of 2.6 wt.%, which conversely meant that 65 % of the Ni precursor has decomposed on the support material. This gave a first indication of an attractive interaction between γ-Al_2O_3 and the Ni-salen complex considering the almost quantitative sublimation of the pure C4 (Figure 3.3 a). Complementary DRIFTS analyses confirmed an interaction of the surface acidic Al_3-OH sites, centered at a wavenumber of 3696 cm^{-1}, with the Ni-salen complex. The absence of the characteristic Al_3-OH band in the spectrum after heating impregnated C4/Al_2O_3 according to the standard pyrolysis conditions, indicated an interaction of the surface absorbed complex with the acidic centers (Figure 3.3 b). Based on the present data, we assumed that the volatility of the Ni-salen complex together with the attractive interaction to Al_2O_3 is beneficial for the formation of catalytically active metal sites.
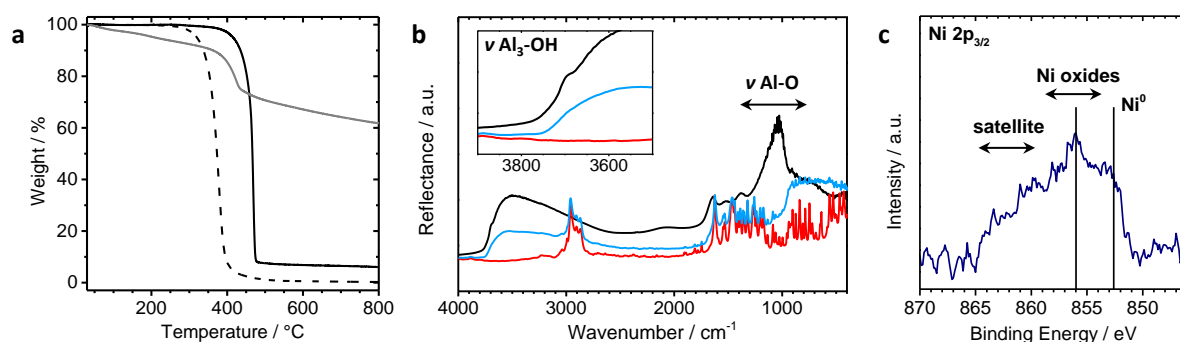
Figure 3.3. (a) TGA analysis of the salen ligand L4 (dashed), the Ni-salen complex C4 (black) and the impregnated C4/Al_2O_3 (grey). (b) DRIFTS analysis of γ-Al_2O_3 (black), Ni-salen complex C4 (red) and the impregnated C4/Al_2O_3 heated to the sublimation temperature. (c) XPS analysis of the Ni 2p$_{3/2}$ region of Ni/Al_2O_3.

(2) Formation of a nitrogen-doped carbon shell for the stabilization of nickel nanoparticles. The EDX analysis of the Ni/Al_2O_3 catalyst and overlapping EELS element maps of the near environment of two Ni nanoparticles (Figure 3.2 b) revealed the latter embedded in a nitrogen-doped carbon matrix covering the entire support material. Further XPS analysis gave a small signal for nitrogen in the N 1s region, which may be a remanent of the salen ligand or its decomposition products. The analysis of the Ni 2p$_{3/2}$ region (Figure 3.2 c) indicated the combination of a metallic Ni^0 signal located at 852.6 eV and a broad signal located at around 854.6 eV which we assigned to oxidized Ni^{2+}. According to this, the particles were surface oxidized Ni nanoparticles. We concluded, from EELS and XPS investigations that N-doped carbon layer is formed by the decomposition of the salen ligand during the catalyst generation.

We assume that this layer is necessary for the particle stabilization, with the appropriate layer thickness defined by the pyrolysis process. (3) Determination of the carbon supply during the pyrolysis step. We observed the formation of carbon nanotubes when the pyrolysis of impregnated C4/Al_2O_3 is carried out in a sealed glass ampoule with confined gas space. As the sublimation of complex C4 is partially suppressed, carbon nanotubes with a diameter of 30-40 nm grew starting from metal particles of the same size. It is conceivable that excess carbon in the form of the salen ligand and its decomposition products could not be removed due to the lack of a constant gas flow. In addition, the magnitude of the gas flow in the standard catalyst synthesis process was identified as a decisive pyrolysis parameter since the removal of the gaseous intermediates is reduced. The activity of a Ni/Al_2O_3 catalyst prepared at a very low gas flow significantly collapsed in the reductive amination. This led us to conclude that the volatility of the Ni-salen complex in combination with judiciously chosen pyrolysis parameters regulated the carbon supply during catalyst preparation.

We were motivated to develop a novel nickel catalyst for the selective hydrogenation of olefins based on the observation that the catalytic activity of nanostructured nickel catalysts can be promoted via the choice of the Ni-salen precursor. The results of our previous study on the Ni/Al_2O_3 system prompted us to use the coordination compound Ni-salen(prop)(di-*tert*-butyl) as metal precursor. For a sustainable catalysis concept, not only earth-abundant metals but also low-cost supports should be used. Following this idea, the Ni-salen complex was combined with an activated carbon support to synthesize the Ni/C catalyst in a practical two-step process, depicted in Figure 3.4. After wet-impregnation of the carbon support with the Ni-salen complex, a pyrolysis step was performed in constant N_2 flow at 700 °C and followed by a reduction step at 550 °C in forming gas.
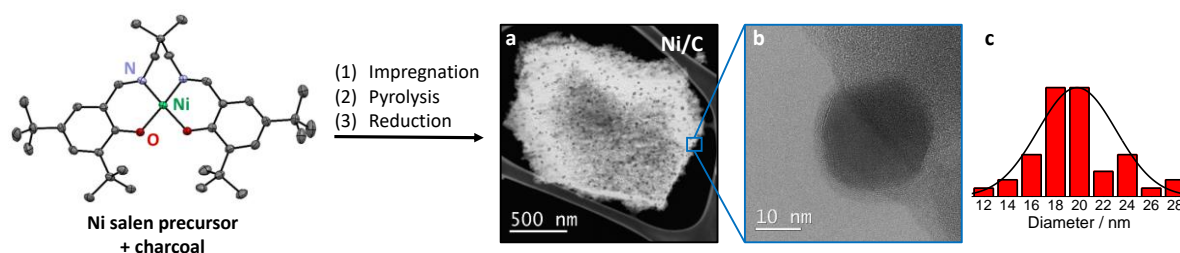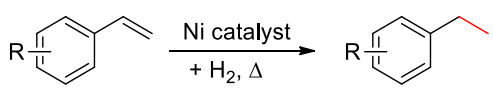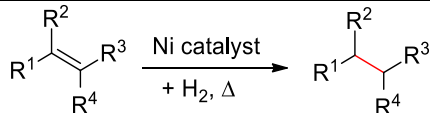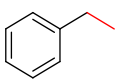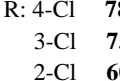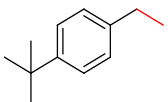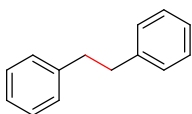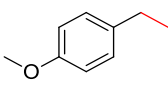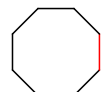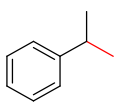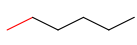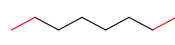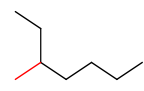

Figure 3.4. Synthesis concept of the Ni/C catalyst. (a) HAADF-TEM analysis of the Ni/C catalyst. (b) Magnification by TEM showed a single Ni nanoparticle surrounded by a carbon layer. (d) Size distribution of Ni particles with a mean diameter of 19.5 nm.

By HAADF-STEM analysis of the catalyst material, Ni nanoparticles with an average size of 19.5 nm were observed homogeneously distributed on the support with a rather broad size distribution (Figure 3.4 a, c). Figure 3.4 b is a detailed TEM analysis of a single Ni nanoparticle that is covered by a 2-3 nm thick carbon layer. Elemental analysis of the Ni/C catalyst confirmed that 0.8 wt.% nitrogen from the decomposition of the salen ligand was present. As shown in our previous study, we believed that the tailored decomposition of the salen precursor led to a nitrogen-doped carbon layer that

embedded the Ni nanoparticles on the support. ICP-OES analysis revealed a nickel content of 2.7 wt.%. We performed XPS analyses to gain more insight into the catalyst material. In the Ni $2p_{3/2}$ region, the combination of metallic Ni (852.6 eV) and oxidized Ni^{2+} (854.6 eV) was measured, with an intensity ratio of 83 % Ni^0. Together with the reflections of cubic Ni^0 indexed in the PXRD pattern, this supported our hypothesis of partially surface oxidized Ni nanoparticles with metallic core. The binding energy of the N 1s signal is centered at 398.5 eV, possibly pointing to a remanent of the nitrogen-containing Ni-salen precursor and its decomposition products. This low-cost and easy-to-use nickel catalyst was investigated in the selective hydrogenation of C-C double bonds. The hydrogenation of styrene to ethylbenzene as a catalytic benchmark reaction proceeded with quantitative yield at conditions of 1.35 mol% Ni, 0.2 MPa H_2 and 40 °C. Even at 0.1 MPa H_2 and room temperature, a 50 % yield of ethylbenzene was obtained, which highlighted the hydrogenation activity of the Ni/C catalyst. In comparison with commercial oxidic support materials (Al_2O_3, CeO_2, SiO_2, TiO_2), the combination of the Ni-salen precursor and the activated carbon support was shown to be crucial for the high catalytic activity. Remarkably, only the catalyst on silica support showed moderate catalytic activity. Both, electron-withdrawing and -donating functional groups were well tolerated. Furthermore, pure aliphatic and aromatic olefins were selectively converted under slightly harsher conditions of 1 MPa H_2 and 80 °C to give the corresponding saturated products. Not only mono-substituted substrates but also more challenging 1,2- and 1,1-disubstituted olefins were hydrogenated in high yields (Table 3.1).

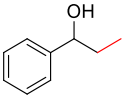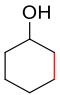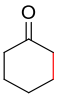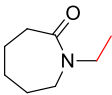**Table 3.1.** Hydrogenation of styrene derivatives and non-functionalized olefins with Ni/C.[a]
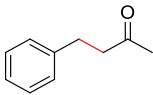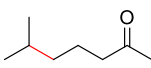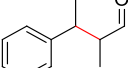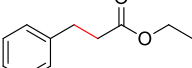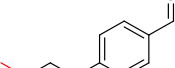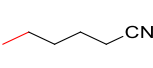
[a] 0.5 mmol substrate, 2.5 ml MeOH, 1.35 mol% Ni (14.7 mg Ni/C, 2.7 wt.% Ni), 40 °C, 0.2 MPa H_2, 20 h. Yields were determined by GC using *n*-dodecane as an internal standard. Products were analyzed by GC-MS.

To our delight, the Ni/C catalyst exhibited a high chemoselectivity in the hydrogenation of C-C double bonds in the presence of hydrogenation-sensitive functional groups. A total of 19 examples were smoothly converted, of which some representative examples are listed in Table 3.2. Alcohols, α,β-unsaturated carbonyl compounds, aldehydes, ethers and esters were tolerated in good to excellent yields applying 1.35 mol% Ni, 1 MPa H_2 and 80 °C. Noteworthy, the challenging tetra-substituted double bond in 2-methyl-3-phenylbutenal was selectively hydrogenated in good yields while the easily accessible aldehyde was not attacked. Only a minor trace of alcohol was observed as a byproduct. In

22

addition to the numerous examples of oxygen-containing functional groups, the C≡N triple bond of an aliphatic nitrile was tolerated.

Table 3.2 Hydrogenation of functionalized olefins with Ni/C.[a]

[a] 0.5 mmol substrate, 2.5 ml H_2O, 1.35 mol% Ni (14.7 mg Ni/C, 2.7 wt.% Ni), 80 °C, 1 MPa H_2, 20 h. [b] 2.5 ml MeOH. Yields were determined by GC using *n*-dodecane as an internal standard. Products were analyzed by GC-MS.

The catalyst could be reused for three consecutive cycles without any loss of activity. Thereafter, a slight decrease in the hydrogenation activity was observed, possibly due to leaching effects or deactivating oxidation of the nickel nanoparticles. In an up-scaling, the applicability of the Ni/C catalyst was also demonstrated on a larger scale, as 20 times the amount of styrene (10 mmol, 95 % ethylbenzene) was converted with only slightly reduced activity referred to the 0.5 mmol reaction.

In addition, the *Kempe group* addressed the visible light-driven upgrading of organic compounds. *Tilgner et al.* previously investigated the photocatalytic acceptorless dehydrogenation of alcohols using a Ni/CdS/TiO_2@MIL-101 catalyst. The simultaneous release of H_2 in such processes generates a highly attractive and clean byproduct. In this material, the photoexcitation occurs in the CdS component, and subsequent spatial electron-hole separation is controlled by the CdS/TiO_2 heterojunction. However, an efficient charge separation can also be achieved with co-catalytic metal particles bonded to the semiconducting CdS: After light excitation, the built-in electric field favors the directional electron transfer to the metal particle and reduces the probability of charge recombination. Therefore, we investigated the photocatalytic dehydrogenation of primary amines using a Ni/CdS@MIL-101 catalyst. The metal-organic framework MIL-101 served as the visible light inactive support material of the photocatalyst because it is stable to water and air, exhibits high porosity, and determines the overall size of the catalyst system for the efficient recyclability. The loading of MIL-101 with metal nanoparticles (Ni, Pd, Pt, Ir, Au) and semiconductor components (TiO_2, Fe_2O_3, CdS) for the catalyst synthesis has been established at our department for many years. MIL-101 as structural directing core was covered with CdS particles generated by a simple solvothermal route using DMSO as a sulfur source and cadmium acetate as Cd precursor. Cubic CdS crystallized in a particle size of 20-30 nm, and the lattice

plane was identified by TEM and PXRD. The band gap of CdS was determined by Munk-Kubelka to be 2.44 eV, so photons of wavelengths smaller than 510 nm are absorbed. For the final modification with Ni nanoparticles via MOCVD technique, nickelocene was used as a volatile nickel precursor for the gas phase infiltration and reduced to Ni^0 by hydrogen treatment. ICP-OES analysis verified 5.1 wt.% Ni in the synthesized catalyst material. The octahedral shape of the MIL-101 crystallites remained intact through all synthesis steps.
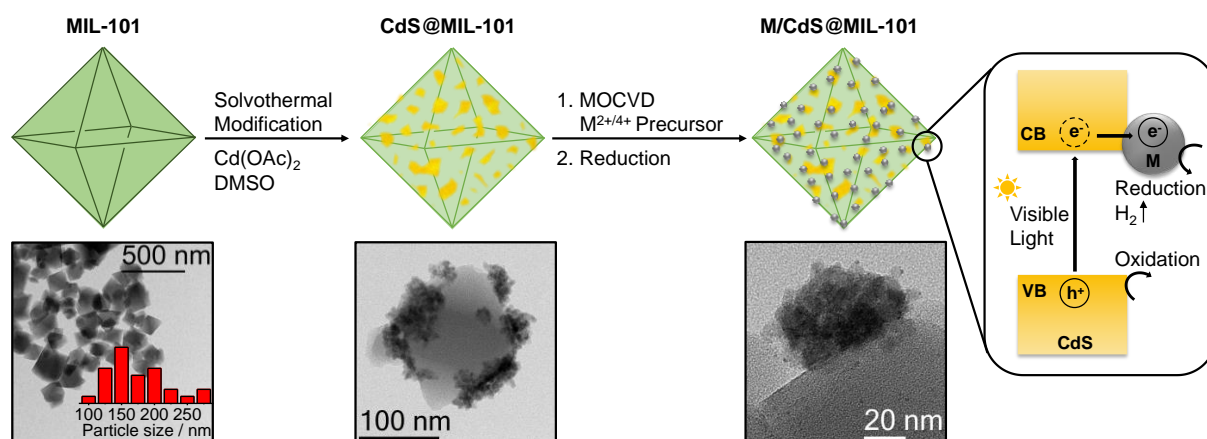

Figure 3.5. Synthesis of the photocatalyst M/CdS@MIL-101 (M: Ni, Pd, Pt). In the semiconductor CdS, the absorption of visible light promotes an electron from the valence band to the conduction band. After the directed electron transfer towards the metal particles, spatially separated redox reactions can be catalyzed. TEM images visualized the synthesis process in adapted magnifications.

The XPS survey showed characteristic elemental signals for Cr, O, and C of the MIL-101 support material and additional signals for Cd, S, and Ni, which formed the photoactive shell. The photocatalyst Ni/CdS@MIL-101 exhibited nearly constant absorbance throughout the visible range. As illustrated in Figure 3.5, we assumed that an electron-hole pair is generated within the semiconducting CdS upon visible light irradiation. After the directional electron transfer from the conduction band of CdS towards the Ni nanoparticle, spatially separated redox reactions can be catalyzed. The reduction half-reaction takes place on the surface of the nickel particles since metal particles are known to be electron reservoirs. The Ni/CdS@MIL-101 photocatalyst was applied in the dehydrogenation of benzylamine upon irradiation with visible light (blue LED, $\lambda=470$ nm). This is the first example of an additive-free and acceptorless amine oxidation with the simultaneous release of one equivalent of H_2 in inert gas atmosphere (Table 3.3). The aldimine formed intermediately by the dehydrogenation of benzylamine reacted with a second equivalent of benzylamine to give the homocoupled product N-benzyl-1-phenylmethanimine. The equimolar release of H_2 was detected by gas-chromatographic analysis of the reaction headspace. The photocatalytic nature of the reaction was confirmed by light-on-off experiments, as H_2 evolution occurred only under illumination. The noble metal-free Ni/CdS@MIL-101 catalyst led to a quantitative yield of imine, whereas byproducts were formed with bare CdS@MIL-101. To our delight, the Ni modified catalyst was recyclable over five consecutive runs.

Table 3.3. Photocatalytic acceptorless dehydrogenation of benzylamine.[a]

Catalyst	Yield / %	Yield H_2 / %
Ni/CdS@MIL-101	99	98
CdS@MIL-101	62	59
Without light	0	0
Without catalyst	0	0

[a] 1 mmol benzylamine, 1.5 mL MeCN, 10 h, 5 mg catalyst, rt, Ar, 470 nm blue LED (50 W). Yields were determined by GC using *n*-dodecane as an internal standard. H_2 was quantified by GC-TDC using methane as an internal standard.

In addition, we developed a general approach to prepare non-symmetric imines by cross-coupling with a second amine that is not attacked by the photocatalyst. As an example, this was investigated for the coupling of benzylamines with cyclohexylamine. The homocoupled imine was formed first, which was rearranged to the hetero-coupled imine in a non-photocatalytic equilibrium reaction. Under visible light irradiation, the equilibrium was shifted to the desired product as released benzylamine was reintroduced into the catalytic cycle. The modifications of CdS@MIL-101 with the noble metals Pd and Pt resulted predominantly in the formation of the symmetric imine in low yield, whereas Ni/CdS@MIL-101 produced mainly the non-symmetric imine. This demonstrated the superior performance of the Ni co-catalyst in the acceptorless dehydrogenation of benzylamine. Next, we were interested in the stability of the semiconducting CdS under catalysis conditions, since the photocorrosion of CdS is a frequently discussed phenomenon and a main challenge in the application of such photocatalysts. Pre- and post-catalytic XPS studies of the sulfur $S2p_{3/2}$ region of CdS@MIL-101 and Ni/CdS@MIL-101 demonstrated the stabilizing effect of the Ni nanoparticles on the CdS component (Figure 3.6 a). Regarding the ratio of metal sulfide (161.5 eV) to surface oxidized metal sulfate (168.7 eV) of the CdS@MIL-101 catalyst, the amount of surface sulfate increased significantly from 14 % pre- to 51 % post-catalysis. Post-catalytic PXRD analysis also indicated the formation of oxidized sulfur species, as several new reflections appeared in addition to the expected reflections of cubic CdS. By contrast, the ratio of sulfide (94 %) to sulfate (6 %) remained constant for pre- and post-catalytic Ni/CdS@MIL-101 as analyzed by XPS. Furthermore, the directional electron transfer from photoexcited CdS across the semiconductor-metal interface to Ni nanoparticles was investigated with fluorescence lifetime imaging microscopy in the frequency domain. In the semiconducting CdS, the absorption of visible light creates an electron-hole pair that recombines after an intrinsic lifetime by emitting a photon. Two lifetime components were identified in the study of M/CdS@MIL-101 materials: the shorter one is interpreted as the luminescence lifetime of CdS, while the longer one was attributed to MIL-101. The modification with Ni shortened the lifetime of CdS (115 ps) to 67 ps, confirming a second decay channel and thus the directional electron transfer (Figure 3.6 b). The charge carrier separation over two different catalyst components leads to the enhanced photocatalytic activity of Ni/CdS@MIL-101 in redox reactions.

Comparing the 3d metal Ni with the noble metals Pd and Pt, the lifetime of pure CdS is most affected by neighboring Ni particles, indicating a faster electron transfer to Ni particles than to Pd or Pt. Moreover, DFT calculations revealed a stronger binding of the substrate benzylamine to a 13-atom Ni icosahedral particle than to a 13-atom Pd icosahedral particle by several hundred meV. This may be advantageous for an efficient charge transfer between the photocatalyst and the substrate.
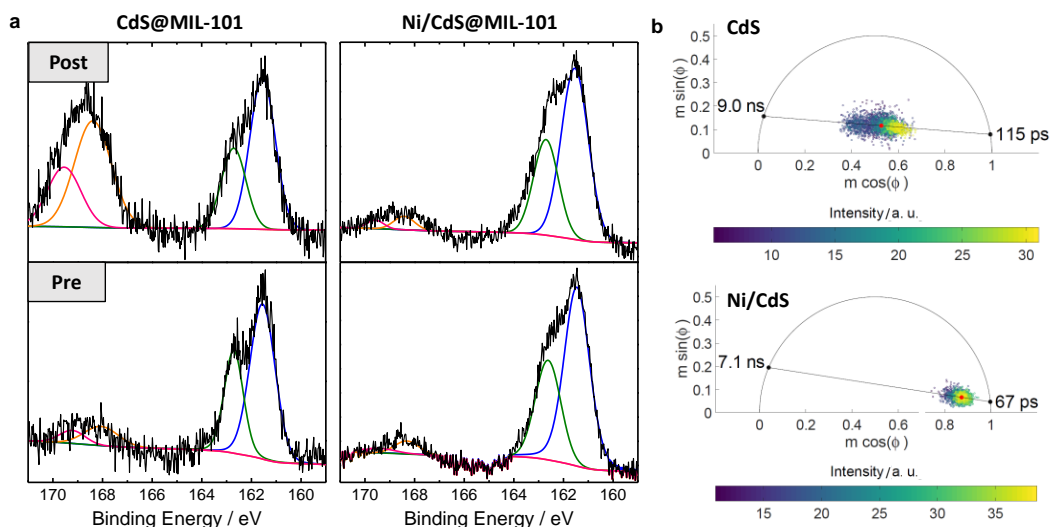

Figure 3.6. (a) Pre- and post-catalytic XPS analysis of S2p$_{3/2}$ region to investigate the photocatalytic stability of CdS@MIL-101 and Ni/CdS@MIL-101. The signal for metal sulfide (CdS) is centered at 161.5 eV and for metal sulfate (CdSO$_4$) at 168.7 eV. (b) Fluorescence lifetime studies of MIL-101 supported neat CdS and Ni/CdS. The shorter lifetime component refers to luminescence lifetime of excited CdS.

Apart from the combination of metallic nickel nanoparticles with a semiconducting material, we were also interested in cooperative effects between them and a molecular iridium photosensitizer. We used a ship-in-a-bottle approach (Figure 3.7) to bring the Ir-L1 complex, which is a modification of the literature-known [Ir(bpy)(ppy)$_2$]$^+$ motif, and metal nanoparticles into spatial proximity within the pores of the Cr-MOF MIL-101. This has already been addressed by *Friedrich* in preliminary work. The photosensitizer Ir-L1 was synthesized stepwise within the pores of MIL-101, which again served as a stable porous host material. The generation of coordinatively unsaturated sites by removing auxiliary water ligands at the secondary building unit of MIL-101 allowed the coordination of the OH-modified bipyridyl ligand L1. The anchoring of L1 by the hydroxyl group was monitored by comparative ssNMR since diagnostic shifts for C atoms close to paramagnetic Cr^{3+} centers of the SBU can identify coordinated species. The ssNMR signals indicated the coordination of the ligand by one hydroxyl group only (Figure 3.8 a). Additional DFT calculations supported this and further predicted that the second hydroxyl group is asymmetrically stabilized via hydrogen bonding to the SBU. On-site formation of the photosensitizer Ir-L1 was achieved by the addition of an Ir-dimer containing predisposed Ir(ppy)$_2$ units.
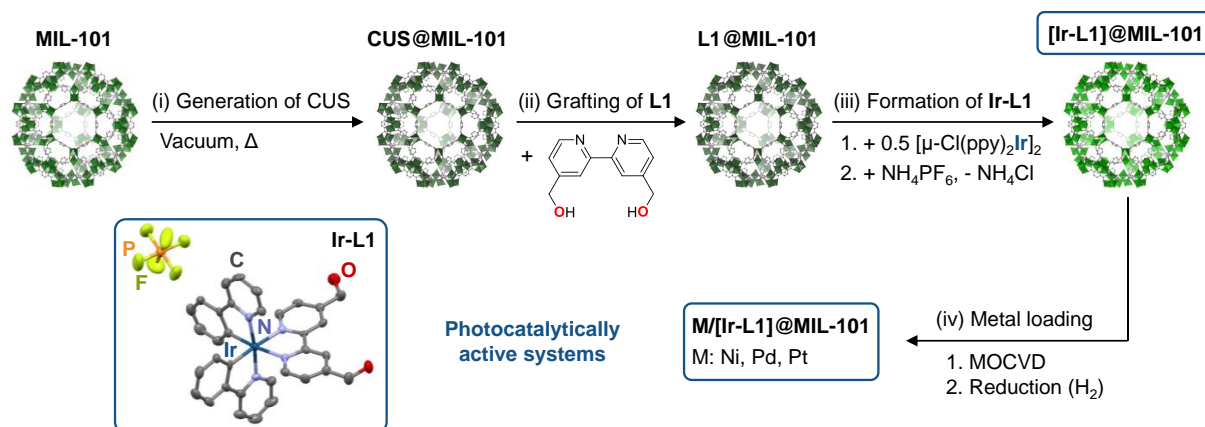
Figure 3.7. Synthesis of M/[Ir-L1]@MIL-101 by ship-in-a-bottle approach (M: Ni, Pd, Pt). (i) Generation of coordinatively unsaturated sites, denoted as CUS@MIL-101. (ii) Grafting of the modified bpy-ligand L1. (iii) Ir-L1 complex formation. (iv) Metal loading by MOCVD technique using volatile metal precursors.

The successful synthesis in the pores of MIL-101 was corroborated by comparative FT-IR analysis. By contrast to the ligand, ssNMR showed no anchoring of Ir-L1 to Cr^{3+} sites, and thus pointing towards a diffusing Ir photosensitizer inside the MIL-101 pore. The incorporation of group 10 metal nanoparticles (5 wt.% each of Ni, Pd, Pt) into the pores of [Ir-L1]@MIL-101 was performed by established MOCVD techniques. Representative EDX elemental maps of Ni/[Ir-L1]@MIL-101 (Figure 3.8 b) showed that Ir as the central atom of the sensitizer and Ni as the nanoparticulate co-catalyst were homogeneously distributed throughout the MOF crystallites. We concluded that the encapsulation of the two catalyst components occurred in a high proportion of the pores and expected this to be similar for the Pd and Pt modifications.
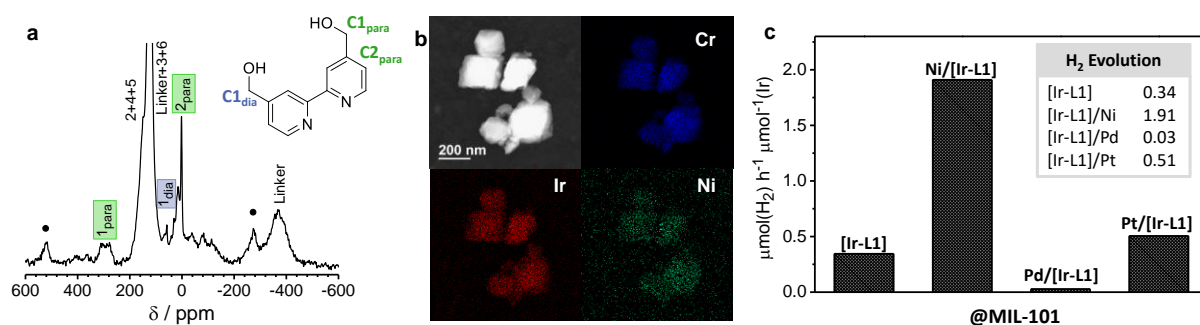

Figure 3.8. (a) ^{13}C ssNMR spectrum of L1@MIL-101 including assignments. The carbon atoms designated as C1$_{para}$ and C2$_{para}$ indicated the coordination to a Cr^{3+} center by the adjacent OH-group, while the carbon atom C1$_{dia}$ was unaffected. (b) HAADF-STEM image of Ni/[Ir-L1]@MIL-101 and representative EDX element maps for Cr, Ir and Ni. (c) H_2 evolution rate for the photocatalytic proton reduction from water for M/[Ir-L1]@MIL-101. Reaction conditions: 2 µmol Ir-L1, 1000 µL THF, 100 µL H_2O, 100 µL TEA, rt, Ar, 470 nm blue LED (50 W). H_2 was quantified by GC-TDC using methane as an internal standard.

We investigated the photocatalysts M/[Ir-L1]@MIL-101 for the visible light-driven (blue LED, λ=470 nm) water reduction using TEA as sacrificial agent. The H_2 evolution rate per hour was

determined by gaseous head-space analysis which showed that [Ir-L1]@MIL-101 was slightly super-stoichiometric after six hours (Figure 3.8 c).

Intriguingly, the deactivating effects of a confined reaction space could be partially remediated by the additional presence of metal nanoparticles. Evidently, Ni and Pt nanoparticles served as promoters of the hydrogen evolution rate, while Pd nanoparticles were inhibitors. Further luminescence lifetime studies on the M/[Ir-L1]@MIL-101 systems did not reveal any clear trend which could explain the activity difference between the co-catalytic metals Ni, Pd, and Pt based on electron transfer processes. It is expected that the spatial proximity between a metal nanoparticle and the Ir photosensitizer would affect the catalytic performance of the system by allowing a direct electron and/or energy transfer between both. Furthermore, we used theoretical calculations to address the question of how transition metal particles can affect the Ir photosensitizer and thus the visible light-driven H_2 evolution from water. We focused on the role of the metal nanoparticles in the light absorption process that initiates the catalytic reaction. Therefore, a model system was designed, which consists of the Ir-L1 photosensitizer and 13-atom icosahedral metal particles M_{13} to represent one of the smallest possible units within a single MIL-101 pore. Time-dependent DFT calculations with an optimally tuned range separated hybrid functional showed that the metal clusters interact with Ir-L1 and form a joint quantum system. The metal clusters significantly affect the photoabsorption process when they are in close proximity (Figure 3.9 a). Further analysis showed that both the M_{13} cluster and the Ir-L1 are involved in charge transfer-like processes starting from 2.2 eV upward. In the latter, the metal cluster is the electron donor and the Ir-L1 acts as the acceptor, as indicated by the differential electronic densities with respect to the ground state (e.g. S_{830}, Figure 3.9 b).
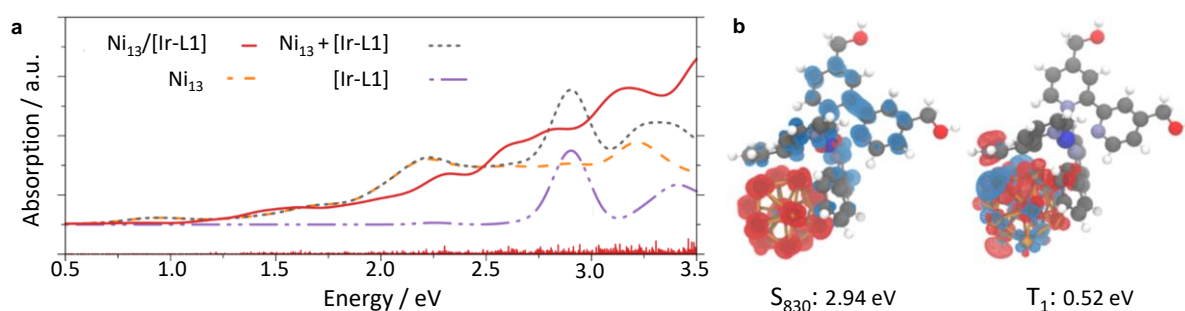

Figure 3.9. (a) Theoretical absorption spectra of Ni_{13}/[Ir-L1] and its bare constituents. The relative oscillator strength of Ni_{13}/[Ir-L1] is indicated by the height of the vertical red bars. (b) Exemplarily, the singlet S_{830} and the lowest spin-flip excitation T_1 of Ni_{13}/[Ir-L1] with negative (area of electron lack, red) and positive (electron gain, blue) difference density are given.

Consequently, the charge transfer occurs during the optical excitation rather than through a subsequent secondary process. The optical excitation mechanism is qualitatively the same for the three M_{13}/[Ir-L1], so this alone could not explain the difference in the overall performance of the metal co-catalysts found in the experiment. By contrast to Ir-L1, we observed a complete collapse of the charge separation in the lowest spin-flip excitation in M_{13}/[Ir-L1] since this excitation is predominantly localized only on the

respective metal cluster (e.g., T_1, Figure 3.9 b). Thus, one could speculate that the lowest spin-flip excitation accessible by intersystem crossing after the optical excitation could be the cause of catalytic deactivation. The rates of intersystem crossings are usually more pronounced for the heavier elements Pd and Pt, respectively, than for Ni. This could be a clue to explain the experimentally determined differences in the photocatalytic activity of the M/[Ir-L1]@MIL-101 systems. Another factor to consider could be the binding affinity between the metal clusters and Ir-L1. Our calculations resulted in Ni_{13} binding most strongly to Ir-L1 which could be advantageous for a better performance of Ni/[Ir-L1]@MIL-101.

3.2 Individual Contributions to Joint Publications

The results published in this thesis were achieved in collaboration with others and are published as indicated below. The contributions of all co-authors to the respective publication are specified. The corresponding author(s) is/are annotated by an asterisk (*).

Chapter 4

This work is published in *ChemCatChem* **2021**, *13*, 3257 – 3261 with the title

Key Parameters for the Synthesis of Active and Selective Nanostructured 3d Metal Catalysts Starting from Coordination Compounds – Case Study: Nickel Mediated Reductive Amination

Mara Klarner, Patricia Blach, Haiko Wittkämper, Niels de Jonge, Christian Papp, Rhett Kempe*

I synthesized and characterized the complexes and catalysts. The catalytic reactions and the associated analytics were carried out by me. Rhett Kempe and I designed the experiments and co-wrote the manuscript. Patricia Blach and Niels de Jonge performed HAADF-STEM coupled with EDX and EELS measurements and were involved in scientific discussions. Christian Papp and Haiko Wittkämper performed XPS analysis, wrote the related part of the publication and were involved in scientific discussions. Rhett Kempe supervised this work, was involved in scientific discussions and the correction of the manuscript.

Chapter 5

This work is published in *Z. Anorg. Allg. Chem.* **2021**, *674*, 2157 – 2161 with the title

Chemoselective Hydrogenation of Olefins Using a Nanostructured Nickel Catalyst

Mara Klarner, Sandra Bieger, Markus Drechsler, Rhett Kempe*

I synthesized and characterized catalyst, carried out the catalytic reactions and the associated analytics and I wrote the manuscript. Rhett Kempe and I designed the experiments. Sandra Bieger performed some initial work and also catalytic reactions during her bachelor thesis. Markus Drechsler performed one part of the TEM analysis. Rhett Kempe supervised this work, was involved in scientific discussions and the correction of the manuscript.

Chapter 6

This work is published in *ChemCatChem* **2020**, *12*, 4593 – 4599 with the title

Visible Light-driven Dehydrogenation of Benzylamine under Liberation of H$_2$

Mara Klarner, Sebastian Hammon, Sebastian Feulner, Stephan Kümmel, Lothar Kador, Rhett Kempe*

I synthesized and characterized the photocatalyst. The catalytic reactions and the associated analytics were carried out by me. Rhett Kempe and I designed the experiments. Sebastian Hammon did the theoretical calculations and wrote the theoretical section of the manuscript. Sebastian Feulner performed the fluorescence lifetime studies. Stephan Kümmel and Lothar Kador were involved in scientific discussions and the correction of the manuscript. Rhett Kempe supervised this work and was involved in the scientific discussions and the correction of the manuscript.

Chapter 7

This work is published in *J. Chem. Phys. C* **2021**, 10.1021/acs.jpcc.1c05756 with the title

Combining Metal Nanoparticles with an Ir(III) Photosensitizer

Sebastian Hammon, Mara Klarner, Gerald Hörner, Birgit Weber, Martin Friedrich, Jürgen Senker, Rhett Kempe,* Thiago Branquinho de Queiroz, Stephan Kümmel*

Sebastian Hammon and I equally contributed to the publication and co-wrote the manuscript. I synthesized and characterized the different photocatalysts. Sebastian Hammon did the theoretical studies on the photocatalytic system. Gerald Hörner did DFT calculations, wrote the related part of the manuscript and was involved in scientific discussions. Birgit Weber corrected the manuscript. Martin Friedrich initially designed the photocatalyst and did some preliminary work regarding the catalytic application. Jürgen Senker was involved in scientific discussions. Thiago Branquinho de Queiroz was involved in scientific discussion and the correction of the manuscript. Stephan Kümmel and Rhett Kempe supervised this work and were involved in scientific discussions and the correction of the manuscript.

4 Key Parameters for the Synthesis of Active and Selective Nanostructured 3d Metal Catalysts Starting from Coordination Compounds – Case Study: Nickel Mediated Reductive Amination

Mara Klarner,[a] Patricia Blach,[b,c] Haiko Wittkämper,[d] Niels de Jonge,[b,c] Christian Papp,[d] Rhett Kempe*[a]

[a]   Anorganische Chemie II – Catalyst Design, Sustainable Chemistry Centre, University of Bayreuth, Universitätsstr. 30, 95440 Bayreuth (Germany)

[b]   INM – Leibniz Institute for New Materials, Campus D2 2, 66123 Saarbrücken (Germany)

[c]   Department of Physics, Saarland University, Campus D2 2, 66123 Saarbrücken (Germany)

[d]   Physical Chemistry II, Department of Chemistry and Pharmacy, University Erlangen-Nürnberg, 91058 Erlangen (Germany)

Abstract: The design of nanostructured catalysts based on earth-abundant metals that mediate important reactions efficiently, selectively and with a broad scope is highly desirable. Unfortunately, the synthesis of such catalysts is poorly understood. We report here on highly active Ni catalysts for the reductive amination of ketones by ammonia employing hydrogen as a reducing agent. The key functions of the Ni-salen precursor complex during catalyst synthesis have been identified: (1) Ni-salen complexes sublime during catalyst synthesis, which allows molecular dispersion of the metal precursor on the support material. (2) The salen ligand forms a nitrogen-doped carbon shell by decomposition, which embeds and stabilizes the Ni nanoparticles on the γ-Al_2O_3 support. (3) Parameters, such as the flow rate of the pyrolysis gas, determine the carbon supply for the embedding process of Ni nanoparticles.

4.1 Introduction

Reductive amination is a very important reaction because the products, alkyl amines, are used intensively as fine and bulk chemicals, pharmaceuticals, and agrochemicals.[1] More specifically, primary amines are the starting material for the production of other amines or N-heterocyclic compounds.[2] The synthesis of primary amines via reductive amination is very challenging, because overalkylation and other side reactions must be avoided. The reductive amination for the synthesis of primary amines with hydrogen as a reducing agent was introduced 100 years ago by Mignonac, employing a Ni catalyst.[3] The use of hydrogen as a potentially sustainable and cost-effective reductant is particularly attractive, however, a catalyst is required for its activation. Furthermore, inexpensive ammonia is utilized as a nitrogen source. Despite the use of Ni catalysts ever since,[4,5] no catalyst system for the synthesis of primary amines with a broad scope and functional group tolerance had been found until 2019. We then presented a nanostructured Ni catalyst for the synthesis of primary amines by reductive amination, using ammonia dissolved in water.[5] Our catalyst had a broad scope and an exceptional tolerance towards functional groups, operated at low temperature and pressure, was highly active, reusable, and easy to handle. The synthesis from a specific Ni complex, namely, a Ni-salen complex, and γ-Al$_2$O$_3$ was straightforward, and the ligand-metal combination of this complex was crucial. Other interesting earth-abundant metal catalysts, synthesized via the pyrolysis of salen complexes, were reported by us[6] and the Beller group.[7,8] The superior performance of catalyst systems based on salen precursor complexes was demonstrated in all these publications. Unfortunately, the role of salen complexes in the pyrolysis-based catalyst synthesis is incompletely understood.

Herein, we report on a highly active Ni catalyst for the reductive amination of ketones by ammonia employing hydrogen as reductant. This Ni/Al$_2$O$_3$ catalyst was obtained by varying the nickel salen complex precursors used for the catalyst synthesis. Thereby, the key functions of the Ni-salen precursor complex during catalyst synthesis have been identified: (1) The volatility of Ni-salen complexes allows the molecular dispersion of the metal precursor on the support material, which enables an optimal bottom-up approach for the preparation of catalytically active metal sites. (2) Tailored decomposition of the carbon and nitrogen containing salen ligand forms a nitrogen-doped carbon shell that covers the catalytically active nickel nanoparticles, thereby stabilizing them. (3) A specific set of parameters during the pyrolysis step in catalyst generation determines the carbon supply, which is crucial for the embedding process of nanoparticles. A too high carbon supply particularly favors the undesired formation of carbon nanotubes.

4.2 Results and Discussion

We developed a Ni complex library to better address the question about the role and the mandatory nature of Ni-salen complexes in the generation of highly active hydrogenation catalysts. Based on this, alumina-supported catalysts were prepared and investigated for their catalytic activity in the reductive

amination of acetophenone as a model reaction. The Ni-salen ligand structures were selected by fine-tuning the steric properties and carbon and nitrogen content by choosing appropriate amine precursors and ring substituents. Starting from the known Ni precursor C1[5] three different aldehydes and four different diamines, including aliphatic, N-heteroaromatic und polyaromatic compounds, were combined. A total of six complexes, C1 to C6, were synthesized, as outlined in Figure 1. The corresponding Ni/Al$_2$O$_3$ composite catalysts Cat-1 to Cat-6 were generated along an established three step protocol for 3d metal catalysts supported on commercial supports:[5,6] The γ-Al$_2$O$_3$ support was wet impregnated with C1 to C6 (ideally 4 wt.% nickel) in acetonitrile. After removal of the solvent, the samples were pyrolyzed in a nitrogen flow up to 700 °C, followed by a reduction step in forming gas at 550 °C. The catalytic activity of the Ni/Al$_2$O$_3$ catalysts Cat-1 to Cat-6 was compared in the reductive amination of acetophenone as a model reaction. The table in Figure 1 gives an overview of the catalytic activity of the catalysts and the respective loading of nickel nanoparticles. We discovered an obvious dependence of the performance of Ni/Al$_2$O$_3$ catalysts on the Ni precursor complex used. Cat-4 showed the highest activity with a yield of 60 % of 1-phenylethylamine, followed by Cat-3 (55 %). By contrast, Cat-5 (2 %) and Cat-6 (9 %) were nearly inactive in the reductive amination of acetophenone under these reaction conditions. It was shown that the catalytic activity of the Ni/Al$_2$O$_3$ catalyst published,[5] Cat-1 (35 %), was surpassed by fine-tuning the salen ligand, which, similar to Cat-2 (34 %), led to only a moderate yield.

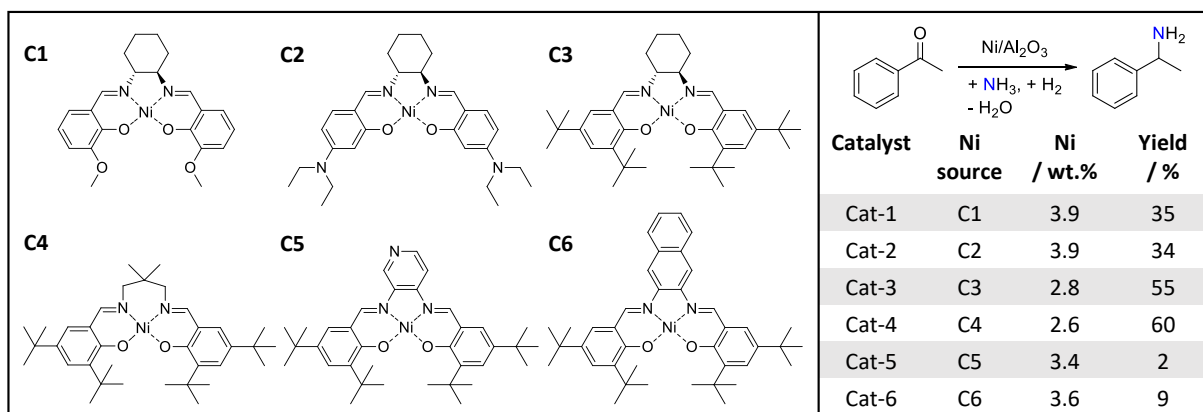| Catalyst	Ni source	Ni / wt.%	Yield / %
Cat-1	C1	3.9	35
Cat-2	C2	3.9	34
Cat-3	C3	2.8	55
Cat-4	C4	2.6	60
Cat-5	C5	3.4	2
Cat-6	C6	3.6	9

Figure 1. A library concept of 6 Ni-salen complex precursors: Ni-salen complexes C1 to C6 synthesized by fine-tuning the steric properties and carbon and nitrogen content (left). The catalytic activity of Ni/Al$_2$O$_3$ catalysts Cat-1 to Cat-6 studied in the reductive amination of acetophenone depending on the Ni source (right). In order to ensure comparability, the reaction conditions from Ref.[5] were adjusted so that no complete conversion of the reactant occurred: 1.2 mol% Ni/Al$_2$O$_3$ catalyst (0.006 mmol Ni, 0.35 mg Ni), 0.5 mmol acetophenone, 0.5 mL aq. NH$_3$ (25 %, 6.7 mmol), 2 mL H$_2$O, 80 °C, 0.5 MPa H$_2$, 20 h. Yields were determined by gas chromatography using *n*-dodecane as an internal standard. Ni content was analysed by ICP-OES.

Salen complexes are known to sublime without decomposition.[9] Consequently, the volatility of the Ni-salen complexes was investigated by thermogravimetric analysis (TGA) analogous to the catalyst preparation parameters (Supporting Information, Figure S1). All Ni-salen complexes C1 to C6 volatilize

into the gas phase above 400 °C (Supporting Information, Table S1). Intriguingly, the compounds C3 and C4 show significantly higher volatility than the other Ni-salen complexes. Possibly, the attached di-*tert*-butyl substituted aromatic rings and aliphatic backbones are beneficial.

Inductively coupled plasma optical emission spectroscopy (ICP-OES) was used to analyze the amount of Ni in the Ni/Al$_2$O$_3$ catalysts. Depending on the volatility of the Ni-salen complex used, the nickel loading of the Al$_2$O$_3$ support decreased due to removal in the gas flow during catalyst preparation. Cat-3 and Cat-4 showed the lowest Ni loadings of 2.8 wt.% and 2.6 wt.%, respectively, while less volatile Ni precursors resulted in higher Ni contents (Figure 1). In addition, the carbon and nitrogen contents were determined by elemental analysis, reflecting the atomic composition of the salen precursors (Supporting Information, Table S2, Figure S2). Transmission electron microscopy (TEM) analysis of Ni/Al$_2$O$_3$ materials (Supporting Information, Figure S3) showed a subordinate dependence of the Ni particle size on the precursor complex. The average Ni particle size of the catalysts varied from 8.0 to 11.0 nm with narrow size distribution. Only Ni-salen complex C2 was decomposed to larger Ni particles of 30 nm in diameter. The Ni particle size did not alter due to catalysis, as exemplified for Cat-4 (Supporting Information, Figure S4). Initial results did not give a clear indication that the Ni particle size and/or the amount of nickel, carbon and nitrogen in the Ni/Al$_2$O$_3$ catalyst is the determining factor for a high catalytic activity. However, we observed a qualitative effect of the precursor complex itself. Since there might be a correlation between the high hydrogenation activity of Cat-4 and the volatility of the Ni-salen complex C4, this led to the hypothesis that volatility might play a crucial role in the generation of catalytically active metal sites. Therefore, we investigated the role of the Ni-salen complex during active catalyst formation exemplified by complex C4. The following three key properties were identified:

(1) Molecular Dispersion of the Metal Precursor on the Support Material. Firstly, we focused on the interaction of the Ni-salen complex C4 with the Al$_2$O$_3$ support material during the impregnation and pyrolysis steps in catalyst preparation. We found by TEM analysis of wet impregnated C4/Al$_2$O$_3$ (Supporting Information, Figure S6) that C4 crystallizes in needles several micrometers long, starting from Al$_2$O$_3$ agglomerates as nucleation centers once the solvent is removed. This method of impregnation does not yield molecular dispersion of C4 on Al$_2$O$_3$ to produce small Ni nanoparticles directly during pyrolysis. Comparative TGA analysis (Figure 2a) of salen ligand L4, Ni-salen complex C4 and impregnated C4/Al$_2$O$_3$ showed that the salen ligand is already volatile, being thermally stabilized by the chelating coordination of nickel. C4 itself sublimes at a temperature of 469 °C without decomposing, confirmed by mass spectrometry of the residue (Supporting Information, Figure S5). As briefly discussed above, a Ni loading of 2.6 wt.% implies that about 65 % of C4 was decomposed on the Al$_2$O$_3$ support during pyrolysis. Considering the almost quantitative sublimation of the pure C4 (92 %), this is a clear indication of an attractive interaction of the Lewis acidic Al$_2$O$_3$ surface and the Ni-salen complex. In addition, we investigated the interaction of the Ni-salen complex C4 with the Al$_2$O$_3$ surface using diffuse reflectance infrared Fourier transform spectroscopy (DRIFTS). As measured in

pure Al_2O_3, the vibrational band of acidic Al_3-OH is centered at 3696 cm^{-1} and the broad signal at 1250-900 cm^{-1} originates from Al-O (Figure 2b).[10] The DRIFTS spectrum shows a very broad band in the hydroxyl spectral region (4000-2500 cm^{-1}) since the untreated Al_2O_3 sample is surface hydrated by physically absorbed water molecules. The DRIFTS spectrum of Ni-salen complex C4 shows signals in the fingerprint region for wavenumbers lower than 1680 cm^{-1}, with the characteristic signal at 1625 cm^{-1} originating from the C=N imine stretching. The bands between 2951 and 2843 cm^{-1} were assigned to C-H stretching vibrations. When impregnated C4/Al_2O_3 was heated to 469 °C as during catalyst formation and then cooled to room temperature, the band at 3696 cm^{-1} was no longer visible in the spectrum. The lack of a characteristic Al_3-OH band suggests a surface-absorbed complex C4 interacting with acidic centers of Al_2O_3. The TEM analysis of this material showed no crystals of C4 (Supporting Information, Figure S6).
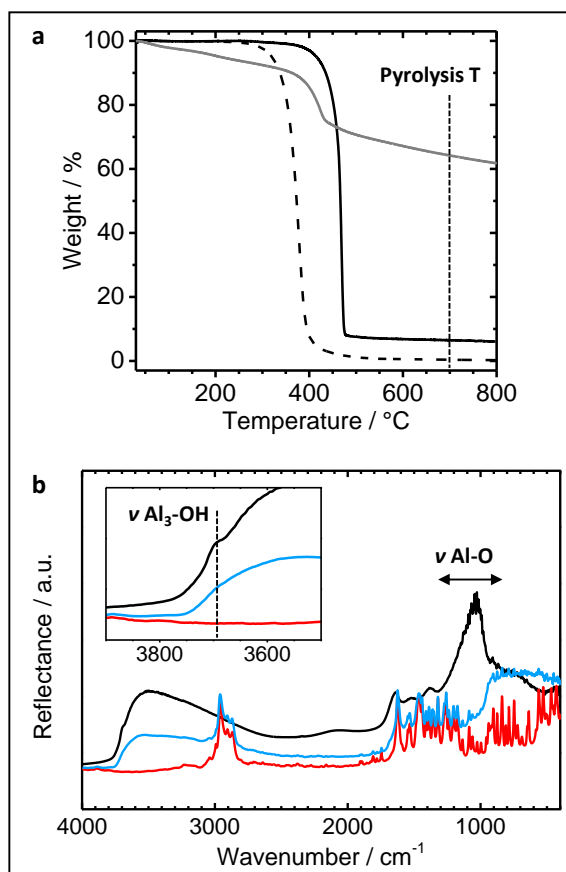
Figure 2. (a) TGA analysis (heating ramp 10 K/min, in N_2 flow) of L4 (dashed), C4 (black) and impregnated C4/Al_2O_3 (grey) demonstrating the volatility of salen compounds. (b) DRIFTS analysis of Al_2O_3 (black), C4 (red) and C4/Al_2O_3 (blue, heated to T_{subl} 469 °C of C4) confirming the interaction of the Ni-salen complex C4 with the Al_2O_3 support. The Al_3-OH band is shown in the inset.

As exemplified for C4, Ni-salen complexes sublime during Ni/Al_2O_3 catalyst generation with negligible decomposition. This property allows the molecular dispersion of single complex molecules on the Al_2O_3 surface from the gas phase. Since this dispersion cannot be achieved by wet impregnation with C4, the

volatility of the complexes plays a key role in this bottom-up approach to generate catalytically active metal sites.

(2) Formation of a Nitrogen-doped Carbon Shell for the Stabilization of Nickel Nanoparticles. We recorded X-ray photoelectron spectroscopy (XPS) survey spectra between 0-1100 eV, given in Figure S7. All expected lines for the Al_2O_3 support were identified, and in addition, carbon and minor traces of nitrogen were found. Small Ni signals were detected in the Ni 2p region (Figure 3b), but further Ni lines were not identified due to their small photoemission cross section and their partial overlap with Al lines. The Ni/Al_2O_3 catalyst shows a combination of metallic Ni^0 signals located at 852.6 eV and a broad signal located at around 854.6 eV which we assigned to oxidized Ni^{2+}. Contributions of Ni^{3+} are also possible due to the width of the signal. The 6 eV satellite of Ni is found as a broad feature between 858.6 and 865 eV.[11] The intensity ratio of Ni^0:Ni^{2+} is approximately 1.5:2.
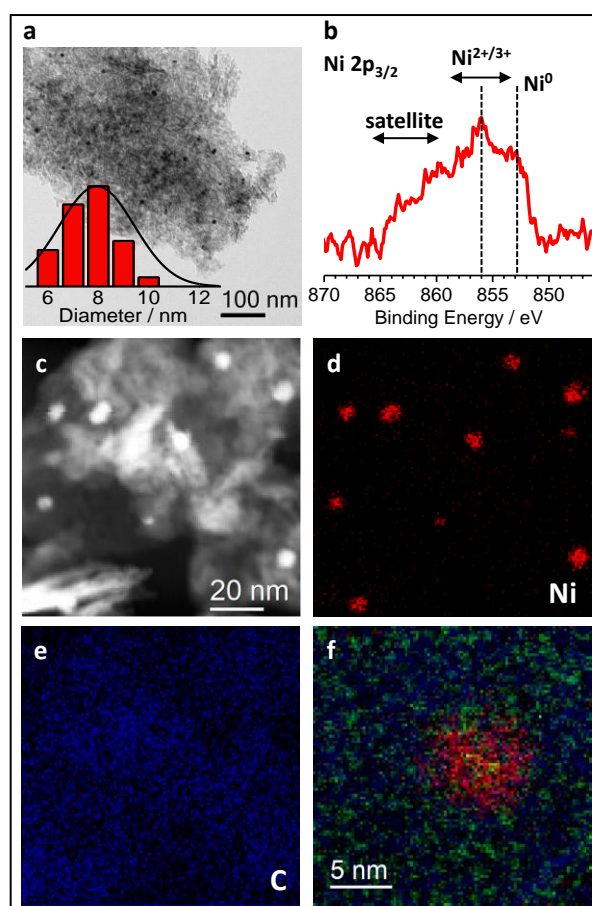
Figure 3. Characterization of Ni/Al_2O_3: (a) TEM image of the Ni/Al_2O_3 catalyst shows that the Al_2O_3 support is covered with homogeneously distributed Ni nanoparticles. The size distribution of Ni particles is given in the inset. (b) XPS analysis of the Ni $2p_{3/2}$ region revealed minor traces of Ni within the composite material. The Ni^0 nanoparticles are surface oxidized to Ni^{2+}/Ni^{3+} species. (c) HAADF-STEM analysis of the Ni/Al_2O_3 catalyst and (d, e) representative EDX element maps of nickel (red) and carbon (blue). (f) Overlapped EELS element maps of nickel (red), carbon (blue) and nitrogen (green) demonstrating the embedding of a Ni particle in a N-doped carbon layer.

The C 1s signal observed at 284.7 eV is close to what is typically observed for graphitic carbon.[12] The binding energy of the N 1s signal observed is at around 399.2 eV, possibly a remnant of the N-containing precursor molecule and its decomposition products (Supporting Information, Figure S7). High-angle annular dark-field scanning TEM (HAADF-STEM) analysis of Ni/Al_2O_3 confirmed the homogeneous distribution of Ni nanoparticles with an average size of 8.0 nm on the Al_2O_3 support material (Figure 3a, c). Energy dispersive X-ray (EDX) elemental maps for nickel and carbon recorded in the same image section illustrate the embedding of Ni nanoparticles in a carbon matrix covering the entire support material (Figure 3d, e). Electron energy loss spectroscopy (EELS) was used to study the near environment of a single nickel nanoparticle. The carbon and the nitrogen component cover the Ni particle and the surrounding support material (Figure 3f). We conclude, from XPS and HAADF-STEM investigations that the decomposition of the salen ligand on γ-Al_2O_3 during catalyst generation provides a defined N-doped carbon shell that stabilizes the Ni nanoparticles on the support material.

(3) Determination of the Carbon Supply During the Pyrolysis Step. Impregnated $C4/Al_2O_3$ material was sealed in a quartz glass ampoule in inert atmosphere and treated according to the standard catalyst synthesis process to suppress the sublimation of Ni-salen complex. Carbon nanotubes with a diameter of 30-40 nm grew in this confined gas space, starting from Ni particles of the same size (Supporting Information, Figure S11). The growth of carbon nanotubes initiated by 3d metal particles is well established.[13] We assume that excess carbon, in the form of the salen ligand and its volatile decomposition products, could not be removed due to the absence of a gas flow, thereby favoring the formation of the carbon nanotubes. In addition, the pyrolysis parameters for heating rate and gas flow were varied during the catalyst synthesis. Changing the heating ramp by ±5 K/min resulted in consistent catalytic activity of the Ni/Al_2O_3 catalysts, as the sublimation properties of C4 were not significantly different within this chosen range (Supporting Information, Figure S12).
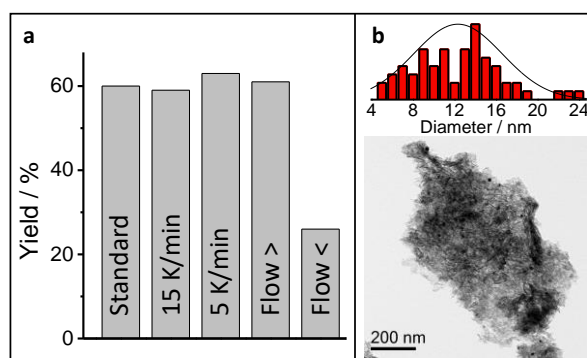

Figure 4. (a) The variation of the heating ramp (standard 10 K/min ± 5 K/min) and N_2 gas flow (1.25x and 0.25x standard flow) during Ni/Al_2O_3 catalyst synthesis identified the flow as a critical parameter during the pyrolysis step. Reaction conditions: 1.2 mol% Ni/Al_2O_3 catalyst (0.006 mmol Ni, 0.35 mg Ni), 0.5 mmol acetophenone, 0.5 mL aq. NH_3 (25 %, 6.7 mmol), 2 mL H_2O, 80 °C, 0.5 MPa H_2, 20 h. Yields were determined by gas chromatography using *n*-dodecane as an internal standard. (b) TEM analysis and the size distribution of nickel particles are shown for Ni/Al_2O_3 synthesized under reduced N_2 flow.

By contrast, changing the N_2 flow has a major impact on the catalytic activity. Reducing the nitrogen flow by 75 % causes the catalytic activity to collapse (Figure 4a), while increasing the gas flow by 25 % to the maximum gas flow of the device shows no effect. The TEM analysis of the less active catalyst material (Figure 4b) revealed a broader Ni particle size distribution and a slightly larger mean diameter of 12.5 nm than for the standard Ni/Al_2O_3 catalyst. The elemental composition of this material also showed higher mass fractions of nickel, carbon, and nitrogen (3.3 wt.% Ni, 8.1 wt.% C, 0.5 wt.% N) compared to Cat-4 (2.6 wt.% Ni, 4.6 wt.% C, 0.3 wt.% N). This led us to conclude that the volatility of the Ni-salen complex in combination with judiciously chosen pyrolysis parameters regulates the carbon supply during catalyst preparation.

4.3 Conclusion

In conclusion, key parameters for the synthesis of active and selective nanostructured 3d metal catalysts starting from a coordination compound were found, which may enable a more rational design of such catalysts in the future.

Acknowledgements

4.4 References

[1]   a) T. Irrgang, R. Kempe, *Chem. Rev.* **2020**, *120*, 9583−9674; b) K. Murugesan, T. Senthamarai, V. G. Chandrashekhar, K. Natte, P. C. J. Kamer, M. Beller, R. V. Jagadeesh, *Chem. Soc. Rev.* **2020**, *49*, 6273-6328; c) O. I. Afanasyev, E. Kuchuk, D. L. Usanov, D. Chusov, *Chem. Rev.* **2019**, *119*, 11857−11911.

[2]   K. Weissermel, H.-J. Arpe, *Industrial Organic Chemistry*; Wiley-VCH, Weinheim, **2008**.

[3]   G. Mignonac, *Compt. Rend.* **1921**, *172*, 223−226.

[4]   a) A. Skita, F. Keil, *Ber. Dtsch. Chem. Ges. B* **1928**, *61B*, 1682−1692; b) C. F. Winans, H. Adkins, *J. Am. Chem. Soc.* **1933**, *55*, 2051−2058; c) C. F. Winans, *J. Am. Chem. Soc.* **1939**, *61*, 3566−3567; d) E. J. Schwoegler, H. Adkins, *J. Am. Chem. Soc.* **1939**, *61*, 3499−3502; e) W.

Wayne, H. Adkins, *J. Am. Chem. Soc.* **1940**, 62, 3314−3316; f) J. C. Robinson, H. R. Snyder, *Org. Synth.* **1943**, *23*, 68; *Org. Synth. Coll.* **1955**, *3*, 717; g) B. S. Biggs, W. S. Bishop, *Org. Synth.* **1947**, *27*, 18; *Org. Synth. Coll.* **1955**, *3*, 229; h) K. W. Merz, H. Pfäffle, *Arch. Pharm.* **1955**, *288*, 86−100; i) N. Elming, N. Clauson-Kaas, E. P. Anderson, N. Eliasson, B. Thorell, *Acta Chem. Scand.* **1956**, *10,* 1603− 1605; j) A. R. Surrey, G. Y. Lesher, J. *Am. Chem. Soc.* **1956**, *78*, 2573− 2576; k) M. Freifelder, W. D. Smart, G. R. Stone, *J. Org. Chem.* **1962**, *27*, 2209; l) G. Grethe, H. L. Lee, M. Uskoković, A. Brossi, *J. Org. Chem.* **1968**, *33*, 491−494; m) M. A. Popov, N. I. Shuikin, *Bull. Acad. Sci. USSR, Div. Chem. Sci.* **1962**, *11*, 1014− 1017; n) K. A. Pollart, R. E. Miller, *J. Org. Chem.* **1962**, *27*, 2392−2394; o) K. Saigo, M. Kai, N. Yonezawa, M. Hasegawa, *Synthesis* **1985**, *2*, 214−216; p) A. S. C. Chan, C.-c. Chen, Y.-c. Lin, *Appl. Catal. A* **1994**, *119*, L1−L5; q) Y. Hirayama, M. Ikunaka, J. Matsumoto, *Org. Process Res. Dev.* **2005**, *9*, 30−38; r) P. Doležal, O. Machalický, M. Pavelek, P. Kubec, K. Hrádková, R. Hrdina, R. Šuláková, *Appl. Catal. A* **2005**, *286*, 202−210; s) N.-T. Le, A. Byun, Y. Han, K.-I. Lee, H. Kim, *Green Sustainable Chem.* **2015**, *5*, 115−127; t) T. Trégner, J. Trejbal, *Chem. Biochem. Eng. Q.* **2018**, *31*, 455−470; u) W. Chen, Y. Sun, J. Du, Z. Si, X. Tang, X. Zheng, L. Lin, S. Liu, T. Lei, *J. Chem. Technol. Biotechnol.* **2018**, *93*, 3028−3034; v) K. Murugesan, M. Beller, R. V. Jagadeesh, *Angew. Chem. Int. Ed.* **2019**, *58*, 5064−5068; w) Y. Zhang, H. Yang, Q. Chi, Z. Zhang, *ChemSusChem* **2019**, *12*, 1246−1255; x) M. Manzoli, E. C. Gaudino, G. Cravotto, S. Tabasso, R. B. N. Baig, E. Colacino, R. S. Varma, *ACS Sustainable Chem. Eng.* **2019**, *7*, 5963−5974; y) H. Yuan, J.-P. Li, F. Su, Z. Yan, B.T. Kusema, S. Streiff, Y. Huang, M. Pera-Titus, F. Shi, *ACS Omega* **2019**, *4*, 2510−2516.

[5] G. Hahn, P. Kunnas, N.de Jonge, R. Kempe, *Nat. Catal.* **2019**, *2*, 71-77.

[6] a) T. Schwob, P. Kunnas, N.de Jonge, C. Papp, H.-P. Steinrück, R. Kempe, *Sci. Adv.* **2019**, *5*, eaav3680; b) T. Schwob, M. Ade, R. Kempe, *ChemSusChem* **2019**, *12*, 3013-3017; c) C. Bäumler, C. Bauer, R. Kempe, *ChemSusChem* **2020**, *13*, 3110–3114.

[7] T. Senthamarai, V. G. Chandrashekhar, M. B. Gawande, N. V. Kalevaru, R. Zboril, P. C. J. Kamer, R. V. Jagadeesh, M. Beller, *Chem. Sci.* **2020**, *11*, 2973-2981.

[8] For a calcination-based synthesis of transition metal doped ceria, see: J. S. Elias, M. Risch, L. Giordano, A. N. Mansour, Y. Shao-Horn, *J. Am. Chem. Soc.* **2014**, *136*, 17193-17200.

[9] a) A. Gleizes, M. Julve, N. Kuzmina, A. Alikhanyan, F. Lloret, Malkerovac, J. L. Sanz, F. Senocq, *Eur. J. Inorg. Chem.* **1998**, 1169-1174; b) M. D.M.C. Ribeiro da Silva, J. M. Goncalves, A. L.R. Silva, P. C.F.C. Oliveira, B. Schröder, M. A.V. Ribeiro da Silva, *J. Mol. Catal. A Chem.* **2004**, *224*, 207-212.

[10] a) X. Liu, *J. Phys. Chem. C* **2008**, *112*, 5066-5073; b) J. Webber, J. E. Zorzi, C. A. Perottoni, S. M. e Silva, R. C. D. Cruz, *J. Mater. Sci.* **2016**, *51*, 5170-5184.

[11] A. Grosvenor, M. C. Biesinger, R. St. C. Smart, N. S. McIntyre, Surface *Science* **2006**, *600*, 1771-1779.

[12]   R. Blume, D. Rosenthal, J.-P, Tessonnier, H. Li, A. Knop-Gericke, R. Schlögl, *ChemCatChem* **2015**, *7*, 2871-2881.

[13]   a) J. Hafner, M. J. Bronikowski, B. R. Azamian, P. Nikolaev, A. G. Rinzler, D. T. Colbert, K. A. Smith, R. E. Smalley, *Chem. Phys. Lett*. **1998**, *296*, 195-202; b) S. Helveg, C. López-Cartes, J. Sehested, P. L. Hansen, B. S. Clausen, J. R. Rostrup-Nielsen, F. Abild-Pedersen, J. K. Nørskov, *Nature* **2004**, *427*, 426-429; c) J. A. Rodríguez-Manzo, M. Terrones, H. Terrones, H. W. Kroto, L. Sun, F. Banhart, *Nat. Nanotechnol.* **2007**, *2*, 307-311; d) T. Schmalz, T. Kraus, M. Günthner, C. Liebscher, U. Glatzel, R. Kempe, G. Motz, *Carbon* **2011**,*49*, 3065-3072.

4.5 Supporting Information

4.5.1 Experimental Procedure

General Methods

All chemicals and solvents were purchased commercially from chemical suppliers with purity over 95 % and used without further purification. γ-Al_2O_3 (gamma-phase, catalyst support, high surface area, bimodal) was purchased from Alfa Aesar.

Elemental analyses (CHN) were performed in tin capsules using an UNICUBE element analyst. Sulfanilamide was used as a standard. NMR spectra were measured using a Bruker Avance III HD 500 MHz spectrometer and a Varian INOVA 400 MHz spectrometer. Chemical shifts are reported in ppm relative to the deuterated solvent. Direct insertion probe-mass spectra (DIP-MS) were measured on a Finnigan MAT 8500 (Thermo Fisher Scientific) by direct injection. Electron ionization was used as ion source. Diffuse reflectance infrared Fourier transform spectroscopy (DRIFTS) was measured on a Bruker alpha II with a spectral resolution of 4 cm^{-1} and 24 co-additions per scan. Thermogravimetric analysis was performed from 30 °C to 1000 °C (10 °C min^{-1}) using a TGA/SDTA 851^e (Mettler) under nitrogen atmosphere. Samples were placed in Al_2O_3 crucibles with lid. The samples were placed in Al_2O_3 crucibles with lid, Al_2O_3 was used as reference material. Catalyst materials were generated by pyrolysis (N_2) and reduction (N_2/H_2, 10/90) on a Chem-BET Pulsar (Quantachrome) using tubes of quartz glass. Experiments in sealed ampoules were performed in a muffle furnace (Nabertherm) with programmable temperature ramps. Inductively coupled plasma optical emission spectroscopy (ICP-OES) was carried out according to standard protocol digestion (4 mL HNO_3/HCl, 3:1), microwave irradiation, 25 min, 195 °C) with a Vista-Pro radial (Varian). Nitrogen physisorption isotherms were determined at -196 °C using a Nova 2000e (Quantachrome) apparatus. Specific surface areas were calculated by using p/p_0-values from 0.05-0.3 by the BET model. Specific total pore volumes were determined by DFT calculations (N_2 at -196 °C on silica (cylindric pore, NLDFT equilibrium model)). For XPS measurements a PHI Quantera II setup equipped with a monochromatic Al Kα X-ray source was used. The system operates at a base pressure of 10^{-10} mbar and utilizes a dual-beam charge

neutralization setup, allowing us to measure non-conductive samples. To correct for additional shifts all spectra were aligned to the main O 1s peak of the Al_2O_3 support at 531.2 eV. The data processing was done using the software package Casa XPS 2.3.22. Transmission electron microscopy (TEM) measurements were carried out using a LEO 922O microscope (Zeiss, 200 kV). The samples were suspended in chloroform and sonicated for 5 min. 2 µL of the suspension were placed on a CF200-Cu-grid or a LC200-Cu-grid (Electron Microscopy Sciences) and allowed to dry. High-angle annular dark-field scanning transmission electron microscopy (HAADF-STEM) measurements were performed using a JEM-ARM200F (JEOL, 200 kV) equipped with an energy-dispersed X-ray analysis (EDX) system (JEOL). In STEM mode, an annular dark-field detector (ADF) with collection angle (inner and outer) 68-280 mrad was used (image size: 1024x1024 pixels; pixel size: 0.13 nm, 0.076 nm, and 0.095 nm; dwell time: 6 µs). For EDX measurements the probe current was set to 1000 pA (image size: 128x128 pixels; pixel size: 0.78 nm; dwell time: 1 ms) and 10 sweep counts were integrated. For electron energy loss spectroscopy analysis (EELS) with an energy dispersion of 0.25 eV, the image collection angle was set to 20.8 mrad and the electron probe convergence semi-angle to 30-35 mrad (image size: 50x50-150x150 pixels; pixel size: 0.46 nm-0.13 nm; dwell time: 100 µs). X-ray powder diffraction (PXRD) analysis in the range of 2-80 °2θ was performed using a XPERT-PRO diffractometer (Panalytical) ($Cu_{K\alpha}$ radiation, 1.54178 Å) in θ-2θ geometry with a position sensitive detector. The reference card number for comparison is 00-001-1260 for cubic Ni and 00-001-1303 for γ-Al_2O_3. Gas chromatography (GC) analyses were performed using an Agilent Technologies 6850 gas chromatograph equipped with a flame ionization detector (FID) and a MN Optima 17 capillary column (30.0 m x 0.32 mm x 0.25 µm) using *n*-dodecane as internal standard. Hydrogenation experiments were carried out with Parr Instrument stainless steel autoclaves N -MT5 300 mL equipped with heating mantles and temperature controller.

Salen-Complex Synthesis

<u>Salen(cy)(methoxy): **L1**</u>[S1]

3-Methoxysalicylaldehyde (3.04 g, 20 mmol, 2 eq.) was dissolved in ethanol (50 mL), trans-1,2-diaminocyclohexane (1.202 mL, 10 mmol, 1 eq.) was added and the reaction mixture was heated to reflux for 30 min. While cooling, a yellow solid crystallized in needles. This solid was filtered off, washed with ethanol, and dried in vacuum to yield the crystalline ligand L1.
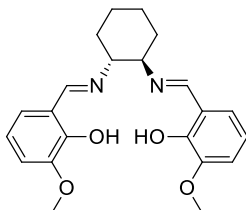
FW ($C_{22}H_{26}N_2O_4$) = 382.44 g mol^{-1}

Yield 3.230 g (8.4 mmol, 85 %)

^{1}H-NMR (CDCl$_3$, 500 MHz) δ = 13.86 (s, 2H, O*H*), 8.25 (s, 2H, C*H*=N), 6.87-6.85 (dd, 2H, Ar-*H*), 6.80-6.78 (dd, 2H, Ar-*H*), 6.74-6.71 (t, 2H, Ar-*H*), 3.87 (s, 6H, C*H*$_3$), 3.33-3.31 (q, 2H, C*H*), 1.96-1.93 (d, 2H, C*H*$_2$), 1.89-1.87 (d, 2H, C*H*$_2$), 1.75-1.68 (m, 2H, C*H*$_2$), 1.51-1.47 (m, 2H, C*H*$_2$) ppm.

CHN C 68.90 (69.09), H 6.79 (6.85), N 7.41 (7.33) %.

<u>Ni-Salen(cy)(methoxy): **C1**</u>[S1]

Salen(cy)(methoxy) L1 (1.912 g, 5 mmol, 1 eq.) was suspended in methanol (80 mL) and nickel acetate tetrahydrate (1.244 g. 5 mmol, 1 eq.) dissolved in methanol (20 mL) was added. The reaction was stirred at room temperature for 2 h, then the orange-brown solid was filtered off, washed with methanol, and dried in vacuum to yield the complex C1 as a brown powder.
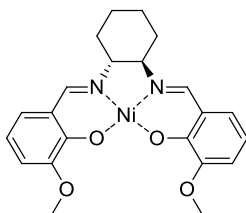
FW (NiC$_{22}$H$_{24}$N$_2$O$_4$) = 439.13 g mol^{-1}

Yield 2.041 g (1.22 mmol, 91 %)

^{1}H-NMR (CD$_2$Cl$_2$, 500 MHz) δ = 7.39 (s, 2H, C*H*=N), 6.75-6.70 (2 dd, 4H, Ar-*H*), 6.49-6.44 (t, 2H, Ar-*H*), 3.81 (s, 6H, C*H*$_3$), 3.1 (m, 2H, C*H*), 1.90 (m, 2H, C*H*$_2$), 1.33 (m, 4H, C*H*$_2$) ppm.

CHN C 60.29 (60.17), H 5.33 (5.51), N 6.69 (6.38) %.

Salen(cy)(diethylamino): **L2**

4-Diethylaminosalicylaldehyde (3.865 g, 20 mmol, 2 eq.) was dissolved in ethanol (50 mL), *trans*-1,2-diaminocyclohexane (1.202 mL, 10 mmol, 1 eq.) was added and the reaction mixture was heated to reflux for 1 h. The solvent was evaporated until a sand-colored powder precipitated. This solid was filtered off, washed with cold diethyl ether, and dried in vacuum to yield the ligand L2.
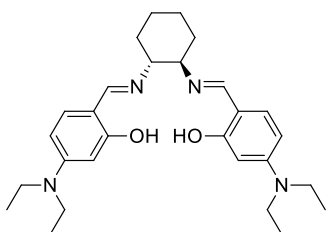

FW ($C_{28}H_{40}N_4O_2$) = 464.63 g mol^{-1}

Yield 4.236 g, 9.1 mmol, 91 %)

^{1}H-NMR (CDCl$_3$, 400 MHz) δ = 13.78 (s, 2H, O*H*), 7.94 (s, 2H, C*H*=N), 6.90-6.89 (s, 2H, Ar-*H*), 6.08-6.06 (d, 2H, Ar-*H*), 6.04-6.03 (d, 2H, Ar-*H*), 3.35-3.31 (q, 8H, C*H*$_2$), 3.17-3.15 (m, 2H, C*H*), 1.96-1.93 (d, 2H, C*H*$_2$), 1.84-1.83 (d, 2H, C*H*$_2$), 1.67-1.60 (m, 2H, C*H*$_2$), 1.47-1.38 (m, 2H, C*H*$_2$), 1.17-1.14 (t, 12H, C*H*$_3$) ppm.

CHN C 72.36 (72.37), H 8.76 (8.68), N 12.07 (12.06) %.

Ni-Salen(cy)(diethylamino): **C2**

Salen(cy)(diethylamino) L2 (1.394 g, 3 mmol, 1 eq.) was suspended in acetone (40 mL) and nickel acetate tetrahydrate (0.740 g, 3 mmol, 1 eq.) dissolved in acetone (20 mL) was added. The reaction was stirred at room temperature for 2 h, then the orange-brown solid was filtered off, washed with methanol, and dried in vacuum to yield the complex C1 as a brown powder.
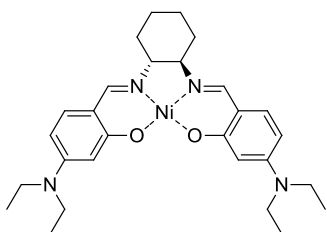
FW (NiC$_{28}$H$_{38}$N$_4$O$_2$) = 521.32 g mol^{-1}

Yield 1.330 g (2.55 mmol, 85 %)

^{1}H-NMR (CDCl$_3$, 400 MHz) δ = 7.09 (s, 2H, C*H*=N), 6.87-6.85 (s, 2H, Ar-*H*), 6.22 (d, 2H, Ar-*H*), 6.02-6.00 (d, 2H, Ar-*H*), 3.34-3.30 (q, 8H, C*H*$_2$), 3.04-3.02 (d, 2H, C*H*), 2.36-3.34 (d, 2H, C*H*$_2$), 1.85-1.84 (d, 2H, C*H*$_2$), 1.31-1.24 (m, 4H, C*H*$_2$), 1.17-1.14 (t, 12H, C*H*$_3$) ppm.

CHN C 64.89 (64.51), H 7.36 (7.35), N 10.79 (10.75) %.

Salen(cy)(di-*tert*-butyl): **L3**

3,5-Di-*tert*-butylsalicylaldehyde (1.172 g, 5 mmol, 2 eq.) was dissolved in ethanol (25 mL), *trans*-1,2-diaminocyclohexane (0.301 mL, 2.5 mmol, 1 eq.) was added at room temperature. Within 30 min, a bright yellow solid crystallized. This solid was filtered off, washed with ethanol, and dried in vacuum to yield the ligand L3.
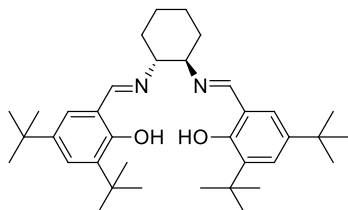
FW ($C_{36}H_{54}N_2O_2$) = 546.84 g mol^{-1}

Yield 1.197 g, 2.2 mmol, 88 %)

^{1}H-NMR (CDCl$_3$, 400 MHz) δ = 13.74 (s, 2H, OH), 8.32 (s, 2H, CH=N), 7.32-7.31 (d, 2H, Ar-H), 7.00 (d, 2H, Ar-H), 3.35-3.33 (q, 2H, CH), 1.97-1.95 (d, 2H, CH_2), 1.90-1.88 (d, 2H, CH_2), 1.78-1.72 (q, 2H, CH_2), 1.50-1.46 (m, 2H, CH_2), 1.43 (s, 18H, C(CH_3)$_3$), 1.25 (s, 18H, C(CH_3)$_3$) ppm.

CHN C 79.13 (79.07), H 9.74 (9.95), N 5.20 (5.12) %.

Ni-Salen(cy)(di-*tert*-butyl): **C3**

Salen(cy)(di-*tert*-butyl) L3 (0.657 g, 1.2 mmol, 1 eq.) was suspended in methanol (15 mL) and nickel acetate tetrahydrate (0.299 g, 1.2 mmol, 1 eq.) dissolved in methanol (15 mL) was added. The reaction was stirred at room temperature for 16 h, then the green solid was filtered off, washed with methanol, and dried in vacuum to yield the complex C3 as a green, fluffy solid.
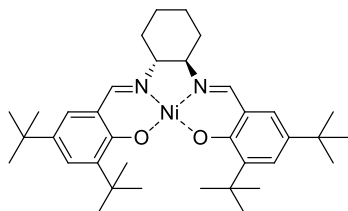
FW (NiC$_{36}$H$_{52}$N$_2$O$_2$) = 603.50 g mol^{-1}

Yield 0.68 g (1.13 mmol, 94 %)

^{1}H-NMR (CDCl$_3$, 400 MHz) δ = 7.40 (s, 2H, CH=N), 7.31 (d, 2H, Ar-H), 6.89-6.88 (d, 2H, Ar-H), 3.03 (m, 2H, CH), 2.44-2.43 (d, 2H, CH_2), 1.9 (d, 2H, CH_2), 1.42 (s, 18H, C(CH_3)$_3$), 1.33-1.32 (m, 4H, CH_2), 1.27 (s, 18H, C(CH_3)$_3$) ppm.

CHN C 71.91 (71.74), H 8.65 (8.41), N 4.75 (4.72) %.

Salen(prop)(di-*tert*-butyl): **L4**

3,5-Di-*tert*-butylsalicylaldehyde (2.344 g, 10 mmol, 2 eq.) was dissolved in ethanol (50 mL), 2,2-dimethylpropan-1,3-diamine (0.600 mL, 5 mmol, 1 eq.) was added at room temperature. A yellow solid crystallized, immediately. This solid was filtered off, washed with ethanol, and dried in vacuum to yield the ligand L4.
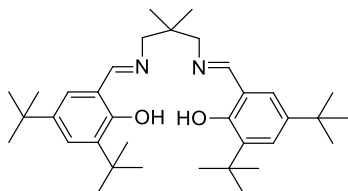
FW ($C_{35}H_{54}N_2O_2$) = 534.82 g mol^{-1}

Yield 5.241 g, 9.8 mmol, 98 %)

^{1}H-NMR (CDCl$_3$, 500 MHz) δ = 13.88 (s, 2H, OH), 8.38 (s, 2H, CH=N), 7.41-7.40 (d, 2H, Ar-H), 7.13-7.12 (d, 2H, Ar-H), 3.49 (s, 4H, CH_2), 1.48 (s, 18H, C(CH_3)$_3$), 1.33 (s, 18H, C(CH_3)$_3$), 1.12 (s, 6H, CH_3) ppm.

CHN C 78.73 (78.60), H 10.13 (10.18), N 5.33 (5.24) %.

Ni-Salen(prop)(di-*tert*-butyl): **C4**

Salen(prop)(di-*tert*-butyl) L4 (1.604 g, 3 mmol, 1 eq.) was suspended in methanol (30 mL) and nickel acetate tetrahydrate (0.747 g, 3 mmol, 1 eq.) dissolved in methanol (15 mL) was added. The reaction was stirred at room temperature for 16 h, then the green solid was filtered off, washed with methanol, and dried in vacuum to yield the complex C4 as a green, fluffy solid.
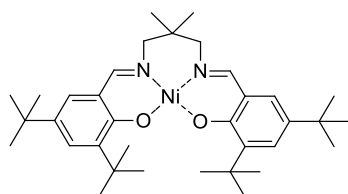
FW (Ni$C_{35}H_{52}N_2O_2$) = 591.49 g mol^{-1}

Yield 1.721 g (2.91 mmol, 97 %)

^{1}H-NMR (CDCl$_3$, 400 MHz) δ = 7.40 (s, 2H, CH=N), 7.31 (d, 2H, Ar-H), 6.89-6.88 (d, 2H, Ar-H), 3.03 (m, 2H, CH), 2.44-2.43 (d, 2H, CH_2), 1.9 (d, 2H, CH_2), 1.42 (s, 18H, C(CH_3)$_3$), 1.33-1.32 (m, 4H, CH_2), 1.27 (s, 18H, C(CH_3)$_3$) ppm.

CHN C 70.90 (71.07), H 9.03 (8.86), N 4.95 (4.74) %.

Zn-Salen(pyr)(di-*tert*-butyl): **L5**[S2]

3,5-Di-*tert*-butylsalicylaldehyde (2.344 g, 10 mmol, 2 eq.) and 3,4-diaminopyridine (0.546 g, 5 mmol, 1 eq.) were dissolved in methanol (11 mL), then zinc acetate tetrahydrate (1.135 g, 5.17 mmol, 1.03 eq.) was added as a template. The reaction mixture was stirred at 50 °C for 30 min to dissolve the reactants. After the addition of triethylamine (2.18 mL, 15.73 mmol, 3.15 eq.) the mixture turned red and was stirred at room temperature for 72 h. The bright red precipitate was filtered off, washed with cold methanol, and suspended in methanol at 0 °C for 1 h. Hereafter, the solid was filtered off, washed with cold methanol, and dried in vacuum to yield the bright red zinc complex L5.
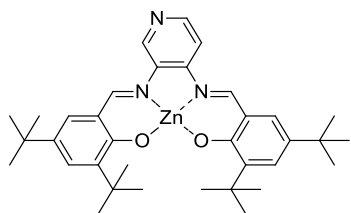
FW (ZnC$_{35}$H$_{45}$N$_3$O$_2$) = 605.13 g mol^{-1}

Yield 2.728 g, 9.0 mmol, 90 %)

^{1}H-NMR (d^6-acetone, 400 MHz) δ = 9.11 (s, 1H, C*H*-N), 8.45 (s, 2H, C*H*=N), 7.95-7.93 (d, 1H, CH-C*H*-N), 7.74-7.73 (d, 1H, C*H*-CH-N), 7.55-7.54 (d, 1H, Ar-*H*), 7.50-7.49 (d, 1H, Ar-*H*), 7.20-7.19 (d, 1H, Ar-*H*), 6.79 (d, 1H, Ar-*H*), 1.57 (s, 9H, C(C*H*$_3$)$_3$), 1.42 (s, 9H, C(C*H*$_3$)$_3$), 1.32-1.30 (s, 18H, C(C*H*$_3$)$_3$) ppm.

CHN C 69.20 (69.47), H 7.48 (7.50), N 7.02 (6.94) %.

Ni-Salen(pyr)(di-*tert*-butyl): **C5**[S2]

Zn-Salen(pyr)(di-*tert*-butyl) L5 (0.607 g, 1.0 mmol, 1 eq.) was suspended in tetrahydrofuran (100 mL) and nickel acetate tetrahydrate (0.280 g, 1.13 mmol, 1.13 eq.) dissolved in tetrahydrofuran (15 mL) was added. The reaction was stirred at reflux temperature (70 °C) for 18 h, then solvent was removed in vacuum. Methanol was added to the residue to precipitate a dark red crystalline solid which was filtered off, washed with methanol, and dried in vacuum to yield the complex C5.
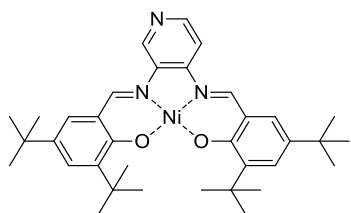
**FW** (NiC$_{35}$H$_{45}$N$_3$O$_2$) = 598.44 g mol^{-1}

Yield 0.505 g (0.84 mmol, 84 %)

^{1}H-NMR (d^6-acetone, 400 MHz) δ = 9.33 (s, 1H, C*H*-N), 8.90 (s, 1H, C*H*=N), 8.86 (s, 1H, C*H*=N), 8.32-8.30 (d, 1H, CH-C*H*-N), 8.01-7.99 (d, 1H, C*H*-CH-N), 7.50-7.48 (dd, 2H, Ar-*H*), 7.41-7.37 (dd, 2H, Ar-*H*), 1.48-1.47 (s, 18H, C(C*H*$_3$)$_3$), 1.32-1.31 (s, 18H, C(C*H*$_3$)$_3$) ppm.

CHN C 70.23 (70.24), H 7.47 (7.58), N 6.93 (7.02) %.

Zn-Salen(naph)(di-*tert*-butyl): **L6**

3,5-Di-*tert*-butylsalicylaldehyde (2.344 g, 10 mmol, 2 eq.) and 2,3-diaminonaphthaline (0.791 g, 5 mmol, 1 eq.) were dissolved in methanol (80 mL), then zinc acetate tetrahydrate (1.135 g, 5.17 mmol, 1.03 eq.) was added as a template. The reaction mixture was stirred at 50 °C for 30 min to dissolve the reactants. After the addition of triethylamine (2.18 mL, 15.73 mmol, 3.15 eq.) the mixture turned yellow and was stirred at 50 °C for 72 h. After the solvent was removed in vacuum, the residue was suspended in diethyl ether and filtered off. The solid was recrystallized in cyclohexane and dried in vacuum to yield the golden yellow zinc complex L7 accompanied by one triethylamine (NEt$_3$) and one acetic acid (HOAc).
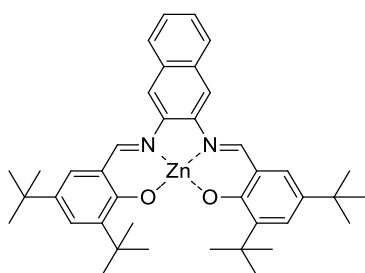
FW (ZnC$_{40}$H$_{48}$N$_2$O$_2$) = 654.20 g mol^{-1}

FW (+C$_6$H$_{15}$N+C$_2$H$_4$O$_2$) = 815.44 g mol^{-1}

Yield 3.180 g (3.9 mmol, 78 %)

^{1}H-NMR (d^6-acetone, 400 MHz) δ = 9.12 (s, 2H, C*H*=N), 8.23 (s, 1H, Ar-*H*), 7.93-7.91 (q, 2H, Ar-*H*), 7.46-7.44 (q, 2H, Ar-*H*), 7.42 (d, 2H, Ar-*H*), 7.22-7.20 (d, 2H, Ar-*H*), 1.54 (s, 18H, C(C*H*$_3$)$_3$), 1.32 (s, 18H, C(C*H*$_3$)$_3$) ppm with 2.67-2.61 (t, 9H, N(C*H*$_2$CH$_3$)$_3$), 1.81(s, 3H, C*H*$_3$), 0.89-0.85 (t, 9H, N(CH$_2$C*H*$_3$)$_3$) ppm.

CHN +NEt$_3$ +HOAc C 70.85 (70.70), H 7.96 (8.28), N 5.16 (5.16) %.

Ni-Salen(naph)(di-*tert*-butyl): **C6**

Zn-Salen(naph)(di-*tert*-butyl) L5 (0.815 g, 1.0 mmol, 1 eq.) was suspended in tetrahydrofuran (100 mL) and nickel acetate tetrahydrate (0.280 g, 1.13 mmol, 1.13 eq.) dissolved in tetrahydrofuran (15 mL) was added. The reaction was stirred at reflux temperature (70 °C) for 18 h, then solvent was removed in vacuum. Cold methanol was added to the residue to precipitate a dark red solid which was filtered off, washed with methanol, and dried in vacuum to yield the complex C7.
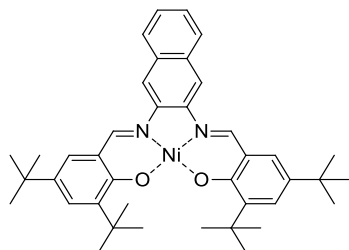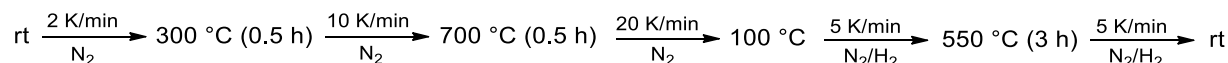

FW (NiC$_{40}$H$_{48}$N$_2$O$_2$) = 647.51 g mol^{-1}

Yield 0.552 g (0.85 mmol, 85 %)

^{1}H-NMR (d^6-acetone, 400 MHz) δ = 8.84 (s, 2H, C*H*=N), 8.49 (s, 1H, Ar-*H*), 7.92-7.91 (m, 2H, Ar-*H*), 7.49-7.46 (m, 4H, Ar-*H*), 7.39 (s, 2H, Ar-*H*), 1.49 (s, 18H, C(C*H*$_3$)$_3$), 1.33 (s, 18H, C(C*H*$_3$)$_3$) ppm.

CHN 74.28 (74.20), H 7.29 (7.47), N 4.45 (4.33) %.

Ni/Al₂O₃ Catalyst Preparation: Cat-1 to Cat-6

A solution of Ni-salen complex, C1 to C6 respectively, (0.178 mmol, 10.4 mg of Ni, 4 wt.% Ni ideally) in 30 mL tetrahydrofuran was added to 250 mg γ-Al₂O₃ and the suspension was stirred vigorously. After evaporation of the solvent at 90 °C, the impregnated sample C/Al₂O₃ was pyrolyzed under N₂ and finally reduced by a N₂/H₂ (90/10) mixture in a ChemBET Pulsar with the following program:

$$rt \xrightarrow[N_2]{2 \text{ K/min}} 300 \text{ °C (0.5 h)} \xrightarrow[N_2]{10 \text{ K/min}} 700 \text{ °C (0.5 h)} \xrightarrow[N_2]{20 \text{ K/min}} 100 \text{ °C} \xrightarrow[N_2/H_2]{5 \text{ K/min}} 550 \text{ °C (3 h)} \xrightarrow[N_2/H_2]{5 \text{ K/min}} rt$$

Experiments to vary the pyrolysis parameters were also carried out on the ChemBET Pulsar. The gas flow was increased by 25 % or reduced by 75 % for the entire program from standard settings. The heating rate was reduced from 10 K/min to 5 K/min or increased to 15 K/min in the second step between 300 °C and 700 °C.

Catalysts were stored in inert atmosphere.

Ni/Al₂O₃ Pyrolysis Experiment in Sealed Quartz Glass Ampoule

250 mg of impregnated C4/Al₂O₃ was weighed into a quartz vial (14 cm³) in inert atmosphere and sealed gas-tight using an H₂/O₂-burner. The work was carried out in nitrogen flow to ensure an inert atmosphere. The pyrolysis program up to 700 °C was carried out in a muffle furnace. The ampoule was then opened, and the material was transferred to the ChemBET Pulsar for the reduction step.

General Procedure for the Reductive Amination of Acetophenone

In a typical experiment, a 5 mL reaction vial was charged with 1.2 mol.% Ni (0.006 mmol Ni, 0.35 mg Ni) in form of the respective Ni/Al₂O₃ catalyst and a magnetic stirring bar. 0.5 mmol acetophenone (58.3 μL), 0.5 mL NH₃ (aq. 25 %, 6.7 mmol) and 2.0 mL H₂O were added. The vial was placed in a 250 mL stainless steel autoclave (Parr Instruments) which was flushed five times with 1 MPa hydrogen. The autoclave was pressurized by 0.5 MPa hydrogen and stirred for 20 h at 80 °C. After the autoclave was cooled to room temperature and the hydrogen pressure was released, the aqueous phase was extracted three times using ethyl acetate. The combined organic layers were dried over Na₂SO₄ and filtered to remove the residual catalyst. Yields were determined by gas chromatography using *n*-dodecane as an internal standard.

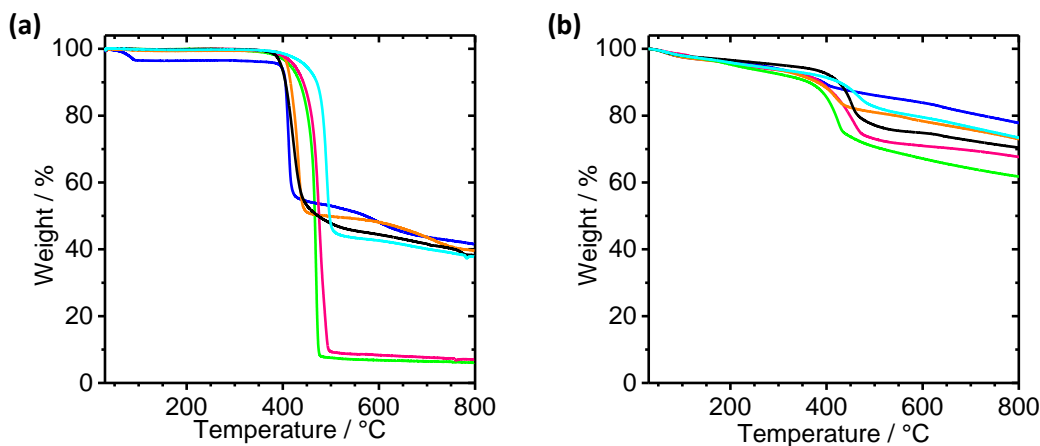### 4.5.2 Material Characterization

Figure S1. TGA analysis of (a) complexes C1-C6 and (b) the impregnated C/Al_2O_3 materials, respectively. Measurements were performed in the range of 30-800 °C (heating ramp 10 K/min) in constant N_2 flow. C1: blue, C2: orange, C3: pink, C4: green, C5: black, C6: cyan.

Table S1. Analysis of TGA measurements in Figure S1(a). The sublimation temperature T_{subl} of complexes at a heating ramp of 10 K/min in N_2 flow was determined by zero of the first derivative of the TGA curve. The mass loss was determined between room temperature and 700 °C which corresponds to the reduction temperature during the catalyst generation.

Complex	T_{subl} / °C	Mass loss / %
C1 Ni-Salen(cy)(methoxy)	411	45
C2 Ni-Salen(cy)(diethylamino)	433	49
C3 Ni-Salen(cy)(di-*tert*-butyl)	476	90
C4 Ni-Salen(prop)(di-*tert*-butyl)	469	92
C5 Ni-Salen(pyr)(di-*tert*-butyl)	420	49
C6 Ni-Salen(naph)(di-*tert*-butyl)	491	55

Table S2. The composition of the resulting Ni/Al_2O_3 catalysts I-VI in terms of Ni, C and N content. [a]Cat-4 pyrolyzed in reduced N_2 flow. Ni content was determined by ICP-OES analysis, C and N content by elemental analysis.

Catalyst	Ni / wt.%	C / wt.%	N / wt.%
Cat-1	3.9	10.5	0.8
Cat-2	3.9	9.8	1.3
Cat-3	2.8	7.0	0.5
Cat-4	2.6	4.6	0.3
Cat-5	3.4	8.9	1.2
Cat-6	3.6	14.1	0.9
Cat-4[a]	3.3	8.1	0.5
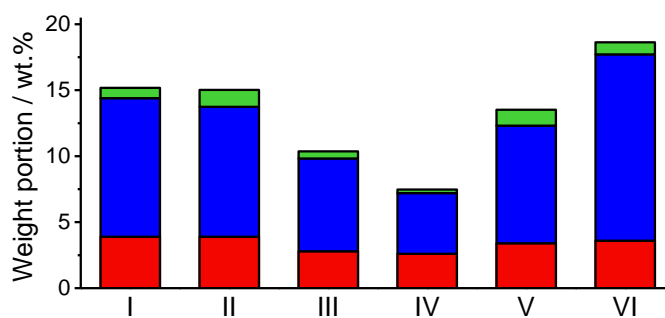
Figure S2. Visualized summary of elemental composition of Ni/Al_2O_3 catalysts Cat-1 to Cat-6. Ni (red) content was determined by ICP-OES analysis, C (blue) and N (green) content by elemental analysis.
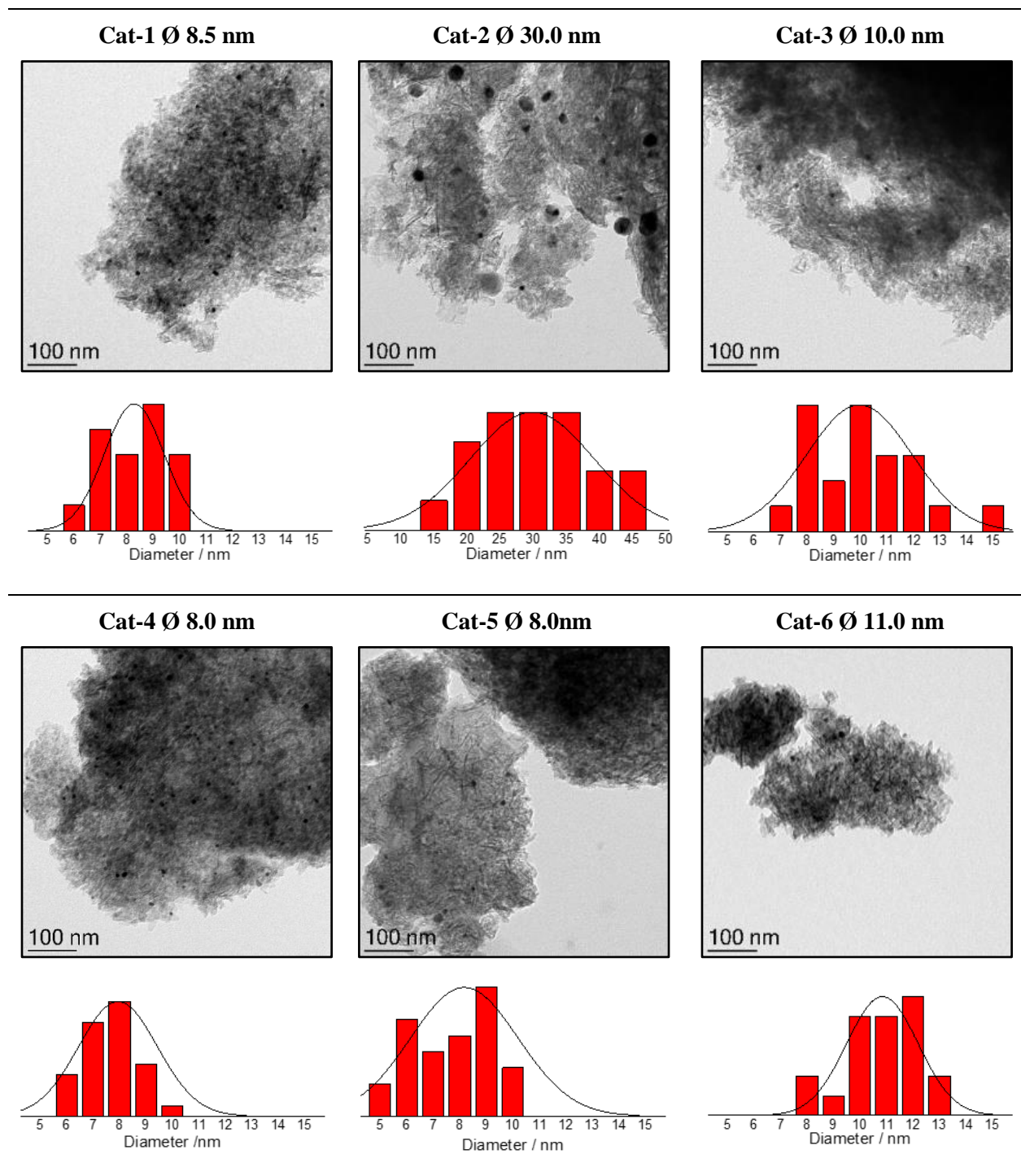
Figure S3. TEM analysis of Ni/Al$_2$O$_3$ catalysts Cat-1 to Cat-6, average size, and size distribution of Ni nanoparticles.

Cat-4 used   **Ø 8.0 nm**
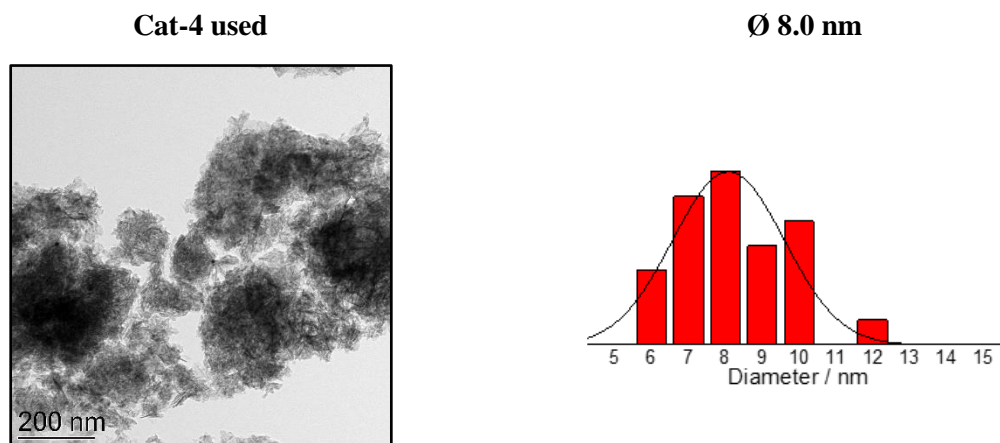
Figure S4. TEM analysis Cat-4 after catalysis and size distribution of Ni nanoparticles.
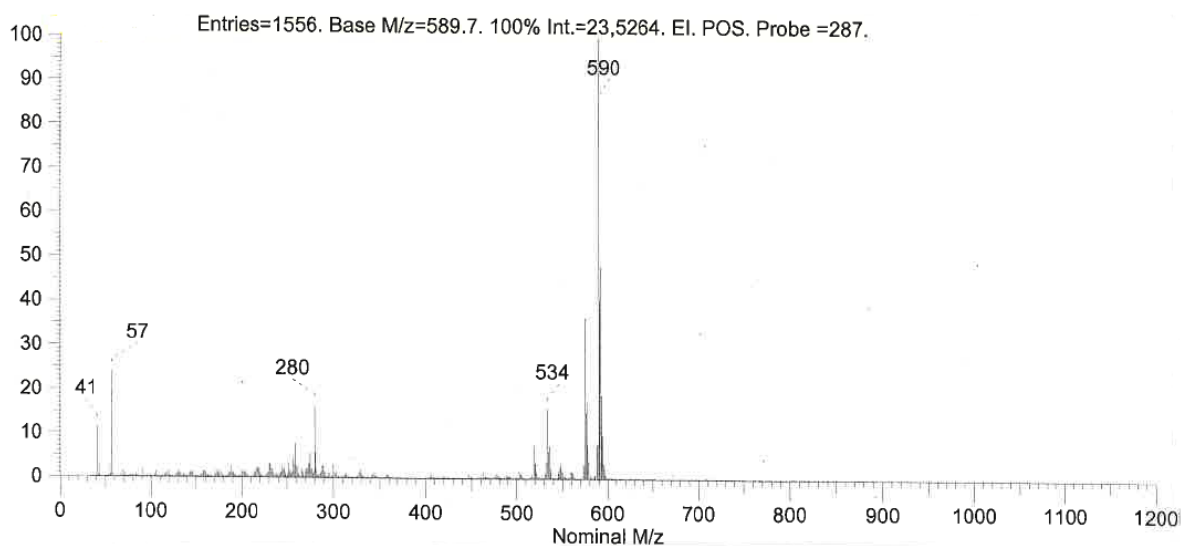
Figure S5. DIP mass spectra (range 0-1200 M/z) of sublimated complex C4 (M(C4)=591.41 g/mol) collected at the gas outlet during catalyst generation.
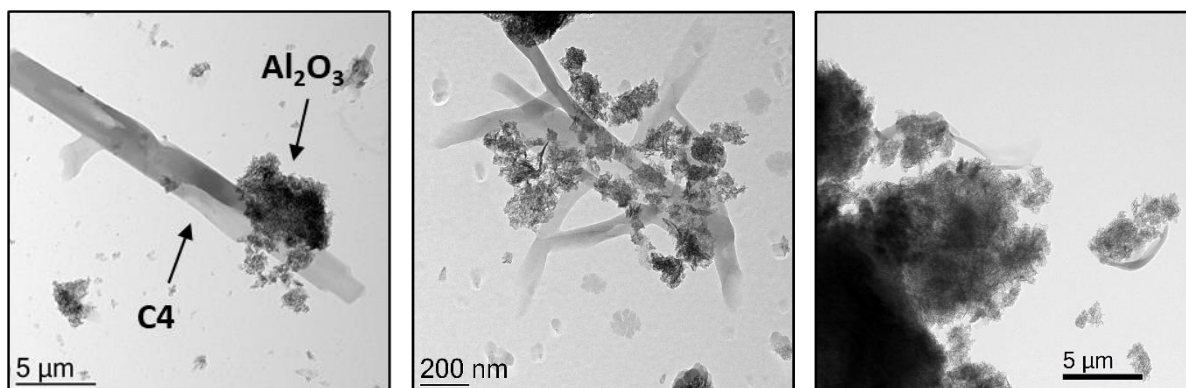
Figure S6. TEM analysis of impregnated Ni salen complex C4 on Al_2O_3 (left, middle) and heated to the sublimation temperature 469 °C of C4 (right).

53
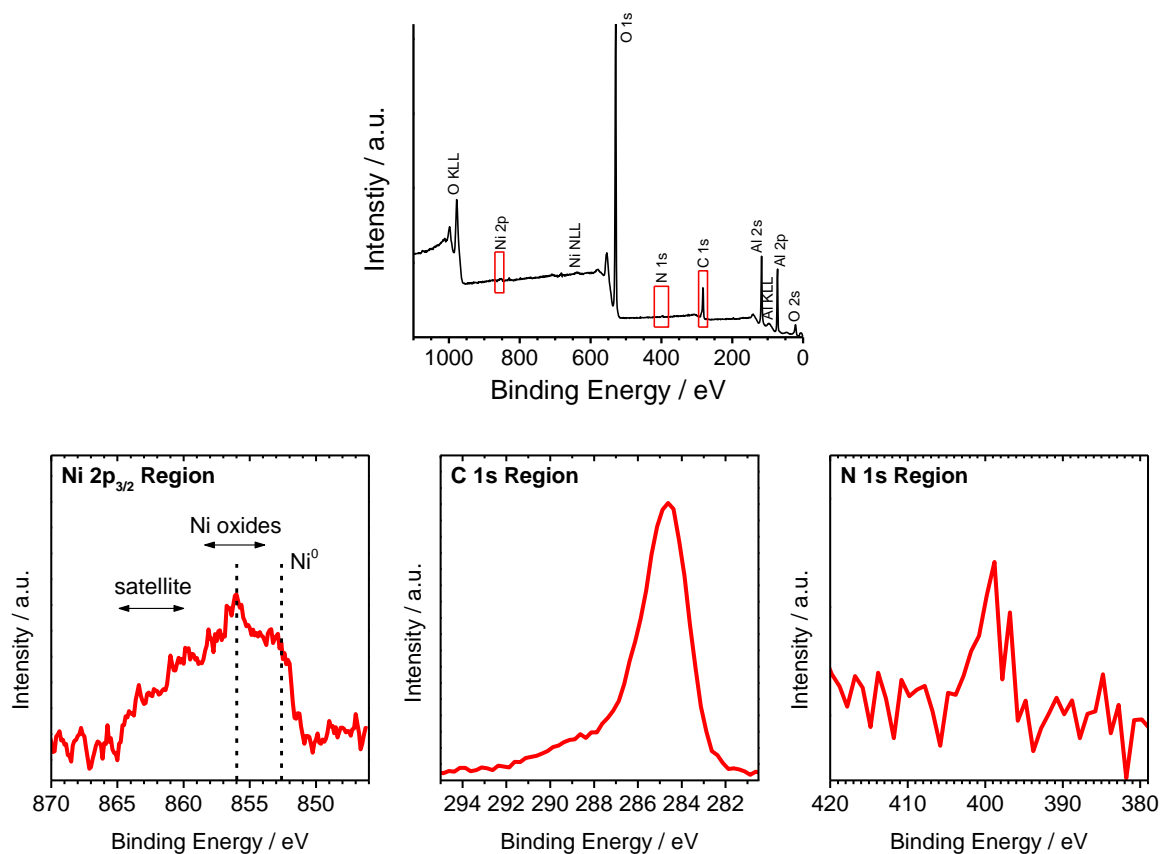
Figure S7. XPS survey of Ni/Al₂O₃ (Cat-4). Regions for which detailed analysis was performed are marked with a red box: C 1s, N 1s and Ni 2p3/2 region of Ni/Al₂O₃. (Al Kα radiation (hν=1486.6 eV))
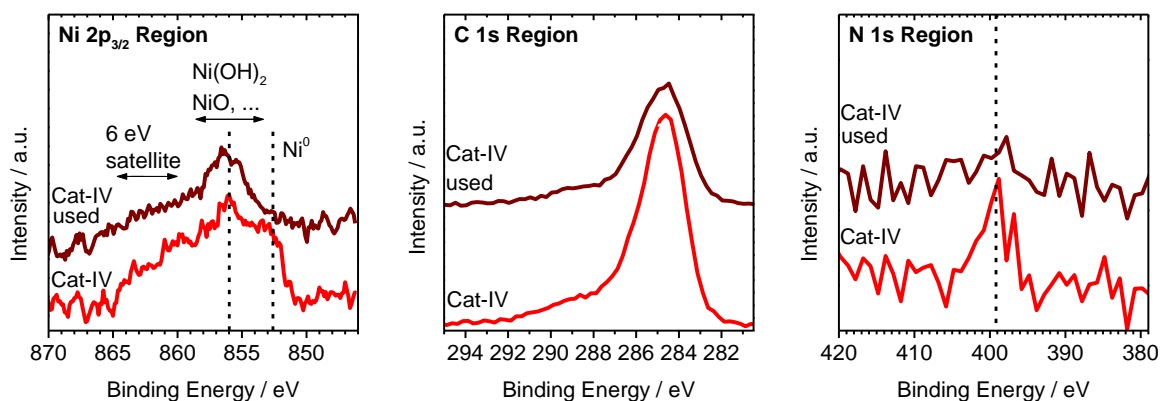
Figure S8. Comparison of XPS analysis of Ni/Al₂O₃ before (Cat-4) and after catalysis (Cat-4 used). C 1s, N 1s and Ni 2p3/2 region of Ni/Al₂O₃. (Al Kα radiation (hν=1486.6 eV))
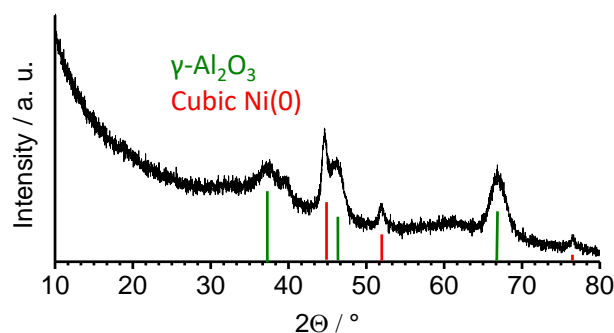
Figure S9. Powder XRD pattern of Cat-4 Ni/Al₂O₃. Reflex positions for cubic Ni(0) (Reference card 00-001-1260) are marked in red, reflex positions for γ-Al₂O₃ (Reference card 00-001-1303) in green.
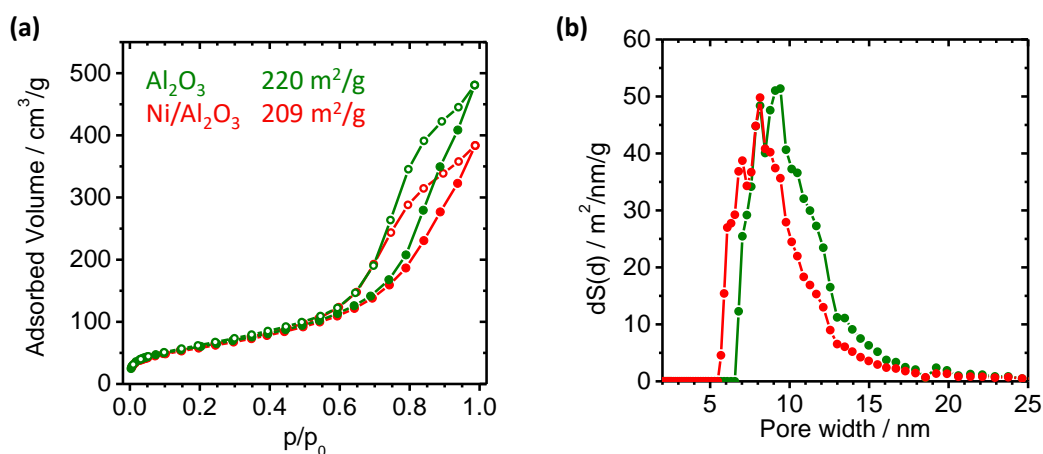
Figure S10. (a) N_2 physisorption isotherms of Al_2O_3 (220 m²/g) and Cat-4 Ni/Al₂O₃ (209 m²/g) with respective surface areas determined by BET-model (0.05-0.3 p/p₀). Adsorption is depicted in filled dots, desorption in rings. (b) Pore size distribution of Al_2O_3 compared to Cat-4 Ni/Al₂O₃. (DFT model: N_2 at -196 °C on silica, cylindric pore, NLDFT equilibrium model).
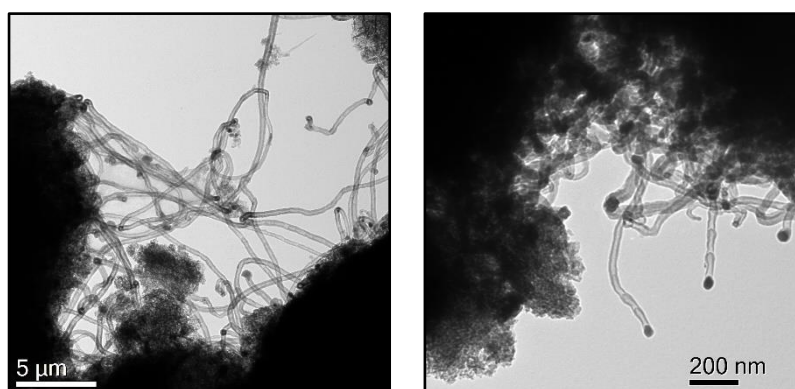

Figure S11. TEM analysis of C4/Al₂O₃ pyrolyzed in a fused silica vial (14 cm³) at 700 °C in N_2 atmosphere.
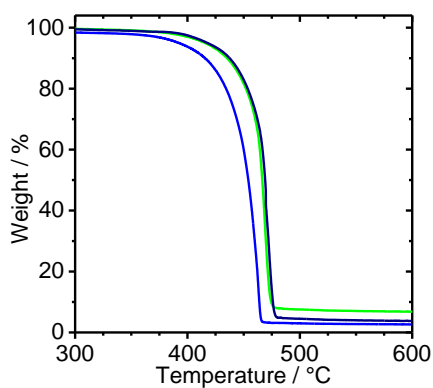
Figure S12. TGA analysis of Ni salen complex C4 at heating ramps of 5 K/min (blue), 10 K/min (green) and 15 K/min (dark blue).

4.5.3 References

[S1]   H.-R. Wen, S.-J. Liu, X.-R. Xie, J. Bao, C.-M. Liu, J.-L. Chen, *Inorg. Chim. Acta* **2015**, *435*, 274–282.

[S2]   S. J. Wezenberg, E. C. Escudero-Adán, J. Benet-Buchholz, A. W. Kleij, *Inorg. Chem.* **2008**, *47*, 2925-2927.

5 Chemoselective Hydrogenation of Olefins Using a Nanostructured Nickel Catalyst

Mara Klarner,[a] Sandra Bieger,[a] Markus Drechsler,[b] Rhett Kempe*[a]

[a]   Inorganic Chemistry II, University of Bayreuth, Universitätsstr. 30, 95440 Bayreuth (Germany)

[b]   Bavarian Polymer Institute (BPI), KeyLab "Electron and Optical Microscopy", University of Bayreuth, Universitätsstr. 30, 95440 Bayreuth (Germany)

Abstract: The selective hydrogenation of functionalized olefins is of great importance in the chemical and pharmaceutical industry. Here, we report on a nanostructured nickel catalyst that enables the selective hydrogenation of purely aliphatic and functionalized olefins under mild conditions. The earth-abundant metal catalyst allows the selective hydrogenation of sterically protected olefins and further tolerates functional groups such as carbonyls, esters, ethers and nitriles. The characterization of our catalyst revealed the formation of surface oxidized metallic nickel nanoparticles stabilized by a N-doped carbon layer on the active carbon support.

5.1 Introduction

The selective hydrogenation of C-C double bonds is a challenging reaction and of high interest in academia and for the production of industrially relevant chemicals.[1,2] More specifically, the selective hydrogenation of olefins plays an important role in the synthesis of vitamins such as biotin and β-carotene.[3] Also drugs such as sertraline (anti-depressant), betamethasone (glucocorticoid), and dihydroergotamine (antimigraine agent) are produced in this way.[4] The hydrogenation of diisobutene to isooctane is important in the petrochemical industry, because it is widely used as an anti-knock additive and as a substitute for the previously used methyl *tert*-butyl ether.[5] Furthermore, the olefin hydrogenation is used for the hardening of natural oils in the food industry for better processing and storage.[6] One possible route for olefin hydrogenation is catalytic transfer hydrogenation[7], which is usually accompanied by the formation of easy-to-remove by-products. Most of the known and industry-relevant catalyst systems are based on the expensive noble metals ruthenium, rhodium, palladium,

platinum and iridium or on difficult to handle and pyrophoric Raney nickel.[8,9] In recent years, hydrogenation with nanostructured 3d metal catalysts step into the focus for many applications as introduced by us[10] and the Beller group.[11] Also, the selective olefin hydrogenation of α,β-unsaturated carbonyls, internal and terminal unsaturated hydrocarbons was addressed with heterogeneous iron[12], cobalt[13] und nickel[14] catalysts. A highlight is the work of Scharnagl *et al.*[13c], who were able to hydrogenate terminal and internal alkenes with a high tolerance of functional groups using a Co@Chitosan catalyst (2.9 mol% Co) at 60 °C and 4 MPa H_2 pressure or at 150 °C and 1 MPa H_2, respectively. Impressively, fatty acids and sunflower oil could also be converted in high yields. Considering Ni catalysts, colloidally stabilized Ni nanoparticles were used for the selective hydrogenation of α,β-unsaturated carbonyl compounds at room temperature and 4 MPa H_2.[14f] In addition, supported systems such as the Ni-phen@SiO_2 catalyst (4 mol% Ni) were developed to selectively convert substrates with different functional groups at 40 °C, 1 MPa H_2.[11e] The application of flow-chemistry techniques for the selective olefin hydrogenation with nickel is particularly used in pharmaceutical manufacturing and in the synthesis of valuable biobased building blocks.[15]

Here, we report on a nanostructured nickel catalyst, which permits the selective hydrogenation of functionalized olefins. This process is chemoselective and hydrogenation-sensitive functional groups such as carbonyl compounds, esters, ethers and nitriles are well tolerated. The Ni/C catalyst is easy-to-synthesize in a two-step procedure starting from inexpensive charcoal as support material. By controlled decomposition of a Ni-salen complex precursor, catalytically active Ni nanoparticles are generated and at the same time stabilized in a nitrogen-doped carbon matrix on the support.[10d–g,11f]

5.2   Results and Discussion

The novel Ni/C catalyst was synthesized in a practical two-step procedure according to the synthesis concept for 3d metal catalysts developed by us[10d-g] (Figure 1): Firstly, the commercially available carbon support (Norit CA1) was wet impregnated with the novel Ni-salen(prop)(di-*tert*-butyl) complex in tetrahydrofuran and the solvent was removed (see Supporting Information for crystallographic data and complex characterization). This was followed by a pyrolysis step at 700 °C in nitrogen atmosphere and a reduction step at 550 °C in forming gas (90/10, N_2/H_2). We assume that the Ni catalyst is generated by molecular dispersion of a defined volatile complex compound on the support material during the pyrolysis step. The subsequent tailored decomposition of the Ni-salen complex leads to the formation of a N-doped carbon layer in which the catalytically active Ni sites are embedded. Our catalyst is very convenient to handle and remains catalytically active for several months when stored in an inert atmosphere (Supporting Information, Table S2). We performed transmission electron microscopy (TEM) and X-ray photoelectron spectroscopy (XPS) analysis to gain more insight into the catalyst structure. The catalyst consists of homogeneously distributed, spherical Ni nanoparticles with an average size of 19.5 nm and a fairly broad size distribution (Figure 1b, c). An additional dark-field TEM

image verified the homogeneous distribution over the entire carbon support (Figure 1f). Detailed analysis of one Ni particle at the edge of an activated carbon platelet showed that the nanoparticle is covered by a 2-3 nm thick carbon layer (Figure 1g). This layer could only be analyzed for exposed particles, so that no average layer thickness could be determined for all supported nickel particles. Referring to our last publication, we claim that the decomposition of the Ni-salen complex leads to a N-doped carbon matrix that stabilizes the Ni particles.[10d] Elemental analysis of the catalyst material confirmed that 0.8 wt.% nitrogen from the decomposition of the Ni-salen complex remained in the Ni/C composite. To date, it is unclear to what extent the thickness and atomic composition of the N-doped carbon layer plays a key role in the catalyst activity. It is conceivable that the layer thickness and composition can be influenced by the gas flow and the choice of salen precursor during the catalyst preparation.
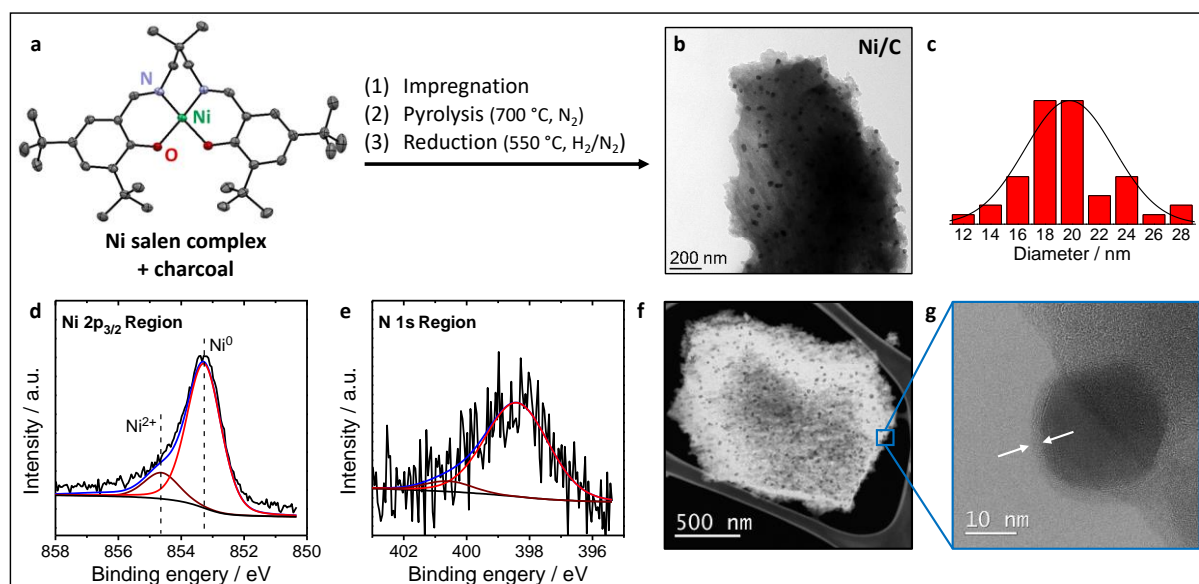

Figure 1. Catalyst Synthesis and Characterization. (a) Synthesis of the Ni/C catalyst by (1) wet impregnation of commercial activated charcoal (Norit CA1) with the Ni-salen(prop)(di-*tert*-butyl) complex (see Supporting Information for crystallographic data and complex characterization), followed by (2) a pyrolysis step at 700 °C in N_2 flow and (3) a reduction step at 550 °C in forming gas. (b, c) TEM analysis verifies the homogenous distribution of Ni nanoparticles with a mean diameter of 19.5 nm. The size distribution of Ni particles is shown as histogram. (d) XPS analysis of the Ni $2p_{3/2}$ region. The Ni^0 nanoparticles are partially surface oxidized to Ni^{2+} species (about 17 %). (e) XPS analysis of the N 1s region. (f) Dark-field TEM analysis of the Ni/C catalyst. (g) Magnification by TEM exemplarily shows one Ni nanoparticle of 23 nm in diameter surrounded by a 2-3 nm thick carbon layer (marked with white arrows).
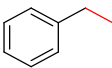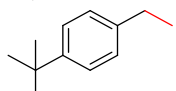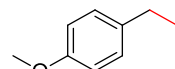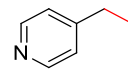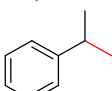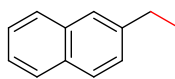
We recorded XPS survey spectra of the Ni/C catalyst in the range of 0-1200 eV (Supporting Information, Figure S5) and observed expected lines for carbon, nickel and traces of nitrogen. In the Ni $2p_{3/2}$ region (Figure 1d), the combination of a metallic Ni^0 signal at 852.6 eV and a broader signal at about 854.6 eV, assigned to oxidized Ni^{2+}, was measured. The comparison of the intensity ratios at the dashed positions showed that 83 % Ni^0 is present. Due to the handling in air, the appearance of surface-oxidized metallic Ni nanoparticles is likely. The binding energy of the N 1s signal observed is centered at 398.5 eV,

possibly a remnant of the N-containing precursor molecule and its decomposition products (Figure 1e). We did not attempt to deconvolute the signal because of the low intensity. The cubic phase of metallic Ni of the freshly prepared catalyst could be indexed in the powder X-ray diffraction pattern (Supporting Information, Figure S6). This supports our thesis of surface oxidized Ni particles with metallic core. Inductively coupled plasma optical emission spectroscopy (ICP-OES) revealed a Ni content of 2.7 wt.%. This value deviates from the targeted 4 wt.% because the amount of Ni deposited on the support decreased due to the volatility of the Ni precursor during the pyrolysis process (Supporting Information, Figure S2). Argon physisorption measurements demonstrated a 26 % decrease in the surface area of the bare carbon support (929 m^2/g) to 688 m^2/g due to the catalyst generation process, including the particle formation (Supporting Information, Figure S7). The DFT model (Ar at 87 K on carbon, cylindrical pores) used to evaluate the pore size distribution showed an identical bimodal pore distribution for the support material and for the Ni/C catalyst. Both materials are predominantly microporous. The catalyst synthesis does not affect the absolute pore size, but only reduces the total pore volume.

We investigated the Ni/C catalyst in the hydrogenation of the C-C double bond of styrene as a catalytic benchmark test. To our delight, a low catalyst loading (1.35 mol% Ni) and very mild reaction conditions (0.2 MPa H_2, 40 °C) were necessary to obtain ethylbenzene in a quantitative yield (Supporting Information, Table S2, S3). A yield of 50 % was still obtained at room temperature and 0.1 MPa H_2 pressure, highlighting the catalytic activity of this base metal catalyst. In comparison with commercial oxidic support materials (Al_2O_3, CeO_2, SiO_2, TiO_2), the combination of the Ni-salen precursor and the activated carbon support was shown to be crucial for the high catalytic activity. Remarkably, only the catalyst on silica support showed moderate catalytic activity. No hydrogenation active Ni/C catalyst could be prepared with nickel acetate as precursor, highlighting the necessity of the Ni-salen complex (Supporting Information, Table S2). Raney-Ni likewise led to quantitative yield in this benchmark reaction. With the optimized reaction conditions in hand, we were interested in the substrate scope. All given product yields were determined by gas chromatography (GC) and identified by GC-mass spectrometry (GC-MS). Isolated yields were determined for selected examples and are given in parentheses. Styrene (Table 1, **1a**, 99 %) and a total of 12 functionalized styrene derivatives were selectively converted to the corresponding ethylbenzene derivatives. Methyl-substituted compounds were tolerated in *para*, *meta* and *ortho* position (Table 1, **1b** to **1d**, 99-84 %), as was the chloro-substituent (Table 1, **1e-g**, 78-60 %) with *ortho* being the most challenging position. Also, the hydrogenation of 4-bromostyrene was realized in moderate yield (Table 1, **1h**, 50 %) without dehalogenation. Electron-donating groups such as *tert*-butyl and methoxy in *para* position (Table 1, **1i** and **1j**) were very well tolerated by the Ni/C catalyst and the corresponding products were obtained in quantitative yields. The double bond of the N-heteroaromatic substrate 2-vinylpyridine, the 1,1-disubstituted α-methoxy styrene and the polyaromatic 2-vinylnaphthalene were hydrogenated in moderate to good yields, respectively (Table 1, **1k** to **1m**). The hydrogenation of styrene at about 60 % was chosen as the test reaction for a recyclability study. The catalyst was used in five consecutive runs

and showed no reduction in activity in the first three (Supporting Information, Figure S8). Then a minor decrease in activity was observed.
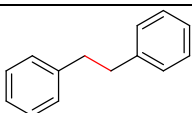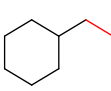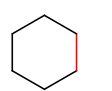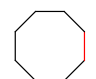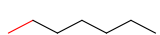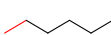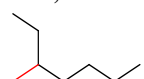
Table 1. Olefin hydrogenation with Ni/C: Investigation of styrene derivatives.[a]

	R: 4-Me **1b, 99 %**	R: 4-Cl **1e, 78 %**
	2-Me **1d, 84 %**	2-Cl **1g, 60 %**
	3-Me **1c, 99 %**	3-Cl **1f, 75 %**
		4-Br **1h, 50 %**
1a, 99 % (98 %)		
1i, 99 %	**1j, 99 %**	**1k,[b] 58 %**
1l, 84 %	**1m, 43 %**	

[a] 0.5 mmol substrate, 2.5 ml MeOH, 1.35 mol% Ni (14.7 mg Ni/C, 2.7 wt.% Ni), 40 °C, 0.2 MPa H_2, 20 h. [b] 80 °C, 1 MPa H_2.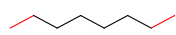 Yields determined by GC using *n*-dodecane as an internal standard. Products were analyzed by GC-MS. Isolated yields are given in parentheses.

Next, we investigated the transformation of purely aliphatic and aromatic unsaturated hydrocarbons. The conversion of these non-functionalized olefins required harsher reaction conditions of 80 °C and 1 MPa H_2, whereas the catalyst loading did not need to be increased (Supporting Information, Table S4).
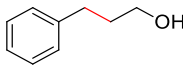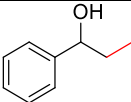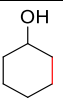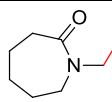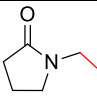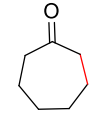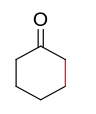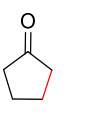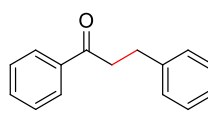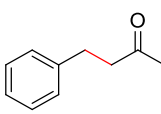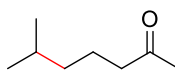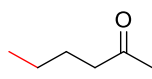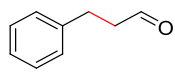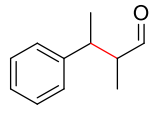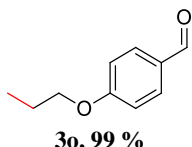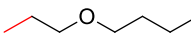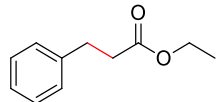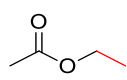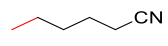
Table 2. Olefin hydrogenation with Ni/C: Investigation of unsaturated hydrocarbons.[a]

2a, 99 % (90 %)	**2b, 99 %**	**2c, 94 %**
2d, 99 % (99 %)	**2e, 99 %**	**2f, 99 %**
2g, 99 %	**2h, 99 %**	**2i, 91 %**

[a] 0.5 mmol substrate, 2.5 ml MeOH, 1.35 mol% Ni (14.7 mg Ni/C, 2.7 wt.% Ni), 80 °C, 1 MPa H_2, 20 h. Yields determined by GC using *n*-dodecane as an internal standard. Products were analyzed by GC-MS. Isolated yields are given in parentheses.

1,2-substituted C-C double bonds as in *trans*-stilbene (Table 2, **2a**, 99 %) and internally cyclic olefins such as cyclohexene, cyclooctene and norbornene were quantitatively converted to the respective saturated compounds (Table 2, **2c** to **2e**). In addition, terminal double bonds in vinylcyclohexane, octa-1,8-diene, 1-heptene, and 1-hexene (Table 2, **2b** and **2f** to **2h**) were hydrogenated in 99 % yield. Furthermore, it was possible to convert a 1,1-disubstituted olefin to obtain the product 3-methlyheptane in 91 % (Table 2, **2i**). The application scope of the catalyst had been further extended to the olefin hydrogenation in the presence of hydrogenation-sensitive functional groups. Water was used as a solvent for C=O functionalized substrates because the methylation of carbonyl functions by the solvent methanol occurred as an undesirable side reaction. A total of 19 examples were selectively converted at 80 °C and 1 MPa H_2 pressure. Alcohol-modified substrates (Table 3, **3a** to **3c**, 92-99 %) did not negatively affect the catalytic hydrogenation of C-C double bonds by Ni/C. Likewise, N-vinyl derivatives of caprolactam and pyrrolidone were quantitatively converted (Table 3, **3d** and **3e**) without attacking the cyclic amide. Our Ni/C catalyst enables the challenging hydrogenation of olefins in the presence of α,β-unsaturated ketones in very good yields. Internal cyclic carbonyl compounds were converted more efficiently (Table 3, **3f** to **3h**, 92-99 %) than non-cyclic ones (Table 3, **3i** and **3j**, 84 % and 74 %).

Table 3. Olefin hydrogenation with Ni/C: Investigation of functional group tolerance.[a]

[a] 0.5 mmol substrate, 2.5 ml H_2O, 1.35 mol% Ni (14.7 mg Ni/C, 2.7 wt.% Ni), 80 °C, 1 MPa H_2, 20 h. [b] 2.5 ml MeOH. Yields determined by GC using *n*-dodecane as an internal standard. Products were analyzed by GC-MS. Isolated yields are given in parentheses.

Furthermore, isolated mono- or trisubstituted C-C double bonds were selectively hydrogenated in the presence of keto groups (Table 3, **3k** and **3l**). Remarkably, hydrogenation-sensitive α,β-unsaturated aldehydes were well tolerated. Not only a 1,2-di-substituted olefin (Table 3, **3m**, 76 %) but also the

challenging 1,2-tetrasubstituted 2-methyl-3-phenylbutenal (Table 3, **3n**, 78 %) was selectively hydrogenated in good yields. Only a minor trace of alcohol was observed as a byproduct. Also, an aromatic and an aliphatic allyl ether (Table 3, **3o** and **3p**) and cinnamic acid ethyl ester (Table 3, **3q**) were quantitatively converted to the respective saturated compounds. For unknown reasons, only a moderate yield of 68 % of ethyl acetate (Table 3, **3r**) could be obtained. In addition to the numerous examples of oxygen-containing functional groups, the C≡N triple bond of an aliphatic nitrile was tolerated (Table 3, **3s**, 99 %). One reaction was performed with 20 times the amount of substrate (10 mmol) to demonstrate the applicability of the Ni/C catalyst on a larger scale. Styrene (95 %) was converted to the corresponding saturated product with slightly reduced activity referred to the 0.5 mmol reaction.

5.3 Conclusion

In summary, we have developed a nickel catalyst that selectively hydrogenates olefins under mild reaction conditions. The Ni/C catalyst showed a high tolerance to hydrogenation-sensitive functional groups such as carbonyl, ether, ester, and nitrile.

Acknowledgements

5.4 References

[1]   H.-U. Blaser, F. Spindler, M. Thommen, J. G. De Vries, C. J. Elsevier, *The Handbook of Homogeneous Hydrogenation*, Wiley-VCH: Weinheim, **2008**.

[2]   L. A. Saudan, *Acc. Chem. Res*. **2007,** *40*, 1309.

[3]   S. Lavielle, S. Bory, B. Moreau, M. J. Luche, A. Marquet, *J. Am. Chem. Soc*. **1978**, *100*, 1558.

[4]   B. Chen, U. Dingerdissen, J. G. E. Krauter, H. G. J. Lansink Rotgerink, K. Möbus, D. J. Ostgard, P. Panster, T. H. Riermeier, S. Seebald, T. Tacke, H. Trauthwein, *Appl. Catal. A* **2005**, *280*, 17.

[5]   B. M. Goortani, A. Gaurav, A. Deshpande, F. T. T. Ng, G. L. Rempel, *Ind. Eng. Chem. Res.* **2015**, *54*, 3570.

[6]   G. List, J. W. King, *AOCS Press*. **2015**, ed. 2.

[7]   D. Wang, D. Astruc, *Chem. Rev*., **2015**, *115*, 6621.

[8]   a) M. Guerrero, N. T. Than Chau, S. Noel, A. Denicourt- Nowicki, F. Hapiot, A. Roucoux, E. Monflier, K. Philippot, *Curr. Org. Chem*. **2013**, *17*, 364; b) B. L. Albuquerque, A. Denicourt-

Nowicki, C. Mériadec, J. B. Domingos, A. Roucoux, *J. Catal.* **2016**, *340*,144; c) M. Tamura, K. Tokonami, Y. Nakagawa, K. Tomishige, *ACS Catal*. **2016**, *6*, 3600.

[9] a) H. Adkins, H. R. Billica, *J. Am. Chem. Soc*. **1948**, *70*, 695; b) A. F. Barrero, E. J. Alvarez-Manzaneda, R. Chahboun, R. Meneses, *Synlett.* **1999**, *10*, 1663; c) X. Ge, J. Pan, X. Chen, C. Qian, S. Zhou, *Int. J. Hydrog. Energy* **2016**, *41*, 18478.

[10] a) G. Hahn, J.-K. Ewert, C. Denner, D. Tilgner, R. Kempe, *ChemCatChem* **2016**, *8*, 2461; b) T. Schwob, R. Kempe, *Angew. Chem. Int. Ed.* **2016**, *55*, 15175; c) C. Bäumler, R. Kempe, *Chem. Eur. J*. **2018**, *24*, 8989; d) G. Hahn, P. Kunnas, N.de Jonge, R. Kempe, *Nat. Catal.* **2019**, *2*, 71; e) T. Schwob, P. Kunnas, N.de Jonge, C. Papp, H.-P. Steinrück, R. Kempe, *Sci. Adv.* **2019**, *5*, eaav3680; f) T. Schwob, M. Ade, R. Kempe, *ChemSusChem* **2019**, *12*, 3013; g) C. Bäumler, C. Bauer, R. Kempe, *ChemSusChem* **2020**, *13*, 3110.

[11] a) R. V. Jagadeesh, A.-E. Surkus, H. Junge, M.-M. Pöhl, J. Radnik, J. Rabeah, H. Huan, V. Schünemann, A. Brückner, M. Beller, *Science* **2013**, *342*, 1073; b) F. A. Westerhaus, R. V. Jagadeesh, G. Wienhöfer, M.-M. Pöhl, J. Radnik, A.-E. Surkus, J. Rabeah, K. Junge, H. Junge, M. Nielsen, A. Brückner, M. Beller, *Nat. Chem.* **2013**, *5*, 537; c) X. Cui, Y. Li, S. Bachmann, M. Scalone, A.-E. Surkus, K. Junge, C. Topf, M. Beller, *J. Am. Chem. Soc*. **2015**, *137*, 10652; d) R. Jagadeesh, K. Murugesan, A. S. Alshammari, H. Neumann, M.-M. Pohl, Marga Martina, J. Radnik, M. Beller, *Science* **2017**, *358*, 326; e) P. Ryabchuk, G. Agostini, M.-M. Pohl, H. Lund, A. Agapova, H. Junge, K. Junge, M. Beller, *Sci. Adv*. **2018**, *4*, eaat0761; f) Senthamarai, V. G. Chandrashekhar, M. B. Gawande, N. V. Kalevaru, R. Zboril, P. C. J. Kamer, R. V. Jadadeesh, M. Beller, *Chem. Sci.* **2020**, *11*, 2973.

[12] a) R. Paul, G. Hilly, *Bull. Soc. Chim*. **1939**, *6*, 218; b) A. F. Thompson, Jr. and S. B. Wyatt, *J. Am. Chem. Soc.* **1940**, *62*, 2555; c) S.-i. Taira, *Bull. Chem. Soc. Jpn*. **1962**, *35*, 840; d) P.-H. Phua, L. Lefort, J. A. F. Boogers, M. Tristany, J. G. de Vries, *Chem. Commun*. *2009*, 3747; e) C. Rangheard, C. Fernandez, P. Phua, J. Hoorn, L. Lefort, J. G. de Vries, *Dalton Trans*. **2010**, *39*, 8464; f) M. Stein, J. Wieland, P. Steurer, F. Tölle, R. Mülhaupt, B. Breit, *Adv. Synth. Catal.* **2011**, *353*, 523; g) R. Hudson, A. Rivière, C. M. Cirtiu, K. L. Luska, A. Moores, *Chem. Commun.* **2012**, *48*, 3360; h) V. Kelsen, B. Wendt, S. Werkmeister, K. Junge, M. Beller, B. Chaudret, *Chem. Commun*. **2013**, *49*, 3416; i) R. Hudson, G. Hamasaka, T. Osako, Y. M. A. Yamada, C.-J. Li, Y. Uozumi, A. Moores, *Green Chem.* **2013**, *15*, 2141; j) T. N. Gieshoff, M. Villa, A. Welther, M. Plois, U. Chakraborty, R. Wolf, A. Jacobi von Wangelin, *Green Chem.* **2015**, *17*, 1408; k) T. N. Gieshoff, U. Chakraborty, M. Villa, A. Jacobi von Wangelin, *Angew. Chem. Int. Ed.* **2017**, *56*, 3585.

[13] a) B. V. Aller, *J. Appl. Chem.* **1958**, *8*, 492; b) S. U. Son, K. H. Park, Y. K. Chung, *Org. Lett*. **2002**, *4*, 3983; c) F. K. Scharnagl, M. F. Hertrich, F. Ferretti, C. Kreyenschulte, H. Lund, R. Jackstell, M. Beller, *Sci. Adv*. **2018**, *4*, eaau1248; d) S. Sandl, F. Schwarzhuber, S. Pöllath, J. Zweck, A. Jacobi v. Wangelin, *Chem. Eur. J.* **2018**, *24*, 3403; e) P. Büschelberger, E. Reyes-

Rodriguez, C. Schöttle, J. Treptow, C. Feldmann, A. Jacobi von Wangelin, R. Wolf, *Catal. Sci. Technol.* **2018**, *8*, 2648; f) T. Song, Z. Ma, Y. Yang, *ChemCatChem* **2019**, *11*, 1313; g) A. Pews-Davtayan, F. K. Scharnagl, M. F. Hertrich, C. Kreyenschulte, S. Bartling, H. Lund, R. Jackstell, M. Beller, *Green Chem.* **2019**, *21*, 5104.

[14]   a) K. Hata, I. Motoyama, K. Sakai, *Org. Prep. Proced. Int*. **1972**, *4*, 179; b) D. Chatterjee, H. C. Bajaj, A. Das, K. Bhatt, *J. Mol. Catal*. **1994**, *92*, 235; c) F. Alonso, M. Yus, *Tetrahedron Lett.* **1996**, *37*, 6925; d) F. Alonso, I.Osante, M. Yus, *Synlett.* **2006**, *18*, 3017; e) V. Polshettiwar, B. Baruwati, R. S. Varma, *Green Chem.* **2009**, *11*, 127; f) M. A. Harrad, P. Valerga, M. C. Puerta, I. Houssini, M. A. Ali, L. El Firdoussi, A. Karim, *Molecules* **2011**, *16*, 367; g) V. M. Mokhov, Y. V. Popov, D. N. Nebykov, *Russ. J. Gen. Chem.* **2016**, *52*, 319; h) M. G. Prakash, R. Mahalakshmy, K. R. Krishnamurthy, B. Viswanathan, *Catal. Sci. Technol*. **2015**, *5*, 3313; i) L. Zaramello, B. L. Albuquerque, J. B. Domingos, *Dalton Trans*. **2017**, *46*, 5082; j) K. O. Sebakhy, G. Vitale, P. Pereira-Almao, *Ind. Eng. Chem. Res*. **2019**, *58*, 8597; k) J.-q. Bai, M. Tamura, Y. Nakagawa, K. Tomishige, *Chem. Commun.* **2019**, *55*, 10519; l) M. Li, J. Fu, S. Xing, L. Yang, X. Zhang, P. Lv, Z. Wang, Z. Yuan, *Appl. Catal. B-Environ*. **2020**, *260*, 118114; m) T. M. Maier, S. Sandl, P. Melzl, J. Zweck, A. Jacobi v. Wangelin, R. Wolf, *Chem. Eur. J.* **2020**, *26*, 6113.

[15]   a) M. Zienkiewicz-Machnik, I. Goszewska, A. Srebowata, A. Kubas, D. Gizinski, G. Slowik, K. Matus, D. Lisovytskiy, M. Pisarek, J. Sa, *Catal. Today* **2018**, *308*, 38; b) L. K. Spare, D. G. Harman, J. R. Aldrich-Wright, T. V. Nguyen, C. P. Gordon, *Adv. Synth. Catal*. **2018**, *360*, 1209; c) B. Mallesham, P. Sudarsanam, B. V. S. Reddy, B. G. Rao, B. M. Reddy, *ACS Omega* **2018**, *3*, 16839; d) B. Szabo, B. Tamas, F. Faigl, J. Eles, I. Greiner, *J. Flow Chem.* **2019**, *9*, 13; d) V. R. Madduluri, K. K. Mandari, V. Velpula, M. Varkolu, S. R. R. Kamaraju, M. Kang, *Fuel* **2020**, *261*, 116339; e) M. Kundra, T. Grall, D. Ng, Z. Xie, C. H. Hornung, *Ind. Eng. Chem. Res.* **2021**, *60*, 1989.

5.5 Supporting Information

5.5.1 Experimental Procedures

General Methods

All chemicals and solvents were purchased commercially from chemical suppliers with purity over 95 % and used without further purification. The activated charcoal CA1 was purchased from Norit.

Elemental analyses (CHN) were performed in tin capsules using an UNICUBE element analyst. Sulfanilamide was used as a standard. NMR spectra were measured using a Varian INOVA 400 MHz and a Bruker Avance III HD 500 MHz spectrometer. Chemical shifts are reported in ppm relative to the deuterated solvent. X-ray crystal structure analysis was performed with a STOE STADIVARI (Mo$_{K\alpha}$ radiation, 0.71073 Å) equipped with an Oxford Cryostream low temperature unit. Structure solution and refinement were achieved with OLEXS.[S1] The structure was visualized using Mercury 4.1.3.[S2] Fourier transform infrared (FT-IR) spectroscopy measurements were performed with a JASCO FT-IR 6100 spectrometer in the range 4000 cm^{-1} to 700 cm^{-1} with a resolution of 4 cm^{-1} an a N$_2$ flow. UV-vis spectra were measured on a CARY 60 (Agilent Technologies).Thermogravimetric analysis was performed from 30 °C to 1000 °C (10 °C min^{-1}) using a TGA/SDTA 851^e (Mettler) under nitrogen atmosphere. Samples were placed in Al$_2$O$_3$ crucibles with lid. Catalyst materials were generated by pyrolysis (N$_2$) und reduction (N$_2$/H$_2$, 10/90) on a Chem-BET Pulsar (Quantachrome) using tubes of quartz glass. Inductively coupled plasma optical emission spectroscopy (ICP-OES) was carried out according to standard protocol digestion with a Vista-Pro radial (Varian). Argon physisorption isotherms were determined at 87 K using a 3P Micro100C (3P Instruments) apparatus equipped with a cryoTune87. Specific surface areas were calculated by using p/p$_0$-values from 0.005-0.1 by the BET model. Specific total pore volumes were determined by DFT calculations (Ar at 87 K on cylindrical pore (MDFT)). X-ray photoelectron spectroscopy (XPS) was performed using a PHI Versa Probe III instrument of Physical Electronics. As X-ray source a monochromatic Al$_{K\alpha}$ with a spot size of 100 µm (24.5 W) was used. The kinetic pass energy of the photoelectrons was determined with a hemispheric analyzer (45°) set to pass energy of 26 eV for high-resolution spectra. Transmission electron microscopy (TEM) measurements were carried out using a LEO 922O microscope (Zeiss, 200 kV) and a JEOL JEM-2200FS (200 kV). The samples were suspended in chloroform and sonicated for 5 min. 2 µL of the suspension were placed on a CF200-Cu-grid or a LC200-Cu-grid (Electron Microscopy Sciences) and allowed to dry. X-ray powder diffraction (PXRD) analysis in the range of 2-80 °2θ was performed using a XPERT-PRO diffractometer (Panalytical) (Cu$_{K\alpha}$ radiation, 1.54178 Å) in θ-2θ geometry with a position sensitive detector. The reference card number for comparison is 00-001-1260 for cubic Ni. Gas chromatography (GC) analyses were performed using an Agilent Technologies 6850 gas chromatograph equipped with a flame ionization detector (FID) and a MN Optima 17 capillary column (30.0 m x 0.32 mm x 0.25 µm) using *n*-dodecane as internal standard. GC-MS analyses were performed using an

Agilent Technologies 7890A gas chromatograph with a MN-MS HP-5 capillary column (30.0 m x 0.32 mm x 0.25 µm) and a coupled mass spectrometer (5975C MSD) as detector. Hydrogenation experiments were carried out with Parr Instrument stainless steel autoclaves N-MT5 300 mL equipped with heating mantles and temperature controller.

Salen Complex Synthesis (adapted from ref. [S3])

Salen(prop)(di-*tert*-butyl)

3,5-Di-*tert*-butylsalicylaldehyde (2.344 g, 10 mmol, 2 eq.) was dissolved in ethanol (50 mL), 2,2-dimethylpropan-1,3-diamine (0.600 mL, 5 mmol, 1 eq.) was added at room temperature. A yellow solid crystallized, immediately. This solid was filtered off, washed with ethanol, and dried in vacuum to yield the ligand salen(prop)(di-*tert*-butyl).
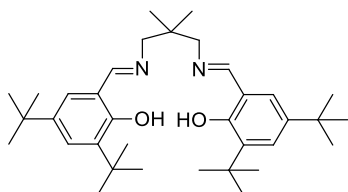
FW ($C_{35}H_{54}N_2O_2$) = 534.82 g mol^{-1}

Yield 5.241 g, 9.8 mmol, 98 %)

^{1}H-NMR (CDCl$_3$, 500 MHz) δ = 13.88 (s, 2H, O*H*), 8.38 (s, 2H, C*H*=N), 7.41-7.40 (d, 2H, Ar-*H*), 7.13-7.12 (d, 2H, Ar-*H*), 3.49 (s, 4H, C*H*$_2$), 1.48 (s, 18H, C(C*H*$_3$)$_3$), 1.33 (s, 18H, C(C*H*$_3$)$_3$), 1.12 (s, 6H, C*H*$_3$) ppm.

CHN C 78.73 (78.60), H 10.13 (10.18), N 5.33 (5.24) %.

Ni-Salen(prop)(di-*tert*-butyl)

Salen(prop)(di-*tert*-butyl) (1.604 g, 3 mmol, 1 eq.) was suspended in methanol (30 mL) and nickel acetate tetrahydrate (0.747 g, 3 mmol, 1 eq.) dissolved in methanol (15 mL) was added. The reaction was stirred at room temperature for 16 h, then the green solid was filtered off, washed with methanol, and dried in vacuum to yield the complex Ni-salen(prop)(di-*tert*-butyl) as a green, fluffy solid. Crystals suitable for X-ray analysis were grown from a saturated solution of the compound in dichloromethane.
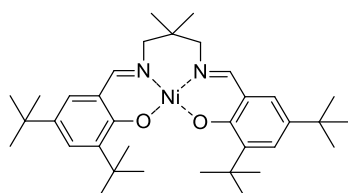
FW (NiC$_{35}$H$_{52}$N$_2$O$_2$) = 591.49 g mol^{-1}

Yield 1.721 g (2.91 mmol, 97 %)

^{1}H-NMR (CDCl$_3$, 500 MHz) δ = 7.30-7.29 (d, 2H, C*H*=N), 7.08 (s, 2H, Ar-*H*), 6.86-6.86 (d, 2H, Ar-*H*), 3.24 (s, 4H, C*H*$_2$), 1.41 (s, 18H, C(C*H*$_3$)$_3$), 1.27 (s, 18H, C(C*H*$_3$)$_3$), 0.89 (s, 6H, C*H*$_3$) ppm.

^{13}C-NMR (CDCl$_3$, 500 MHz) δ =164.10, 162.30, 140.39, 135.88, 129.07, 125.48, 119.81, 67.86, 35.78, 34.29, 33.76, 31.30, 29.54, 25.29 ppm.

CHN C 70.90 (71.07), H 9.03 (8.86), N 4.95 (4.74) %.

Ni/C Catalyst Preparation

A solution of Ni-salen(prop)(di-*tert*-butyl) (0.178 mmol, 10.4 mg of Ni, 4 wt.% Ni ideally) in 30 mL tetrahydrofuran was added to 250 mg activated charcoal and the suspension was stirred vigorously. For comparison, nickel acetate tetrahydrate (0.178 mmol, 10.4 mg of Ni, 4 wt.% Ni) in 15 mL tetrahydrofuran was impregnated on 250 mg activated coal. After evaporation of the solvent at 90 °C, the impregnated sample was pyrolyzed in N_2 and finally reduced by a N_2/H_2 (90/10) mixture in a ChemBET Pulsar with the following program:

$$\text{rt} \xrightarrow[N_2]{2 \text{ K/min}} 300\ °C\ (0.5\ h) \xrightarrow[N_2]{10 \text{ K/min}} 700\ °C\ (0.5\ h) \xrightarrow[N_2]{20 \text{ K/min}} 100\ °C \xrightarrow[N_2/H_2]{5 \text{ K/min}} 550\ °C\ (3\ h) \xrightarrow[N_2/H_2]{5 \text{ K/min}} \text{rt}$$
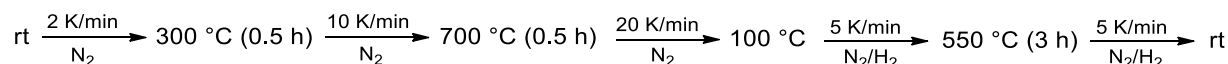
Catalysts were stored in inert atmosphere.

General Procedure for the Hydrogenation of Styrene Derivatives

In a typical experiment, a 5 mL reaction vial was charged with 1.35 mol.% Ni (0.0068 mmol Ni, 0.4 mg Ni) in form of the Ni/C catalyst and a magnetic stirring bar. 0.5 mmol styrene derivative and 2.5 mL methanol were added. The vial was placed in a 250 mL stainless steel autoclave (Parr Instruments) which was flushed five times with 1 MPa hydrogen. The autoclave was pressurized by 0.2 MPa (or 1 MPa) hydrogen and stirred for 20 h at 40 °C (or 80 °C). After the autoclave was cooled to room temperature and the hydrogen pressure was released, the reaction solution was filtered over Na_2SO_4 to remove residual catalyst. Yields were determined by gas chromatography using *n*-dodecane as an internal standard. Products were analyzed by GC-MS by comparing the mass spectra with those in the literature. Selected examples were isolated. After stopping the reaction, the catalyst was removed by centrifugation. The reaction mixture was filtered, and the solvent was removed in vacuo. The isolated products were identified by ^{1}H-NMR analysis.

General Procedure for the Hydrogenation of Olefins

In a typical experiment, a 5 mL reaction vial was charged with 1.2 mol.% Ni (0.0068 mmol Ni, 0.4 mg Ni) in form of the Ni/C catalyst and a magnetic stirring bar. 0.5 mmol olefin and 2.5 mL methanol (or 2.5 mL H_2O) were added. The vial was placed in a 250 mL stainless steel autoclave (Parr Instruments) which was flushed five times with 1 MPa hydrogen. The autoclave was pressurized by 1 MPa hydrogen and stirred for 20 h at 80 °C. After the autoclave was cooled to room temperature and the hydrogen pressure was released, the reaction solution was filtered over Na_2SO_4 to remove residual catalyst. Yields were determined by gas chromatography using *n*-dodecane as an internal standard. Products were analyzed by GC-MS by comparing the mass spectra with those in the literature. Selected examples were isolated. After stopping the reaction, the catalyst was removed by centrifugation. The reaction mixture was filtered, and the aqueous layer was extracted three times with

methyl *tert*-butyl ether, dried over Na_2SO_4, and the solvent was then removed in vacuo. The isolated products were identified by ^{1}H-NMR analysis.

Recyclability Study for Ni/C

The hydrogenation of styrene was chosen as the test reaction for the recyclability study on the Ni/C catalyst. For comparability, runs were performed with about 60 % yield of ethylbenzene. The optimized reaction conditions were used, but the reaction time was shortened to 4 h. The reaction was carried out in the same way as for the Ni/C catalyst. The yield of ethylbenzene was determined by GC using *n*-dodecane as an internal standard. After each run, the reaction mixture was centrifuged, the catalyst was washed three times with methanol and used directly in the next run. Five consecutive runs were performed.

See Supplementary Figure S8.

Large Scale Reactions Using Ni/C

For large-scale reactions, 20 times the amount of substrate (10 mmol) was used, the amount of solvent and catalyst was increased accordingly. The reaction time was increased to 24 h. The upscaling was performed in a 60 mL Schott bottle, which was placed stainless steel autoclave (Parr Instruments). In all other steps, the reaction was carried out analogously to the general procedure.

Reaction conditions: 10 mmol styrene (1146 µL), 50 mL MeOH, 1.35 mol% Ni (294 mg Ni/C, 2.7 wt.% Ni), 40 °C, 0.2 MPa H_2, 24 h.

Crystallographic data of Ni-salen(prop)(di-*tert*-butyl)

Crystals suitable for X-ray analysis were grown from a saturated solution of the compound in dichloromethane.

Deposition Number: 2076115
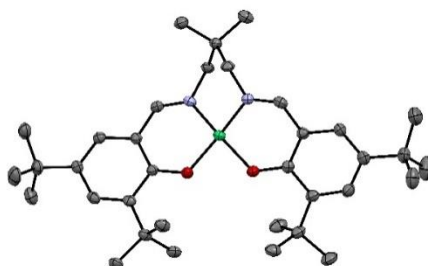
Table S1. Crystallographic details of Ni-salen(prop)(di-tert-butyl) used in this study.

Compound	Ni-salen(prop)(di-*tert*-butyl) SV582
Formula	$C_{35}H_{52}N_2NiO_2$
Formula weight	591.49
Crystal system	triclinic
Space group	P-1
a / Å	10.940(2)
b / Å	12.260(3)
c / Å	14.430(3)
α / °	113.30(3)
β / °	100.60(3)
γ / °	97.60(3)
Cell volume / Å^3	1701.6(7)
Z	2
Crystal size / mm^3	0.47*0.042*0.005
Habit	needle
Color	green
Density / gcm^{-1}	1.154
T / K	293
Theta range	2.921-28.446
Unique reflections	8021
Observed reflections [I>2s(I)]	5757
Parameters	376
wR2 all data	0.2148
R [I>2s(I)]	0.0739

5.5.2 Material Characterization

Salen ligand and Ni-salen complex
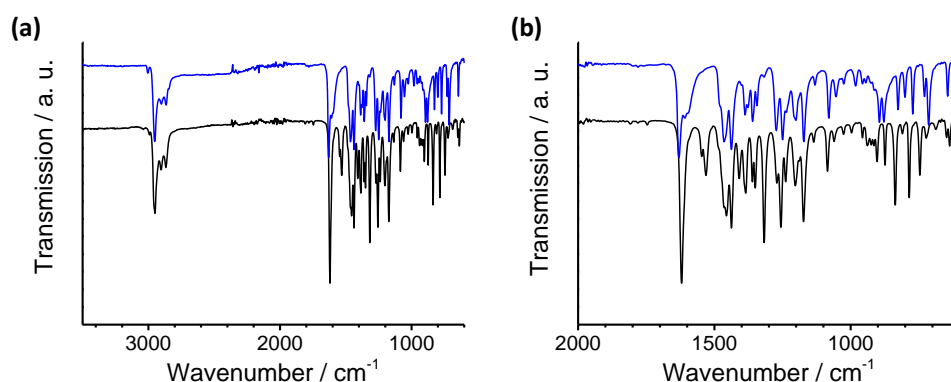
Figure S1. FT-IR analysis of the salen ligand (blue) and the Ni-salen(prop)(di-tert-butyl) complex (black).
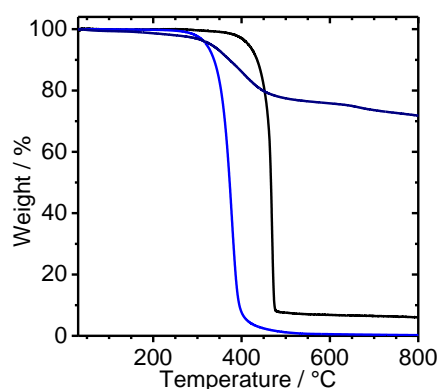
Figure S2 TGA analysis of salen ligand (blue), Ni-salen(prop)(di-*tert*-butyl) complex (black) and impregnated complex on charcoal (dark blue). Measurements were performed in the range of 30-800 °C (heating ramp 10 K/min) in constant N_2 flow. The sublimation temperature (T_{subl} = 469 °C) of Ni-salen(prop)(di-*tert*-butyl) was determined from the zero of the first derivative of the TGA curve.
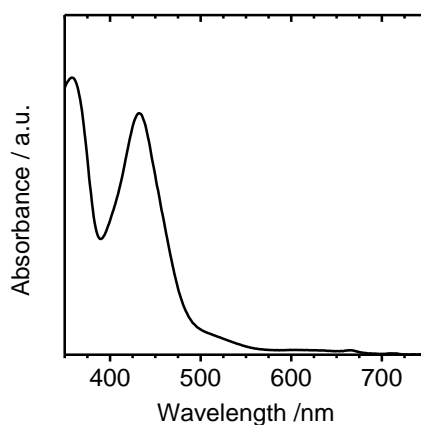
Figure S3 UV-vis spectrum of Ni-salen(prop)(di-*tert*-butyl) measured in tetrahydrofuran in the range of 350-750 nm.
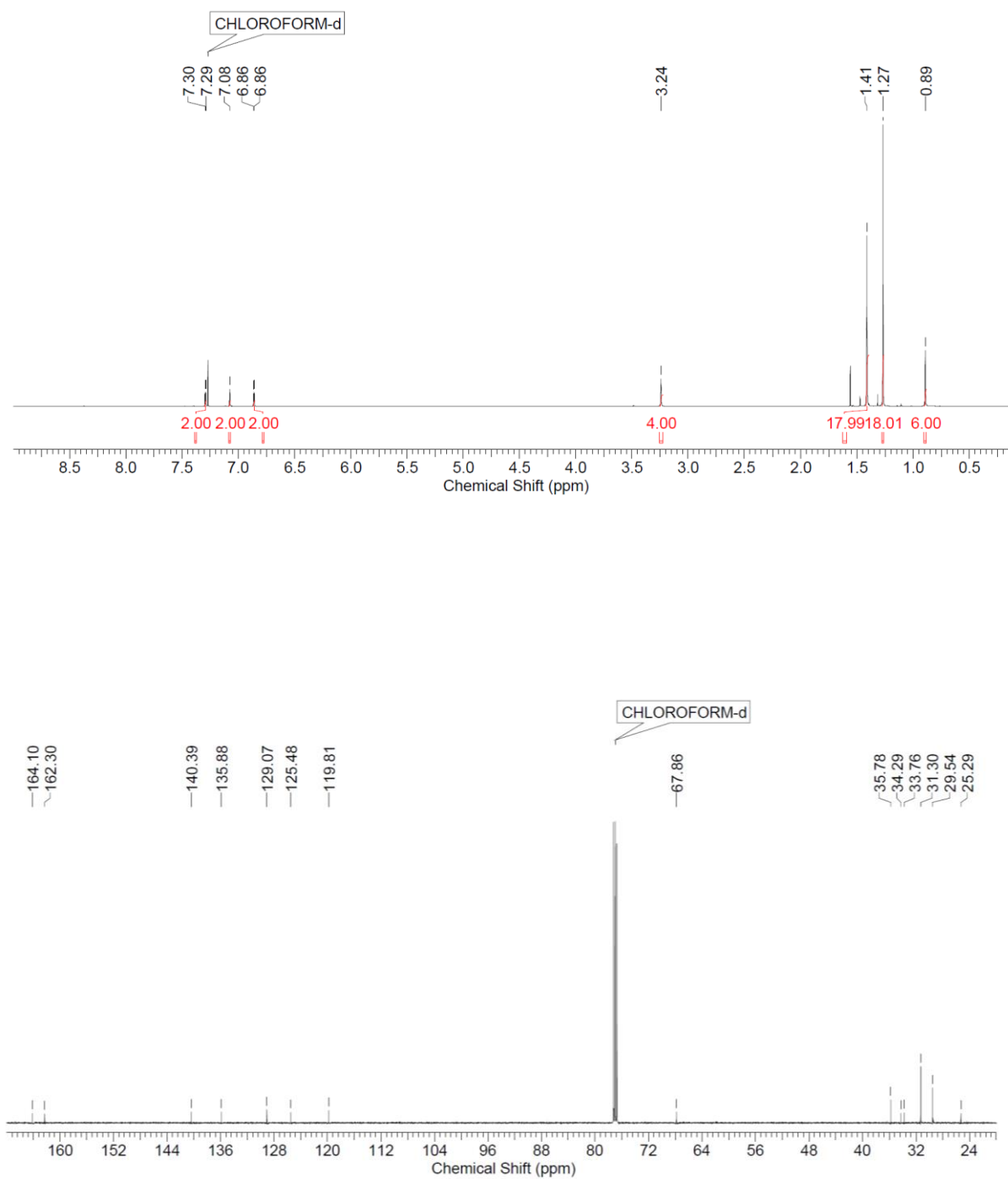
Figure S4 ^{1}H- and ^{13}C-NMR of Ni-salen(prop)(di-*tert*-butyl) complex in CDCl$_3$ (500 MHz).

Ni/C Catalyst
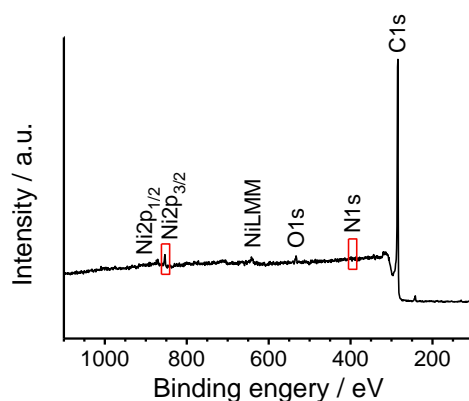
Figure S5. XPS survey spectrum of Ni/C. Regions for which a detailed analysis was performed are marked with a red box.
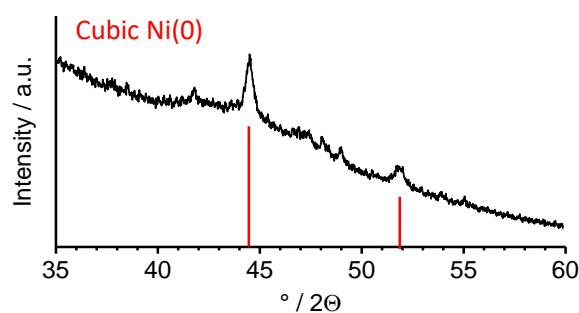
Figure S6. Powder XRD pattern of Ni/C. Reflex positions for cubic Ni(0) are marked in red.
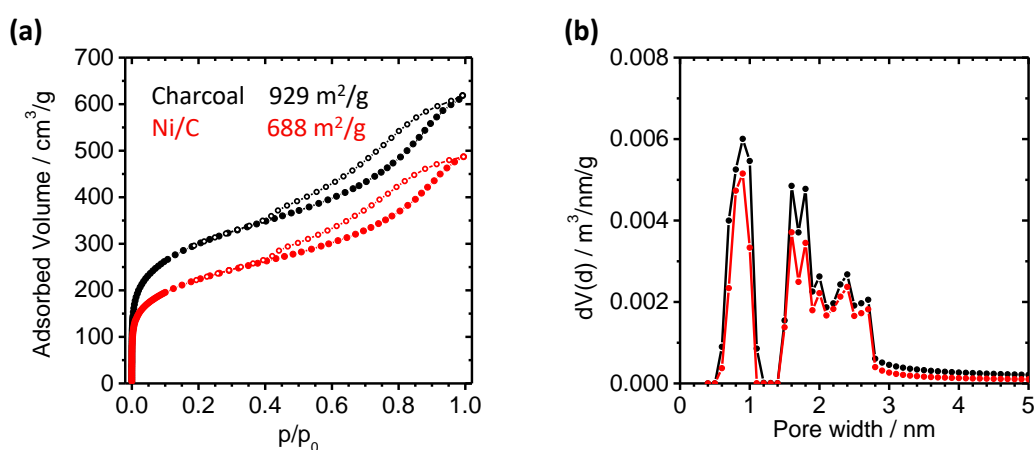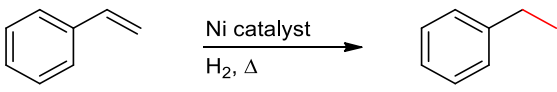
Figure S7. (a) Ar physisorption isotherms of charcoal (929 m²/g) and Ni/C (688 m²/g) with respective surface areas determined by the BET model (0.005 0.1 p/p0). Adsorption is depicted in filled dots, desorption in rings. (b) Pore size distribution of charcoal compared to Ni/C.

5.5.3 Catalytic Reactions
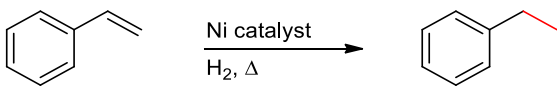
Table S2. Screening of hydrogen pressure and reaction temperature.

Catalyst	Temperature / °C	H$_2$ pressure / MPa	Yield / %
Ni/C	50	2	99
Ni/C	40	0.5	99
Ni/C	40	0.2	99
Ni/C[a]	40	0.2	99
Ni/C	rt	0.1	50
Ni/C[b]	40	0.2	22
Ni/C[c]	40	0.2	0
Ra-Nickel[d]	40	0.2	99
Ni/Al$_2$O$_3$	40	0.2	0
Ni/CeO$_2$	40	0.2	0
Ni/SiO$_2$	40	0.2	64
Ni/TiO$_2$	40	0.2	0

Reaction conditions: 0.5 mmol styrene, 2.5 ml MeOH, 1.35 mol% Ni (14.7 mg Ni/C, 2.7 wt.% Ni), 20 h. Yields determined by GC using *n*-dodecane as an internal standard. [a] Stored in Ar atmosphere for 4 months. [b] 0.68 mol.% Ni (7.4 mg Ni/C, 2.7 wt.% Ni)). [c] Nickel acetate tetra hydrate (4 wt.%) was used as Ni precursor for the catalyst synthesis on the carbon support. [d] 1.35 mol.% Raney-Ni.
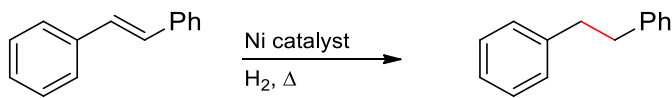
Table S3 Screening of solvent and amount of solvent in the styrene hydrogenation.

Solvent	Amount of solvent / ml	Yield / %
Methanol	2.5	99
Ethanol	2.5	87
H$_2$O[a]	2.5	79
Toluene	2.5	43
Methylcyclohexane	2.5	0
Acetonitrile	2.5	24
Methanol	1.0	31
Methanol	1.5	73
Methanol	2.0	81
Methanol	3.0	56

Reaction conditions: 0.5 mmol styrene, solvent, 1.35 mol% Ni (14.7 mg Ni/C, 2.7 wt.% Ni), 40 °C, 0.2 MPa H$_2$, 20 h. Yields determined by GC using *n*-dodecane as an internal standard. [a] Aqueous phase was extracted with ethyl acetate und dried over Na$_2$SO$_4$ before analysis.
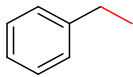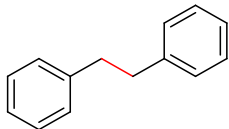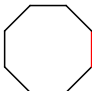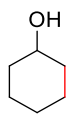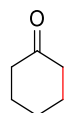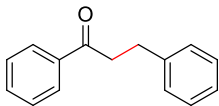
74

Table S4 Screening of temperature and H_2 pressure in the olefin hydrogenation.

Catalyst	Temperature / °C	H_2 pressure / MPa	Yield / %
Ni/C	40	0.2	21
Ni/C	60	0.5	66
Ni/C	60	0.1	73
Ni/C	80	0.5	72
Ni/C	80	0.1	99

Reaction conditions: 0.5 mmol *trans*-stilbene, 2.5 ml MeOH, 1.35 mol% Ni (14.7 mg Ni/C, 2.7 wt.% Ni), 20 h. Yields determined by GC using *n*-dodecane as an internal standard.

Table S5 List of isolated products and ^{1}H-NMR data.

Saturated Product	
	Yield 98 % **^{1}H-NMR** δ = 7.39-7.28 (m, 5H), 2.77-2.72 (q, 2H), 1.36-1.32 (t, 3H) ppm
	Yield 90 % **^{1}H-NMR** δ = 7.46-7.42 (m, 4H), 7.37-7.33 (m, 6H), 3.08 (s, 4H) ppm
	Yield 99 % **^{1}H-NMR** δ = 1.54 (s, 16H) ppm
	Yield 97 % **^{1}H-NMR** δ =3.59-3.55 (sept, 1H), 2.22 (s, 1H), 1.88-1.87 (m, 2H), 1.72-1.70 (m, 2H), 1.53-1.50 (m, 1H), 1-27-1.20 (m, 4H) 1.15 (m, 1H) ppm
	Yield 99 % **^{1}H-NMR** δ = 2.26-2.22 (t, 4H), 1.80-1.74 (m, 4H), 1.66-1.60 (m, 2H) ppm
	Yield 80 % **^{1}H-NMR** δ = 8.03-8.01 (d, 2H), 7.64-7.60 (t, 1H), 7.53-7.49 (t, 2H), 7.39-7.25 (m, 5H), 3.39-3.35 (t, 2H), 3.10-3.21 (t, 2H) ppm

^{1}H-NMR measured in CDCl3 at 400 MHz. For reaction conditions refer to General Procedure.
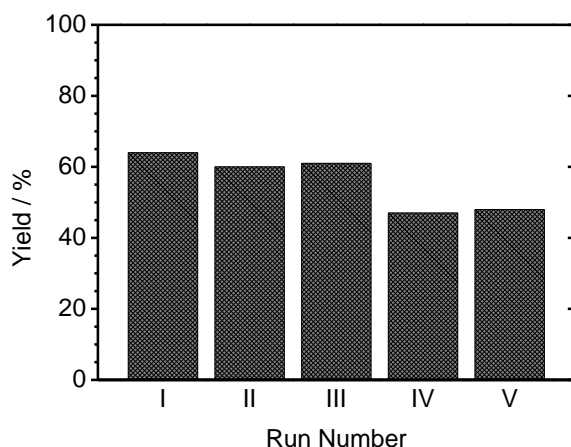
Figure S8. Recyclability study using the hydrogenation of styrene at about 60 % yield. Reaction conditions: 0.5 mmol styrene, 2.5 mL MeOH, 1.35 mol% Ni (14.7 mg Ni/C, 2.7 wt.% Ni), 40 °C, 0.2 MPa H_2, 4 h. Yields were determined by GC using *n*-dodecane as an internal standard.

5.5.4 References

[S1]   O. V. Dolomanov, L. J. Bourhis, R. J. Gildea, J. A. K. Howard, H. Puschmann, *J. Appl. Cryst.* **2009**, *42*, 339-341.

[S2]   C. F. Macrae, I. Sovago, S. J. Cottrell, P. T. A. Galek, P. McCabe, E. Pidcock, M. Platings, G. P. Shields, J. S. Stevens, M. Towler and P. A. Wood, *J. Appl. Cryst*. **2020**, *53*, 226-235.

[S3]   H.-R. Wen, S.-J. Liu, X.-R. Xie, J. Bao, C.-M. Liu, J.-L. Chen, *Inorg. Chim. Acta* **2015***, 435***,** 274–282.

6 Visible Light-driven Dehydrogenation of Benzylamine under Liberation of H₂

Mara Klarner,[a] Sebastian Hammon,[b] Sebastian Feulner,[c] Stephan Kümmel,[b] Lothar Kador,[c] Rhett Kempe*[a]

[a]   Inorganic Chemistry II, University of Bayreuth, Universitätsstr. 30, 95440 Bayreuth (Germany)

[b]   Theoretical Physics IV, University of Bayreuth, Universitätsstr. 30, 95447 Bayreuth (Germany)

[c]   Institute of Physics, Bayreuth Institute of Macromolecule Research (BIMF), University of Bayreuth, Universitätsstr. 30, 95447 Bayreuth (Germany)

Abstract: The visible light-driven transformation of chemical compounds in combination with the liberation of H₂ is highly attractive. Herein, we report on a photocatalyst that allows the acceptorless dehydrogenation of benzylamine. Upon light absorption, free charge carriers are generated and used for the concerted imine formation and liberation of H₂. Our photocatalyst consists of CdS as a light harvesting semiconductor supported on colloidal metal-organic framework crystallites. The decoration with co-catalytic nickel nanoparticles promotes hydrogen evolution and, in addition, stabilizes the CdS component under irradiation.

6.1 Introduction

The solar-driven upgrading of organic compounds is a promising and sustainable way to produce value-added products.[1] The simultaneous liberation of H₂ during such upgrading processes generates an additional, highly attractive byproduct. Meanwhile, a well investigated approach is the photocatalytic acceptorless dehydrogenation of alcohols (alcohol splitting) to yield carbonyl compounds (Scheme 1, top).[2] In a similar way, amines may be transformed into imines and H₂ (Scheme 1, bottom). The photocatalytic amine dehydrogenation described so far requires sacrificial agents, mostly molecular oxygen (aerobic amine oxidation). The visible light-mediated aerobic amine oxidation is catalyzed by semiconductor materials including CdS,[3] graphitic carbon nitride,[4] Nb₂O₅,[5] WS₂,[6] WO₃[7] and bismuth oxyhalides.[8] Zhao and coworkers developed a Ni/CdS catalyst system for the visible light-

driven H_2 generation from water in combination with the coupling of amines.[9] Furthermore, heterojunction photocatalysts,[10] plasmonic composite catalysts[11] and MOF-based photocatalysts[12] are described to yield homocoupled imines via aerobic amine oxidation. The transformation of two different amines into a non-symmetric imine is more challenging, requiring high temperatures and oxygen pressure.[13]

Acceptorless Alcohol Dehydrogenation
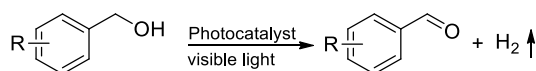
Pt/CdS	Pt/Zn$_3$In$_2$S$_6$
Vela and coworkers 2012[4a]	Chen and coworkers 2018[4d]
Ni/CdS	Ni/CdS/TiO$_2$@MIL-101
Xu and coworkers 2016[4b]	Kempe and coworkers 2019[4e]
Co/CdS	
Du and coworkers 2018[4c]	

This Work: Acceptorless Amine Dehydrogenation
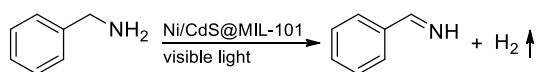
Scheme 1. State of the art in visible light-mediated photocatalytic dehydrogenation of alcohols with liberation of H_2 (alcohol splitting) and the acceptorless dehydrogenation of benzylamine (amine splitting) introduced here.

Herein, we report on the photocatalytic and visible light-driven acceptorless dehydrogenation of benzylamine (amine splitting). The reaction proceeds additive-free, without requiring an electron acceptor, and involves amine oxidation towards an imine in combination with liberation of one equivalent of H_2. The synthesis of non-symmetric imines is possible by using a second, non-benzylic amine that is not dehydrogenated by the photocatalyst. To accomplish amine splitting, we developed a novel metal-organic framework-based photocatalyst system (Ni/CdS@MIL-101). Ni/CdS@MIL-101 is composed of three components. a) The metal organic framework (MOF) known as MIL-101(Cr) is used as the visible light inactive support material that acts as a molecular sponge permitting the semiconductor and catalyst synthesis and determines the overall size of the photocatalyst for efficient recycling.[14] b) CdS is the visible light absorbing semiconductor material. c) Nickel nanoparticles are an efficient co-catalyst for H_2 evolution and enhance the stability of CdS under photocatalytic conditions since the oxidation of sulfide to sulfate is prevented. Fluorescence lifetime measurements indicate a faster electron transfer from the conduction band of CdS to the Ni particles in comparison to nanoparticles of noble metals such as Pd or Pt. Thereby, the probability of charge recombination within the semiconductor is reduced. In addition, DFT calculations suggest a stronger substrate binding of the amine to the Ni than to Pd nanoparticles.

6.2 Results and Discussion

The photocatalytically inactive MOF MIL-101 with its characteristic pore structure (Supporting Information, Figure S2a) was shown to have a surface area of 2700 m^2/g.[15] The MIL-101 crystallite size, between 100 and 300 nm, is desirable for the generation of active and reusable core-shell catalysts. The MIL-101 crystallites are small enough to exhibit a proper outer surface area for the modification with photoactive components.[16] This is combined with the easy separation of the colloidal photocatalyst, since the crystallites are, on the other hand, large enough to ensure recyclability by centrifugation. The highly porous and size optimized support material can be selectively loaded with precursor molecules permitting the catalyst synthesis. The outer surface of single MIL-101 crystallites is decorated with visible light-absorbing CdS particles by a simple solvothermal route. Cadmium acetate is infiltrated into MIL-101 in dimethyl sulfoxide as sulfur source and crystallizes as cubic CdS under solvothermal conditions at 180 °C to yield CdS@MIL-101.[17] Transmission electron microscopy revealed the arrangement of CdS particles with an average size between 20 and 30 nm on the structure determining core MIL-101 (Scheme 2; Supporting Information, Figure S4). The gas phase infiltration of volatile metal-organic precursors into the porous CdS@MIL-101 composite material allows for the generation of metal nanoparticles, denoted as M/CdS@MIL-101. For the modification with nickel nanoparticles, bis(cyclopentadienyl)nickel(II) [Ni(C_5H_5)$_2$] was infiltrated at room temperature by applying static vacuum and subsequently reducing to Ni_0 at 90 °C and 10 bar H_2.[18] We modified CdS@MIL-101 with different amounts of nickel, 1 wt.%, 5 wt.%, and 10 wt.%. (η_3-Allyl)(η_5-cyclopentadienyl)-palladium(II) [Pd(C_3H_5)(C_5H_5)] was used to generate 5 wt.% Pd_0 nanoparticles by sublimation at 32 °C in dynamic vacuum and reduction at 70 °C and 70 bar H_2.[19] The modification with 5 wt.% Pt_0 proceeds via the gas phase loading of trimethyl-(methylcyclopentadienyl)-platinum(IV) [$Me_3Pt(CH_3$-C_5H_4)] into the pores of CdS@MIL-101 at 37 °C in static vacuum, followed by a reduction step at 80 °C and 50 bar H_2.[20] TEM analysis (Scheme 2; Supporting Information, Figure S3) indicated a homogeneous distribution of metallic nanoparticles smaller than 2 nm which are located on the CdS particles, forming an interface with the visible light-absorbing semiconducting material. The metal content of M_5CdS@MIL-101 catalysts (theoretically 5 wt.%) was examined by inductively coupled plasma optical emission spectroscopy (ICP-OES) and found to be 5.1 wt.% Ni, 5.2 wt.% Pd, and 4.9 wt.% Pt, respectively (Supporting Information, Table S1). The calculated weight percentage of CdS is 45 wt.% for each catalyst material. The final M/CdS@MIL-101 core-shell composite showed the original octahedral shape determined by the MIL-101. The metal nanoparticles are assumed to serve as an electron reservoir, since a directed electron transfer from the conduction band of the semiconductor CdS across the semiconductor/nanoparticle interface has been postulated.[21] Scheme 2 presents the general photocatalytic concept of M/CdS@MIL-101: An electron-hole pair is generated upon visible light excitation of CdS. The electron is transferred from the conduction band (CB) of CdS to a metal particle by the built-in electric field, thereby reducing the possibility of charge recombination. Subsequently, spatially separated redox reactions can be catalyzed. Electrons reduce

protons for molecular hydrogen generation at the co-catalytic nanoparticles and, simultaneously, holes in the CdS valence band are consumed by oxidizing substrates.
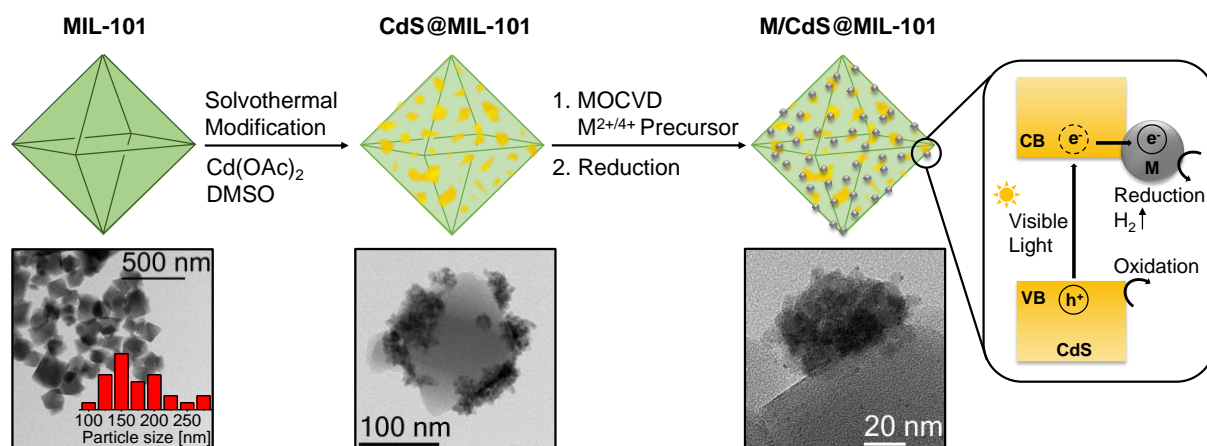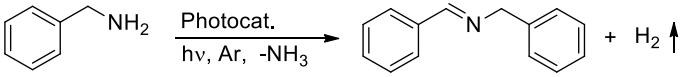
Scheme 2. Synthesis of the photocatalyst M/CdS@MIL-101. The decoration with CdS semiconductor particles proceeds via a solvothermal modification. The metal precursor (Ni: [Ni(C$_5$H$_5$)$_2$]; Pd: [Pd(C$_3$H$_5$)(C$_5$H$_5$)]; Pt: [Me$_3$Pt(CH$_3$-C$_5$H$_4$)]) is infiltrated into MIL-101 (green) by gas phase deposition and reduced by hydrogen treatment. In the semiconductor CdS (yellow) an electron is promoted from the valence band (VB) to the conduction band (CB) by the absorption of visible light. After the directed electron transfer towards the metal particles (grey), spatially separated redox reactions can be catalyzed.

For determining the absorbance characteristics of Ni$_5$CdS@MIL-101, we performed diffuse-reflectance ultraviolet-visible spectroscopy (DRS) between 350 and 700 nm. As compared to bare MIL-101 absorbing around 600 and 450 nm, an increased absorption was observed for the dark yellow CdS@MIL-101 (Supporting Information, Figure S4a). Upon generating the photoactive compound, the characteristic absorbance of MIL-101 is extinguished. Photons of wavelengths smaller than 510 nm are predominantly absorbed, corresponding to the band gap of the semiconductor CdS. With the Munk-Kubelka equation, the optical band gap of CdS was determined as 2.44 eV, in agreement with the literature value for cubic CdS (Supporting Information, Figure S4b). The photocatalyst Ni$_5$CdS@MIL-101 exhibited nearly constant absorbance throughout the visible range. We examined the surface area and the pore size distribution of the different compounds during synthesis of the photocatalyst by nitrogen physisorption measurements. The modification of porous MIL-101 with CdS results in a significant decrease of the initial surface area by 53 %. Further modification with Ni nanoparticles leads only to a minor additional decrease of the surface area to 1040 m^2/g. X-ray powder diffractometry (PXRD) reveals the exclusive formation of cubic CdS particles (Supporting Information, Figure S8a) showing reflections at 26.5°, 43.9°, and 51.9° (2θ). The reflections from 2° to 20° (2θ) are assigned to the preserved MIL-101 core. X-ray photoelectron spectroscopy (XPS) indicated the formation of metallic Ni nanoparticles (Supporting Information, Figure S5). The major peak within the S2p region at a binding energy of 161.5 eV is assigned to metallic sulfide (CdS). Traces of metal sulfate were identified at a binding energy of 169 eV; they are ascribed to surface oxidation of CdS due to the handling in air. The XPS survey shows characteristic elemental signals for Cr, O, and C of the

MIL-101 support material and additional signals for Cd, S, and Ni, which form the photoactive shell. The homogeneous distribution of Ni particles on the CdS@MIL-101 material was confirmed by energy dispersive X-ray (EDX) elemental mapping (Supporting Information, Figure S6). Furthermore, we performed Fourier-transform infrared spectroscopy (FT-IR) of Ni$_5$CdS@MIL-101 and the intermediate materials during synthesis (Supporting Information, Figure S7a). Due to the surface modification with the light harvesting CdS, MIL-101 signals are reduced between 700 and 2000 cm^{-1}. A total weight loss of 42 % was observed for the Ni$_5$CdS@MIL-101 photocatalyst as compared to 72 % for MIL-101 in thermogravimetric analysis (TGA) (Supporting Information, Figure S7b). By covering the MOF core with the photocatalytic active shell, the temperature stability of the system is enhanced.

Next, we performed the photocatalytic acceptorless dehydrogenation of benzylamine via liberation of molecular H$_2$. Thereby, the intermediate aldimine reacts with a second equivalent of benzylamine in a condensation reaction to yield the homocoupled product *N*-benzyl-1-phenylmethanimine (Figure 1a). The elimination of gaseous ammonia was verified by gas chromatography (thermal conductive detector, GC-TCD). The flat band potential of CdS is sufficiently positive (VB 1.7 V vs NHE)[22] to thermodynamically allow for the oxidation of benzylamine (standard reduction potential 0.9 V vs NHE).[23] The photocatalytic amine dehydrogenation by Ni$_5$CdS@MIL-101 was performed under an inert-gas atmosphere at room temperature without the use of any additives or acceptor molecules. In the presence of co-catalytic Ni nanoparticles, the dehydrogenation of benzylamine proceeds with quantitative yield, whereas the neat CdS@MIL-101 leads to the formation of the tertiary amine as a byproduct (Table 1, Entry 1, 2). We confirmed the equimolar liberation of molecular H$_2$ by analyzing the reaction headspace via GC-TCD (Figure 1b). Switching the light on and off verified the release of H$_2$ only under visible light illumination (Supporting Information, Figure S10). The reusability of Ni$_5$CdS@MIL-101 photocatalyst was investigated by the acceptorless dehydrogenation of benzylamine. We performed five consecutive runs without a remarkable loss of activity (Supporting Information, Figure S11).

Table 1. Photocatalytic acceptorless dehydrogenation of benzylamine.[a]

	Catalyst	Yield [%] [b]	Yield H$_2$ [%] [c]
1	Ni$_5$CdS@MIL-101	99	98
2	CdS@MIL-101	62	59
3	Without hν	0	0
4	Without catalyst	0	0

[a] 1 mmol benzylamine, 1.5 mL MeCN, 10 h, 5 mg catalyst, rt, Ar, 470 nm blue LED (50 W). [b] Determined by GC using *n*-dodecane as an internal standard. [c] Quantified by GC-TDC using methane as an internal standard.

We also developed an approach to access non-symmetric imines using a second, non-benzylic amine which is not dehydrogenated by the photocatalyst under the given conditions. Figure 1c describes the cross-coupling of benzylamine and cyclohexylamine via the dehydrogenation of benzylamine and subsequent reversible transimination to yield the hetero- coupled *N*-cyclohexyl-1-phenylmethanimine (Figure 1c, d). This exchange is a non-photocatalytic equilibrium reaction, in which one equivalent of benzylamine is liberated and fed back into the dehydrogenation cycle. Under visible light illumination, the equilibrium is shifted towards the non-symmetric imine, guaranteeing its predominant formation (Supporting Information, Table S5).
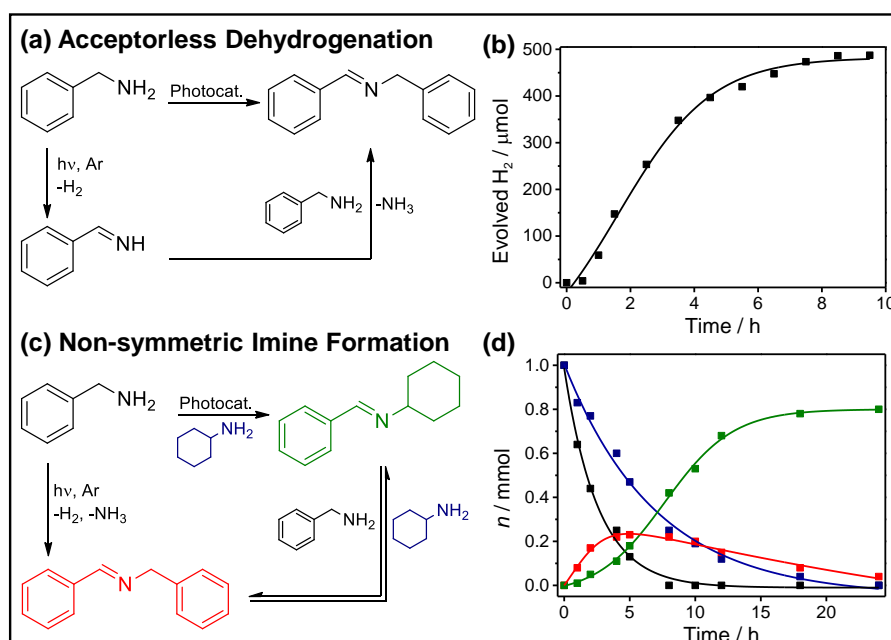
Figure 1. (a) Acceptorless dehydrogenation of benzylamine. (b) H$_2$ liberation from benzylamine (1 mmol) is observed under visible light illumination and quantified by GC-TCD. (c) Non-symmetric imine formation by cross-coupling benzylamine and cyclohexylamine. (d) Kinetic study (color code refers to (c))

We synthesized the Ni$_x$CdS@MIL-101 catalyst systems with different Ni contents (x equal to 1, 5, 10 wt.% Ni) to investigate the influence of the co-catalytic nanoparticles on the dehydrogenative cross-coupling. To convert 1 mmol of substrates under optimized reaction conditions, 5 mg Ni$_5$CdS@MIL-101 were suspended in 1.5 ml ethanol and illuminated with a 50 W blue LED (470 nm) (Supporting Information, Figure S1, Table S3 and S4). CdS@MIL-101 loaded with 5 wt.% Ni showed the best catalytic performance yielding 74 % heterocoupled product **1** and 7 % homocoupled product **2** (Table 2, Entry 2). With increasing Ni content, the nanoparticles covering the CdS crystals reduce the light absorbance and, thereby, the generation of free charge carriers resulting in 17 % of **1** and 37 % of **2** (Table 2, Entry 3). With 1 wt.% Ni, the photocatalytic activity is similar to neat CdS@MIL-101 (Table 2, Entry 1). The MIL-101 support is essential, since Ni-modified commercial CdS shows a significantly lower activity (Table 2, Entry 4). Also, the unmodified CdS@MIL-101 shows a lower catalytic activity (Table 2, Entry 5) underlining the importance of Ni nanoparticles which was already

observed for the formation of the homocoupled product *N*-benzyl-1-phenylmethanimine **2**. We found no photocatalytic activity without the light-harvesting CdS component in both Ni@MIL-101 and the neat support MIL-101 (Table 2, Entries 6, 7). The modification with the noble metals Pd and Pt as co-catalysts leads mainly to the formation of the homocoupled product **2** (Table 2, Entries 8, 9). This fact highlights the superior performance of co-catalytic non-noble Ni nanoparticles. The composite material Ni$_5$CdS@MIL-101 catalyzes the cross-coupling of amines as shown by several control experiments: Without the catalyst and without visible light illumination no conversion of the substrates occurs (Table 2, Entries 10, 11). Interestingly, a significantly reduced yield is observed in air (Table 2, Entry 12).

Table 2. Photocatalytic dehydrogenation of benzylamine and cross-coupling with cyclohexylamine. Comparison of different Ni contents, different metal nanoparticles and different reaction conditions.[a]

	Catalyst	Metal [wt %] [b]	Yield 1 [%] [c]	Yield 2 [%] [c, d]
1	Ni$_1$CdS@MIL-101	1	45	12
2	**Ni$_5$CdS@MIL-101**	**5.1[e]**	**74**	**7**
3	Ni$_{10}$CdS@MIL-101	10	17	37
4	Ni@CdS[f]	5	18	4
5	CdS@MIL-101	-	42	17
6	Ni@MIL-101	5	0	0
7	MIL-101	-	0	0
8	Pd$_5$CdS@MIL-101	5.2[e]	8	34
9	Pt$_5$CdS@MIL-101	4.9[e]	7	51
10	Without hν	5.1[e]	0	0
11	Without catalyst	-	0	0
12	Ambient air	5.1[e]	11	23

[a] 1 mmol benzylamine, 1 mmol cyclohexylamine, 1.5 mL EtOH, 5 mg catalyst, 470 nm blue LED (50 W), 20 h, rt, Ar. [b] Co-catalytic metal nanoparticles (Ni, Pd, Pt). [c] Determined by GC using *n*-dodecane as an internal standard. [d] Referred to 0.5 mmol. [e] Determined by ICP-OES analysis. [f] Commercial CdS (Alfa Aesar).

Next, we studied the stability of the semiconducting CdS component of Ni$_5$CdS@MIL-101 under photocatalytic conditions. The corrosion of CdS is a frequently discussed phenomenon and a main challenge in the use of such photocatalysts.[24] Recently, DiMeglio and co-workers reported on the benzylamine mediated oxidation of sulfide during the non-aqueous dehydrogenation of benzylamine with O$_2$ as a sacrificial agent.[25] The standard reduction potential of benzylamine thermodynamically allows for the oxidation of CdS via the formation of the amine-radical cation. In a typical photocatalytic

set-up, the photocatalysts $Ni_5CdS@MIL-101$ and $CdS@MIL-101$ were illuminated in the presence of benzylamine and ethanol as solvent in an inert gas atmosphere. The pre-catalytic $CdS@MIL-101$ exhibits one major sulfur signal at $^2P_{3/2}$ 161.5 eV (86 %) corresponding to metal sulfide and a small signal for metal sulfate at $^2P_{3/2}$ 168.7 eV (14 %) (Figure 2, (1) and (2)). Post-catalytic PXRD analysis indicates the formation of oxidized sulfur species due to the presence of several reflections besides those of cubic CdS (Supporting Information, Figure S8). XPS analysis in the S^2p region confirms an increase in surface sulfate to 51 %. The modification with Ni nanoparticles improves the stability of the CdS component since no corrosion effects are observed in PXRD. The ratio of CdS (94 %) to $CdSO_4$ (6 %) is constant for pre- and post-catalytic $Ni_5CdS@MIL-101$ (Figure 2, (3) and (4)). We performed several control experiments without either visible light illumination, or the presence of benzylamine or solvent and, in addition, in dry acetonitrile. PXRD analysis of post-catalytic $Ni_5CdS@MIL-101$ materials showed no evidence for CdS corrosion in all these cases, which supports the idea of benzylamine-mediated sulfide oxidation in an oxygen-containing solvent (Supporting Information, Figure S8). The observed stability of CdS is decisive for the catalytic recyclability of $Ni_5CdS@MIL-101$. Further experiments on $Pd_5CdS@MIL-101$ and $Pt_5CdS@MIL-101$ photocatalysts revealed that the supposed stabilizing effect of metal nanoparticles on the CdS semiconductor occurs also with these noble metals.
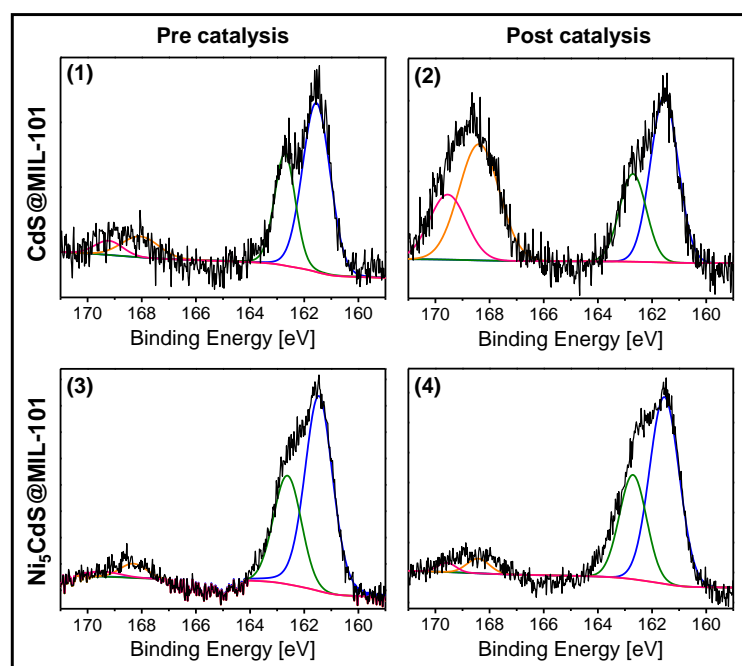
Figure 2. XPS studies of $Ni_5CdS@MIL-101$ and $CdS@MIL-101$ demonstrating the enhanced photocatalytic stability of CdS in the presence of Ni nanoparticles. $Ni_5CdS@MIL-101$ does not show significant degradation of the surface of CdS [(3), (4)], whereas CdS in $CdS@MIL-101$ is oxidized under photocatalytic conditions [(1), (2)]. For details see text

The directed electron transfer from photo-excited CdS across the semiconductor-metal interface to Ni nanoparticles was investigated with fluorescence lifetime imaging microscopy in the frequency domain (FD-FLIM). A custom-built apparatus was used with a semiconductor laser at 487 nm and modulation frequencies between 110 and 155 MHz (adapted from Ref. [26]). The combination of the semiconductor

material CdS with metallic particles opens up an additional decay channel of charge carriers in the conduction band of CdS. By absorbing visible light, an electron-hole pair is generated in the CdS component which can recombine after an intrinsic lifetime by emitting a photon. FD-FLIM data are conveniently plotted in the so-called polar-plot representation, where the quadrature component of the normalized fluorescence signal is plotted versus the component which is in phase with the excitation. Single-exponential decays correspond to data on a characteristic semi-circle with radius 0.5 around the point (0.5; 0) in this plot. Data points within the semi-circle, on the other hand, represent fluorescence decays featuring more than one lifetime component and can be linearly decomposed in the complex plane.[27] The photoluminescence lifetime of neat CdS supported on MIL-101 is determined by drawing a straight line through the data points in the polar plot and extrapolating it to the intersections with the semicircle (Figure 3a). Two lifetime components are extracted which are independent of the modulation frequency (Supporting Information, Figure S9). The shorter lifetime is interpreted as the luminescence lifetime of CdS, whereas the longer one is ascribed to the luminescence of the MIL-101. The position of the data points on the straight line represents the relative contributions of the two lifetime components to the luminescence signal.
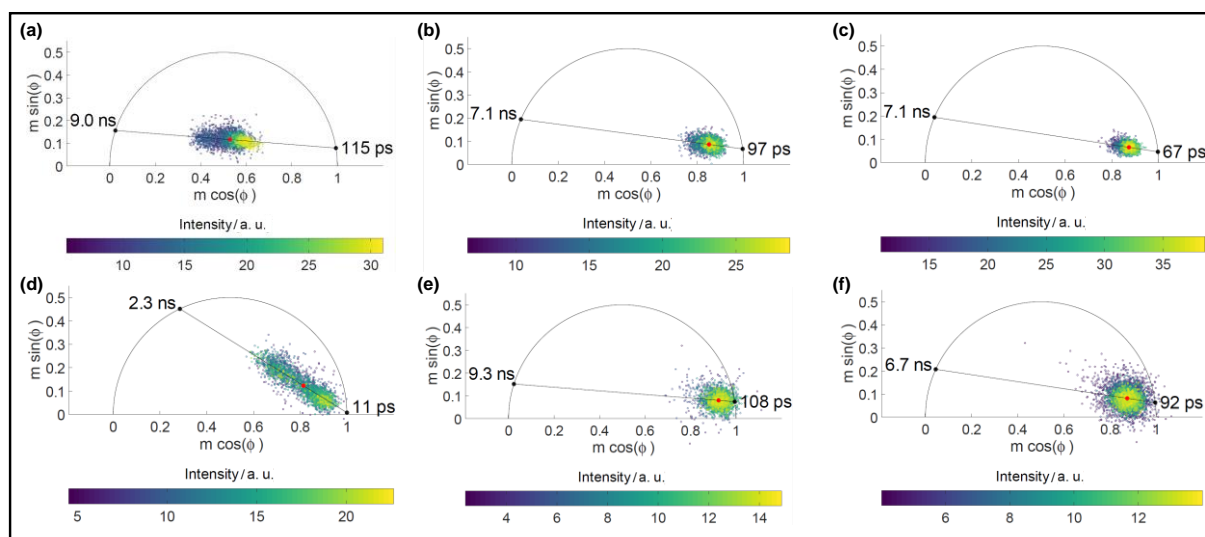
Figure 3. Fluorescence lifetime studies of MIL-101 supported catalysts confirming the directed electron transfer from excited CdS to Ni nanoparticles. Polar- plot representations of the data for Ni$_x$CdS@MIL-101 and M$_5$CdS@MIL-101: (a) neat CdS, (b) 1 wt.% Ni, (c) 5 wt.% Ni, (d) 10 wt.% Ni, (e) 5 wt.% Pd and (f) 5 wt.% Pt. The fluorescence lifetime of CdS decreases with increasing Ni content (right end point of the straight line on the semi-circle). It also depends on the metal nanoparticle (Ni, Pd, Pt; 5 wt.%) indicating an influence of the latter on the electron transfer efficiency. Data points correspond to diffraction-limited spots on the sample within an area of size 10×10 μm, the red dot indicating their center of mass. The fluorescence intensity of each spot is color-coded. The modulation frequency of the laser was 110 MHz. For further details see text.

With increasing Ni content, the CdS lifetime gradually shortens from 115 ps (CdS@MIL-101) to 97 ps (Ni$_1$CdS@MIL-101), 67 ps (Ni$_5$CdS@MIL-101) and 11 ps (Ni$_{10}$CdS@MIL-101), respectively, verifying the directed electron transfer (Figure 3a-d). The relative variation of these lifetimes is reliable; the absolute numbers are subject to an uncertainty of about a factor two to three, however, given the

comparatively low modulation frequencies. In accordance with the observed photocatalytic activity, the efficiency of the charge transfer increases with the Ni content. The charge carrier separation over two different catalyst components leads to the enhanced photocatalytic activity of Ni/CdS@MIL-101 in redox reactions. Comparing the 3d metal Ni with the noble metals Pd and Pt, the lifetime of neat CdS is most strongly affected by neighboring Ni particles, indicating faster electron transfer to Ni particles than to either Pd or Pt (Figure 3c, e, f). Comparing catalyst systems with 5 wt.% of the three metals, the lifetime of neat CdS is reduced from 115 ps to 108 ps (Pd$_5$CdS@MIL-101), 92 ps (Pt$_5$CdS@MIL-101) and 67 ps (Ni$_5$CdS@MIL-101). This result underlines the superior performance of Ni particles in the discussed photocatalytic reactions.

In addition to a faster electron transfer from CdS to Ni in comparison to Pd or Pt particles, another reason for the superior photocatalytic performance of Ni/CdS@MIL-101 may be the interaction or binding of benzylamine with the metal nanoparticles. As a straightforward test we computed the binding energy of benzylamine to the metal nanoparticles. While this type of calculation can be performed using density functional theory (DFT) in principle, it requires careful considerations in practice: The structure of metal particles in general is difficult to determine due to the existence of many isomers of similar energy,[28] yet it may influence binding energies. Furthermore, common exchange-correlation approximations may reach their accuracy limits for d-electron systems.[29] For these reasons, we focused on 13-atom clusters of Ni and Pd as two representative test cases. Both form similar and stable cluster geometries, such as the icosahedron.[28,30] Our calculations suggest that the icosahedral structure is arguably the most relevant one for Ni$_{13}$ and Pd$_{13}$ at room temperature in solution (Supporting Information, Theoretical Procedure). Therefore, we investigated the binding energy of one benzylamine molecule to one 13-atom metal cluster (Ni$_{13}$ or Pd$_{13}$) by computing the electronic and geometric structure using TURBOMOLE[31] (Supporting Information, Theoretical Procedure). We checked for possible limitations of the predictive power of the DFT calculations due to the presence of d-electrons by computing the binding energies with different exchange-correlation functionals.[32] In particular, the importance of localization and self-interaction was investigated by using functionals with different amounts of exact exchange.
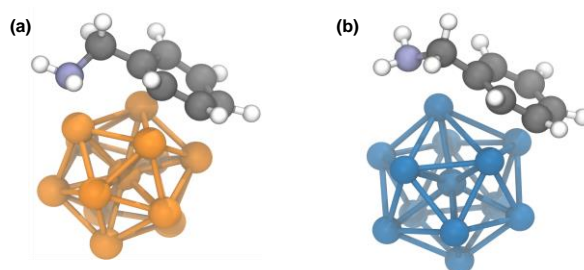
Figure 4. Lowest energy geometries obtained from Born-Oppenheimer DFT molecular dynamics simulations in which a benzylamine molecule binds to a 13-atom Pd icosahedral particle (a) and a 13-atom Ni icosahedral particle (b).

We found the general trend that benzylamine binds stronger to Ni$_{13}$ than to Pd$_{13}$ by several hundred meV (Supporting Information, Table S8). The lowest energy geometries are depicted in Figure 4. This result correlates with a previous study on the binding energy of benzyl alcohol to Ni$_{13}$ and Pd$_{13}$.[17a] Furthermore, we calculated the binding energy for the dehydrogenated intermediate (C$_7$H$_7$N). This intermediate also shows a higher binding energy to Ni$_{13}$ than to Pd$_{13}$, yet overall slightly lower than benzylamine (Supporting Information, Theoretical Procedure).

6.3 Conclusion

In conclusion, we have reported the first example of photocatalytic, visible light-driven acceptorless amine dehydrogenation (amine splitting). The noble metal-free photocatalyst Ni/CdS@MIL-101 oxidizes benzylamine with the liberation of one equivalent of H$_2$ most efficiently. The synthesis of non-symmetric imines is possible by adding a second amine which is not dehydrogenated by the photocatalyst under the given conditions. The MOF-supported colloidal photocatalyst is composed of the visible light-absorbing semiconductor CdS and Ni nanoparticles. We confirmed the directed electron transfer from the conduction band of CdS to metallic nanoparticles (Ni, Pd and Pt) and observed a faster electron transfer to the abundant non-noble metal Ni. The co-catalytic Ni (as well as Pd and Pt) also enhances the stability of CdS against photo-corrosion in the presence of benzylamine. In addition, DFT calculations reveal a stronger binding of benzylamine to Ni than to Pd clusters.

Acknowledgements

6.4 References

[1]   G. Han, Y.-H. Jin, R. A. Burgess, N. E. Dickenson, X.-M. Cao, Y. Sun, *J. Am. Chem. Soc.* **2017**, *139*, 15584–15587.

[2]   a) T. P. A. Ruberu, N. C. Nelson, I. I. Slowing, J. Vela, *J. Phys. Chem. Lett.* **2012**, *3*, 2798–2802; b) Z. Chai, T.-T. Zeng, Q. Li, L.-Q. Lu, W.-J. Xiao, D. Xu, *J. Am. Chem. Soc.* **2016**, *138*, 10128–10131; c) D. Jiang, X. Chen, Z. Zhang, L. Zhang, Y. Wang, Z. Sun, R. M. Irfan, P. Du, *J. Catal.* **2018**, *357*, 147–153; d) S. Meng, X. Ye, J. Zhang, X. Fu, S. Chen, *J. Catal.* **2018**, *367*, 159–170; e) D. Tilgner, M. Klarner, S. Hammon, M. Friedrich, A. Verch, N. de Jonge, S.

Kümmel, R. Kempe, *Aust. J. Chem.* **2019**, *72*, 842–847; f) T. Mitkina, C. Stanglmair, W. Setzer, M. Gruber, H. Kisch, B. Koenig, *Org. Biomol. Chem.* **2012**, *10*, 3556–3561; g) K. Imamura, H. Tsukahara, K. Hamamichi, N. Seto, K. Hasimoto, H. Kominami, *Appl. Catal. A* **2013**, *450*, 28–33.

[3]   a) W. Zhao, C. Liu, L. Cao, X. Yin, H. Xu, B. Zhang, *RSC Adv.* **2013**, *3*, 22944–22948; b) R. Wu, S. Wang, Y. Zhou, J. Long, F. Dong, W. Zhang, *ACS Appl. Nano Mater.* **2019**, *2*, 6818–6827.

[4]   a) F. Su, S. C. Mathew, L. Möhlmann, M. Antonietti, X. Wang, S. Blechert, *Angew. Chem. Int. Ed.* **2011**, *50*, 657–660; *Angew. Chem.* **2011**, *123*, 683– 686; b) A. Kumar, P. Kumar, C. Joshi, S. Ponnada, A. K. Pathak, A. Ali, B. Sreedhar, S. L. Jain, *Green Chem.* **2016**, *18*, 2514–2521.

[5]   S. Furukawa, Y. Ohno, T. Shishido, K. Teramura, T. Tanaka, *ACS Catal.* **2011**, *1*, 1150–1153.

[6]   a) F. Raza, J. H. Park, H.-R. Lee, H.-I. Kim, S.-J. Jeon, J.-H. Kim, *ACS Catal.* **2016**, *6*, 2754–2759; b) H. Liang, B.-Q. Zhang, J.-M. Song, *ChemCatChem* **2019**, *11*, 6288–6294.

[7]   N. Zhang, X. Li, H. Ye, S. Chen, H. Ju, D. Liu, Y. Lin, W. Ye, C. Wang, Q. Xu, J. Zhu, L. Song, J. Jiang, Y. Xiong, *J. Am. Chem. Soc.* **2016**, *138*, 8928– 8935.

[8]   A. Han, H. Zhang, G.-K. Chuah, S. Jaenicke, *Appl. Catal. B* **2017**, *219*, 269– 275.

[9]   W. Yu, D. Zhang, X. Guo, C. Song, Z. Zhao, *Catal. Sci. Technol.* **2018**, *8*, 5148–5154.

[10]   a) S. Samanta, S. Khilari, D. Pradhan, R. Srivastava, *ACS Sustainable Chem. Eng.* **2017**, *5*, 2562–2577; b) K. Zhang, H. Su, H. Wang, J. Zhang, S. Zhao, W. Lei, X. Wei, X. Li, J. Chen, *Adv. Sci.* **2018**, *5*, 1800062.

[11]   a) S. Naya, K. Kimura, H. Tada, *ACS Catal.* **2013**, *3*, 10–13; b) S. Sarina, H. Zhu, E. Jaatinen, Q. Xiao, H. Liu, J. Jia, C. Chen, J. Zhao, *J. Am. Chem. Soc.* **2013**, *135*, 5793–5801; c) H. Chen, C. Liu, M. Wang, C. Zhang, N. Luo, Y. Wang, H. Abroshan, G. Li, F. Wang, *ACS Catal.* **2017**, *7*, 3632–3638.

[12]   a) D. Sun, L. Ye, Z. Li, *Appl. Catal. B* **2015**, *164*, 428–432; b) H. Liu, C. Xu, D. Li, H.-L. Jiang, *Angew. Chem. Int. Ed.* **2018**, *57*, 5379–5383; *Angew. Chem.* **2018**, *130*, 5477–5481.

[13]   a) A. Grirrane, A. Corma, H. Garcia, *J. Catal.* **2009**, *264*, 138–144; b) L. Liu, S. Zhang, X. Fu, C.-H. Yan, *Chem. Commun.* **2011**, *47*, 10148–10150; c) X. Qiu, C. Len, R. Luque, Y. Li, *ChemSusChem* **2014**, *7*, 1684–1688; d) M. Largeron, M.-B. Fleury, *Chem. Eur. J.* **2015**, *21*, 3815–3820.

[14]   a) D. Tilgner, M. Friedrich, J. Hermannsdörfer, R. Kempe, *ChemCatChem* **2015**, *7*, 3916–3922; b) D. Tilgner, R. Kempe, *Chem. Eur. J.* **2017**, *23*, 3184–3190; c) D. Tilgner, M. Friedrich, A. Verch, N. de Jonge, R. Kempe, *ChemPhotoChem* **2018**, *2*, 349–352; d) D. Tilgner, M. Klarner, S. Hammon, M. Friedrich, A. Verch, N. de Jonge, S. Kümmel, R. Kempe, *Aust. J. Chem.* **2019**, *72*, 842–847.

[15]   G. Ferey, C. Mellot-Draznieks, C. Serre, F. Millange, J. Dutour, S. Surble, I. Margiolaki, *Science* **2005**, *309*, 2040–2042.

[16]   J. Hermannsdörfer, M. Friedrich, R. Kempe, *Chem. Eur. J.* **2013**, *19*, 13652–13657.

[17]   a) D. Tilgner, M. Klarner, S. Hammon, M. Friedrich, A. Verch, N. de Jonge, S. Kümmel, R. Kempe, *Aust. J. Chem.* **2019**, *72*, 842–847; b) Y. Wang, Y. Zhang, Z. Jiang, G. Jiang, Z. Zhao, Q. Wu, Y. Liu, Q. Xu, A. Duan, C. Xu, *Appl. Catal. B* **2016**, *185*, 307–314; c) J. He, Z. Yan, J. Wang, J. Xie, L. Jiang, Y. Shi, F. Yuan, F. Yu, Y. Sun, *Chem. Commun.* **2013**, *49*, 6761– 6763; d) D. Ding, Z. Jiang, J. Jin, J. Li, D. Ji, Y. Zhang, L. Zan, *J. Catal.* **2019**, *375*, 21–31.

[18]   J. Hermannsdörfer, M. Friedrich, N. Miyajima, R. Albuquerque, S. Kümmel, R. Kempe, *Angew. Chem. Int. Ed.* **2012**, *51*, 11473–11477; *Angew. Chem.* **2012**, *124*, 11640–11644.

[19]   J. Hermannsdörfer, R. Kempe, *Chem. Eur. J.* **2011**, *17*, 8071–8077.

[20]   S. Proch, J. Hermannsdörfer, R. Kempe, C. Kern, A. Jess, L. Seyfarth, J. Senker, *Chem. Eur. J.* **2008**, *14*, 8204–8212.

[21]   a) T. Simon, N. Bouchonville, M. J. Berr, A. Vaneski, A. Adrovic, D. Volbers, R. Wyrwich, M. Döblinger, A. S. Susha, A. L. Rogach, F. Jäckel, J. K. Stolarczyk, J. Feldmann, *Nat. Mater.* **2014**, *13*, 1013–1018; b) Y. Xu, R. Xu, *Appl. Surf. Sci.* **2015**, *351*, 779–793; c) S. Cao, C.-J-Wang, X.-J. Lv, Y. Chen, W.-F. Fu, *Appl. Catal. B* **2015**, *162*, 381–391; d) Z. Chai, T.-T. Zeng, Q. Li, L.-Q. Lu, W.-J. Xiao, D. Xu, *J. Am. Chem. Soc.* **2016**, *138*, 10128–10131; e) G. Han, Y.-H. Jin, R. A. Burgess, N. E. Dickenson, X.-M. Cao, Y. Sun, *J. Am. Chem. Soc.* **2017**, *139*, 15584–15587.

[22]   A. J. Bard, M. S. Wrigthon, *J. Electrochem. Sci. Technol.* **1977**, *124*, 1706– 1710.

[23]   K. Ohkubo, T. Nanjo, S. Fukuzumi, *Bull. Chem. Soc. Jpn.* **2006**, *79*, 1489– 1500.

[24]   a) A. Henglein, *Ber. Bunsenges. Phys. Chem.* **1982**, *86*, 301–305; b) D. Meissner, C. Brenndorf, R. Memming, *Appl. Surf. Sci.* **1987**, *27*, 423–436; c) Y. H. Hsieh, C. P. Huang, *Colloids Surf.* **1991**, *53*, 275–295.

[25]   J. L. DiMeglio, B. M. Bartlett, *Chem. Mater.* **2017**, *29*, 7579–7586.

[26]   S. Zahner, L. Kador, K. R. Allakhverdiev, E. Yu. Salaev, M. F. Huseyinoğlu, *J. Appl. Phys.* **2014**, *115*, 043504.

[27]   a) G. I. Redford, R. M. Clegg, *J. Fluoresc.* **2005**, *15*, 805–815; b) M. A. Digman, V. R. Caiolfa, M. Zamai, E. Gratton, *Biophys. J.* **2008**, *94*, L14-L16.

[28]   L. Leppert, R. Kempe, S. Kümmel, *Phys. Chem. Chem. Phys.* **2015**, *17*, 26140–26148.

[29]   T. Schmidt, S. Kümmel, *Computation* **2016**, *4*, 33-1–33-15.

[30]   a) G. L. Gutsev, C. W. Weatherford, K. G. Belay, B. R. Ramachandran, P. Jena, *J. Chem. Phys.* **2013**, *138*, 164303; b) J. P. Chou, C. R. Hsing, C. M. Wei, C. Cheng, C. M. Chang, *J. Phys. Condens. Matter* **2013**, *25*, 125305; c) A. M. Köster, P. Calaminici, E. Orgaz, D. R. Roy, J. U. Reveles, S. N. Khanna, *J. Am. Chem. Soc.* **2011**, *133*, 12192–12196; d) B. Fresch, H.-G. Boyen, F. Remacle, *Nanoscale* **2012**, *4*, 4138–4147.

[31]   TURBMOLE V7.3 **2018**, (University of Karlsruhe and Forschungszentrum Karlsruhe GmbH, Karlsruhe, Germany).

[32]   a) J. P. Perdew, K. Burke, M. Ernzerhof, *Phys. Rev. Lett.* **1996**, *77*, 3865– 3868; b) J. P. Perdew, K. Burke, M. Ernzerhof, *Phys. Rev. Lett.* **1997**, *78*, 1396; c) J. P. Perdew, M. Ernzerhof, *J. Chem. Phys.* **1996**, *105*, 9982; d) C. Adamo, V. Barone *J. Chem. Phys.* **1999**, *110*, 6158; e) A. D. Becke, *J. Chem. Phys.* **1993**, *98*, 5648–5652; f) P. J. Stephens, F. J. Devlin, C. F. Chabalowski, M. J. Frisch, *J. Phys. Chem.* **1994**, *98*, 11623–11627; g) J. Tao, J. P. Perdew, V. N. Staroverov, G. E. Scuseria, *Phys. Rev. Lett.* **2003**, *91*, 146401; h) V. N. Staroverov, G. E. Scuseria, J. Tao, J. P. Perdew, *J. Chem. Phys.* **2003**, *119*, 12129–12137; i) V. N. Staroverov, G. E. Scuseria, J. Tao, J. P. Perdew, *J. Chem. Phys.* **2004**, *121*, 11507–11507; j) J. Sun, A. Ruzsinszky, J. P. Perdew, *Phys. Rev. Lett.* **2015**, *115*, 036402.

6.5 Supporting Information

6.5.1 Experimental Procedures

General Methods

All chemicals and solvents were purchased commercially from chemical suppliers with purity over 95 % and used without further purification. Ethanol was degassed by three consecutive *freeze-pump-thaw-*cycles. Benzylamine (Merck) was vacuum distilled and stored under argon. All manipulations including air or moisture sensitive compounds were carried out under dry and oxygen-free argon atmosphere (Schlenk techniques) or in a nitrogen-filled glovebox (mBraun 120) with a high-capacity recirculator (below 0.1 ppm of oxygen and water).

Reduction of precursor compounds were carried out with Parr Instrument stainless steel autoclaves N-MT5 300 mL equipped with heating mantles and temperature controller. Solvothermal syntheses were performed in a muffle furnace (Nabertherm) with programmable temperature ramps. Inductively coupled plasma optical emission spectroscopy (ICP-OES) was carried out according to standard protocol digestion (4 mL HNO$_3$/HCl 3:1, microwave irradiation, 25 min, 195 °C) with a Vista-Pro radial (Varian). Fourier transform infrared (FT-IR) spectroscopy measurements were performed with a Cary 630 FTIR spectrometer (Agilent Technologies) over a range from 2000 cm^{-1} to 700 cm^{-1}. Thermogravimetric analysis was performed from 30 °C to 700 °C (10 °C min^{-1}) using a TGA/SDTA 851^e (Mettler) under nitrogen atmosphere. Gas chromatography (GC) analyses were performed using an Agilent Technologies 6850 gas chromatograph equipped with a flame ionization detector (FID) and a MN Optima 17 capillary column (30.0 m x 0.32 mm x 0.25 µm) using *n*-dodecane as internal standard. GC-MS analyses were performed using an Agilent Technologies 6890 gas chromatograph with a MN-MS HP-5 capillary column (30.0 m x 0.32 mm x 0.25 µm) and a coupled mass spectrometer as detector. Gas mixtures were analyzed using a 6890N gas chromatograph (Agilent Technologies) equipped with an Agilent special Plot + Molsieve capillary column (30.0 m x 0.32 mm x 0.25 µm). Methane was used as internal standard. Nitrogen physisorption isotherms were determined at -196 °C

using a Nova 2000e (Quantachrome) apparatus. Specific surface areas were calculated by using p/p_0-values from 0.05-0.3 by the BET model. Specific total pore volumes were determined by DFT calculations (N_2 at -196 °C on silica (cylindric pore, NLDFT equilibrium model)). Transmission electron microscopy (TEM) measurements were carried out using a LEO 922o microscope (Zeiss, 200 kV) equipped with a LaB6 electron source and an omega energy filter. The samples were suspended in chloroform and sonicated for 2 min. 2 µL of the suspension were placed on a CF200-Cu-grid (Electron Microscopy Sciences) and allowed to dry. EDX (energy dispersive X-ray spectroscopy) measurements were performed by using a Zeiss Ultra Plus with an acceleration voltage of 20 kV. The sample coating with platinum (1.3 µm) was performed with a Sputter Coater 208HR (Cressington). Diffuse reflectance ultraviolet-visible spectra were measured using a CARY 300 (Agilent Technologies) with an Ulbricht sphere in the range of 350 to 700 nm. For optical band gap determination, a tauc plot was used applying the Munk-Kubelka equation. X-ray powder diffraction (XRD) analysis in the range of 2-80° 2θ was performed using a XPERT-PRO diffractometer (Panalytical) ($Cu_{K\alpha}$ radiation, 1.54178 Å) in θ-2θ geometry with a position sensitive detector. The reference card number for comparison is 01-080-0019 for CdS. X-ray photoelectron spectroscopy (XPS) was performed using a PHI Versa Probe III instrument of Physical Electronics. As X-ray source a monochromatic $Al_{K\alpha}$ with a spot size of 100 µm (24.5 W) was used. The kinetic pass energy of the photoelectrons was determined with a hemispheric analyzer (45°) set to pass energy of 26 eV for high-resolution spectra. Photoluminescence studies were conducted with a custom-built confocal fluorescence lifetime imaging microscope operating in the frequency domain (FD-FLIM). It is equipped with an amplitude-modulated cw diode laser at 488 nm (Toptica; iBEAM-SMART-488-S) with adjustable output power (set to 20 mW) and a miniature photomultiplier module (Hamamatsu H10721-01) as detector. The microscope objective is a Leica PL FLUOTAR L (100× / 0.75). Modulation frequencies between 110 MHz and 155 MHz were used. Data acquisition was performed with an integration time of 30 ms per data point. The sample was flushed with nitrogen gas for minimizing photobleaching effects. Samples are prepared by spin coating thin films of powder material dispersed in a polystyrene (M_w 200k g/mol) matrix on cover slips (26 mm x 20 mm x 200 µm). 2 mg of the sample material were suspended in a polystyrene/toluene solution (300 µL, 185 mg/mL). Spin coating was performed at 750 rpm for 15 s, 1500 rpm for 30 s, 3000 rpm for 60 s.

Material Synthesis

Synthesis of MIL-101

The synthesis was carried out according to a previous work to obtain an average crystallite size of 180 nm.[S1] Chromium(III) nitrate nonahydrate (480 mg, 1.20 mmol), terephthalic acid (198 mg, 1.20 mmol), hydrofluoric acid 46 wt% (10 μL, 0.228 mmol) and deionized H_2O (12.00 mL) were sealed in a 23 mL teflon-lined hydrothermal autoclave. The mixture was heated for 8 h at 220 °C (3.3 °C min^{-1}). The reaction mixture was cooled down fast to 160 °C and slowly to 30 °C (cooling rate: 2.7 °C h^{-1}). Excessively crystallized terephthalic acid was removed by filtration over a pore 3 filter. The product was separated from the aqueous solution by centrifugation (1800 rpm, 45 min), refluxed in ethanol/water (90/10 vol.-%) for 12 h, and centrifugalized (1800 rpm, 45 min) to remove the CrOOH impurities and to separate the MIL-101 crystals with different size distribution. The green MIL-101 was dried under vacuum (10^{-4} mbar, 85 °C, 24 h).

BET: 2700 m^2 g^{-1}.

PXRD: (°2θ) 2.78, 3.26, 3.41, 3.94, 4.30, 4.84, 5.13, 5.59, 5.85, 6.24, 6.48, 8.10, 8.40, 8.58, 8.86, 9.02, 9.71, 9.86, 10.30, 11.22, 16.50.

Synthesis of CdS@MIL-101

The synthesis was carried out according to a modified literature procedure.[S2] 400 mg MIL-101 was suspended in 35 mL of dimethyl sulfoxide in a 125 mL teflon-lined hydrothermal autoclave. 600 mg (2.25 mmol) of Cd(OAc)$_2$ · 2 H_2O cadmium(II) acetate dihydrate was added and the reaction mixture was stirred for 2 h. The mixture was heated at 180 °C for 10 h (heating rate: 2.5 °C min^{-1}). After cooling down to room temperature, the resulting CdS@MIL-101 was separated by filtration and washed with ethanol. The material was combined with 40 mL of ethanol and heated at 100 °C for 10 h (heating rate: 1.2 °C min^{-1}) in a 125 mL teflon-lined hydrothermal autoclave. After cooling down, the material was separated by filtration and dried under vacuum (10^{-4} mbar, 85 °C, 24 h).

Synthesis of Ni$_x$CdS@MIL-101, Ni@MIL-101[S3]

100 mg dry CdS@MIL-101 was placed in a two-chamber-tube with Ni(Cp)$_2$ bis(cyclopentadienyl)-nickel(II) (16.6 mg, 0.088 mmol, 5 wt.%) separated by a glass frit. The gas phase infiltration of the Ni precursor occurred at room temperature (25 °C) in static vacuum (10^{-4} mbar) for 20 h. The reduction of the Ni precursor was performed under hydrogen atmosphere (10 bar H_2) at 90 °C for 20 h in a Parr Instruments steel autoclave. The resulting Ni$_5$CdS@MIL-101 was evacuated (10^{-4} mbar, 85 °C, 20 h) in order to remove former metal ligand residue. The weight percentage of nickel (x wt.%) was varied by the amount of Ni(Cp)$_2$ to yield Ni$_x$CdS@MIL-101.

Synthesis of Pd$_5$CdS@MIL-101[S3]

100 mg CdS@MIL-101 were placed in a two-chamber-tube with (Cp)Pd(allyl) allyl(cyclopentadienyl)-palladium(II) (10.2 mg, 0.048 mmol, 5 wt.%) separated by a glass frit. The gas phase infiltration of the Pd precursor occurred at 32 °C in dynamic vacuum (10^{-4} mbar) for 24 h. The reduction of the Pd precursor was performed at 70 bar H$_2$ and 70 °C for 24 h. The resulting Pd$_5$CdS@MIL-101 was evacuated (10^{-4} mbar, 85 °C, 20 h) in order to remove former metal ligand residue.

Synthesis of Pt$_5$CdS@MIL-101[S4]

100 mg CdS@MIL-101 were placed in a two-chamber-tube with (Me)$_3$Pt(Cp') trimethyl-(methylcyclopentadienyl)platinum(IV) (8.2 mg, 0.026 mmol, 5 wt.%) separated by a glass frit. The gas phase infiltration of the Pt precursor occurred at 37 °C in static vacuum (10^{-4} mbar) for 20 h. The reduction of the Pt precursor was performed at 50 bar H$_2$ and 80 °C for 24 h. The resulting Pt$_5$CdS@MIL-101 was evacuated (10^{-4} mbar, 85 °C, 20 h) in order to remove former metal ligand residue.

Synthesis of *N*-cyclohexyl-1-phenylmethanimine (compound **1**)

1020 μL (10 mmol) benzaldehyde were stirred in a round bottom flask, then 1146 μL (10 mmol) cyclohexylamine were added dropwise. After 15 min, the turbid emulsion was diluted with 10 mL diethyl ether and dried over NaSO$_4$. After removing the solvent under reduced pressure, the product was obtained as yellow oil.

^{1}H NMR: (300 MHz, CDCl$_3$) δ 8.32 (s, 1H); 7.73-7.71 (t, 2H); 7.41-7.39 (t, 3H); 3.25-3.15 (quint, 1H); 1.87-1.59 (m, 7H); 1.41-1.29 (m, 3H).

Synthesis of *N*-benzyl-1-phenylmethanimine (compound **2**)

1020 μL (10 mmol) benzaldehyde were stirred in a round bottom flask, then 1090 μL (10 mmol) benzylamine were added dropwise. The turbid emulsion was diluted with 10 mL diethyl ether and dried over NaSO$_4$. After removing the solvent under reduced pressure, the product was obtained as colorless oil.

^{1}H NMR: (300 MHz, CDCl$_3$) δ 8.32 (s, 1H); 7.83-7,79 (m, 2H); 7.47-7.25 (m, 8H); 4.77 (s, 2H).

General Procedure for Photocatalytic Experiments

A 50 mL reaction vial was charged with a magnetic stir bar, $Ni_xCdS@MIL-101$ catalyst (5 mg), benzylamine (109 µL, 1 mmol) and cyclohexylamine (115 µL, 1 mmol). The vial was sealed with a rubber septum, evacuated to remove the air atmosphere, and flushed with argon. Dry and degassed solvent (1.5 mL) was added, then the vial was further purged with argon for 1 min and connected to a wash bottle to generate an open reaction system under inert atmosphere. The vial was illuminated for 20 h by a 50 W blue LED (470 nm, distance 2 cm, ~15000 lx) and cooled by a fan (Figure S1). The reaction temperature was measured to be 27 °C. *n*-dodecane (100 µL, 0.44 mmol) was added as internal standard and the catalyst was separated from the reaction solution by centrifugation (9000 rpm, 9 min) before quantitative analysis by GC. The amount of H_2 evolved from benzylamine (109 µL, 1 mmol) was determined by injecting 500 µL of methane as internal standard in a sealed reaction vial before LED illumination. The gas phase of the reaction was analyzed by GC-TDC. Acetonitrile (1.5 mL) was chosen as solvent for quantifying the H_2 liberation from benzylamine to preclude the H_2 generation by the oxidation of ethanol.
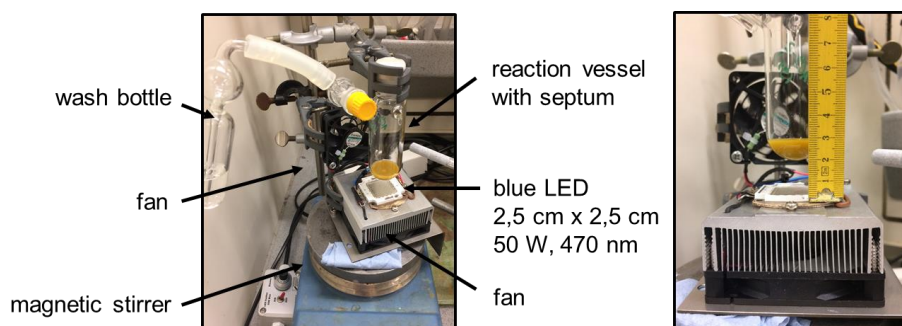
Figure S1. Experimental set-up for photocatalytic experiments. The reaction mixture is illuminated by a 50 W blue LED (470 nm) from below.

Kinetic Study of the Cross-Coupling of Benzylamine and Cyclohexylamine

The general procedure for photocatalytic experiments was applied. A 50 mL reaction vial was charged with 5 mg $Ni_5CdS@MIL-101$ catalyst, benzylamine (109 µL, 1 mmol) and cyclohexylamine (115 µL, 1 mmol). The vial was sealed, evacuated to remove the air atmosphere, and flushed with argon, before dry and degassed ethanol (1.5 mL) was added. A single photocatalytic reaction was performed for each time interval of the kinetic study. Therefor the period of illumination by a 50 W blue LED (470 nm, distance 2 cm, ~15000 lx) was varied. *n*-dodecane (100 µL, 0.44 mmol) was added as internal standard and the catalyst was separated from the reaction solution by centrifugation (9000 rpm, 9 min) before quantitative analysis by GC.

Evaluating the Photocatalytic Stability of Catalysts

The general procedure for photocatalytic experiments was applied. A 50 mL reaction vial was charged with 5 mg catalyst, benzylamine (109 μL, 1 mmol) and cyclohexylamine (115 μL, 1 mmol). The vial was sealed, evacuated to remove the air atmosphere, and flushed with argon, before dry and degassed solvent (1.5 mL) was added. The vial was illuminated for 48 h by a 50 W blue LED (470 nm, distance 2 cm, ~15000 lx). The catalyst was separated from the reaction solution by centrifugation (9000 rpm, 9 min), washed with ethanol and dried in vacuum before analysis by PXRD and XPS. The post-photocatalysis solutions were analyzed for leached Cd und Ni by ICP-OES. Samples were prepared by removing volatile organic compounds in vacuum and diluting in 5 % nitric acid solution. The leaching of $Ni_5CdS@MIL$-101 and $CdS@MIL$-101 was determined to be < 50 ppm (Cd) and < 12 ppm (Ni).

Recyclability Study of $Ni_5CdS@MIL$-101

For the recyclability study, a 50 mL reaction vial was charged with a magnetic stir bar, $Ni_5CdS@MIL$-101 catalyst (5 mg) and benzylamine (109 μL, 1 mmol). The vial was sealed with a rubber septum, evacuated to remove the air atmosphere, and flushed with argon. Dry and degassed acetonitrile (1.5 mL) was added, then the vial was further purged with argon for 1 min. The vial was illuminated for 3 h by a 50 W blue LED (470 nm, distance 2 cm, ~15000 lx) and cooled by a fan. *n*-dodecane (100 μL, 0.44 mmol) was added as internal standard and the catalyst was separated from the reaction solution by centrifugation (9000 rpm, 9 min) before quantitative analysis by GC. The amount of evolved H_2 was determined by injecting 500 μL of methane as internal standard in a sealed reaction vial before LED illumination. The gas phase of the reaction was analyzed by GC-TDC. $Ni_5CdS@MIL$-101 catalyst was purified in acetonitrile and ethanol (washing, centrifuging at 9000 rpm, 9 min) three times between the runs.

6.5.2 Material Characterization
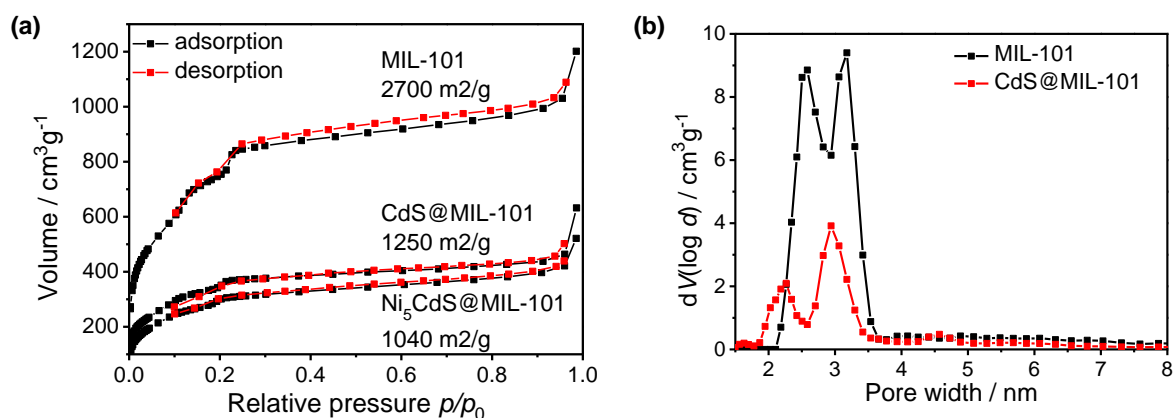
Figure S2. (a) N$_2$-physisorptions isotherms of MIL-101, CdS@MIL-101 and Ni$_5$CdS@MIL-101 with respective surface areas determined by BET-model (0.05-0.3 p/p$_0$). (b) Pore size distribution of MIL-101 compared to CdS@MIL-101.
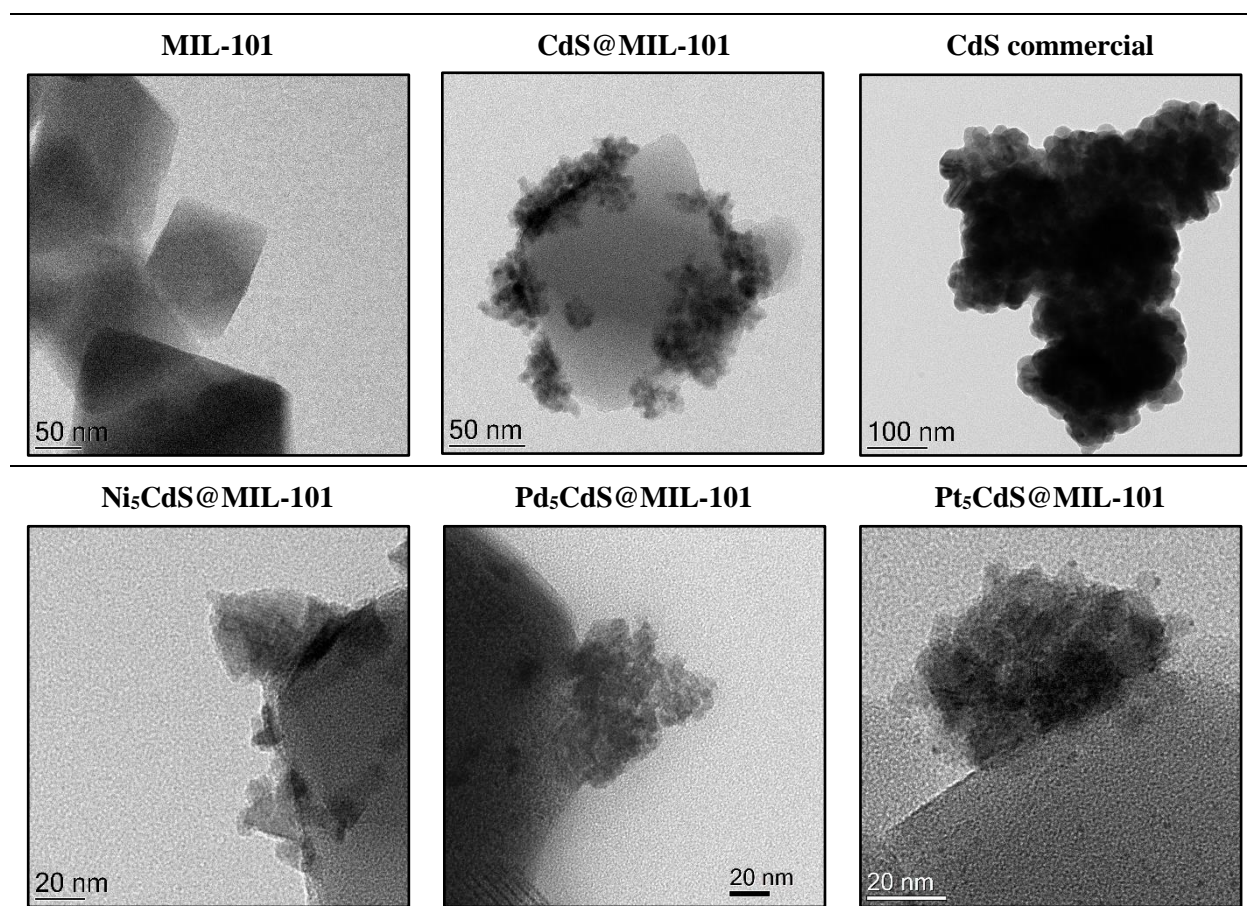
Figure S3. TEM analysis of as-synthesized octahedral-shaped MIL-101 and CdS@MIL-101 showing the core-shell morphology. For comparison TEM analysis of commercial CdS (Alfa Aesar) was performed. TEM analysis of Ni$_5$CdS@MIL-101, Pd$_5$CdS@MIL-101 and Pt$_5$CdS@MIL-101.

Table S1. ICP-OES analysis of CdS@MIL-101, Ni₅CdS@MIL-101, Pd₅CdS@MIL-101 und Pt₅CdS@MIL-101 with contents given in wt.%.

Compound	Cr	Cd	CdS[a]	Ni	Pd	Pt
CdS@MIL-101	11.7	36.3	46.6	-	-	-
Ni₅CdS@MIL-101	9.8	34.9	44.9	5.1		
Pd₅CdS@MIL-101	8.9	35.5	45.6	-	5.2	-
Pt₅CdS@MIL-101	8.4	35.4	45.5	-	-	4.9

[a] Calculated based on Cd content.
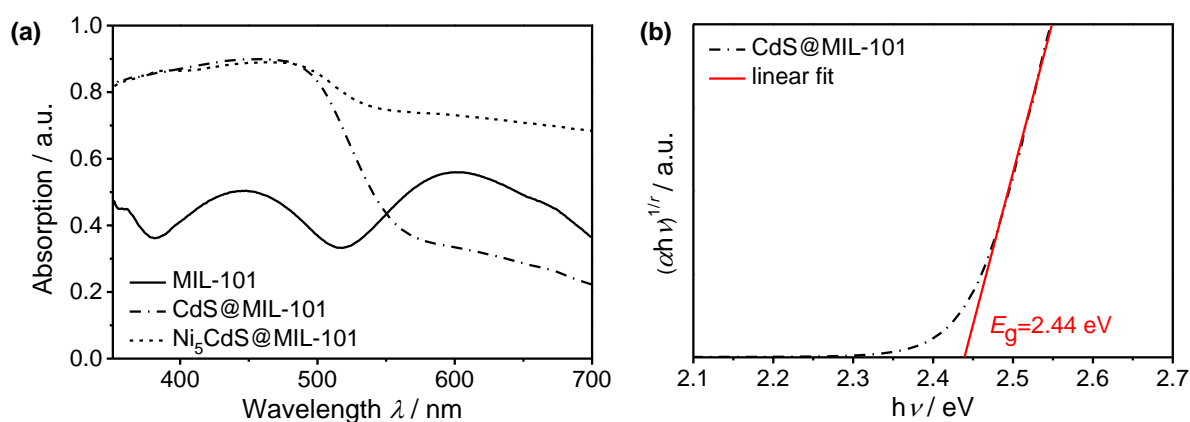
Figure S4. (a) Diffuse reflectance spectra of MIL-101, CdS@MIL-101 and Ni₅CdS@MIL-101 in the range of 350-700 nm. (b) Tauc plot for CdS@MIL-101 (applying the Munk-Kubelka equation).

Table S2. Linear fitting parameters and R^2-value (squared correlation coefficient) for the optical band gap determination by the tauc plot (see Figure S4).

	Intercept	Stand. error intercept	Slope	Stand. error slope	R^2-value
CdS@MIL-101	-885.5	14.9	363.1	5.9	0.99602
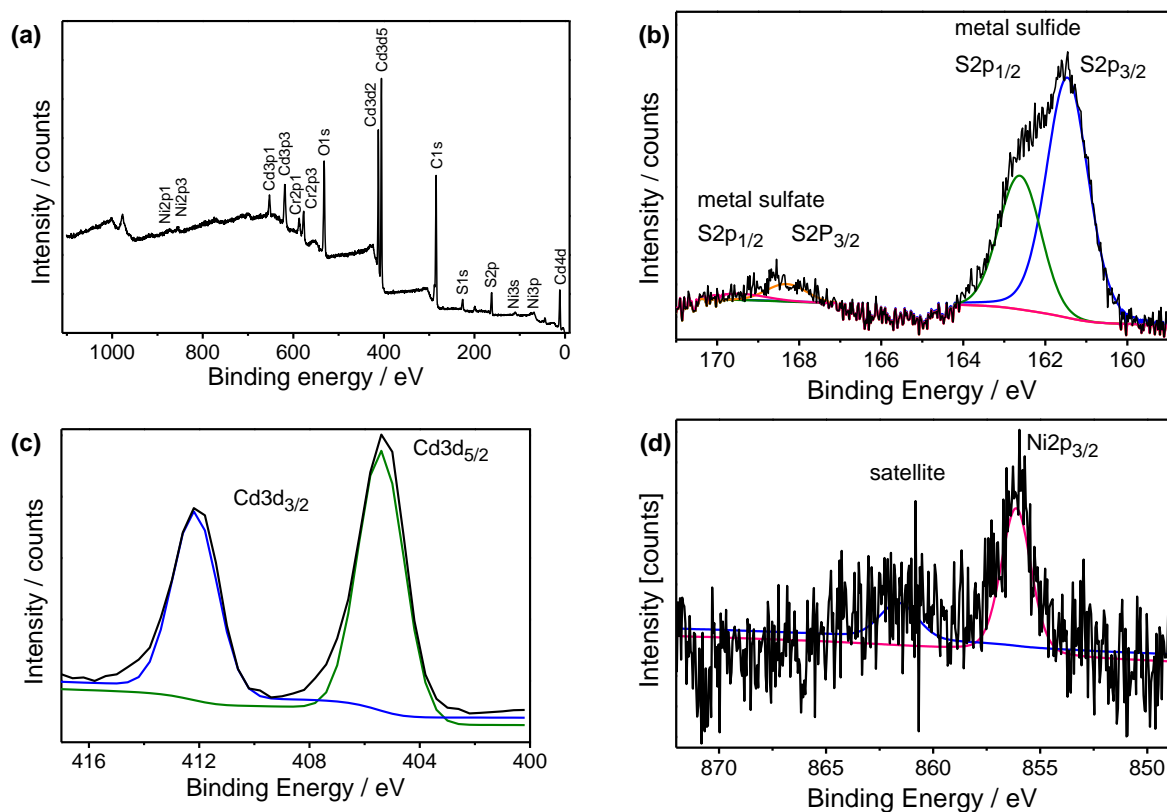
Figure S5. XPS spectra of $Ni_5CdS@MIL$-101. (a) Survey spectrum, (b) the S2p region, (c) the Cd3d region and (d) the Ni2p region in detail.
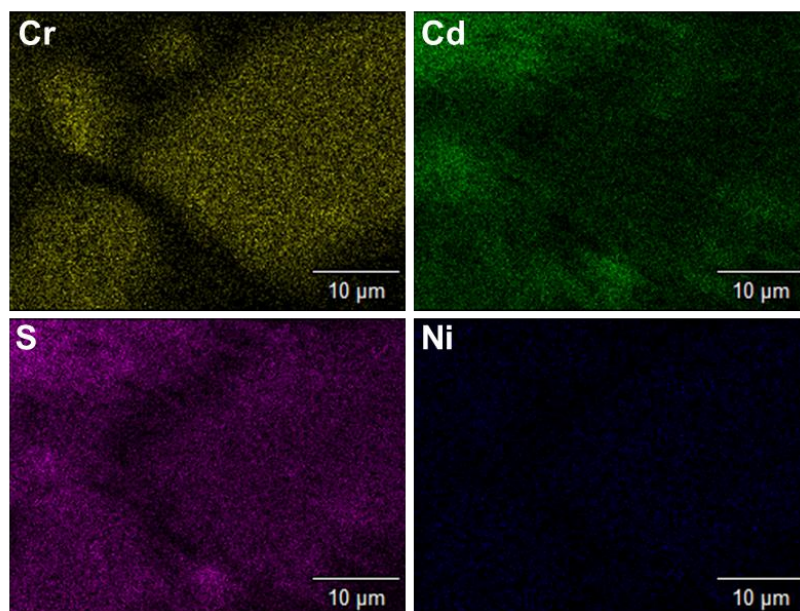
Figure S6. EDX elemental mapping of $Ni_5CdS@MIL$-101 shows the deposition of CdS on MIL-101 crystals and homogeneously distributed Ni particles.
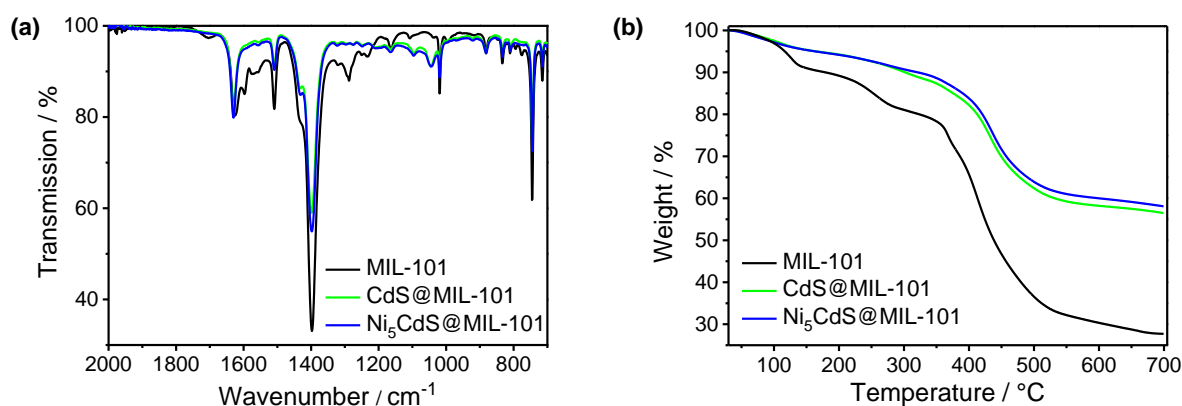
Figure S7. (a) FT-IR spectra and (b) thermogravimetric analysis of MIL-101, CdS@MIL-101 and $Ni_5CdS@MIL-101$.
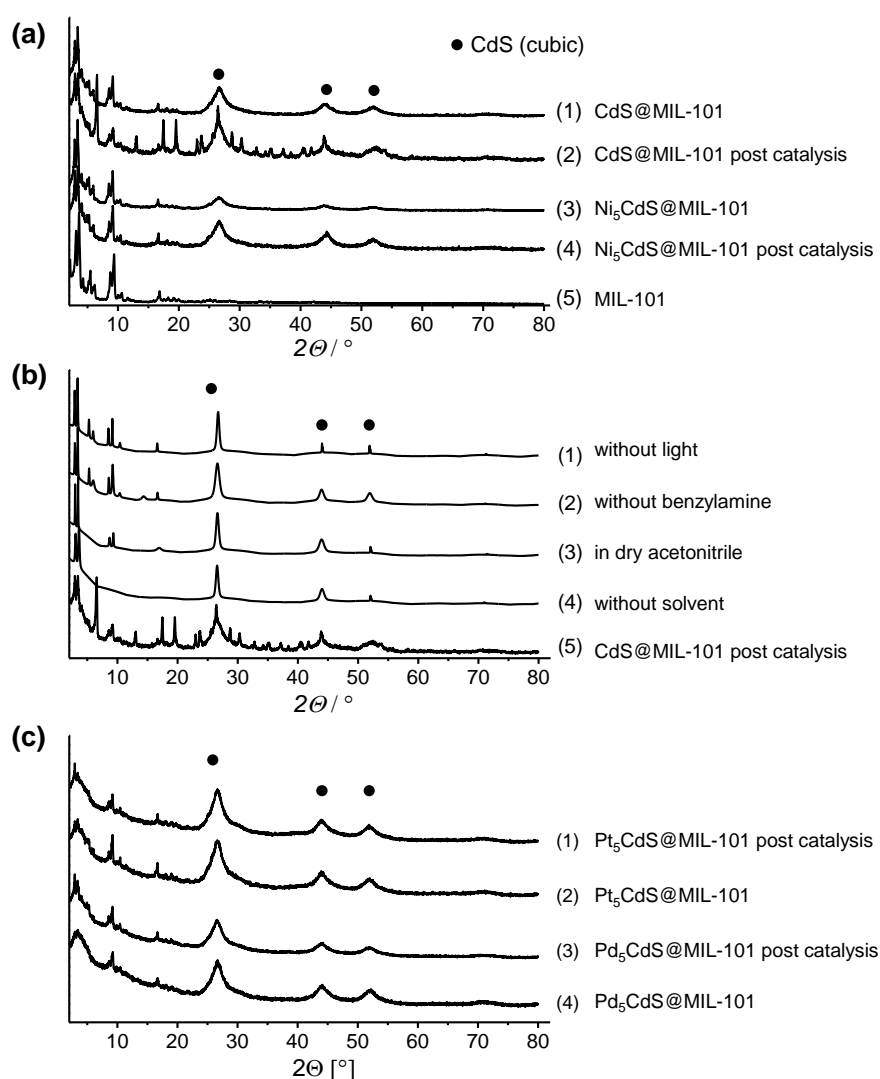
Figure S8. XRD of CdS@MIL-101 catalysts to evaluate the stability of CdS. (a) $Ni_5CdS@MIL-101$ and CdS@MIL-101 catalysts pre and post catalysis (1)-(4) compared to neat MIL-101 (5). (b) CdS@MIL-101 catalyst exposed to different catalytic conditions: (1) without light, (2) without benzylamine, (3) in dry acetonitrile, (4) without solvent, (5) standard catalytic conditions. (c) $Pt_5CdS@MIL-101$ and $Pd_5CdS@MIL-101$ catalysts pre and post catalysis (1)-(4).
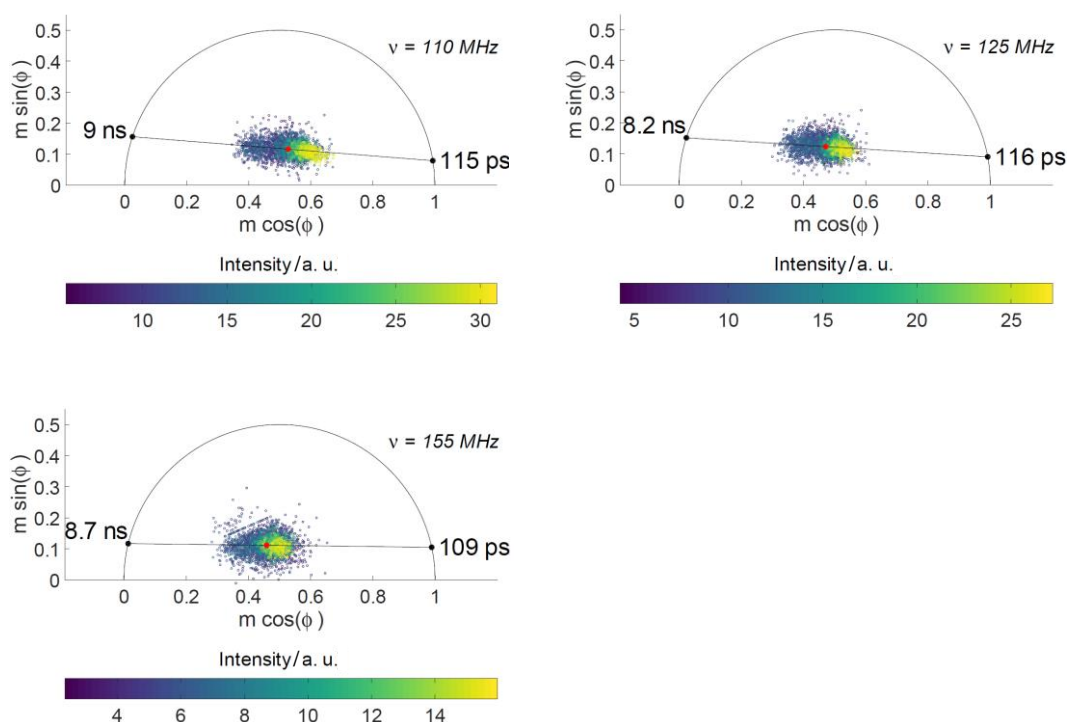
Figure S9. Fluorescence lifetime measurements in the frequency domain performed on neat CdS@MIL-101 at modulation frequencies of 110 MHz, 125 MHz, and 155 MHz confirm that the results do not depend on the laser modulation frequency within the experimental error.

6.5.3 Photocatalytic Experiments

Table S3. Solvent screening for the photocatalytic non-symmetric coupling of benzylamine and cyclohexylamine.[a]

Entry	Solvent	Yield 1 [%] [b]	Yield 2 [%] [b, c]
1	acetonitrile	26	53
2	methanol	13	31
3	**ethanol**	**74**	**7**
4	tetrahydrofuran	8	28
5	toluene	29	34
6	hexane	26	48
7	dimethylformamide	19	13
8	pyridine	17	11
9	dimethoxyethane	7	51
10	no solvent	34	22

[a] 1 mmol benzylamine, 1 mmol cyclohexylamine, 1.5 mL solvent, 5 mg Ni$_5$CdS@MIL-101, 470 nm blue LED (50 W), 20 h, rt, Ar. [b] Determined by GC using *n*-dodecane as an internal standard. [c] Referred to 0.5 mmol.

Table S4. Screening of the amount of solvent and amount of catalyst for the photocatalytic coupling of benzylamine and cyclohexylamine.[a]

Entry	Ethanol [mL]	Catalyst [mg]	Yield 1 [%] [b]	Yield 2 [%] [b, c]
1	0.5	5	34	6
2	1	5	52	6
3	**1.5**	**5**	**74**	**7**
4	2	5	60	10
5	3	5	2	41
6	1.5	2	54	11
7	**1.5**	**5**	**74**	**7**
8	1.5	7	65	12
9	1.5	10	57	14

[a] 1 mmol benzylamine, 1 mmol cyclohexylamine, different volumes of ethanol, different amount of Ni$_5$CdS@MIL-101, 470 nm blue LED (50 W), 20 h, rt, Ar. [b] Determined by GC using *n*-dodecane as an internal standard. [c] Referred to 0.5 mmol.

Table S5. Reversible transimination of homocoupled *N*-benzyl-1-phenylmethan-imine with cyclohexylamine to yield *N*-cyclohexyyl-1-phenylmethanimine applying different reaction conditions.[a]

	Yield 1 [%] [b]	Free benzylamine [%]
CdS@MIL-101	67	0
Ni$_5$CdS@MIL-101	80	0
Without hν	26	31
Without catalyst	28	28

[a] 0.5 mmol **2**, 1 mmol cyclohexylamine, 1.5 mL EtOH, 20 h, 5 mg catalyst, rt, Ar, 470 nm blue LED (50 W). [b] Determined by GC using *n*-dodecane as an internal standard.
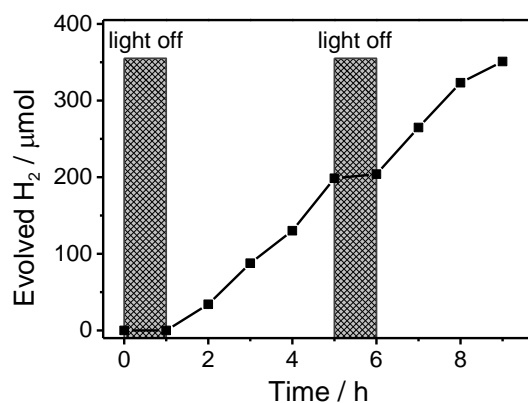
Figure S10. Photocatalytic H_2 generation from benzylamine by $Ni_5CdS@MIL$-101 during a light on/off experiment.[a] H_2 evolution was just observed under visible light illumination. [a] 1 mmol benzylamine, 5 mg $Ni_5CdS@MIL$-101, 1.5 mL acetonitrile, 500 µL methane, 470 nm blue LED (50 W), rt, Ar.
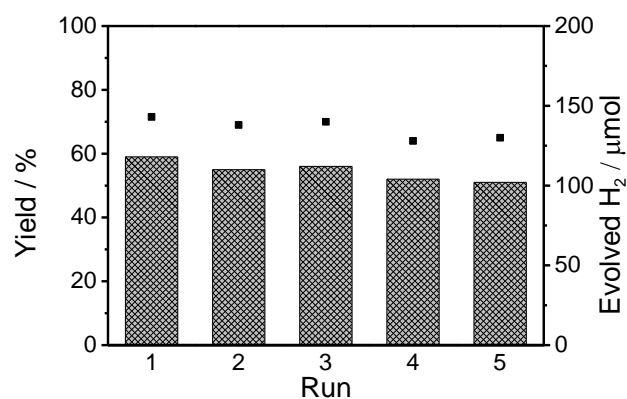
Figure S11. Recycling study of $Ni_5CdS@MIL$-101 in the photocatalytic acceptorless dehydrogenation of benzylamine.[a] No remarkable loss of activity was observed for five successive runs. [a] 1 mmol benzylamine, 5 mg $Ni_5CdS@MIL$-101, 1.5 mL acetonitrile, 500 µL methane, 3 h, 470 nm blue LED (50 W), rt, Ar, closed system.

6.5.4 Theoretical Procedure

The molecular model that we studied contained benzylamine (C_7H_9N) and the intermediate (C_7H_7N), respectively, in combination with either one Ni_{13} or Pd_{13} cluster (cp. Figure 4). The joint organometallic system is denoted MNP_{13}/C_7H_9N and MNP_{13}/C_7H_7N, respectively, with MNP_{13} referring to the metal nanoparticle Ni_{13} or Pd_{13}. Our computational procedure follows the line of our previous work.[S5] We used the TURBOMOLE[S6] program package for our Density Functional Theory (DFT) study. We performed geometry optimizations (GO) to obtain reliable molecular structures. All GOs and further electronic ground state calculations utilized the def2-TZVP[S7] basis set. All our calculations considered van-der-Waals' interactions via the scheme of Grimme.[S8] Dealing with transition metal particles requires a careful choice of the xc energy functional, as pointed out in the main manuscript. The Coulomb energy (Hartree term) that is present in DFT,[S9] contains a self-interaction energy contribution that is generally more prominent in localized than in delocalized electronic states.[S10] It is one of the responsibilities of the exchange-correlation (xc) energy functional to compensate for that spurious energy contribution.[S11] In practice, e.g., hybrid xc approximations partly remove self-interaction by including exact Fock exchange fractionally. Dealing with Ni_{13} and Pd_{13} is further complicated by the fact that their ground state is spin-polarized,[S12- S16] which is a more general finding for transition metal clusters.[S13-S22] Consequently, the introduction of a certain amount of Fock exchange might also lead to an overestimation of the spin-polarization and spin magnetic moment, respectively. For this reason, we complemented our Perdew-Burke-Ernzerhof (PBE)[S23] generalized gradient approximation (GGA) calculations with further using three hybrid xc functionals containing different percentages of Fock exchange: The TPSSh[S24] (10 %), B3LYP[S25] (20 %) and PBE0[S26] (25 %). Additionally, we checked our results with TPSS[S27] and SCAN[S28] and thus, incorporated xc functionals from the meta-GGA rung. We determined the spin multiplicity of the ground state for each xc functional. For the latter, the most stable spin state was found by calculating a set of GO or ground state calculations with fixed multiplicities of a pertinent range (see below).

Starting our investigation, we performed GOs for benzylamine, the intermediate and both metal clusters (Ni_{13}, Pd_{13}) to obtain reliable structures and total energies of each. The total energies E_{tot}^{xc} are reported in Table S6 and S7 for the organic molecules and clusters, respectively, and were used to calculate the binding energies of the joint systems thereafter. Our calculations and further, yet unpublished data strongly suggest that the icosahedral structure is arguably the most relevant one for Ni_{13} and Pd_{13} at room temperature in solution. Thus, we started from an icosahedral metal geometry for both clusters. See [S5] for a discussion of structural isomers of the metal particles. Table S7 additionally features the spin magnetic moment $\mu^{(xc)}$ of the corresponding electronic ground state (predicted by a certain xc functional); e.g., a spin moment of 8 μ_B corresponds to a spin multiplicity $m = 9$, whereas $m = 2S + 1$ and S denotes the spin quantum number.

Table S6. Total energy E_{tot}^{xc} for the singlet ground state of one benzylamine (C$_7$H$_9$N) and the intermediate (C$_7$H$_7$N) in dependence of the xc functional approximation.

xc	E_{tot}^{xc}(C$_7$H$_9$N) [eV]	E_{tot}^{xc}(C$_7$H$_7$N) [eV]
PBE	-8887.3941	-8854.5669
PBE0	-8888.3540	-8855.2789
B3LYP	-8893.5866	-8860.6359
TPSS	-8900.6394	-8867.5979
TPSSh	-8899.7185	-8866.6023
SCAN	-8894.8616	-8861.8326

Table S7. Total energy E_{tot}^{xc} and spin magnetic moment μ^{xc} for the corresponding ground state of icosahedral Ni$_{13}$ and icosahedral Pd$_{13}$ in dependence of the xc functional. A relativistic core-potential[S13] was used for Pd.

xc	E_{tot}^{xc}(Ni$_{13}$) [eV]	μ^{xc}(Ni$_{13}$) [μ_B]	E_{tot}^{xc}(Pd$_{13}$) [eV]	μ_B^{xc}(Pd$_{13}$) [μ_B]
PBE	-533506.0785	8	-45270.8245	8
PBE0	-533493.3678	16	-45254.5648	8
B3LYP	-533554.0148	16	-45250.4232	8
TPSS	-533604.0066	8	-45249.6988	8
TPSSh	-533587.3274	8	-45244.9208	8
SCAN	-533632.9777	8	-45273.0666	8

For the icosahedral Pd$_{13}$ all xc functionals predicted a spin magnetic moment of 8 μ_B for the ground state, agreeing with related previous studies.[S12,S15,S16] The situation for the icosahedral Ni$_{13}$, however, proved to be more delicate, as the holistic finding of previous DFT studies already indicated.[S5,S12,S13,S29] Our PBE GGA, meta-GGA (TPSS, SCAN) and hybrid TPSSh calculations predicted 8 μ_B. Yet, both hybrid functionals containing a larger amount of Fock exchange (PBE0, B3LYP) preferred a higher magnetic state of 16 μ_B. As discussed previously,[S5] the magnetic, high spin state predicted by hybrid functionals (PBE0, B3LYP), seems to conform with recent X-ray magnetic circular dichroism spectroscopy experiments of cationic Ni$_{13}^+$ that were independently reported by Langenberg *et al.* and Meyer *et al.*.[S17,S18] Prior to these, however, Stern-Gerlach studies on Ni$_{13}$ predicted a lower total magnetic moment.[S19,S20]

In order to obtain realistic structures that also incorporate potential temperature effects, we utilized DFT Born-Oppenheimer Molecular Dynamics (BOMD) simulations with a Nosé-Hoover thermostat[S30] for our model system. Our BOMD setup was the following: The temperature was set to 298 K. We employed the PBE (GGA) in combination with the def2-SVP[S31] basis set. The Conductor-like Screening Model[S32] (COSMO) considers the change of the relative permittivity ε_R of the medium caused by the presence of a substrate. We used COSMO for benzylamine (ε_R=4.6).[S33] Based on first

PBE GO test calculations that indicated a reduction of the magnetic moment for Pd_{13}/C_7H_9N, but not for Ni_{13}/C_7H_9N, we chose a fixed spin magnetic moment of $8 \mu_B$ and $4 \mu_B$, respectively. Furthermore, we fixed $8 \mu_B$ for Ni_{13}/C_7H_9N and $2 \mu_B$ for Pd_{13}/C_7H_7N since similar calculations implied a further quenching of the magnetic moment. The relaxation time equaled approximately 560 a.u. (13.0 fs) and 400 a.u. (9.3 fs) for systems containing Pd_{13} and Ni_{13}, respectively. We chose a time step of 80 a.u (1.9 fs). The total simulation time was circa 6 ps, which was enough to observe several low energy structures in all calculations. We extracted those structures that corresponded to the most prominent energy minima of the BOMD simulation (*i.e.*, 4 structures for Ni_{13}/C_7H_9N, Pd_{13}/C_7H_9N, Ni_{13}/C_7H_7N and 5 for Pd_{13}/C_7H_7N). For these structures, we carried out GOs to further relax them and to determine their magnetic ground state. For the latter, we carried out a set of GOs with PBE and fixed spin magnetic moments (in μ_B) in the range of $[0,2,\ldots,10]$ for each of these structures. Finally, we determined the binding energy (E_B^{xc}) for each structure by subtracting the total energies (E_{tot}^{xc}) of the bare systems (see Table S6, S7; here first for C_7H_9N and later C_7H_7N):

$$E_B^{xc} (MNP_{13}/C_7H_9N) = E_{tot}^{xc} (MNP_{13}/C_7H_9N) - E_{tot}^{xc} (MNP_{13}) - E_{tot}^{xc} (C_7H_9N), \qquad (1)$$

xc refers to PBE (GGA) here and further below to the rest of the aforementioned functionals. As a result, we found with PBE that Ni_{13}/C_7H_9N ($8 \mu_B$) is bound by -3.54 to -3.55 eV and Pd_{13}/C_7H_9N ($4 \mu_B$) by -2.73 to -2.75 eV. In the BOMD simulation, we started from a geometry in which the benzylamine's benzene ring was close to the MNP_{13} and the functional group (-NH_2) was pointing away from the MNP_{13}. An additional finding was that during these BOMD simulations, the functional group aligned towards Ni_{13} and Pd_{13}, respectively, and further resided in that orientation. The lowest energy geometries, *i.e.*, those corresponding to -3.55 and -2.75 eV, are depicted in the main manuscript (Figure 4), which clearly show an orientation of the functional group towards the metal clusters.

To check whether the observed trend in binding energy is robust, we also computed the electronic structure with PBE0, B3LYP, TPSSh, TPSS and SCAN. For this purpose, we kept the two lowest energy geometries fixed and carried out ground state calculations. We determined the ground state by varying the magnetic moment (in μ_B) in the range of $[0,2,\ldots,\mu^{xc}(MNP_{13}) + 2]$ (μ^{xc} according to Table S2, e.g. $\mu^{PBE0}(Ni_{13})=16 \mu_B$).

Table S8 shows the results of our study: We calculated the difference in binding energy by $\Delta E_B^{xc} = E_B^{xc}(Ni_{13}/C_7H_9N) - E_B^{xc}(Pd_{13}/C_7H_9N)$ to find a potential preference of the binding of benzylamine to one of the metal clusters. We found the general trend that benzylamine binds more strongly to Ni_{13} than to Pd_{13} by several hundred meV, yet with the exception for PBE0. However, we believe that the very high spin state ($\mu^{PBE0}(Ni_{13})=14 \mu_B$) is responsible for that outlier. We consider that the true binding is more accurately represented by the other xc functionals. Furthermore, these functionals (B3LYP, TPSS, TPSSh, SCAN) confirmed our results for PBE qualitatively. We therefore consider using PBE to be enough in the study of the intermediate (C_7H_7N). We then calculated the binding energies for the intermediate following the exact same procedure as for benzylamine. The trend that emerged from our

GO calculations with PBE is that Ni$_{13}$/C$_7$H$_7$N (8 μ_B) is bound by -3.48 to -3.54 eV and Pd$_{13}$/C$_7$H$_9$N (2 μ_B) by -3.08 to -3.12 eV. In conclusion, the intermediate binds stronger to Ni$_{13}$ than to Pd$_{13}$, yet overall slightly weaker compared to benzylamine.

Table S8. Total energies E$_{tot}^{xc}$, binding energies E_B^{xc} and spin magnetic moments μ^{xc} for the corresponding ground states of *MNP*$_{13}$/C$_7$H$_9$N in dependence of the xc functional. The difference in binding energy $\Delta E_B^{xc} = E_B^{xc}$(Ni$_{13}$/C$_7H_9$N) – E_B^{xc}(Pd$_{13}$/C$_7H_9$N). A relativistic core-potential[S13] was used for Pd. An energetically degenerated state w.r.t. magnetic moment is indicated by two entries.

xc	Ni$_{13}$/C$_7$H$_9$N			Pd$_{13}$/C$_7$H$_9$N			ΔE_B^{xc} [eV]
	E_{tot}^{xc} [eV]	E_B^{xc} [eV]	μ^{xc} [μ_B]	E_{tot}^{xc} [eV]	E_B^{xc} [eV]	μ^{xc} [μ_B]	
PBE	-542397.0177	-3.55	8	-54160.9728	-2.75	4	-0.70
PBE0	-542383.5580	-1.84	14	-54145.0317	-2.11	6	0.27
B3LYP	-542449.2869	-1.69	8	-54145.0658	-1.06	6	-0.63
TPSS	-542508.4642	-3.82	8	-54153.1524	-2.81	4	-1.01
TPSSh	-542490.7932	-3.75	8	-54147.2927	-2.65	4, 6	-1.10
SCAN	-542531.5333	-3.69	8	-54170.8508	-2.92	4, 6	-0.77

6.5.5 References

[S1]   J. Hermannsdörfer; M. Friedrich, R. Kempe, *Chem. Eur. J.* **2013**, *19*, 13652-13657.

[S2]   D. Tilger, M. Klarner, S. Hammon, M. Friedrich, A. Verch, N. de Jonge, S. Kümmel, R. Kempe, *Austrl. J. Chem.* **2019**. *72*. 842-847.

[S3]   J. Hermannsdörfer, M. Friedrich, N. Miyajima, R. Q. Albuquerque, S. Kümmel, R. Kempe, *Angew. Chem. Int. Ed.* **2012,** *51*, 11473-11477.

[S4]   S. Proch, J. Hermannsdörfer, R. Kempe, C. Kern, A. Jess, L. Seyfarth, J. Senker, *Chem. Eur. J.* **2008**, *14*, 8204-8212.

[S5]   D. Tilgner, M. Klarner, S. Hammon, M. Friedrich, A. Verch, N. de Jonge, S. Kümmel, R. Kempe, *Austr. J. Chem.* **2019**, *72*, 842-847

[S6]   TURBMOLE°V7.3 **2018**, (University of Karlsruhe and Forschungszentrum Karlsruhe GmbH, Karlsruhe, Germany).

[S7]   A. Weigend, R. Ahlrichs, *Phys. Chem. Chem. Phys*. **2005**, *7*, 3297–3305.

[S8]   S. Grimme, *Inc. J. Comput. Chem*. **2004**, *25*, 1463–1473.

[S9]   W. Kohn, L. J. Sham, *Phys. Rev*. **1965**, *140,* A1133.

[S10]   T. Körzdörfer, S. Kümmel, N. Marom, L. Kronik, *Phys. Rev. B* **2009**, *79*, 201205.

[S11]   J. P. Perdew, Alex Zunger, *Phys. Rev. B* **1981**, *23*, 5048-5079.

[S12]   L. Leppert, R. Kempe, S. Kümmel, *Phys. Chem. Chem. Phys.* **2015**, *17*, 26140-26148.

[S13]   G. L. Gutsev, C. W. Weatherford, K. G. Belay, B. R. Ramachandran, P. Jena, *J. Chem. Phys.* **2013**, *138*, 164303.

[S14]   J. P. Chou, C. R. Hsing, C. M. Wei, C. Cheng, C. M. Chang, *J. Phys.: Condens. Matter* **2013**, *25*, 125305.

[S15]   A. M. Köster, P. Calaminici, E. Orgaz, D. R. Roy, J. U. Reveles, S. N. Khanna, *J. Am. Chem. Soc.* **2011**, *133*, 12192-12196.

[S16]   B. Fresch, H.-G. Boyen, F. Remacle, *Nanoscale* **2012**, *4*, 4138–4147.

[S17]   A. Langenberg, K. Hirsch, A. Ławicki, V. Zamudio-Bayer, M. Niemeyer, P. Chmiela, B. Langbehn, A. Terasaki, B. v. Issendorff, J. T. Lau, *Phys. Rev. B* **2014**, *90*, 184420.

[S18]   J. Meyer, M. Tomber, T. van Wüllen, G. Niedner-Schattenburg, S. Peredkob, W. Eberhardt, M. Neeb, S. Palutke, M. Martins, W. Wurth, *J. Chem. Phys.* **2015**, *143*, 104302.

[S29]   M. B. Knickelbein, *J. Chem. Phys.* **2002**, *116*, 9703-9711.

[S20]   S. E. Apsel, J. W. Emmert, J. Deng, L. A. Bloomfield, *Phys. Rev. Lett.* **1996**, *76*, 1441-1444.

[S21]   A. J. Cox, J. G. Louderback, S. E. Apsel, L. A. Bloomfield, *Phys. Rev. B* **1994**, *49*, 12295-12298.

[S22]   M. Martins, W. Wurth *J. Phys.: Condens. Matter* **2016**, *28*, 503002.

[S23]   a) J. P. Perdew, K. Burke, M. Ernzerhof, *Phys. Rev. Lett.* **1996**, *77*, 3865-3868; b) J. P. Perdew, K. Burke, M. Ernzerhof, *Phys. Rev. Lett.* **1997**, *78*, 1396.

[S24]   a) V. N. Staroverov, G. E. Scuseria, J. Tao, J. P. Perdew, *J. Chem. Phys.* **2003**, *119*, 12129–12137; b) V. N. Staroverov, G. E. Scuseria, J. Tao, J. P. Perdew, *J. Chem. Phys.* **2004**, *121*, 11507–11507.

[S25]   a) A. D. Becke, *J. Chem. Phys.* **1993**, *98*, 5648-5652; b) P.J. Stephens, F. J. Devlin, C. F. Chabalowski, M. J. Frisch, *J. Phys. Chem.* **1994**, *98*, 11623-11627.

[S26]   a) J. P. Perdew, Matthias Ernzerhof, *J. Chem. Phys.* **1996**, *105*, 9982; b) C. Adamo, V. Barone *J. Chem. Phys.* **1999**, *110*, 6158.

[S27]   J. Tao, J. P. Perdew, V. N. Staroverov, G. E. Scuseria, *Phys. Rev. Lett.* **2003**, *91*, 146401.

[S28]   J. Sun; A. Ruzsinszky; J. P. Perdew., *Phys. Rev. Lett.* **2015**, *115*, 036402.

[S29]   R. Singh, P. Kroll, *Phys. Rev. B* **2008**, *78*, 245404.

[S30]   a) W. G. Hoover, *Phys. Rev. A* **1985**, *31*, 1695–1697; b) S. Nosé, *J. Chem. Phys.* **1984**, *81*, 511–519.

[S31]   A. Schäfer, H. Horn, R. Ahlrichs, *J. Chem. Phys.* **1992**, *97*, 2571–2577.

[S32]   A. Klamt, G. Schuurmann, *J. Chem. Soc.* **1993**, *2*, 799–805.

[S33]   A. A. Maryott, E. R. Smith, *National Bureau of Standards*, **1951**, 26.

7 Combining Metal Nanoparticles with an Ir(III) Photosensitizer

Sebastian Hammon,[a,e] Mara Klarner,[b] Gerald Hörner,[c] Birgit Weber,[c] Martin Friedrich,[b] Jürgen Senker,[d] Rhett Kempe,*[b] Thiago Branquinho de Queiroz,[e] Stephan Kümmel*[a]

[a]   Theoretical Physics IV, University of Bayreuth, Bayreuth D-95447, Germany

[b]   Inorganic Chemistry II – Sustainable Chemistry Centre, University of Bayreuth, Bayreuth D-95447, Germany

[c]   Inorganic Chemistry IV, University of Bayreuth, Bayreuth D-95447, Germany

[d]   Inorganic Chemistry III, University of Bayreuth, Bayreuth D-95447, Germany

[e]   Centro de Ciencias Naturais e Humanas, Universidade Federal do ABC, Santo André, Sao Paulo 09210-580, Brazil

Abstract: We report on a new photocatalytic system that consists of an iridium-based photosensitizer that has been encapsulated into the pores of the metal-organic framework (MOF) MIL-101, which have then been loaded with metal nanoparticles. Loading with Ni leads to substantially increased photocatalytic hydrogen evolution rates, whereas loading with Pt and Pd leads to only a small increase or none at all, respectively. These experimental findings triggered us to theoretically study the combination of the photosensitizer and metal cluster in detail. Time-dependent density functional theory calculations with an optimally tuned range-separated hybrid functional show that the optical excitations of systems, in which the iridium-based photosensitizer is combined with a metal cluster, involve a pronounced charge transfer from the metal to the photosensitizer. Density functional calculations show that the binding energy between the photosensitizer and the metal cluster is considerably larger for Ni than for Pd and Pt.

7.1 Introduction

Photocatalysis is one of the processes that have the potential to make an important contribution to meeting mankind's energy needs sustainably, e.g., by generating hydrogen that can replace fossil fuels. There has thus been a great interest in the photophysical properties of 2-phenylpyridyl- (ppy) and/or

2,2′-bipyridyl- (bpy) ligand-based Ir(III) photosensitizers, and insights have been gained from theoretical and experimental efforts in recent years.[1-9] It has been shown that these sensitizers have a lowest triplet state (T_1) that is associated with a long-lived charge separation. The latter can facilitate redox reactions that ultimately lead to the generation of hydrogen. In such triplet photosensitizers, the triplet excitations can rapidly be accessed after optical excitation through intersystem crossing, as the central Ir atom introduces a pronounced spin-orbit coupling, and the lowest triplet excitation T_1 is reached through internal conversion. Generally, T_1 is long-lived, e.g., with a photoluminescence (PL) lifetime of $\tau_{PL} \approx 0.1\text{-}14$ µs for most heteroleptic Ir photosensitizers.[9] The electronic nature of T_1 can usually be characterized as ligand-centered, metal-ligand to ligand charge transfer (MLLCT) or a varying mix of both.[9] [Ir(bpy)(ppy)$_2$]$^+$ (named Ir-L0 in the following) is a prime example of such a redox-active triplet photosensitizer, since it exhibits a long-lived T_1 ($\tau_{PL} = 370$ ns in degassed tetrahydrofuran (THF))[10] with a distinct Ir/ppy → bpy charge-transfer character, designated as MLLCT(bpy).[4,5,10,11]

In the present study, which combines first experiments with a detailed theoretical study, we discuss that metal nanoparticles (MNPs) can modify the properties of a photosensitizer and substantially enhance the hydrogen evolution rate. We confined a visible light photosensitizer with the [Ir(bpy)(ppy)$_2$]$^+$ motif (cf. Figure 1, named Ir-L1 in the following) into MIL-101, which was subsequently loaded with Ni, Pd, and Pt nanoparticles. Upon loading with Ni, we observe a significantly enhanced photocatalytic activity for hydrogen evolution, whereas Pt and Pd lead to just a small enhancement or none at all, respectively. Relying on density functional theory (DFT) and time-dependent (TD) DFT with a range-separated hybrid functional[12-15] and a range-separation parameter that is determined by nonempirical optimal tuning,[8,16-27] we analyze how the presence of metal particles changes the electronic structure and the excitations of the photosensitizer. We find that there is a strong electronic interaction between the metal particles and the Ir-L1 in the ground state, with a clear trend in the binding affinity between the MNPs and Ir-L1: In the model systems that we studied, the Ni particle binds considerably stronger to Ir-L1 than Pd and Pt. The presence of the metals also substantially changes the character of the excitations. The absorption spectrum shows many densely lying excitations, and we find clear signatures of a charge transfer from the MNP to the Ir-L1 in the optical transitions. We discuss possible differences between the mechanisms of hydrogen evolution in the MNP-loaded samples and the mechanism discussed above for the bare Ir(III) photosensitizer and put our findings into perspective in the concluding section.

7.2 Synthesis and Hydrogen Evolution

The three-dimensional metal−organic framework MIL-101(Cr) is made from the linkage of terephthalic acid and secondary building units (SBUs, Cr$_3$O) where two out of three Cr^{3+} cations exhibit an accessible coordinatively unsaturated site (CUS).[28] The activated host material CUS@MIL-101 is yielded by the removal of auxiliary water ligands and, thereafter, can engage in adsorption processes of guest

molecules. In recent years, the grafting of various alcohols to Lewis-acidic coordinatively unsaturated Cr^{3+} sites was demonstrated.[29-32] Hence, we designed a bipyridyl ligand L1 that contains hydroxyl groups in the backbone and allows homogeneously distributed grafting to CUS. This serves as a basis for the targeted encapsulation of an iridium photosensitizer with an Ir-L0 motif within MIL-101 following a ship-in-a-bottle approach. We compared the new heteroleptic iridium photosensitizer Ir-L1 (cf. Figure 1) to the established [Ir(dtbbpy)(ppy)₂]⁺ (4,4′-di-*tert*-butyl-2,2′-bipyridyl, named Ir-L2) in means of optical absorption characteristics and redox potentials, two crucial factors for efficient photocatalysis, and found no significant differences, as shown in the Supporting Information (SI). The theoretical comparison with Ir-L0 further corroborates the photocatalytic functionality of Ir-L1, as discussed in the section Ir-L1 Triplet Photosensitizer.[33] Therefore, we consider the photosensitizer Ir-L1 suitable for our study on a confined photocatalyst system. The composite material M/[Ir-L1]@MIL-101 was synthesized along a four-step route as outlined in Figure 1 (M: Ni, Pd, Pt).
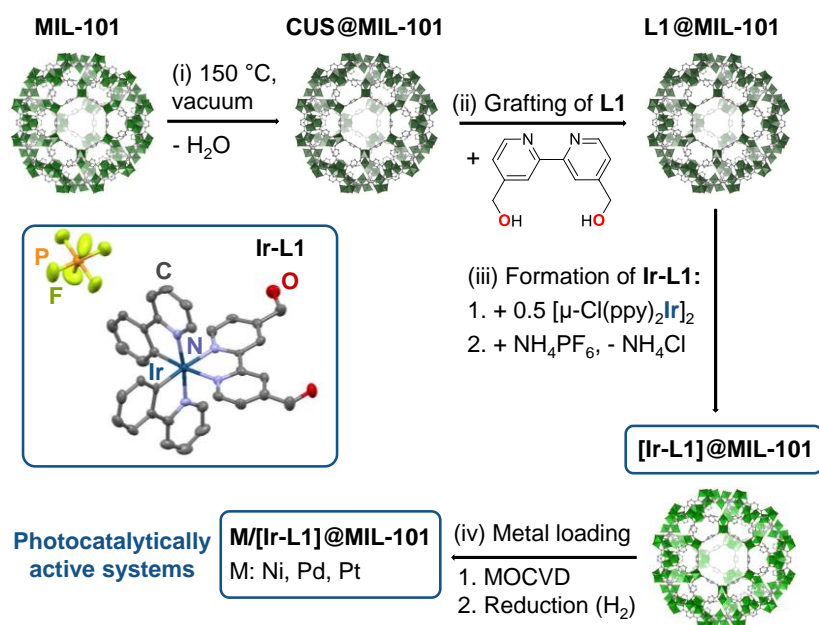

Figure 1. Synthesis of M/[Ir-L1]@MIL-101 by the ship-in-a-bottle approach: Step (i): CUS@MIL-101 is generated by removing auxiliary H₂O ligands from the SBU. Step (ii): After grafting the ligand L1 to CUS@MIL-101, step (iii): the iridium dimer [(μ-Cl)(ppy)₂Ir]₂ was added for the Ir-L1 complex formation. The anion was exchanged by noncoordinating hexafluorophosphate. Step (iv): For metal loaded catalysts, a suitable metal precursor was infiltrated into MIL-101 by metal-organic chemical vapor deposition (MOCVD) and reduced by H₂ treatment. The molecular structure of Ir-L1 was determined by X-ray single crystal structure analysis. For crystallographic data and complex characterization, see SI.

Step (i): The activated form of the host material CUS@MIL-101 was generated from native MIL-101 by removal of up to two molecules of water per SBU, which originated from the hydrothermal synthesis of MIL-101.[28] Therefore, MIL-101 was heated to 150 °C in vacuum for 12 h, resulting in CUS@MIL-101 crystallites with an intact octahedral shape (cf. SI, Figure S4(a)). Compared to as-synthesized MIL-101, no significant changes in crystallinity were observed (cf. SI, Figure S4(b)).

Step (ii): In order to ensure a homogeneous distribution of the bulky iridium complex Ir-L1

($\sim 13.3 \times 10.0$ Å), we followed a ship-in-a-bottle approach: The 2,2′-bipyridyl-4,4′-dimethanol ligand L1 was homogeneously grafted to the activated MOF through coordination at the unsaturated Cr^{3+} sites of the SBU as monitored by Fourier transform IR (FTIR) and magic angle spinning (MAS) nuclear magnetic resonance (NMR) spectroscopy (cf. Figure 2(a)). The assignments of ^{13}C MAS NMR shifts were made by a comparative study of MIL-101, L1, and Ir-L1. Paramagnetic MAS NMR previously proved a very useful tool for identifying coordination species,[34] revealing diagnostic hyperfine shifts for C atoms close to paramagnetic centers. Accordingly, the MAS NMR spectra of MIL-101 showed massive negative paramagnetic shifts for the skeletal terephthalic linker (-370 ppm) as compared to noncoordinated molecules (cf. Figure 2(b)). In keeping with this finding, the paramagnetic shift for C1 (1_{para} 292 ppm) and C2 (2_{para} 2 ppm) signals of the grafted ligand L1 gave clear evidence for the successful incorporation of the ligand at defined sites of the SBU (cf. Figure 2(b) and SI, Figure S6(a,b)). A diamagnetic shift for C1 (1_{dia} 58 ppm) indicated the coordination of the ligand by one hydroxyl group only. For further interpretation of the MAS NMR shifts, the grafting process of L1 was analyzed with DFT methods (cf. SI for details). Truncated models of the trinuclear SBU (cf. Figure 2(a)) have been optimized in the native form (SBU^{DFT}) and in the ligand-grafted form concomitant with partial dehydration ($L1@SBU^{DFT}$). Incorporation of L1 via coordination at the open coordination site of Cr^{3+} accommodates the cleft between neighboring terephthalic moieties. L1 is found well-suited to bind via strong hydrogen bonding at a second site of the same SBU. The dis-symmetric interaction with two different Lewis sites of only one of the hydroxyl groups in the ligand backbone of L1 thus well-matches the outcomes of ^{13}C MAS NMR spectra. In keeping with this, computation of $L1@SBU^{DFT}$ reveals small but significant Mulliken spin densities ρ at C1 and C2 (with $\rho(C1) \ll \rho(C2)$) but none at the H-bridged ligand arm at C1′ and C2′. Two-point anchoring of L1 at one single SBU as in optimized $L1@SBU^{DFT}$ serves to fix the pyridine moieties of L1 in a close-to-coplanar *cis*-arrangement, which is suitable for on-site construction of the Ir photosensitizer. IR spectra computed of grafted $L1@SBU^{DFT}$ qualitatively match the experimental data (cf. SI, Figure S15).

Step (iii): On-site formation of the Ir-L1 complex was achieved by adding a [(μ-Cl)(ppy)₂Ir]₂ dimer with predisposed Ir(ppy)₂ units and incorporation of noncoordinating hexafluorophosphate through anion metathesis to yield [Ir-L1]@MIL-101. The successful encapsulation of the Ir photosensitizer within the MOF pores was corroborated by FT-IR spectroscopy (cf. SI, Figure S8) and MAS NMR spectroscopy (cf. SI, Figure S6(c,d)). In contrast to ligand grafting, the ^{13}C MAS NMR spectrum of [Ir-L1]@MIL-101 did not indicate direct grafting via Cr^{3+} sites, since signals were observed only within the typical diamagnetic shift region (0-180 ppm). In particular, there were no signs of dis-symmetric attachment. We believe that the formation of the sterically demanding Ir-L1 photosensitizer within the mesopores of MIL-101 was associated with the decoordination of L1 from the Cr^{3+} sites. High-angle annular dark-field scanning transmission electron microscopy (HAADF-STEM) images indicated a homogeneous distribution of Ir in the MOF crystallites (cf. Figure 2(c)). Analysis via inductively coupled plasma optical emission spectroscopy revealed the presence of 5.8 wt.% Ir due to Ir-L1

encapsulated in MIL-101, which corresponds to 0.3 μmol(Ir) mg^{-1}(MIL-101). Diffuse-reflectance ultraviolet-visible spectroscopy of yellow-green [Ir-L1]@MIL-101 showed absorption at wavelengths below 600 nm (see SI, Figure S9). This finding is highly consistent with the optical absorption properties of Ir-L1, which strongly absorbs at wavelengths λ < 525 nm (2.36 eV). We investigated this photocatalyst [Ir-L1]@MIL-101 for the proton reduction from water using triethylamine as a sacrificial agent. For this purpose, degassed H_2O and triethylamine were dissolved in degassed THF, the photocatalyst was added, and the slurry was illuminated with a blue LED (470 nm, 50 W). Discontinuous headspace analysis through gas chromatography quantified the amount of H_2 evolved after 6 h, from which the H_2 evolution rate per hour was calculated. [Ir-L1]@MIL-101 was found to produce about 0.34 μmol(H_2) h^{-1} μmol(Ir)$^{-1}$ at the selected reaction condition, i.e., the photoreaction was slightly superstoichiometric after 6 h. Confinement of the photosensitizer Ir-L1 affects its photophysical properties. We report an investigation of the stability of [Ir-L1]@MIL-101 in the SI. Time-resolved luminescence spectroscopy of [Ir-L1]@MIL-101 demonstrated a multiexponential PL decay with lifetime components in the time range of only a few nanoseconds, while Ir-L1 gave leading decay components in the time range of several hundreds of nanoseconds (see SI, Figure S13 and Table S2). Thus, the composite [Ir-L1]@MIL-101 opens deactivation pathways for Ir-L1 that can be related to its confinement, steric distortion, and/or the open-shell skeleton of the MOF. Nevertheless, and in spite of the reduced excited state lifetime, confined [Ir-L1]@MIL-101 still is active toward photochemical hydrogen production.
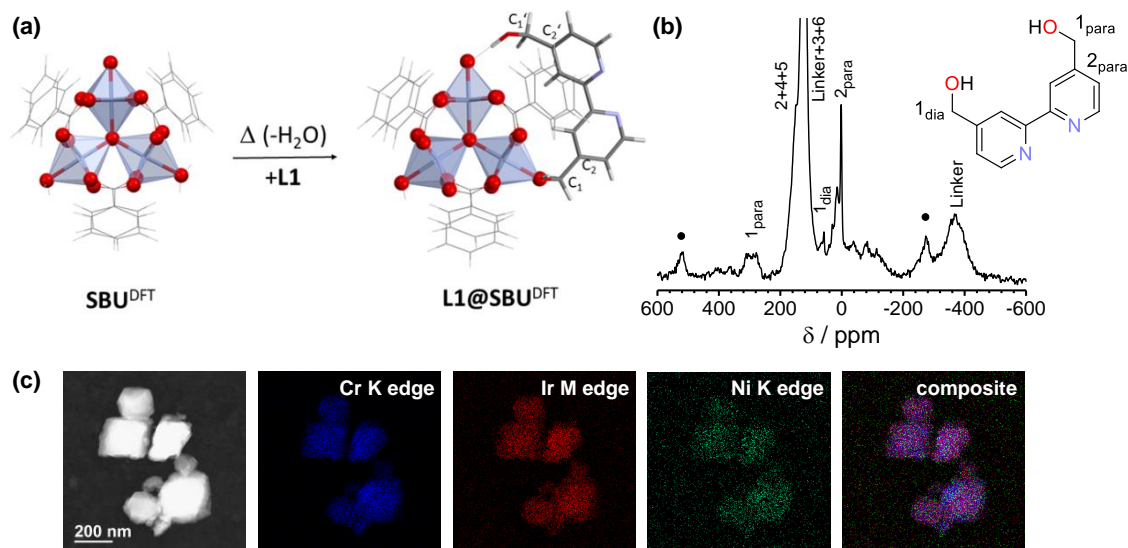

Figure 2. (a) DFT optimized structures of a truncated model of SBU^{DFT} and of its adduct L1@SBU^{DFT}; diagnostic ^{13}C MAS NMR carbon sites are highlighted. (b) ^{13}C MAS NMR spectrum of L1@MIL-101 including assignments; spinning side bands were marked with a dot. (c) HAADF-STEM of Ni/[Ir-L1]@MIL-101 and representative EDX elemental maps of Cr, Ir and Ni. Additionally, overlapped element maps are given.

Step (iv): Incorporation of group 10 MNPs (Ni, Pd, Pt; 5 wt.%) within the pores of [Ir-L1]@MIL-101 was achieved by a metal-organic chemical vapor deposition approach with suitable precursors and

on-site reduction to metallic nanoparticles by hydrogen treatment (cf. SI, Table S1). Exemplarily, we recorded a HAADF-STEM image and representative energy-dispersive X-ray spectroscopy (EDX) elemental maps of Ni/[Ir-L1]@MIL-101 (cf. Figure 2(c)). The spatial distribution of Cr atoms matched the octahedral shape of the MIL-101 crystallites, which was obviously retained throughout all modifications. Ir and Ni are likewise detected homogeneously distributed over the MOF. The additional presence of group 10 MNPs did not significantly alter the PL of (non-metal-loaded) [Ir-L1]@MIL-101, except for a small increase in the PL lifetime (see SI, Figure S13 and Table S2). Regarding the photocatalytic activity (cf. Figure 3), palladium almost entirely quenches the hydrogen evolution ($0.03\ \mu mol(H_2)\ h^{-1}\ \mu mol(Ir)^{-1}$). Loading with the well-established reduction (co)catalyst Pt leaves the activity largely unaffected ($0.51\ \mu mol(H_2)\ h^{-1}\ \mu mol(Ir)^{-1}$). It was surprising to find the 3d metal nickel boosting the hydrogen evolution rate by a factor of 5.6 to $1.91\ \mu mol(H_2)\ h^{-1}\ \mu mol(Ir)^{-1}$, thereby outperforming the established precious metals (cf. Figure 3). In conclusion, the distinction in cocatalytic efficiency cannot be correlated with effects of Ni, Pd, and Pt on the photoluminescence of the [Ir-L1]@MIL-101. However, we see a clear qualitative effect of the metal element itself. The MOF stabilizes the metal nanoparticles without blocking their surface and ensures the spatial proximity of the metal and the photosensitizer. The proximity of the metal can be expected to have an effect on electron transfer and energy transfer between the metal and the photosensitizer and thus affect the catalytic activity. Our experiments show a highly beneficial effect for the 3d metal nickel. In the following, we take steps to understanding this effect better via computational analysis.
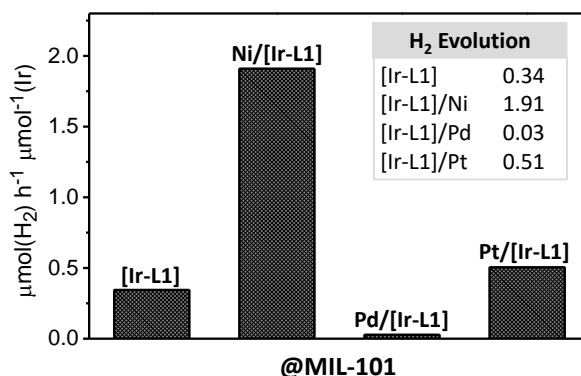

Figure 3. Hydrogen evolution rate for the photocatalytic proton reduction from water for [Ir-L1]@MIL-101 and M/[Ir-L1]@MIL-101 (M: Ni, Pd, Pt). For general procedure for photocatalytic experiments, see SI.

7.3 Analysis of the Electronic Structure and Excitations

For further understanding we have performed a computational analysis of key elements of the experimental system, with a focus on the combination of Ir-L1 with Ni, Pd, and Pt and the corresponding charge-transfer properties.

Ir-L1 Triplet Photosensitizer. As a first step, we checked whether adding the anchor groups to the photosensitizer leads to any unexpected effects. We calculated the optical absorption spectra of the Ir-L1

structure that underlies the experiments and the basic motif Ir-L0, which is an intensively studied triplet photosensitizer (cf. Introduction). The former differs from the latter by the anchor group (-CH$_2$OH) that is attached to the bpy ligand. Figure 4 shows that the spectra calculated with TDDFT[35,36] (cf. SI, Computation Details) are qualitatively very similar. The strongest vis singlet excitations of both complexes are located around ~3 eV. The brightest one of Ir-L1 (S$_4$, 3.03 eV) shows a slightly increased oscillator strength (0.1023) compared to the brightest one of Ir-L0 (2.99 eV, 0.0886). Note that in this and all following figures, we folded the calculated oscillator strengths with Gaussians to guide the eye (scale on the left edge of the figure), whereas the oscillator strength itself was plotted on a scale of [0, 0.2]. We also calculated the electronic difference densities of the singlet and triplet excitations, respectively, with the singlet ground state, as depicted in the inset of Figure 4 for the brightest excitation S$_4$(Ir-L1) and T$_1$(Ir-L1). T$_1$ shows a clear long-range MLLCT(bpy) character, as illustrated by the red and blue wireframes that indicate negative (area of electron lack) and positive (gain) in these and the following difference densities. An isovalue of 0.0005 a_0^{-3} was used in the plots of the difference densities throughout the paper. The MLLCT(bpy) of Ir-L1 is qualitatively very similar to the one of Ir-L0 (cf. SI, Figure S17). In total, Ir-L1 inherits the key photophysical properties of Ir-L0 and can function as a triplet photosensitizer via the previously discussed mechanism.[25] The findings from the calculations are thus in line with the experimental observations that also point to a negligible influence of the anchor groups (SI, Figure S2).
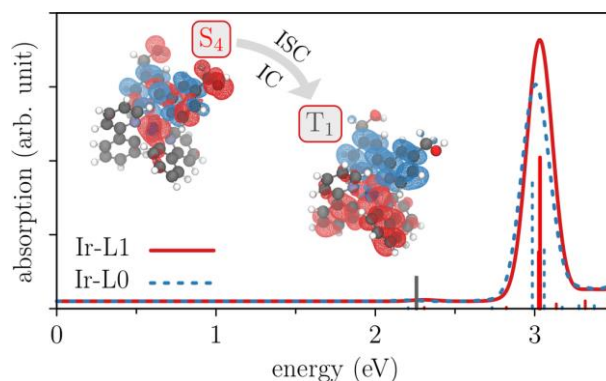

Figure 4. Vis absorption spectrum of the modified Ir-L1 and standard Ir-L0: The excitation spectra were calculated using TDDFT with the nonempirical optimally tuned ωPBE (ω_{opt}(Ir-L1) = 0.16 bohr^{-1}, ω_{opt}(Ir-L0) = 0.16 bohr^{-1}). The relative oscillator strength is indicated by the height of the vertical red and blue bars for Ir-L1 and Ir-L0, respectively. T$_1$(Ir-L1) is marked by the single grey bar. For a better visualization, the spectrum is shifted vertically by a constant of 0.02 arb. unit. Inset: Difference densities for the brightest singlet S$_4$ (3.03 eV) and the lowest triplet excitation T$_1$ (2.26 eV), with schematic allusion to intersystem crossing and internal conversion. See the main text for details about the difference densities.

Influence of Metal Nanoparticles on Ir-L1. As studying the complete system of Ir-L1 and an MNP inside MIL-101 with first-principles methods is computationally unfeasible and the main electronic effects are expected to occur in the interaction between the metals and Ir-L1, we are studying a model system that contains a 13-atom metal cluster (M_{13} = Ni$_{13}$, Pd$_{13}$, Pt$_{13}$) and one Ir-L1 molecule. Obviously, the 13-atom clusters are smaller than the nanoparticles that fill the MOF pores in the experiments,[37] but

given the computational restrictions, we consider 13-atom clusters minimalistic structures that are suitable for studying the metal-Ir-L1 interaction for several reasons: They are known to form a variety of stable isomers,[38-47] and similar geometries occur for all three metals. This allows the different metals to be compared on a similar structural basis. Furthermore, we have generally observed in Born-Oppenheimer DFT molecular dynamics[48,49] (BOMD) simulations at room temperature that 13-atom metal clusters can adapt their structure to their environment, e.g., when they are in solution or bind to a molecule. Therefore, versatile aspects of a possible interaction between the metal cluster and Ir-L1 can be captured. Finally, the choice is also supported by the finding that all three M_{13} bind to Ir-L1 (see below) and may thus be interpreted to represent a small subsystem inside a pore. Note that transition metal clusters require special attention with respect to the choice of the exchange-correlation approximation, because the partially localized d-orbitals are prone to be affected by self-interaction errors, and different density functionals are sensitive to this problem to different degrees.[50] For the reasons discussed in refs [51] and [52], we used the semilocal generalized gradient approximation Perdew-Burke-Ernzerhof[53,54] (PBE) for DFT geometry optimizations, to calculate binding energies and for BOMD simulations, and the optimally tuned range-separated hybrid functional ωPBE,[55,56] composed of PBE exchange in the short-range, exact exchange in the long-range, and PBE correlation, to compute photophysical properties such as the photoabsorption spectrum (cf. SI, Analysis of the electronic structure and excitations). All calculations using PBE and ωPBE were carried out with the TURBOMOLE[57] and QCHEM[58] code, respectively. For determining the structures of the combined metal-Ir-L1 systems, we performed a BOMD simulation at room temperature for each system M_{13}/[Ir-L1] employing the def2-SVP basis set.[59] We started from an icosahedral structure for all three metal clusters, and initially, M_{13} had been displaced from (ppy)$_2$ by a distance of $\sim$7 Å^{-1} between the centers of gravity of M_{13} and Ir-L1. We observed that all three metal clusters were "drawn" into the gap between the two ligands (cf. Figure 5). Ni$_{13}$ and Pt$_{13}$ retained their icosahedral structures, whereas Pt$_{13}$ assumed different geometries in the course of the simulation. We propagated each system for about 4 ps and then determined the energetically most favorable structure of each run by checking the total energy data. We further relaxed the thus-found structures in geometry optimizations using PBE with van der Waals corrections (DFT-D3)[60] and the def2-TZVP basis set.[61] The resulting geometries are depicted in Figure 5 and served as the basis for the following calculations.

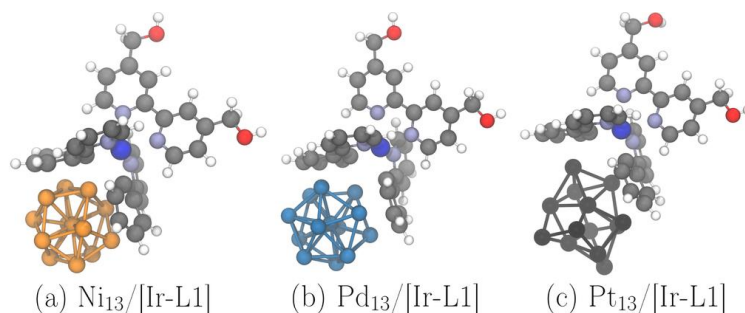(a) Ni$_{13}$/[Ir-L1]   (b) Pd$_{13}$/[Ir-L1]   (c) Pt$_{13}$/[Ir-L1]

Figure 5. Molecular structures used to study the direct influence of the metals on the photophysical properties: (a) Ni$_{13}$/[Ir-L1]; (b) Pd$_{13}$/[Ir-L1], (c) Pt$_{13}$/[Ir-L1].

We calculated the binding energy between the metal clusters and Ir-L1 by taking the difference of the total energies of the separated and the combined systems, using the fully relaxed structures. With a binding energy of -5.76 eV, Ni_{13}/[Ir-L1] is more strongly bound than Pd_{13}/[Ir-L1] (-4.72 eV) and Pt_{13}/[Ir-L1] (-3.39 eV). The binding energy is thus an observable in which the Ni-based system differs noticeably from the Pt- and Pd-based ones. The pronounced binding energy that is observed in all cases also indicates that there is substantial interaction between the metals and Ir-L1. Analyzing the density of states of M_{13}/[Ir-L1] corroborates this finding. If there would be no interaction between the constituents of a system, then the density of states of the combined system would result from summing up the density of states of the separate subsystems. Our calculations, however, show that the DOS of M_{13}/[Ir-L1] can neither quantitatively nor qualitatively be understood from the superposition of the densities of states of M_{13} and Ir-L1. This is discussed in greater detail in the SI (cf. Figure S18), and reassuringly, this observation is not specific to a particular exchange-correlation approximation, as both PBE and ωPBE consistently yield the same trend (cf. SI, Figure S18(a) and S19(a)). One might wonder whether our observation of a pronounced interaction between Ir-L1 and the metal clusters is specific just for the 13-atom clusters. Therefore, we have repeated the analysis for the considerably larger system Ni_{38}/[Ir-L1]. In the SI, we show that also for this larger system, the density of states clearly shows a pronounced electronic interaction between the metal particle and the photosensitizer. We further show (Figure S22) that the highest occupied orbital is delocalized in a qualitatively similar way over Ir-L1 and the metal for both the small and the larger cluster. Thus, the above conclusions are not specific to just small clusters. The potentially most interesting observable in the context of photocatalytic activity is the photoabsorption spectrum. Analogously to the previous reasoning about the density of states, the absorption spectrum of M_{13}/[Ir-L1] would result from the superposition of the individual spectra of Ir-L1 and M_{13} if the interaction between the constituents would be negligible. Figure 6 compares the absorption spectra of M_{13}/[Ir-L1] to those of the individual molecular components, and the superposition of the latter. We applied a Gaussian broadening of 0.08 eV to guide the eye. Panel (a) depicts the data for Ni_{13}/[Ir-L1], panel (b) depicts the data for Pd_{13}/[Ir-L1], and panel (c) depicts the data for Pt_{13}/[Ir-L1]. The superposition, labeled M_{13} + Ir-L1 in Figure 6, is the sum of the individual spectra of M_{13} and Ir-L1. As M_{13}/[Ir-L1] and M_{13} have a spin-polarized ground state (cf. SI, Table S4), the labeling of the excitations in Figure 6 and the following discussion need extra explanation. For the bare Ir-L1 system, an excitation that preserves the spin leads to a singlet state, and we therefore denoted such excitations with S, and the ones in which one spin was flipped were denoted with T. A spin-conserving excitation of, for example, M_{13}/[Ir-L1] does not lead to a singlet state but keeps the magnetic moment that is introduced by the metal particle. Nevertheless, we continue to label spin-conserving excitations with S and spin-flip excitation with T to ease the comparison between the spectrum of the combined system M_{13}/[Ir-L1] and the spectra of the separate constituents. In the SI, we present the details about the spin configurations. In order to put this comparison on a firm footing, we paid attention to two aspects: (i) We calculated the spectrum of M_{13} and Ir-L1 (separately) in the fixed structure as they are in M_{13}/[Ir-L1]

(cf. Figure 5) to avoid spectral differences that are just a consequence of structural differences. (ii) Due to its implicit density dependency, the optimally tuned range-separation parameter ω_{opt} is system-specific and, thus, differs for M_{13}/[Ir-L1], M_{13}, and Ir-L1 (cf. SI, Table S4). To eliminate these exchange-correlation-functional-related differences, we used $\omega_{opt}(M_{13}$/[Ir-L1]) to calculate the absorption spectrum of M_{13} and Ir-L1 in (i). For this reason, the absorption spectra of Ir-L1 shown in Figure 6 differ from each other and the one of Figure 4. The noticeable red shift is mostly due to the smaller range-separation parameter and not geometry-related. Figure 6 clearly shows that the superposition of the absorption spectra of M_{13} and Ir-L1 cannot explain the spectra of the combined systems M_{13}/[Ir-L1] for any of the systems.
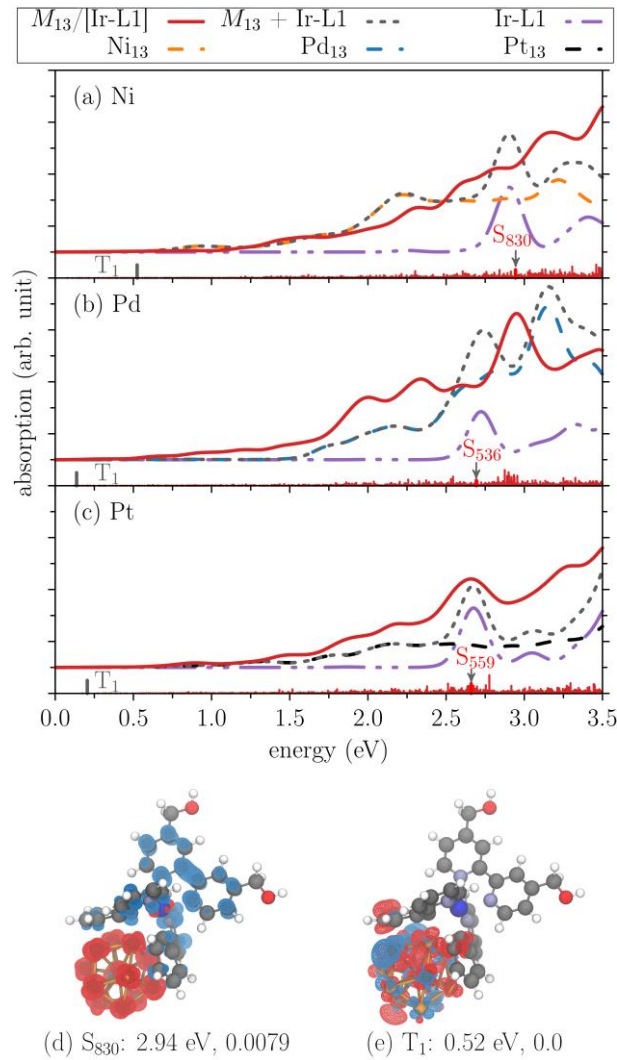

Figure 6. Top: Vis absorption spectrum of M_{13}/[Ir-L1], M_{13}, Ir-L1 and the superposition M_{13} + Ir-L1. The spectra were obtained from TDDFT with ωPBE. Vertical red bars and the single grey bar show the relative oscillator strength and lowest spin-flip excitation for M_{13}/[Ir-L1], respectively. All absorption spectra are shifted vertically by 0.24 arb. unit for easy distinction from the horizontal axis. The spectra depicted in panels (a-c) each use the optimally tuned ω_{opt} of the respective M_{13}/[Ir-L1]. (a) Ni$_{13}$/[Ir-L1] ($\omega_{opt} = 0.14$ bohr^{-1}). (b) Pd$_{13}$/[Ir-L1] ($\omega_{opt} = 0.12$ bohr^{-1}). (c) Pt$_{13}$/[Ir-L1] ($\omega_{opt} = 0.11$ bohr^{-1}). Bottom: Difference densities of selected excitations of Ni$_{13}$/[Ir-L1] with the given energy and oscillator strength (marked in (a)). (d) Difference density of the optical excitation S$_{830}$ shows a metal particle to ligand charge transfer. (e) Difference density of the lowest spin-flip excitation T$_1$, which we denote by T$_1$ in analogy to the previous section.

117

When comparing the spectra of the M_{13}/[Ir-L1] systems to the one of the bare Ir-L1, one notices pronounced differences in all cases: (i) The vis photoabsorption of M_{13}/[Ir-L1] is overall larger than the one of Ir-L1. (ii) When one compares the oscillator strength of the brightest excitation of M_{13}/[Ir-L1] to the oscillator strength of the brightest excitation of Ir-L1, one notices that it decreases by approximately 1 order of magnitude upon addition of the metal. (iii) On the other hand, the number of excited states increases enormously. Figure S23 in the SI shows that this is directly due to the metal clusters. These results clearly show that all three metals influence the photoabsorption process significantly.

In order to analyze the situation further, we computed the difference densities between the most relevant electronic excitations and the ground state. Figures S24-S26 in the SI show these difference densities for the 30 excitations with the highest oscillator strength in the energy range up to 3.2 eV. (We chose the value 3.2 eV as the upper limit, because this is approximately the threshold between vis and UV.) These difference densities reveal that for all three metals, the metal cluster takes on the role of an electron donor and charge is transferred to Ir-L1. The metal particle to ligand charge transfer extends over the whole Ir complex; however, the trend of a long-range charge-transfer $M_{13} \rightarrow$ bpy is also noticeable for all M_{13}/[Ir-L1] (cf. SI, Figure S24, e.g., S_{485}, S_{813}, S_{947} of Ni$_{13}$/[Ir-L1]; Figure S25, S_{356}, S_{649}, S_{747} of Pd$_{13}$/[Ir-L1]; Figure S26, S_{451}, S_{559}, S_{747} of Pt$_{13}$/[Ir-L1]). This long-range charge-transfer character is shown exemplary for S_{830} of Ni$_{13}$/[Ir-L1] in Figure 6(d). S_{830} shows overlap with the main peak of Ir-L1 in Figure 6(a), and the comparison to Figure 4 clearly demonstrates that the addition of the metal cluster changes the excitation mechanism. We found qualitatively similar features for Pd$_{13}$/[Ir-L1] (cf. S_{536}) and Pt$_{13}$/[Ir-L1] (cf. S_{559}). The metal particle to ligand charge-transfer process in the M_{13}/[Ir-L1] systems is particularly pronounced for excitation energies above ~2.3 eV and extends to 3.2 eV and further into the UV. Excitations of similar character can also be found at lower energies but less frequently and with a lower oscillator strength (e.g., S_{245}(Ni$_{13}$/[Ir-L1]): 1.62 eV, 0.003). In summary, our calculated photoabsorption spectra show that all three metals have a pronounced influence on the photoabsorption process and, compared to the bare Ir-L1 system, change the charge-transfer characteristics. We also investigated in how far the interaction between the metal cluster and the Ir-L1 depends on their relative spatial proximity. To this end, we calculated photoabsorption spectra for a series of structures in which we successively increased the distance between the center of mass of the metal cluster and Ir-L1 in steps of a few bohr while keeping other structural features fixed. The metal particles have a noticeable influence on the photoabsorption up to distances that are about 10 bohr larger than the equilibrium distance. This shows that our findings can be expected to hold on more general grounds and are not specific to a particular binding geometry. The calculations also show a qualitative trend that the interaction persists more pronouncedly for the Ni$_{13}$ cluster than for the other metals (Figure S28). Finally, we took a look at the lowest spin-flip excitation of M_{13}/[Ir-L1], in analogy to the analysis of T_1(Ir-L1) in Figure 4. Panel (e) in Figure 6 depicts the difference density for the exemplary case of the lowest spin-flip transition of Ni$_{13}$/[Ir-L1]. In contrast to the situation for the bare Ir-L1 there is little

charge-transfer character in this excitation: the difference density is predominantly localized on the metal cluster (cf. SI, Figure S27).

7.4 Discussion and Conclusion

We have reported the synthesis of a new photocatalytic system in which a heteroleptic Ir(III) photosensitizer has been encapsulated in the pores of MIL-101, which have then been loaded with three different metals. This setup ensures spatial proximity between the photosensitizer and the metals. In comparison to the bare photosensitizer, loading with Pd strongly reduces the hydrogen evolution rate, loading with Pt slightly increases it, and loading with the earth-abundant metal Ni significantly increases the rate by a factor of more than five. Understanding the mechanism behind this effect is challenging because of the difficulty to obtain insight into the processes within the pores in situ. Based on the experimental results, it is difficult to disentangle in how far the effect is directly related to photophysical and photochemical properties and in how far it may depend on other phenomena, e.g., ones of steric nature. In order to take first steps toward an understanding, we have done a detailed theoretical-computational investigation of the photosensitizer in combination with Ni, Pd, and Pt clusters. The calculations show a strong interaction between all of the metals and the photosensitizer. The presence of the metal clusters changes the photoabsorption significantly: Instead of the few excitations with large oscillator strength that characterize the bare photosensitizer, the combination with the metal leads to a very dense excitation spectrum covering a broader range of energies. We have analyzed many of the excitations in detail via difference densities and found that for the combined systems, many of the optically active excitations involve a charge transfer from the metal to the photosensitizer ligands. It is conceivable that this can play a role in the photophysics and chemistry. However, we did not find any substantial, qualitative differences between the combination of the photosensitizer with the three different metals with respect to the electronic excitations. Taking into account the finding that the lowest spin-flip excitation does not have charge-transfer character when the photosensitizer is combined with the metal particles, one might speculate that the photophysical mechanism for the M_{13}/[Ir-L1] systems differs from the one in the bare Ir-L1 sensitizer: In the latter, accessing the triplet state is beneficial, because it leads to a long-lived charge-separated state. In the former, accessing the spin-flipped state may be detrimental, because the excitations in which the spin does not change show charge-transfer character, whereas the spin-flipped state does not. The presence of heavier atoms in the Pt and Pd metal particles may lead to a stronger spin orbit coupling than for the Ni system and thus a higher probability to end up in the spin-flipped and, therefore, unfavorable noncharge separated state. Such a reasoning could explain the larger hydrogen evolution rate of Ni, but of course, other explanations are also possible. For example, it is conceivable that the different hydrogen evolution rates are not directly related to differences in the photophysical properties but have other reasons. Our calculations revealed, for example, that the binding between the Ni cluster and the photosensitizer is much stronger than the binding between the photosensitizer and the Pd and Pt cluster. This may influence the spatial

arrangement of the constituents in the pore and thus also the hydrogen evolution rate. In summary, our work is a proof of concept showing in a combination of experiment and theory that the spatial proximity of metal particles and a photosensitizer leads to significant interaction and potentially interesting effects. Further work will be needed to reach a detailed understanding of the photophysics and chemistry of these complex systems and to further explore the possibilities that such systems offer in practice. The increased hydrogen evolution rates that we observe for the combination of Ni with Ir-L1 are a strong incentive for further studies in this direction.

Acknowledgement

7.5 References

[1]   Goldsmith, J. I.; Hudson, W. R.; Lowry, M. S.; Anderson, T. H.; Bernhard, S.; *J. Am. Chem. Soc.* **2005**, *127*, 7502.

[2]   Tinker, L.; McDaniel, N.; Curtin, P.; Smith, C.; Ireland, M.; Bernhard, S.; *Chem. Eur. J.* **2007**, *13*, 8726.

[3]   Curtin, P. N.; Tinker, L. L.; Burgess, C. M.; Cline, E. D.; Bernhard, S., *Inorg. Chem.* **2009**, *48*, 10498.

[4]   Wu, S. H.; Ling, J. W.; Lai, S. H.; Huang, M. J.; Cheng, C. H.; Chen, I. C.; *J. Chem. Phys. A* **2010**, *114*, 10339.

[5]   Gärtner, F.; Denurra, S.; Losse, S.; Neubauer, A.; Boddien, A.; Gopinathan, A.; Spannenberg, A.; Junge, H.; Lochbrunner, S.; Blug, M.; Hoch, S.; Busse, J.; Gladiali, S.; Beller, M.; *Chem. Eur. J.* **2012**, *18*, 3220.

[6]   Bokarev, S. I.; Bokareva, O. S.; Kühn, O.; *J. Chem. Phys.* **2012**, *136*, 214305.

[7]   Bokarev, S. I.; Hollmann, D.; Pazidis, A.; Neubauer, A.; Radnik, J.; Kühn, O.; Lochbrunner, S.; Junge, H.; Beller, M.; Brückner, A.; *Phys. Chem. Chem. Phys.* **2014**, *16*, 4789.

[8]   Bokareva, O. S.; Möhle, T.; Neubauer, A.; Bokarev, S. I.; Lochbrunner, S.; Kühn, O.; *Inorganics* **2017**, *5*, 23.

[9]   DiLuzio, S.; Mdluli, V.; Connell, T. U.; Lewis, J.; VanBenschoten, V.; Bernhard, S.; *J. Am. Chem. Soc.* **2021**, *143*, 1179.

[10]   Neubauer, A.; Grell, G.; Friedrich, A.; Bokarev, S. I.; Schwarzbach, P.; Gärtner, F.; Surkus, A. E.; Junge, H.; Beller, M.; Kühn, O.; Lochbrunner, S.; *J. Phys. Chem. Lett.* **2014**, *5*, 1355.

[11]   Wilde, A. P.; King, K. A.; Watts, R. J.; *J. Chem. Phys.* **1991**, *95*, 629.

[12]   Savin, A.; *Theor. Comput. Chem.* **1996**, *4*, 327.

[13]   Baer, R.; Neuhauser, D.; *Phys. Rev. Lett.* **2005**, *94*, 043002.

[14]   Gill, P. M. W.; Adamson, R. D.; Pople, J. A.; L; *Mol. Phys.* **1996**, *88*, 1005.

[15]   Iikura, H.; Tsuneda, T.; Yanai, T.; Hirao, K. A; *J. Chem. Phys.* **2001**, *115*, 3540.

[16]   Levy, M.; Perdew, J. P.; Sahni, V.; *Phys. Rev. A: At., Mol., Opt. Phys.* **1984**, *30*, 2745.

[17]   Stein, T.; Kronik, L.; Baer, R.; *J. Am. Chem. Soc.* **2009**, *131*, 2818.

[18]   Autschbach, J.; *ChemPhysChem* **2009**, *10*, 1757.

[19]   Baer, R.; Livshits, E.; Salzner, U.; *Annu. Rev. Phys. Chem.* **2010**, *61*, 85.

[20]   Kronik, L.; Stein, T.; Refaely-Abramson, S.; Baer, R.; *J. Chem. Theory Comput.* **2012**, *8*, 1515.

[21]   Zheng, Z.; Phillips, H.; Geva, E.; Dunietz, B. D.; *J. Am. Chem. Soc.* **2012**, *134*, 6944.

[22]   Zheng, Z.; Geva, E.; Dunietz, B. D.; *J. Chem. Theory Comput.* **2013**, *9*, 1125.

[23]   Phillips, H.; Zheng, Z.; Geva, E.; Dunietz, B. D.; *Org. Electron.* **2014**, *15*, 1509.

[24]   Karolewski, A.; Stein, T.; Baer, R.; Kümmel, S.; *J. Chem. Phys.* **2011**, *134*, 151101.

[25]   Bokarev, S. I.; Bokareva, O. S.; Kühn, O.; *Coord. Chem. Rev.* **2015**, *304-305*, 133.

[26]   De Queiroz, T. B.; Kümmel, S.; *J. Chem. Phys.* **2015**, *143*, 034101.

[27]   Kümmel, S.; *Adv. Energy Mater.* **2017**, *7*, 1700440.

[28]   Férey, G.; Mellot-Draznieks, C.; Serre, C.; Millange, F.; Dutour, J.; Surblé, S.; Margiolaki, I.; *Science* **2005**, *309*, 2040.

[29]   Vimont, A.; Goupil, J. M.; Lavalley, J. C.; Daturi, M.; Surblé, S.; Serre, C.; Millange, F.; Férey, G.; Audebrand, N.; *J. Am. Chem. Soc.* **2006**, *128*, 3218.

[30]   Vimont, A.; Leclerc, H.; Maugé, F.; Daturi, M.; Lavalley, J. C.; Surblé, S.; Serre, C.; Férey, G.; *J. Phys. Chem. C* **2007**, *111*, 383.

[31]   Wickenheisser, M.; Jeremias, F.; Henninger, S. K.; Janiak, C.; *Inorg. Chim. Acta.* **2013**, *407*, 145.

[32]   Saha, B. B.; El-Sharkawy, I. I.; Miyazaki, T.; Koyama, S.; Henninger, S. K.; Herbst, A.; Janiak, C.; *Energy* **2015**, *79*, 363.

[33]   Condie, A. G.; Gonzalez-Gomez, J. C.; Stephenson, C. R. J.; *J. Am. Chem. Soc.* **2010**, *132*, 1464.

[34]   Wittmann, T.; Mondal, A.; Tschense, C. B.; Wittmann, J. J.; Klimm, O.; Siegel, R.; Corzilius, B.; Weber, B.; Kaupp, M.; Senker, J.; *J. Am. Chem. Soc.* **2018**, *140*, 2135.

[35]   Casida, M. E.; *Recent Advances in Density Functional Methods* **1995**, *1*, 155.

[36]   Casida, M. E.; J. *Chem. Phys.* **2005**, *122*, 054111.

[37]   Hermannsdörfer, J.; Friedrich, M.; Miyajima, N.; Albuquerque, R. Q.; Kümmel, S.; Kempe, R.; *Angew. Chem., Int. Ed.* **2012**, *51*, 11473.

[38]   Nava, P.; Sierka, M.; Ahlrichs, R.; *Phys. Chem. Chem. Phys.* **2003**, *5*, 3372.

[39]   Aprà, E.; Fortunelli, A.; *J. Phys. Chem. A* **2003**, *107*, 2934.

[40]   Wang, L. L.; Johnson, D. D.; *Phys. Rev. B Condens. Matter Mater. Phys.* **2007**, *75*, 235405.

[41]   Piotrowski, M. J.; Piquini, P.; Da Silva, J. L.; *Phys. Rev. B Condens. Matter Mater. Phys.* **2010**, *81*, 155446.

[42]   Köster, A. M.; Calaminici, P.; Orgaz, E.; Roy, D. R.; Reveles, J. U.; Khanna, S. N.; *J. Am. Chem. Soc.* **2011**, *133*, 12192.

[43]   Chaves, A. S.; Rondina, G. G.; Piotrowski, M. J.; Tereshchuk, P.; Da Silva, J. L.*; J. Phys. Chem. A* **2014**, *118*, 10813.

[44]   Leppert, L.; Kempe, R.; Kümmel, S.; *Phys. Chem. Chem. Phys.* **2015**, *17*, 26140.

[45]   Piotrowski, M. J.; Ungureanu, C. G.; Tereshchuk, P.; Batista, K. E.; Chaves, A. S.; Guedes-Sobrinho, D.; Da Silva, J. L.; *J. Phys. Chem. C* **2016**, *120*, 28844.

[46]   Chaves, A. S.; Piotrowski, M. J.; Da Silva, J. L.; *Phys. Chem. Chem. Phys.* **2017**, *19*, 15484.

[47]   Van Den Bossche, M.; *J. Phys. Chem. A* **2019**, *123*, 3038.

[48]   Nosé, S. A; *J. Chem. Phys.* **1984**, *81*, 511.

[49]   Hoover,W. G.; *Phys. Rev. A: At., Mol., Opt. Phys.* **1985**, *31*, 1695.

[50]   Schmidt, T.; Kümmel, S.; *Computation* **2016**, *4*, 33.

[51]   Tilgner, D.; Klarner, M.; Hammon, S.; Friedrich, M.; Verch, A.; de Jonge, N.; Kümmel, S.; Kempe, R.; *Aust. J. Chem.* **2019**, *72*, 842.

[52]   Klarner, M.; Hammon, S.; Feulner, S.; Kümmel, S.; Kador, L.; Kempe, R.; *ChemCatChem* **2020**, *12*, 4593.

[53]   Perdew, J. P.; Burke, K.; Ernzerhof, M.; *Phys. Rev. Lett.* **1996**, *77*, 3865.

[54]   Perdew, J. P.; Burke, K.; Ernzerhof, M.; *Phys. Rev. Lett.* **1997**, *78*, 1396.

[55]   Rohrdanz, M. A.; Herbert, J. M.; *J. Chem. Phys.* **2008**, *129*, 034107.

[56]   Henderson, T. M.; Janesko, B. G.; Scuseria, G. E.; *J. Chem. Phys.* **2008**, *128*, 194105.

[57]   TURBOMOLE V7.4 2019, a development of University of Karlsruhe and Forschungszentrum Karlsruhe GmbH,1989-2007, TURBOMOLE GmbH, since 2007; available from http://www.turbomole.org.

[58]   Shao, Y.; Gan, Z.; Epifanovsky, E.; Gilbert, A. T.; Wormit, M.; Kussmann, J.; Lange, A. W.; Behn, A.; Deng, J.; Feng, X. et al. *Mol. Phys.* **2015**, *113*, 184.

[59]   Schäfer, A.; Horn, H.; Ahlrichs, R.; *J. Chem. Phys.* **1992**, *97*, 2571.

[60]   Grimme, S.; *J. Comput. Chem.* **2004**, *25*, 1463.

[61]   Weigend, F.; Ahlrichs, R.; *Phys. Chem. Chem. Phys.* **2005**, *7*, 3297.

7.6 Supporting Information

7.6.1 Synthesis and Hydrogen Evolution

General Methods

All chemicals and solvents were purchased commercially from chemical suppliers with purity over 95 % and used without further purification. All manipulations including air or moisture sensitive compounds were carried out under dry and oxygen-free argon atmosphere (Schlenk techniques) or in a nitrogen-filled glovebox (mBraun 120) with a high-capacity recirculator (below 0.1 ppm of oxygen and water).

Reduction of precursor compounds were carried out with Parr Instrument stainless steel autoclaves N-MT5 300 mL equipped with heating mantles and temperature controller. Solvothermal syntheses were performed in a muffle furnace (Nabertherm) with programmable temperature ramps. Inductively coupled plasma optical emission spectroscopy (ICP-OES) was carried out according to standard protocol digestion (4 mL HNO_3/HCl 3:1, microwave irradiation, 25 min, 195 °C) with a Vista-Pro radial (Varian). Elemental analyses were performed by using an Elementar Vario EL III. NMR spectra were measured using a Bruker Avance III HD 500 MHz spectrometer. Chemical shifts are reported in ppm relative to the deuterated solvent. ^{13}C MAS spectra were acquired on a Bruker Avance III HD spectrometer (9.4 Tesla) using a 1.9 mm triple resonance probe and a spinning speed of 40 kHz or 12.5 kHz. A Hahn-echo pulse sequence with an interpulse distance of 25 µs and 80 µs (one rotor period) was applied for background suppression, respectively. Due to fast spinning hetero-nuclear proton broadband decoupling did not have an influence on the spectral resolution and was thus omitted. The 90° pulse length and recycle delay were set to 2.0 µs and 50 ms, respectively. The average temperature in the rotor at v_{rot} = 40 kHz was determined to 325 K by referencing with $Pb(NO_3)$. The spin-lattice relaxation times T_1 were obtained with the inversion recovery method with a recycle delay of 0.3 s and time increments ranging from 0.5 to 256 ms. The ^{13}C-^{1}H REDOR-type recoupling experiments were performed with two 180° pulses on the ^{1}H channel at the centre of each of the two rotation periods (τ_{deph} = 50 µs) while a 180° pulse was applied on the ^{13}C at the centre of the two rotation periods. ^{1}H and ^{13}C 180° pulse lengths are 2.8 and 4 µs, respectively. Fourier transform infrared (FT-IR) spectroscopy measurements were performed with a JASCO FT IR 6100 spectrometer in the range 4000 cm^{-1} to 700 cm^{-1} with a resolution of 4 cm^{-1} an a N_2 flow. Gas mixtures were analyzed using a 6890N gas chromatograph (Agilent Technologies) equipped with an Agilent special Plot + Molsieve capillary column (30.0 m x 0.32 mm x 0.25 µm). Methane was used as internal standard. Nitrogen physisorption isotherms were determined at -196 °C using a Nova 2000e (Quantachrome) apparatus. Specific surface areas were calculated by using p/p$_0$-values from 0.05-0.3 by the BET model. Specific total pore volumes were determined by DFT calculations (N_2 at -196 °C on silica (cylindric pore, NLDFT equilibrium model)). Transmission electron microscopy (TEM) measurements were carried out using a LEO 922O microscope (Zeiss, 200 kV). The samples were suspended in chloroform and sonicated for 5 min. 2 µL

of the suspension were placed on a CF200-Cu-grid or a LC200-Cu-grid (Electron Microscopy Sciences) and allowed to dry. High-angle annular dark-field scanning transmission electron microscopy (HAADF-STEM) measurements were performed using a ARM200F (JEOL, 200 kV) equipped with aspherical aberration corrector (CEOS) and an energy-dispersed X-ray analysis (EDX) system (JEOL). Diffuse reflectance ultraviolet-visible spectra were measured using a CARY 300 (Agilent Technologies) with an Ulbricht sphere in the range 400 nm to 750 nm. UV-vis spectra were measured on a CARY 60 (Agilent Technologies). Fluorescence spectra in the were recorded on a JASCO FP8300 spectrofluorometer with an excitation wavelength of 420 nm. Excitation and emission bandwidth were set to 10 nm, response time to 0.1 s and the scan speed to 200 nm/min. Cyclic voltametric measurements were carried out in solution under moisture and oxygen-free conditions using a three-electrode assembly connected to a potentiostat (Model 263A, EG&G Princeton Applied Research) at a scanning rate of $100 \ mV \cdot s^{-1}$. A solution of tetra-*n*-butylammonium hexafluorophosphate in acetonitrile with a concentration of 0.1 M was used as the electrolyte solution. As working electrode, a platinum disk electrode in the respective solution of iridium complex dissolved in acetonitrile was used. A platinum wire in the electrolyte solution and $Ag/AgNO_3$ in acetonitrile (0.1 M) were used as counter and reference electrodes, respectively. Each measurement was calibrated by the internal standard ferrocene/ferrocenium. X-ray crystal structure analysis was performed with a STOE STADIVARI $[(\lambda(Mo\text{-}K_\alpha) = 0.71073 \ Å]$ equipped with an Oxford Cryostream low temperature unit. Structure solution and refinement were achieved with SIR97[S1], SHELXL-2014[S2] and WinGX.[S3] The structure was visualized using Mercury 4.1.3.[S4] Powder X-ray powder diffraction (PXRD) analysis in the range of 2-80 °2θ was performed using a STOE STADI-P diffractometer (CuK_α radiation, 1.54178 Å) in θ-2θ geometry with a position sensitive detector. The samples were sealed in glass capillaries (mark-tubes, Hilgenberg, No. 10, diameter 0.7mm) in inert atmosphere. Time-resolved photoluminescence studies were carried out with a fluorescence lifetime imaging microscope (FLIM) MicroTime200 (Pico Quant). It is equipped with a picosecond diode laser (405 nm) with adjustable output power (set to 0.5 μW), a dichroic filter 405rdc-UF3 and a longpass filter 561 nm. The optical core is an inverted microscope IX 73 (Olympus) with a confocal unit and a piezo stage for z stacks. The data were recorded with a water immersion objective (60×, NA 1.2.). A single-photon counting APD module (SPAD) is used. Data acquisition is based on time-correlated single photon counting (TCSPC) performed by a TimeHarp 260 Pico board (Pico Quant). Samples are prepared by spin coating thin films of powder material dispersed in a polystyrene (M_w 200k g/mol) matrix on cover slips (Ø 18 mm). 2 mg of the sample are suspended in a degassed polystyrene / toluene solution (300 μL, 200 mg/mL). Spin coating is performed at 1500 rpm for 90 s under inert gas atmosphere.

Material Synthesis

Dimethyl(2,2'-bipyridine)-4,4'-dicarboxylate

4,4'-Dicarboxy-2,2'-bipyridine (488 mg, 2 mmol) was suspended in methanol (80 mL) and 20 drops of 96 % H_2SO_4 were added. After refluxing for 20 h, the reaction mixture was poured into 100 mL of water and the pH was carefully adjusted to pH 8 using a NaOH solution. Afterwards the mixture was extracted three times with 100 mL DCM and the combined organic layers were dried over $NaSO_4$. The solvent was evaporated to yield a white, crystalline solid.
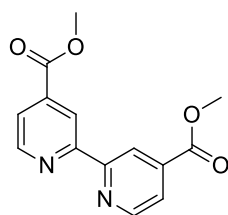
FW ($C_{14}H_{12}N_2O_4$) = 272.26 g mol^{-1}

Yield 467 mg (1.72 mmol, 86%)

^{1}H-NMR (CDCl$_3$, 500 MHz) δ = 8.96 (s, 2H, pyr-3-CH), 8.87 (d, 2H, pyr-6-CH, J = 4.90 Hz), 7.90 (dd, 2H, pyr-5-CH, J = 4.90 Hz), 4.00 (s, 6H, O-CH$_3$) ppm.

2,2'-Bipyridine-4,4'-dimethanol: **L1**

Dimethyl(2,2'-bipyridine)-4,4'-dicarboxylate (467 mg, 1.72 mmol, 1 eq) was dissolved in 2 mL methanol and 50 mL DCM and NaBH$_4$ (519 mg, 13.7 mmol, 8 eq) was added. The reaction was heated to reflux for 20 h. Another portion of NaBH$_4$ (519 mg, 13.7 mmol, 8 eq) was added and the solution was heated to reflux for another 20 h. Afterward, the solvent was removed, and the residue dissolved in 100 mL of water. This solution was extracted three times with 100 mL of ethyl acetate. The combined organic layers were dried over $NaSO_4$ and the solvent removed to obtain the white, crystalline ligand **L1**.
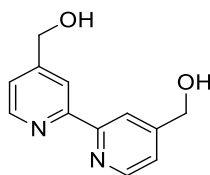
FW ($C_{12}H_{12}N_2O_2$) = 216.24 g mol^{-1}

Yield 263 mg (1.22 mmol, 71%)

^{1}H-NMR (Methanol-d$_4$, 500 MHz) δ = 8.58 (d, 2H, pyr-6-CH, J = 5.05 Hz), 8.26 (s, 2H, pyr-3-CH), 7.43 (d, 2H, pyr-5-CH, J = 5.05 Hz), 4.74 (s, 4H; CH$_2$) ppm.

^{13}C-NMR (Methanol-d$_4$, 125 MHz) δ = 157.34, 154.45, 150.30, 122.82, 120.31, 63.74 ppm.

[(μ-Chloro)(di-2-phenylpyridine)iridium(III)]-dimer

IrCl₃ x H₂O (256 mg, 0.81 mmol, 1 eq) was dissolved in 3 mL H₂O and 18 mL 2-ethoxyethanol and subsequently degassed by bubbling argon through the solution. After addition of 2-phenylpyridine (255 µL, 1.78 mmol, 2.2 eq, ppy) the reaction was heated to reflux for 20 h under inert atmosphere, whereby a yellow solid precipitated. After cooling, the mixture was washed twice with 20 mL diethyl ether. The yellow precipitate was filtrated off and washed another time with diethyl ether. The solid was dried under vacuum.
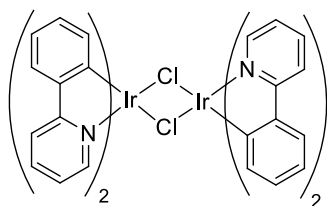
FW ($C_{44}H_{32}Cl_2N_4Ir_2$) = 1072.10 g mol^{-1}

Yield 327 mg (0.43 mmol, 53 %)

^{1}H-NMR (CDCl₃, 500 MHz) δ = 9.25 (d, 4H J = 5.82 Hz), 7.88 (d, 4H, J = 8.09 Hz), 7.74 (t, 4H, J = 7.70 Hz), 7.49 (d, 4H, J = 7.72 Hz), 6.76 (q, 8H, J = 7.61 Hz), 6.57 (t, 4H, J = 7.49 Hz), 5.94 (d, 4H, J = 7.72 Hz) ppm.

^{13}C-NMR (CDCl₃, 125 MHz) δ = 168.53, 151.67, 145.33, 143.68, 136.13, 130.56, 129.08, 123.63, 122.09, 121.29, 118.36 ppm.

2,2'-Bipyridine-4,4'-(di-*tert*-butyl)bis(2-phenylpyridine)iridium(III)hexafluorophosphate[S5]: **Ir-L2**

[(μ-Cl)(ppy)₂Ir(III)]₂ (100 mg, 0.093 mmol, 1 eq) was dissolved in 1 mL H₂O and 3 mL 2-ethoxyethanol. 4,4'-di-*tert*-butyl-2,2'-bipyridine (50 mg, 0.186 mmol, 2 eq, dtbbpy) was added and the reaction mixture was refluxed for 20 h. After cooling to room temperature, the solution was poured on an aqueous solution of ammonium hexafluorophosphate (1 g, 6.13 mmol, in 10 mL H₂O). The precipitating solid was filtered off, washed with H₂O, and dried under vacuum, yielding a yellow-orange powder denoted as [(dtbbpy)(ppy)₂IrPF₆].
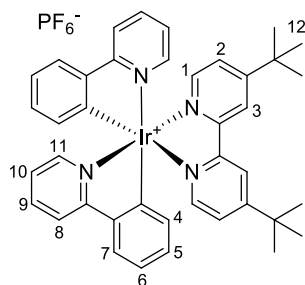
FW ($C_{40}H_{40}F_6IrN_4P$) = 913.95 g mol^{-1}

Yield 146 mg (0.160 mmol, 86 %)

^{1}H-NMR (Methanol-d₄, 500 MHz) δ = 8.9 (d, 2H, CH-1, J = 4.83 Hz), 8.28 (dd, 2H, CH-11, J = 8.33, 1.42 Hz), 8.04 (d, 2H, CH-2, J = 4.83 Hz), 7.98 (dt, 2H, CH-10, J = 8.44, 0.7 Hz), 7.92 (dd, 2H, CH-5, J = 8.0, 1.1 Hz), 7.83 (d, 2H, CH-7, J = 4.43 Hz), 7.74 (dd, 2H, CH-2, J = 4.83 Hz), 7.15 (dt, 2H, CH-9, J = 8.44, 0.7 Hz), 7.06 (dt, 2H, CH-4, J = 5.0, 1.4 Hz), 6.99 (dt, 2H, CH-6, J = 8.0, 1.4 Hz), 6.37 (dd, 2H, CH-8, J = 7.7, 1.0 Hz), 1.44 (s, 18H, CH3-12) ppm.

^{13}C-NMR (Methanol-d₄, 125 MHz) δ = 168.2, 164.6, 155.9, 150.8, 149.3, 144.3, 139.0, 131.9, 130.5, 125.5, 124.9, 123.7, 122.9, 122.6, 120.0, 35.8, 29.9 ppm.

<u>(2,2'-Bipyridine-4,4'-dimethanol)bis(2-phenylpyridine)iridium(III)hexafluorophosphate: **Ir-L1**</u>

[(μ-Cl)(ppy)$_2$Ir(III)]$_2$ (100 mg, 0.093 mmol, 1 eq) was dissolved in 1 mL H$_2$O and 3 mL 2-ethoxyethanol. 2,2'-Bipyridine-4,4'-diyldimethanol (40.2 mg, 0.186 mmol, 2 eq) was added and the reaction mixture was refluxed for 20 h. After cooling to room temperature, the solution was poured an aqueous solution of ammonium hexafluorophosphate (1 g, 6.13 mmol, in 10 mL H$_2$O). The precipitating solid Ir-L1 was filtered off, washed with H$_2$O, and dried under vacuum, yielding a yellow-orange powder. Suitable crystals for single crystal X-Ray analysis were yielded by vapor phase diffusion technique, using acetone and ether as solvents.

FW (C$_{34}$H$_{28}$F$_6$IrN$_4$O$_2$P + C$_3$H$_6$O) = 861.81 g mol^{-1} (+ 58.08 g mol^{-1})

Elemental analysis C 48.31, H 3.73 N 6.09; found: C 48.20, H 3.61, N 6.06 %.

Yield 141 mg (0.164 mmol, 88 %)
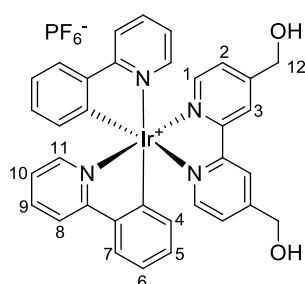
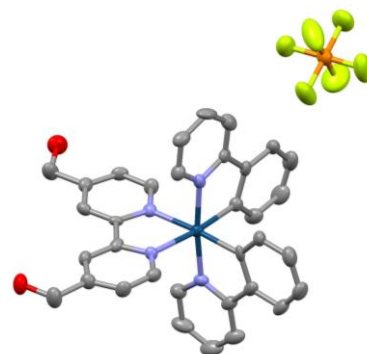**^{1}H-NMR** (Methanol-d$_4$, 500 MHz) δ = 8.61 (d, 2H, CH-1, J = 4.83 Hz), 7.82 (dd, 2H, CH-11, J = 8.33, 1.42 Hz), 7.77 (d, 2H, CH-2, J = 4.83 Hz), 7.73 (dt, 2H, CH-10, J = 8.44, 0.7 Hz), 7.67 (dd, 2H, CH-5, J = 8.0, 1.1 Hz), 7.61 (d, 2H, CH-7, J = 4.43 Hz), 7.47 (dd, 2H, CH-2, J = 4.83 Hz), 7.28 (dt, 2H, CH-9, J = 8.44, 0.7 Hz), 6.97 (dt, 2H, CH-4, J = 5.0, 1.4 Hz), 6.85 (dt, 2H, CH-6, J = 8.0, 1.4 Hz), 6.24 (dd, 2H, CH-8, J = 7.7, 1.0 Hz), 4.84 (s, 4H, CH$_2$-12) ppm.

^{13}C-NMR (Methanol-d$_4$, 125 MHz) δ = 168.2, 164.6, 155.9, 150.8, 149.3, 144.3, 139.0, 131.9, 130.5, 125.5, 124.9, 123.7, 122.9, 122.6, 120.0, 65.9 ppm.

<u>Crystallographic Data of</u>

<u>(2,2'-Bipyridine-4,4'-dimethanol)bis(2-phenylpyridine)iridium(III)hexafluorophosphate</u>

Crystals suitable for X-ray analysis were grown from a saturated solution of the compound in acetone.

Compound	Ir-L1 (t632apma)	Deposition Number: 2083161
Formula	C$_{34}$H$_{28}$F$_6$IrN$_4$O$_2$P + C$_3$H$_6$O	
Formula weight	919.85	
Crystal system	triclinic	
Space group	P-1	
a / Å	9.5070(4)	
b / Å	14.0350(6)	
c / Å	14.2210(6)	
α / °	67.234(3)	
β / °	82.061(3)	
γ / °	89.857(3)	
Cell volume / Å^3	1730.22(13)	
Z	2	
Crystal size / mm^3	0.18*0.17*0.14	
Habit	block	
Color	yellow	
Density / gcm^{-1}	1.766	
T / K	133	
Theta range	1.57-26.665	
Unique reflections	6935	
Observed reflections [I>2s(I)]	6071	
Parameters	474	
wR2 all data	0.0639	
R [I>2s(I)]	0.0264	

Synthesis of MIL-101

Chromium(III)nitrate nonahydrate (800 mg, 2 mmol) and terephthalic acid (332 mg, 2 mmol) were dissolved in a 0.05 M tetramethylammonium hydroxide solution (10 mL). The mixture was sealed in a 23 mL containing, Teflon-lined hydrothermal autoclave. The autoclave was heated to 180 °C (heating rate: 2.6 °C min^{-1}), the temperature was kept for 24 h and slowly cooled down to 30 °C within 12 hours (cooling rate: 0.2 °C min^{-1}). Excessively crystallized terephthalic acid was removed by filtration over a pore 3 filter. The green slurry was again filtered using a fine pore paper filter. MIL-101 was dried under vacuum (10^{-4} mbar, 85 °C, 24 h).

Generation of coordinatively unsaturated sites in MIL-101 (CUS@MIL-101)[S6]

400 mg of MIL-101 were stirred at 150 °C and dynamic vacuum (10^{-4} mbar) for 12 hours. The resulting material denoted as CUS@MIL-101 was handled under exclusion of water and oxygen.

Grafting of (2,2'-Bipyridine)-4,4'-diyldimethanol: **L1@MIL-101**

2,2'-Bipyridine-4,4'-dimethanol (21.6 mg, 0.1 mmol) was dissolved in 8 mL of dry methyl *tert*-butyl ether. This solution was added to CUS@MIL-101 (400 mg,) under inert atmosphere and stirred at reflux for 20 h. The solid was filtered off, washed with methyl *tert*-butyl ether, and dried under vacuum. The material is denoted as L1@MIL-101.

Synthesis of **[Ir-L1]@MIL-101**

L1@MIL-101 (400 mg) was suspended in 8 mL 1,2-dichloroethane and [(μ-Cl)(ppy)$_2$Ir(III)]$_2$ (53.6 mg, 0.05 mmol) was added. The suspension was heated to reflux temperature and stirred for 48 h. The resulting [Ir-L1-Cl]@MIL-101 was filtered off using a small-pore paper filter and dried under vacuum. The material was added to a solution of ammonium hexafluorophosphate (1 g, 6.13 mmol, in 10 mL H$_2$O) and stirred for 10 minutes at room temperature. The solid [Ir-L1-PF6]@MIL-101 (abbreviated as [Ir-L1]@MIL-101) was filtered off using a small-pored paper filter and dried in vacuum.

Synthesis of **Ni/[Ir-L1]@MIL-101**[S7]

100 mg dry [Ir-L1]@MIL-101 were placed in a two-chamber-tube with [Ni(Cp)$_2$] bis(cyclopentadienyl)nickel(II) (16.6 mg, 0.088 mmol, 5 wt.%) separated by a glass frit. The gas phase infiltration of the Ni precursor occurred at room temperature (25 °C) in static vacuum (10^{-4} mbar) for 20 h. The reduction of the Ni precursor was performed under hydrogen atmosphere (10 bar H$_2$) at 90 °C for 20 h in a Parr Instruments steel autoclave. The resulting Ni/[Ir-L1]@MIL-101 was evacuated (10^{-4} mbar, 85 °C, 20 h) to remove former metal ligand residue.

<u>Synthesis of **Pd/[Ir-L1]@MIL-101**[S7]</u>

100 mg dry [Ir-L1]@MIL-101 were placed in a two-chamber-tube with [(Cp)Pd(allyl)] allyl(cyclopentadienyl)palladium(II) (10.2 mg, 0.048 mmol, 5 wt.%) separated by a glass frit. The gas phase infiltration of the Pd precursor occurred at 32 °C in dynamic vacuum (10^{-4} mbar) for 24 h. The reduction of the Pd precursor was performed at 70 bar H_2 and 70 °C for 24 h. The resulting Pd/[Ir-L1]@MIL-101 was evacuated (10^{-4} mbar, 85 °C, 20 h) to remove former metal ligand residue.

<u>Synthesis of **Pt/[Ir-L1]@MIL-101**[S8]</u>

100 mg dry [Ir-L1]@MIL-101 were placed in a two-chamber-tube with [(Me)$_3$Pt(Cp')] trimethyl(methylcyclopentadienyl)platinum(IV) (8.2 mg, 0.026 mmol, 5 wt.%) separated by a glass frit. The gas phase infiltration of the Pt precursor occurred at 37 °C in static vacuum (10^{-4} mbar) for 20 h. The reduction of the Pt precursor was performed at 50 bar H_2 and 80 °C for 24 h. The resulting Pt/[Ir-L1]@MIL-101 was evacuated (10^{-4} mbar, 85 °C, 20 h) to remove former metal ligand residue.

General Procedure for Photocatalytic Experiments

In a typical experiment, M/[Ir-L1]@MIL-101 (x mg, 2 μmol Ir, ideally 5 wt.% Ir) catalyst was placed in a 10 mL Schlenk tube and sealed with a rubber septum and flushed with argon after evacuation. Then, degassed THF (1000 μL), degassed H_2O (100 μL, 5.55 mmol) and triethylamine (100 μL, 0.72 mmol) were added to the vial. To analyze the reaction headspace by gas chromatography, methane (500 μL) was injected as internal standard. The Schlenk tube was illuminated by a 50 W blue LED (470 nm, distance 2 cm, ~15000 lx). The reaction temperature was regulated by fans to 27 °C. The amount of H_2 evolved was determined by analyzing 500 μL of the reaction headspace by GC-TDC.

Recyclability of the embedded photosensitizer [Ir-L1]@MIL-101

Reactions conditions: N-phenyl-1,2,3,4-tetrahydroisoquinoline + nitromethane

                                        2 mol% [Ir-L1]@MIL-101

                                        0.025 mmol (5.2 mg) N-Phenyl-1,2,3,4-Tetryhydroisoquinolin

                                        18.6 mmol (1 ml) CH_3NO_2

                                        in 10 ml Schlenk tube + O_2 balloon

                                        50 W blue LED (470 nm) at room temperature for 30 min

Yield: reaction mixture was centrifuged (7000 rpm, 7 min)

                                        nitromethane was removed from solution in vacuum,

                                        50 μl MeCN were added

                                        residue was dissolved in $CDCl_3$ and turnover was determined by ¹H NMR

Recyclability: catalyst was washed with nitromethane twice and once with dry THF

                                        solvents were removed in vacuum
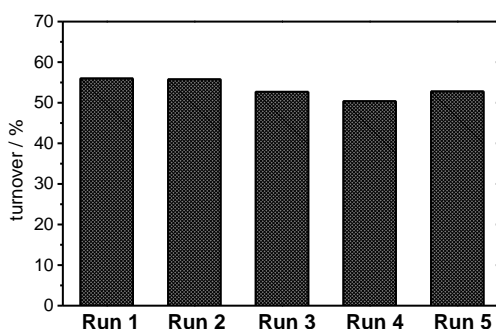
Figure S1. Recyclability demonstration for the [Ir-L1]@MIL-101 system.

Computational Details

DFT calculations were performed using ORCA2.9.1.[S9] Large TZVP basis sets were used throughout.[S10] A truncated trinuclear chromium(III) cluster was chosen as a model of the extended structure of MIL-101; ligand L1 was added to hemi- and fully hydrated SBU^{DFT}, to receive optimized hybrids L1@SBU^{DFT} and L1@SBU^{DFT} (hyd.). The structures of the (ligand modified) chromium(III) clusters were optimized with the generalized gradient approximation functional BP86[S11]; numerical frequency calculations were performed in order to extract the IR spectra of the received minima and to prove the optimized structures to be stationary points; it is noted that an (apparent) imaginary mode was detected at very low frequency in SBU^{DFT}, owing to a skeleton torsion. Dispersion contributions were approximated using Grimme's DFT-D3 atom pairwise dispersion corrections of the parent BP86 functional.[S12] Solvent effects were accounted for in a dielectric continuum approach (COSMO), parametrized for MeCN.[S13] The dielectric solvent cage was included, in order to suppress artificial bond contraction due to uncompensated Coulomb attraction between anions and cations.

7.6.2 Material Characterization

Complex Characterization of Ir-L1
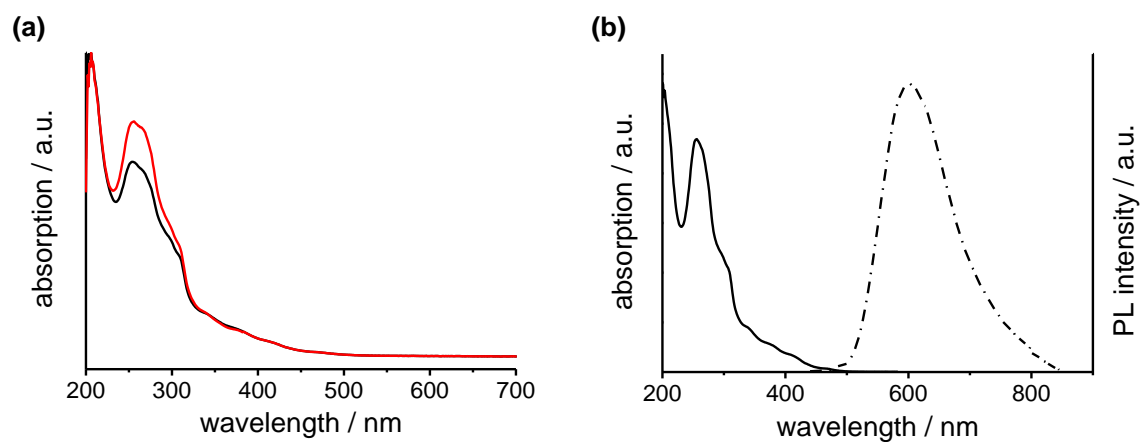
(a)

(b)

Figure S2. (a) UV-vis absorption spectra of Ir-L1 (black) compared to Ir-L2 (red) in the range of 200-700 nm. (b) Absorption and photoluminescence emission (excitation 420 nm) of Ir-L1.
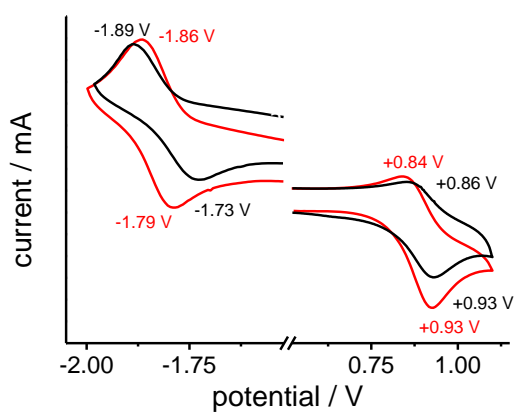

Figure S3. Cyclic voltammogram of Ir-L1 (black) compared to Ir-L2 (red).
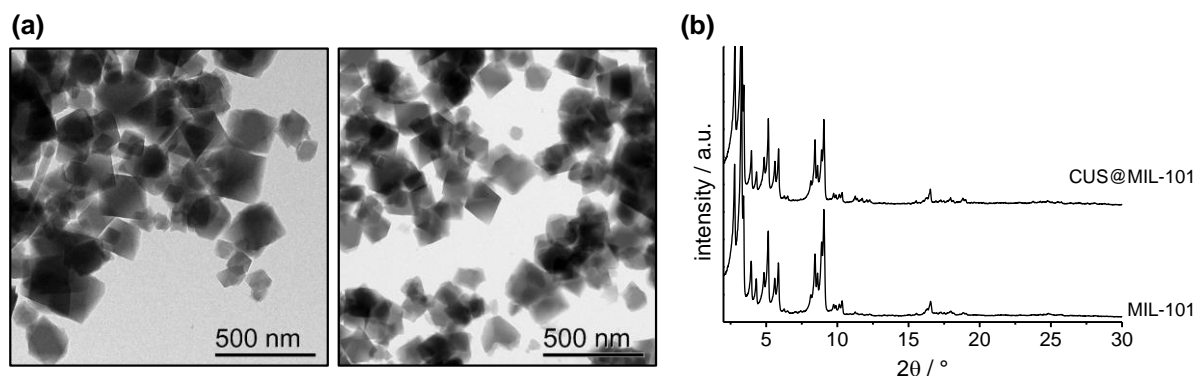
Catalyst Characterization of M/[Ir-L1]@MIL-101

(a)

(b)

Figure S4. (a) TEM images of as-synthesized MIL-101 (left) and after the successful generation of CUS@MIL-101 at 150 °C in vacuum for 12 hours, showing the same morphology. (b) Powder XRD patterns of MIL-101 and CUS@MIL-101. No changes in crystallinity due to generation of CUS were observed.

(a)

(b)
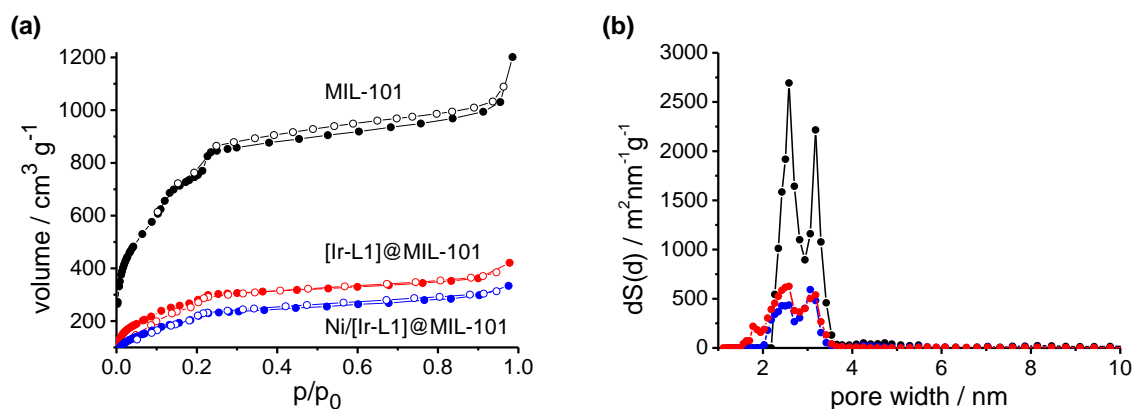
Figure S5. (a) N_2-physisorption isotherms of MIL-101 (2750 m^2/g), [Ir-L1]@MIL-101 (1000 m^2/g) and Ni/[Ir-L1]@MIL-101 (750 m^2/g) with respective surface areas determined by BET-model (0.05-0.3 p/p$_0$). Adsorption is depicted in filled dots, desorption in rings. (b) Pore size distribution of MIL-101 compared to [Ir-L1]@MIL-101 and Ni/[Ir-L1]@MIL-101.
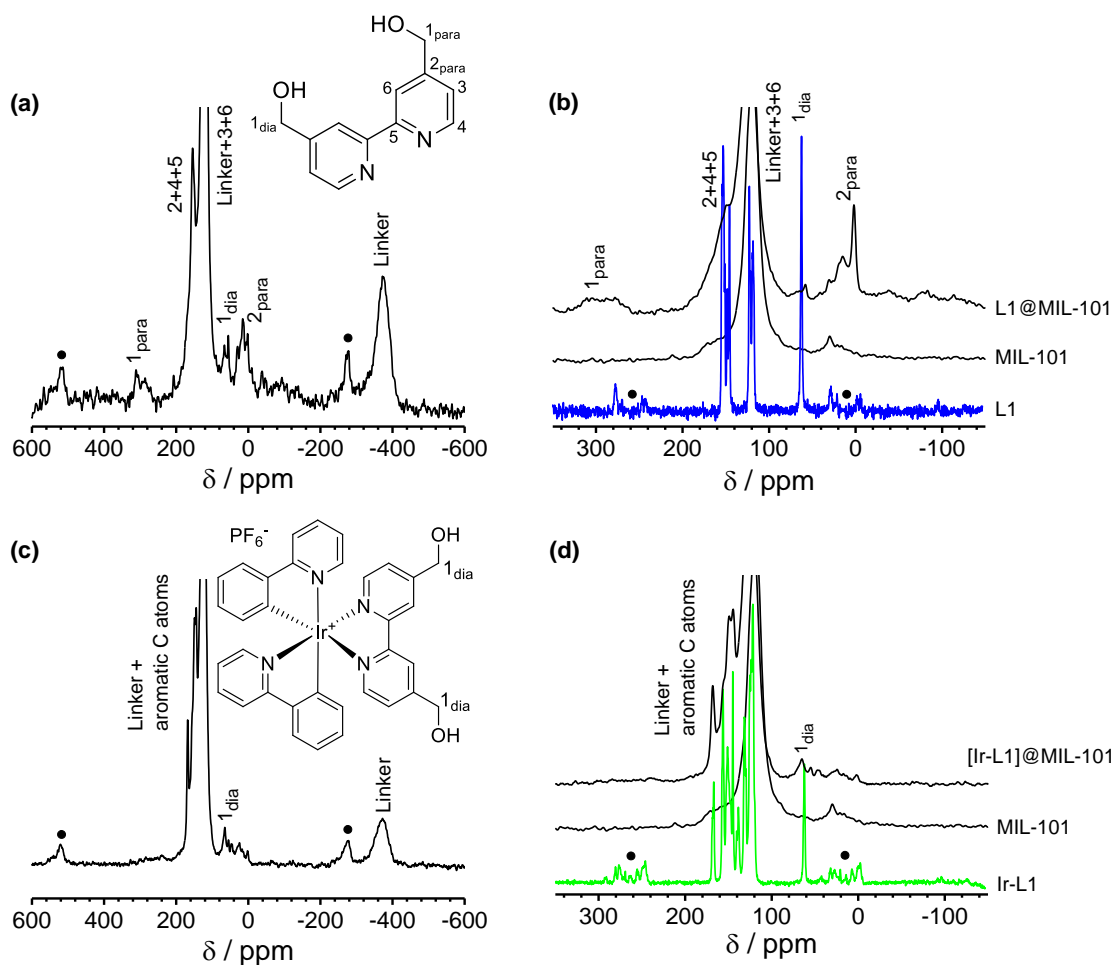
Figure S6. ^{13}C MAS NMR spectra monitoring the L1 grafting and the Ir-L1 complex formation including assignments; spinning side bands are marked with a dot (12.5 kHz or 40 kHz); signals assigned to the terephthalic acid of MIL-101 are marked as linker: (a) L1@MIL-101 and (b) L1, MIL-101 and L1@MIL-101 for comparison. (c) [Ir-L1]@MIL-101 and (d) Ir-L1, MIL-101 and Ir-L1@MIL-101 for comparison.
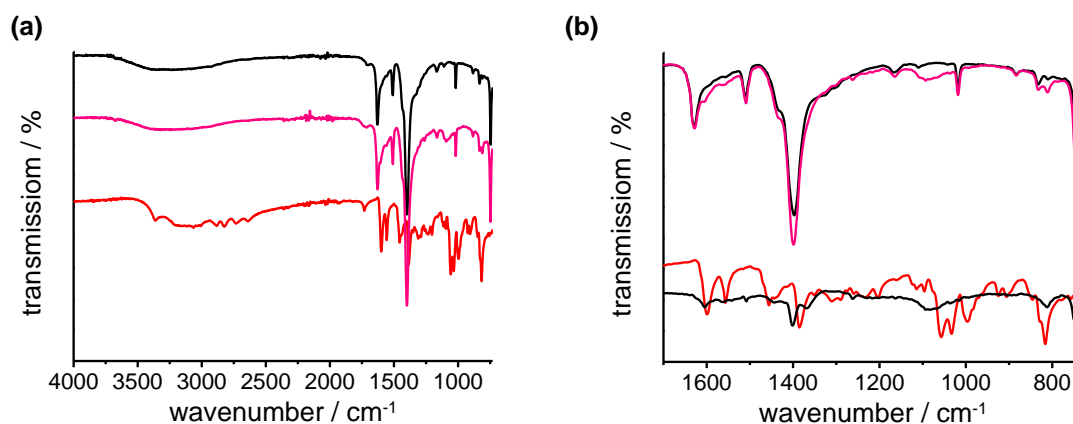

Figure S7. (a) FT-IR spectra of MIL-101 (black), L1@MIL-101 (pink) and L1 (red) in the range of 4000 cm^{-1} to 730 cm^{-1}. (b) In the range of 1700 to 730 cm^{-1}, an overlay of and L1@MIL-101 and MIL-101 is made. In comparison, the difference spectrum (black) of those and the L1 ligand are shown.

(a)

(b)
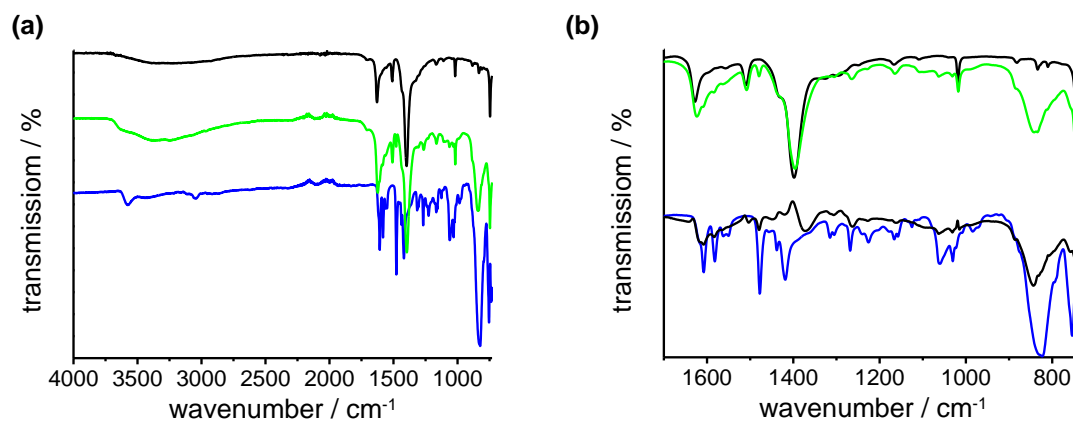
Figure S8. (a) FT-IR spectra of MIL-101 (black), [Ir-L1]@MIL-101 (green) and Ir-L1 (blue) in the range of 4000 to 730 cm^{-1}. (b) In the range of 1700 to 730 cm^{-1}, an overlay of and [Ir-L1]@MIL-101 and MIL-101 is made. In comparison, the difference spectrum of those (black) and the Ir-L1 complex are shown.
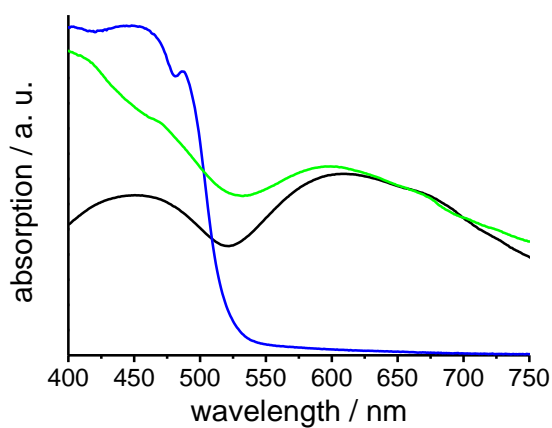

Figure S9. Diffuse reflectance spectra of MIL-101 (black), Ir-L1 (blue) and [Ir-L1]@MIL-101 (green) in the range of 400-750 nm.
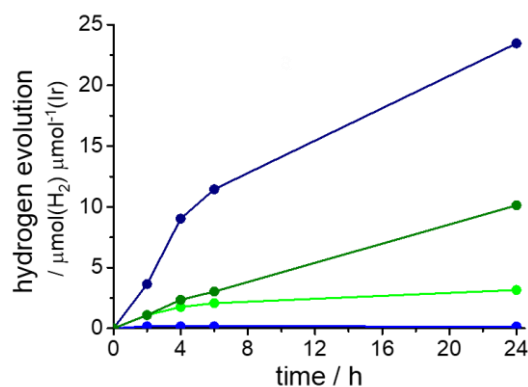

Figure S10. Hydrogen evolution over time; molecular hydrogen was detected by GC-TDC with methane as internal standard: H$_2$ evolution for [Ir-L1]@MIL-101 (green), Ni/[I-L1r]@MIL-101 (dark blue), Pd/[Ir-L1]@MIL-101 (blue) and Pt/[Ir-L1]@MIL-101 (dark green) over 24 h.
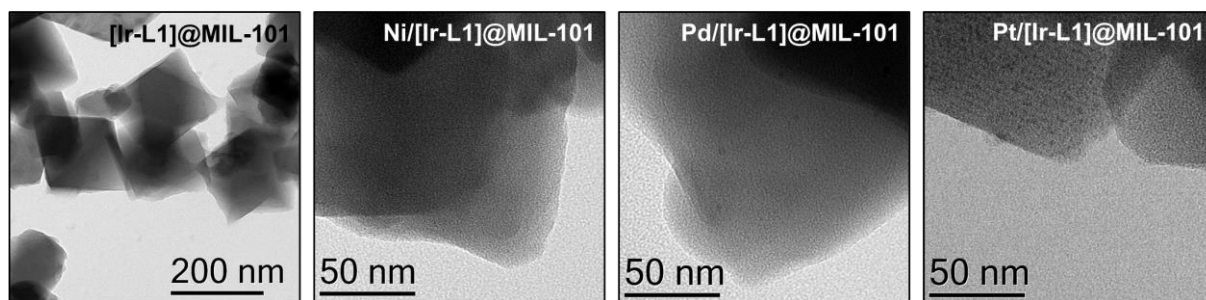
Figure S11. TEM images of [Ir-L1]@MIL-101, Ni/[Ir-L1]@MIL-101, Pd/[Ir-L1]@MIL-101 and Pt/[Ir-L1]@MIL-101.
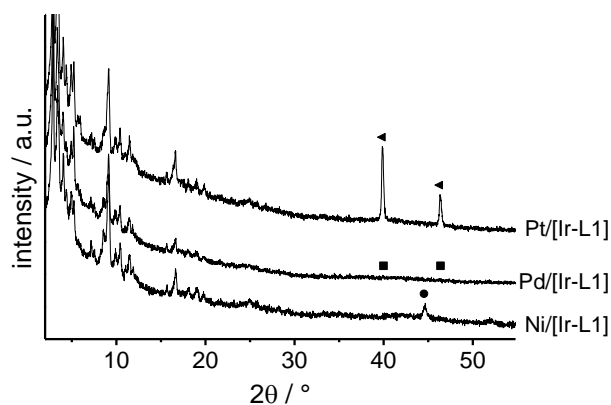

Figure S12. Powder XRD of Ni/[Ir-L1]@MIL-101, Pd/[Ir-L1]@MIL-101 and Pt/[Ir-1]@MIL-101 for comparison. Highlighted reflexes for cubic Ni(0) (circle), cubic Pd(0) (square), cubic Pt(0) triangle.

Table S1. ICP-OES analysis of [Ir-L1]@MIL-101 and M/[Ir-L1]@MIL-101 (M=Ni, Pd, Pt) with contents given in wt.%.

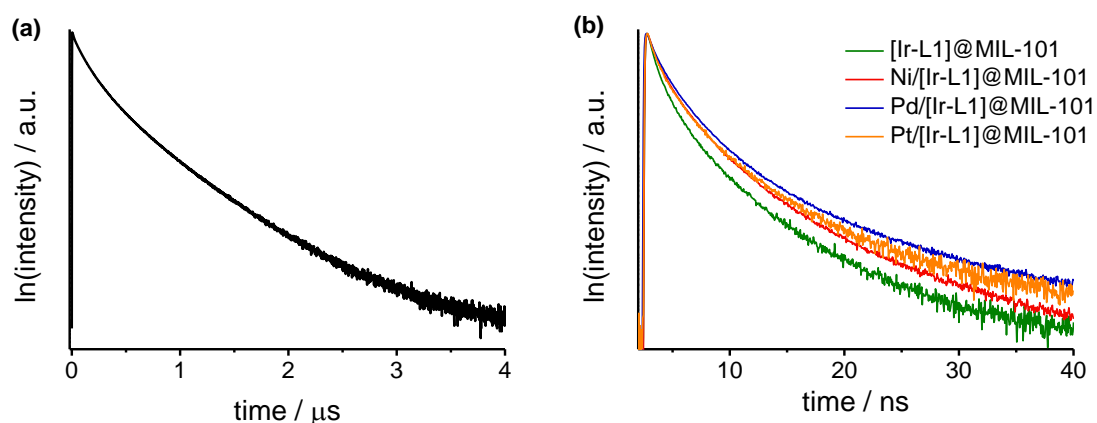| Compound	Ir	Ni	Pd	Pt
[Ir-L1]@MIL-101	5.83	-	-	-
Ni/[**Ir**-L1]@MIL-101	4.59	5.09		
Pd/[**Ir**-L1]@MIL-101	5.05	-	5.11	-
Pt/[**Ir**-L1]@MIL-101	4.81	-	-	6.30

Figure S13. TRPL studies of (a) Ir-L1 and (b) MIL-101 supported catalysts [Ir-L1]@MIL-101, Ni/[Ir-L1]@MIL-101, Pd/[Ir-L1]@MIL-101 and Pt/[Ir-L1]@MIL-101 at excitation wavelength 405 nm. Normalized TCSPC traces are in semi-log representation.

Table S2. Lifetime determination by fitting the TCSPC traces of excited Ir-L1 in TRPL studies. Curves were fitted with a 4-fold exponential decay function. The IRF has not been taken into account in the data analysis.

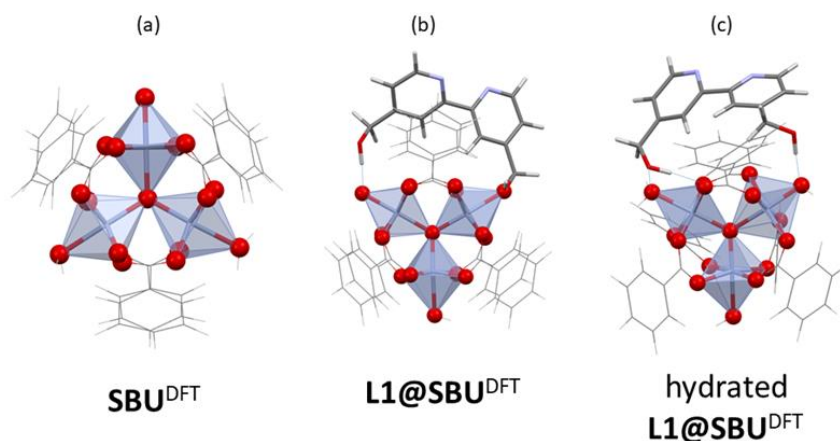| Compound	Fluorescence lifetime / ns	Amplitude / a. u.
Ir-L1	121	107
	297	63
	42	23
	569	10
[Ir-L1]@MIL-101	1.70	11
	0.56	8.5
	4.70	4.1
	16.00	0.22
Ni/[Ir-L1]@MIL-101	2.59	40
	0.83	28
	7.00	8.3
	29.00	0.44
Pd/[Ir-1]@MIL-101	2.81	39
	1.00	28
	8.30	7.3
	34.00	0.68
Pt/[Ir-1]@MIL-101	2.10	5.7
	0.66	3.2
	5.80	2.0
	23.00	0.12

Additional Figures, Tables and IR Spectra of L1@SBU^{DFT} from DFT

Figure S14. Optimized structures of (a) the trinuclear truncated MOF model (SBU^{DFT}), (b) the adduct L1@SBU^{DFT} of ligand L1 with mono-dehydrated SBU^{DFT}. Alternative scenarios imply *trans*-configured donor moieties of L1 that are significantly disfavored on our level of approximation (Δ(*cis-trans*) = 5.5 kJ mol^{-1} = 0.057 eV. (c) The adduct of L1 with the fully hydrated SBU^{DFT}; corner-linked CrO$_6$ octahedra given in blue; hydrogen bonding is highlighted as dashed lines.

Harmonic frequencies computed for the SBU^{DFT} well match the energy and intensity of asymmetric and symmetric CO stretching modes located at ca. 1600 cm^{-1} (198.4 meV) and 1400 cm^{-1} (173.6 meV) in the experimental IR spectra, respectively (cf. Fig. S15)
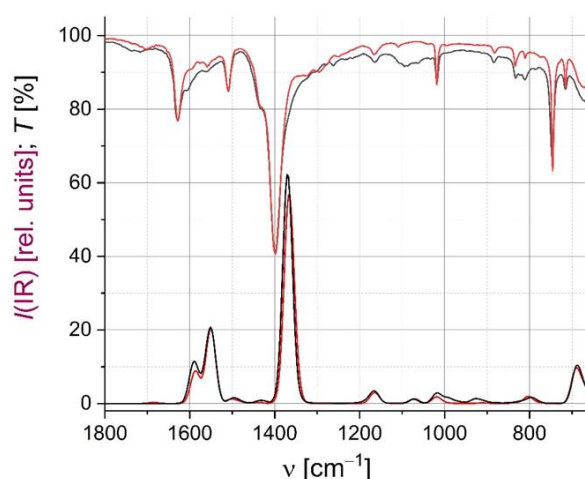

Figure S15. Comparison of experimental and computed IR spectra. (Top; transmission T) Spectra of MIL-101 (top; red) and L1@MIL-101 (top; black). (Bottom; *I*(IR)) Spectra of the model SBU^{DFT} (red) and L1@SBU^{DFT} (black).
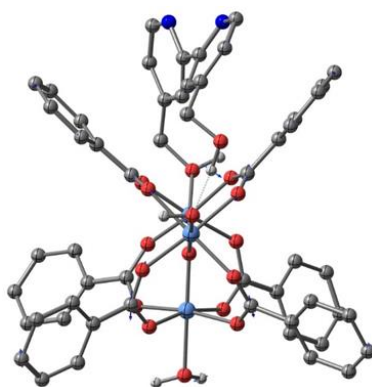
Figure S16. Diagnostic IR mode of the hybrid L1@SBU^{DFT} at $\nu = 1557$ cm^{-1}; arrows denote direction of prominent displacements (an animation of the mode is available in gif-format as Electronic Supporting Information.)

Evidently in the truncated models, the threefold symmetry of the solid state structure is conserved as are individual bond lengths within the chromium(III) coordination spheres (cf. Table S3).

Table S3. Pertinent metrical data of chromium(III) inner coordination and hydrogen bonding [Å] in DFT optimized structures.[a]

	X-ray [b]	SBU^{DFT}	L1@SBU^{DFT}	L1@SBU^{DFT} (hyd)
Cr(1)-O$_{eq}$	1.971(8)	1.985(15)	1.979(15)	1.992(20)
Cr(1)-O$_{ax}$	2.025	2.152	2.153	2.123
Cr(1)-O$_{cen}$	1.897	1.874	1.876	1.890
Cr(2)-O$_{eq}$	1.978(5)	2.004(5)	1.998(5)	2.002(10)
Cr(2)-O$_{ax}$	2.058	2.053	1.935	1.935
Cr(2)-O$_{cen}$	1.886	1.904	1.976	1.979
Cr(3)-O$_{eq}$	1.965(10)	1.989(15)	1.983(15)	1.988(15)
Cr(3)-O$_{ax}$	2.067	2.147	2.142	2.133
Cr(3)-O$_{cen}$	1.899	1.873	1.878	1.877
Cr(1)-O$_{ax}$H···O(H)-C(1)	--	--	--	1.670
Cr(1)-O$_{eq}$···HO-C(1)	--	--	--	1.837
Cr(2)-O$_{ax}$···HO-C(1')	--	--	1.592	1.638

[a] BP86/TZVP level of theory; [b] crystal data (unpublished).

7.6.3 Analysis of the Electronic Structure and Excitations

In the following we present additional information and details about the calculations that are reported in the section "Analysis of the electronic structure and excitations" of the main paper.

Computational Details

Small transition metal clusters such as M_{13} can prefer spin-polarized electronic ground states.[S14,S15,S16,S17,S18] To find the most stable spin state of a system, we ran a set of density functional (DFT) geometry optimizations (GO) or ground state calculations with a fixed spin magnetic moment m_s of a pertinent interval and evaluated the total energy. The interval for, e.g., M_{13}/[Ir-L1], was chosen according to the preferred magnetic moment of M_{13} stated below in terms of $[0, 2, ..., m_s(M_{13}) + 2] \mu_B$. All geometry optimizations used the Perdew-Burke-Ernzerhof[S19,S20] (PBE) exchange-correlation functional with van-der-Waals corrections (DFT-D3)[S21] and the def2-TZVP basis set.[S22] The binding energies E_B of M_{13}/[Ir-L1] were computed from the difference of the molecular total energies E_{tot} obtained from ground state DFT calculations (PBE-D3 + def2-TZVP):

$$E_B(M_{13}/[\text{Ir-L1}]) = E_{tot}(M_{13}/[\text{Ir-L1}]) - E_{tot}(M_{13}) - E_{tot}(\text{Ir-L1}) . \qquad (S1)$$

The def2-ecp effective core potential was used for Pd, Pt and Ir in combination with the def2 basis sets.[S22] The ground state calculations utilized the relaxed PBE-D3 geometries of the respective system. Note that the relaxed structures of M_{13}/[Ir-L1] were obtained according to the procedure given in the main manuscript. The relaxed structures of Ni$_{13}$/[Ir-L1] and Pd$_{13}$/[Ir-L1] showed an icosahedral (ico) structure of the metal clusters (cf. main manuscript, Fig. 5 panel (a) and (b)). PBE(-D3) predicts $8\,\mu_B$ for the vacuum structure of both Ni$_{13}$(ico) and Pd$_{13}$(ico).[S14,S15,S16,S23] Furthermore, PBE(-D3) favors $4\,\mu_B$ for the structure seen for Pt$_{13}$ (cf. Fig. 5 panel (c)), which is consistent with one that was reported in Ref. S24. For further discussions on structural isomers of M_{13}, we refer to Ref. S14 and references therein. Table S4 lists the spin magnetic moment of the ground state of all systems studied in the section regarding the analysis of the electronic structure and excitations. Reassuringly, PBE and the tuned range-separated hybrid ωPBE (see below) yielded the same spin magnetic moment for each system. This consistency check has special relevance for the Ni systems, since some hybrid exchange-correlation functionals predict a higher spin magnetic moment for Ni$_{13}$.[S23,S25,S26] For a discussion on the spin magnetic moment of Ni$_{13}$, see Ref. S25 and S26. A series of concluding comments regarding spin-polarized systems: A spin moment of, e.g., $8\,\mu_B$ corresponds to a spin multiplicity $M=9$ (nonet state), whereas $M=2S+1$ and S denotes the spin quantum number. For example, our DFT calculations predict a spin magnetic moment of $8\,\mu_B$ for Ni$_{13}$/[Ir-L1]. Thus, the optical (spin-conserving) excitations are nonet $\rightarrow$ nonet transitions. The spin-flip excitation to the next lower magnetic moment ($6\,\mu_B$) is a nonet $\rightarrow$ septet transition. To ease the comparison between all spin-conserving and spin-flip excitations (as further explained in the main manuscript), we refer to these uniformly as S_n and T_n, respectively, with n being the n'th excitation. DFT Born-Oppenheimer molecular dynamics (BOMD) simulations with a Nosé-Hoover thermostat[S27,S28] of M_{13}/[Ir-L1] utilized the PBE exchange-correlation functional

in combination with the def2-SVP basis set[S29] (M_{13}=Ni$_{13}$, Pd$_{13}$, Pt$_{13}$). We used a thermostat temperature of 298 K and a time step of 80 a.u. ($\approx$ 1.94 fs). The total simulation time was circa 4 ps and the relaxation time equaled 560 a.u. ($\approx$ 13.55 fs) for Pt$_{13}$/[Ir-L1] and 400 a.u. ($\approx$ 9.68 fs) for both Pd$_{13}$/[Ir-L1] and Ni$_{13}$/[Ir-L1]. For the BOMD simulations of M_{13}/[Ir-L1] we chose a fixed spin magnetic moment of 8 μ_B for the Ni, 4 μ_B for the Pd and 2 μ_B for the Pt system. These choices were based on the spin magnetic moment of the electronic ground state that we determined for preliminary structures of M_{13}/[Ir-L1] by running a set of DFT geometry optimizations, as explained above.

Table S4. Spin magnetic moment m_s of the electronic ground state of different molecular systems obtained from DFT ground state calculations. PBE and ωPBE using the non-empirically optimized range-separation parameter ω_opt of each system consistently yield the same m_s. ω_opt was obtained according to Eq. S2. The ground state calculations utilized the relaxed PBE-D3 geometries of the respective system.

System	m_s (μ_B)	ω_opt (bohr^{-1})
Ir-L1	0	0.16
Ir-L0	0	0.16
Ni$_{13}$	8	0.18
Pd$_{13}$	8	0.17
Pt$_{13}$	4	0.17
Ni$_{13}$/[Ir-L1]	8	0.14
Pd$_{13}$/[Ir-L1]	4	0.12
Pt$_{13}$/[Ir-L1]	2	0.11

Range-separated hybrid exchange-correlation functionals typically split the Coulomb operator ($1/r$) into a short- and long-range term.[S30,S31] This is implemented here by the error function $\mathrm{erf}(r\omega)$ in terms of $1/r = [1 - \mathrm{erf}(r\omega)]/r + \mathrm{erf}(r\omega)/r$, with ω being the range-separation parameter.[S32,S33] We employed the version of ωPBE[S34,S35] that uses pure semi-local PBE exchange in the short-range, exact Hartree-Fock exchange only in the long-range and PBE correlation without range-separation. Note that all calculations utilizing ωPBE were carried out in a generalized Kohn-Sham (GKS) framework as implemented by QCHEM.[S36] In this study, the non-empirical tuning process of ωPBE aims to satisfy the DFT version of Koopmans' theorem,[S37] since it usually leads to a trustworthy description of photophysical properties (cf. main manuscript, Introduction). The theorem establishes a physical meaning of the highest occupied Kohn-Sham eigenvalue ϵ_HOMO in exact ground state DFT, which also holds within GKS.[S38] It rigorously guarantees that $-\epsilon_\mathrm{HOMO}(N)$ equals the first vertical ionization energy $IP(N)$ of an N-electron system. $IP(N)$ is defined as the difference between the total energy E_tot of the cationic and neutral system (for "frozen" core positions), $IP(N) = E_\mathrm{tot}(N-1) - E_\mathrm{tot}(N)$. To obey as closely as possible to the latter, we tune the range-separation parameter such that ω_opt minimizes $J(\omega)$ of

$$J^2(\omega) = [IP^\omega(N) + \epsilon_\mathrm{HOMO}(N)]^2 + [IP^\omega(N+1) + \epsilon_\mathrm{HOMO}(N+1)]^2. \tag{S2}$$

To this end, we iterate through an interval for ω in discrete steps of 0.01 bohr^{-1} and compute the electronic ground state of the neutral (N), cationic ($N - 1$) and anionic ($N + 1$) system for each value of the interval within the structure of the neutral system. These yielded ϵ_{HOMO} and the total energies needed to calculate IP^{ω} from the definition above. The ground state calculations of Ir-L0, Ir-L1, M_{13} utilized the def2-TZVP basis set and M_{13}/[Ir-L1] used def2-SVP. Table S4 contains the optimally tuned ω_{opt} of molecular systems studied with ωPBE in the main manuscript.

Excitation spectra and densities were obtained from linear response time-dependent DFT (TDDFT) calculations in the Casida formalism.[S39,S40] For this, we used ωPBE and the LANL2DZ basis set in combination with the LANL2DZ-ecp effective core potential for Ni, Pd, Pt and Ir as implemented by QCHEM.[S36] For better visualization, absorption spectra were obtained by convoluting the TDDFT excitation spectra with a Gaussian of width 0.08 eV. Note that we also tested the accuracy of the Tamm-Dancoff approximation[S41] (TDA) by calculating the excitation spectra of M_{13}/[Ir-L1] (within their equilibrium geometry). This test showed that the TDA yields the qualitatively same trend as the full linear-response TDDFT calculation for the excitation spectrum and excitation densities. For this reason, the study on the distance dependency of the interaction between the metal nanoparticles and the Ir photosensitizer was carried out within the TDA. Spin-flip excitations of M_{13}/[Ir-L1] were also obtained within the TDA for technical reasons within QChem. Each of the M_{13} exhibits a characteristically dense excitation spectrum (cf. Fig. S23). Consequently, it is necessary to calculate several hundred and up to about 1000 excitations only for the VIS excitation spectrum of M_{13} and M_{13}/[Ir-L1], respectively. This in turn means that an increasingly elaborate diagonalization is necessary to obtain the roots of the Casida matrix equations. Note that this can be a more general bottleneck to obtaining UV excitation spectra of systems containing (transition) metal clusters from Casida linear response TDDFT calculations. All calculations using the range-separated hybrid ωPBE and generalized gradient approximation PBE(-D3) were carried out with the QCHEM[S36] and TURBOMOLE[S42] code, respectively.

Ir-L0 Triplet Photosensitizer

Figure S17 shows the electronic difference density of the lowest triplet excitation T_1 and the ground state of [Ir(bpy)(ppy)$_2$]$^+$ (named Ir-L0) obtained from TDDFT. For this calculation, the range-separated hybrid exchange-correlation functional ωPBE and the LANL2DZ basis set were used. The red and blue wireframes indicate negative (electron lack) and positive (gain) areas in the difference densities presented in this section, respectively.
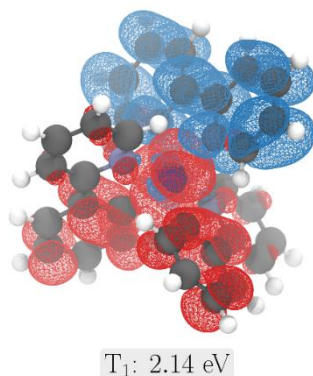
T₁: 2.14 eV

Figure S17. Electronic difference density of T_1 of [Ir(bpy)(ppy)$_2$]$^+$ (Ir-L0). Obtained from a TDDFT calculation with the non-empirical optimally tuned ωPBE (ω_{opt}(Ir-L0)=0.16 bohr^{-1}). See main text for details.

Density of States of M_{13}/[Ir-L1]

We compared the density of states (DOS) of M_{13}/[Ir-L1] to that of its molecular constituents M_{13} and Ir-L1. The DOS is (approximately) computed from the Kohn-Sham ground state eigenvalues. Figure S18 shows the DOS of M_{13}/[Ir-L1], M_{13} and Ir-L1 obtained from a DFT ground state calculation with ωPBE and LANL2DZ (Ni$_{13}$/[Ir-L1] panel (a), Pd$_{13}$/[Ir-L1] panel (b), Pt$_{13}$/[Ir-L1] panel (c)). For better visualization, the eigenvalue spectrum was convoluted with a Gaussian of width 0.08 eV. Analogous to the comparison of absorption spectra discussed in the main manuscript, we paid attention to two aspects: (i) We calculated the ground state of M_{13} and Ir-L1 (separately) in the fixed structure as they are in M_{13}/[Ir-L1] (cf. main manuscript, Fig. 3). This eliminates effects that would just be due to structural differences. (ii) To eliminate exchange-correlation functional related differences, we used the optimally tuned range-separation parameter, ω_{opt}, of M_{13}/[Ir-L1] also to calculate the DOS of M_{13} and Ir-L1 in (i). Following these considerations, Figure S18 clearly shows that the total spectra differ from the respective individual spectra. In particular, the DOS of M_{13}/[Ir-L1] shows no overlap with that of the respective metal cluster for energies approximately higher than -8 eV. Therefore, the DOS of M_{13}/[Ir-L1] cannot even be explained qualitatively from the superposition of M_{13} and Ir-L1. Reassuringly, calculating the DOS of M_{13}/[Ir-L1] with the generalized gradient approximation PBE consistently yields the same trend as the range-separated hybrid functional ωPBE, as shown exemplarily for Ni$_{13}$/[Ir-L1] in Fig. S19. Note that consideration (i) was also applied for the calculations with PBE. The confirmation by another class of exchange-correlation functionals shows the robustness of our results.
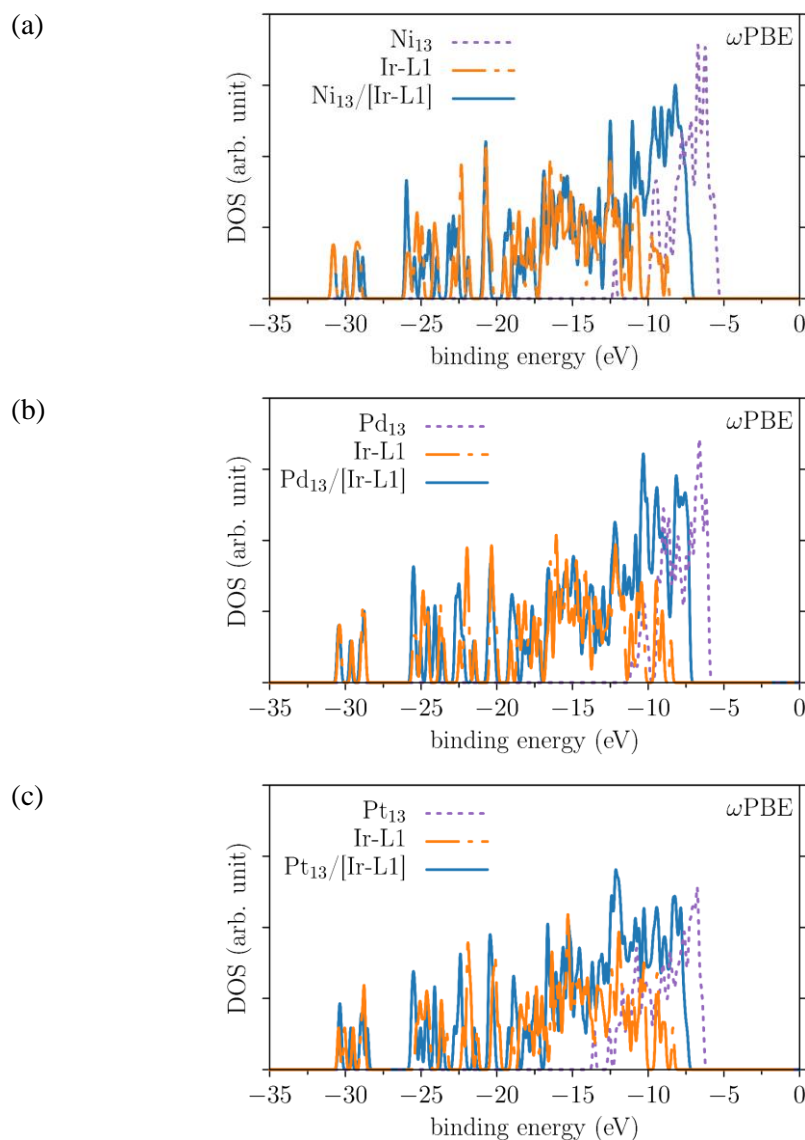
(a)

(b)

(c)

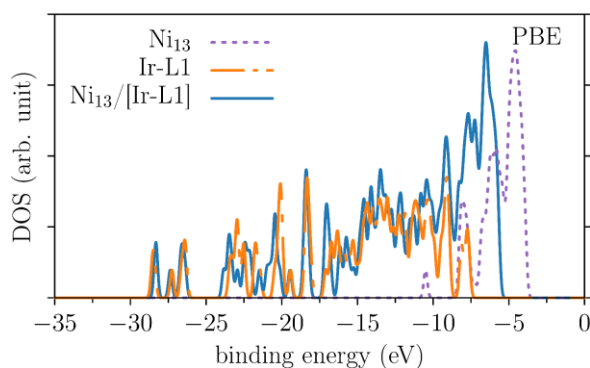**Figure S18.** Theoretical density of states of M_{13}/[Ir-L1], M_{13} and Ir-L1 obtained from DFT ground state calculations with the non-empirical optimally tuned ωPBE. (a) Comparison for Ni$_{13}$/[Ir-L1]. The respective calculations used ω_{opt}=0.14 bohr^{-1}, as explained in the main text. (b) Pd$_{13}$/[Ir-L1] (ω_{opt}=0.12 bohr^{-1}). (c) Pt$_{13}$/[Ir-L1] (ω_{opt}=0.11 bohr^{-1}).

Figure S19. Theoretical density of states of Ni$_{13}$/[Ir-L1], M_{13} and Ir-L1 obtained from DFT ground state calculations with PBE. See main text for details.

Density of States of Ni$_{38}$/[Ir-L1]

In order to make sure that these findings are not special only for the 13-atom clusters we also studied a considerably larger system, Ni$_{38}$, in combination with Ir-L1. To this end we started from a 38-atom cluster geometry from Ref. S23 that corresponds to a cut-out of the bulk structure and optimized it using the PBE functional and the def2-SVP basis set. We then placed the Ir-L1 complex in the vicinity of the metal cluster and optimized the geometry of the combined system. We again observe that the metal cluster and the photosensitizer approach each other during the optimization, i.e., the way in which the geometries evolve already suggests that there is an interaction. Fig. S20 shows the final lowest energy geometry.
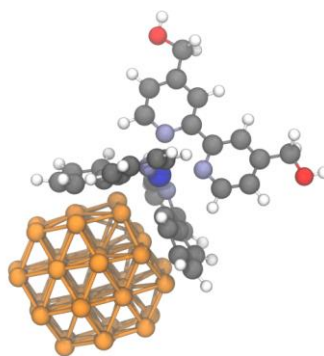
Figure S20. Optimized geometry of Ni$_{38}$/[Ir-L1]. See main text for details.

We then analyzed the Kohn-Sham DOS in the same way as for Ni$_{13}$/[Ir-L1], i.e., we compare the DOS of the combined system with the DOS of the subsystems. The results are depicted in Fig. S21. For the sake of clarity, we also show the sum of the two independently calculated DOS (line labeled Ir-L1 + Ni$_{38}$). The figure shows that the DOS of the combined system differs markedly from the sum of the two independent DOS. This clearly confirms that also for the larger metal particle there is a pronounced interaction between the photosensitizer and the metal.
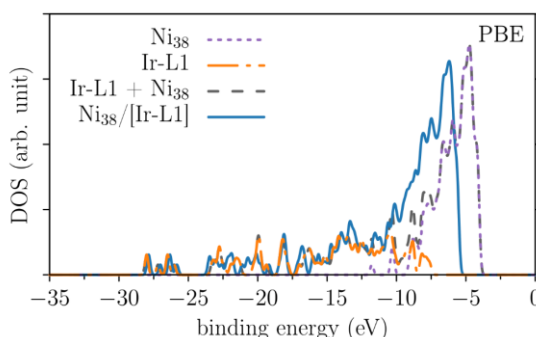

Figure S21. Theoretical density of states of Ni$_{38}$/[Ir-L1], Ni$_{38}$, Ir-L1, and the sum of the independently computed DOS of Ir-L1 and Ni$_{38}$ obtained from DFT ground state calculations with PBE. See main text for details.

Finally, a plot of the highest occupied orbitals, shown in Fig. S22 for Ni_{13}/[Ir-L1] and Ni_{38}/[Ir-L1], further confirms the significant interaction: The orbital (as well as lower ones that are not shown in the plot) spreads over both the Ir-L1 and the metal particle, i.e., electron density is truly shared between the two systems.
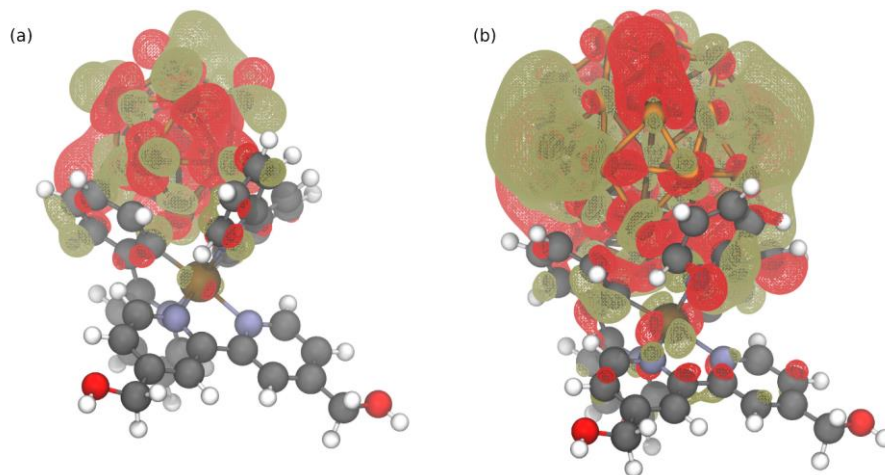

Figure S22. Isosurface plots of the highest-occupied orbital (in one spin channel, with PBE) for Ir-L1 in combination with Ni_{13} (a) and Ni_{38} (b). See main text for details.

Absorption Spectra of M_{13}

Fig. S23 shows the gas-phase absorption spectra of M_{13} obtained from TDDFT calculations with ωPBE. The non-empirically optimized range-separation parameter of the respective 13-atom metal cluster was used (cf. Table S1). The absorption spectra were obtained by convoluting the TDDFT excitation spectra with a Gaussian of width 0.08 eV. To avoid misunderstandings, it should be noted that the absorption spectra of each M_{13} (Fig. S23) differ from those shown in the main manuscript (Fig. 5), since a different range-separation parameter was used in each case. Due to using the optimally tuned range-separation parameter of each M_{13} cluster, the absorption spectra shown here are more accurate compared to those of Fig. 5. Therefore, the absorption spectra shown in Fig. S23 should be considered for, e.g., the comparison with the gas-phase experiment of M_{13}.
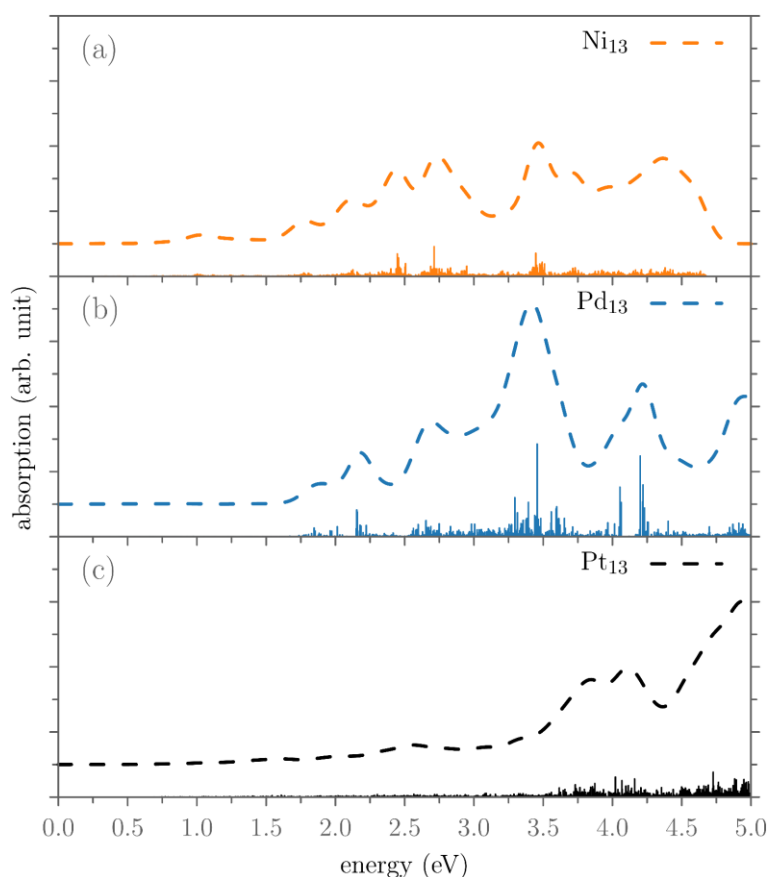

Figure S23. Theoretical absorption spectrum of M_{13}. The excitation spectra are obtained from TDDFT calculations with the non-empirical optimally tuned ωPBE, plotted on a scale of [0,2.4] arb. unit. For better visualization, all absorption spectra are shifted vertically by 0.3 arb. units. Vertical bars show the relative oscillator strength, plotted on a second scale of [0,0.2] (labels and tick marks omitted). Spectra of M_{13} with the optimally tuned ω_{opt} of each M_{13}: (a) Ni$_{13}$ (ω_{opt}=0.18 bohr^{-1}) (b) Pd$_{13}$ (ω_{opt}=0.17 bohr^{-1}). (c) Pt$_{13}$ (ω_{opt}=0.17 bohr^{-1}).

Excitation Difference Densities of M₁₃/[Ir-L1]

The difference densities of the 30 excitations with the highest oscillator strength up to 3.2 eV and the ground state are shown in Fig. S24 for Ni$_{13}$/[Ir-L1], in Fig. S25 for Pd$_{13}$/[Ir-L1] and in Fig. S26 for Pt$_{13}$/[Ir-L1]. The red and tan wireframes indicate areas of electron lack and gain, respectively. For further details, see main manuscript.

Figure S27 shows the difference density of the lowest spin-flip excitation and the ground state of *M$_{13}$*/[Ir-L1]: For Ni$_{13}$/[Ir-L1] (panel (a)) this is a nonet → septet transition, for Pd$_{13}$/[Ir-L1] (panel (b)) a quintet → triplet and for Pt$_{13}$/[Ir-L1] (panel (c)) a triplet → singlet.

The study on the distance dependency of the interaction between the metal nanoparticles and the Ir photosensitizer showed differences between the metal clusters, as further discussed in the main manuscript. To this end, *M$_{13}$* was successively displaced from Ir-L1 along the line connecting their centers of mass, starting from the equilibrium position. Following this procedure, we expected that the metal particle to ligand charge-transfer observed in the equilibrium position (cf. Figs. S24-S26) will successively decrease. At the same time, the excitation character should become successively more similar to those of the separate components of *M$_{13}$*/[Ir-L1]. Finally, at a certain distance, the interaction should become negligible and the photophysical observables should be directly explainable by a superposition of those of the constituents. It was particular instructive to analyze an additional separation between 7 and 10 bohr, as difference between the metal particles became evident: Firstly, the difference densities of the excitations indicated that the metal particle → ligand charge-transfer remains most pronounced for Ni$_{13}$/[Ir-L1] compared to Pd$_{13}$ and Pt$_{13}$. The fading interaction is reflected by the excitation character becoming more similar to that of the bare components: The intramolecular charge-transfer character of the bare Ir-L1 becomes more pronounced again and/or the excitation is (partly) localized on the metal particle or not at all. Secondly, the influence of Pt$_{13}$ subsided more strongly compared to Ni$_{13}$ and Pd$_{13}$ and is probably already negligible for an additional distance of about 10 bohr. These latter changes can be seen in the difference densities of *M$_{13}$*/[Ir-L1] depicted in Fig. S28. We exemplarily show the five excitations with the highest oscillator strength up to 3.2 eV of *M$_{13}$*/[Ir-L1] for an additional distance of 10 bohr. Note that we also checked the following five excitations with lower oscillator strengths, which further confirm the addressed changes of the excitation character. At an additional distance of ca. 15 bohr, the interaction between Ir-L1 and both Ni$_{13}$ and Pd$_{13}$ became fully negligible.
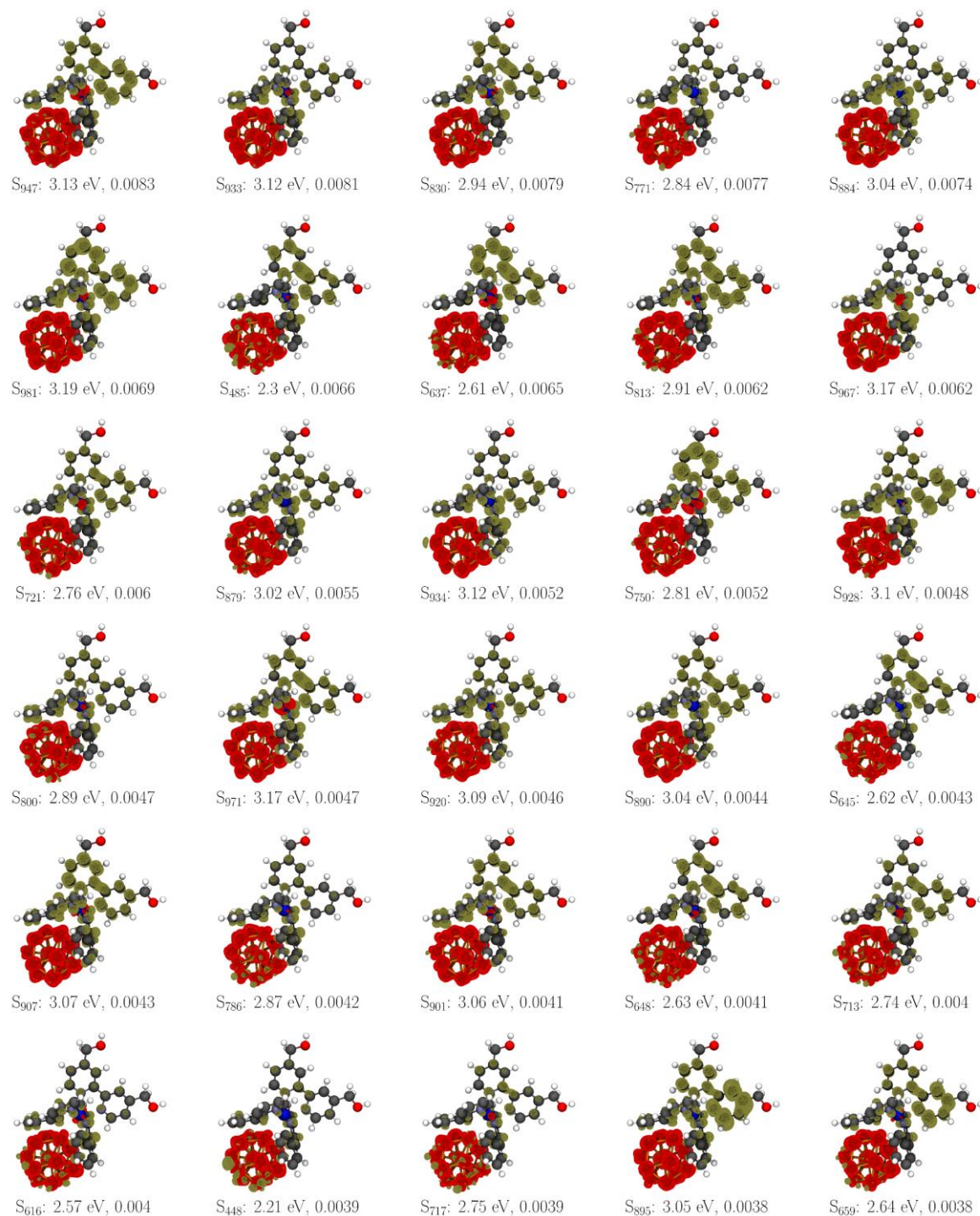
S_{947}: 3.13 eV, 0.0083 S_{933}: 3.12 eV, 0.0081 S_{830}: 2.94 eV, 0.0079 S_{771}: 2.84 eV, 0.0077 S_{884}: 3.04 eV, 0.0074

S_{981}: 3.19 eV, 0.0069 S_{485}: 2.3 eV, 0.0066 S_{637}: 2.61 eV, 0.0065 S_{813}: 2.91 eV, 0.0062 S_{967}: 3.17 eV, 0.0062

S_{721}: 2.76 eV, 0.006 S_{879}: 3.02 eV, 0.0055 S_{934}: 3.12 eV, 0.0052 S_{750}: 2.81 eV, 0.0052 S_{928}: 3.1 eV, 0.0048

S_{800}: 2.89 eV, 0.0047 S_{971}: 3.17 eV, 0.0047 S_{920}: 3.09 eV, 0.0046 S_{890}: 3.04 eV, 0.0044 S_{645}: 2.62 eV, 0.0043

S_{907}: 3.07 eV, 0.0043 S_{786}: 2.87 eV, 0.0042 S_{901}: 3.06 eV, 0.0041 S_{648}: 2.63 eV, 0.0041 S_{713}: 2.74 eV, 0.004

S_{616}: 2.57 eV, 0.004 S_{448}: 2.21 eV, 0.0039 S_{717}: 2.75 eV, 0.0039 S_{895}: 3.05 eV, 0.0038 S_{659}: 2.64 eV, 0.0038

Figure S24. Difference density of optical excitations and the ground state of Ni_{13}/[Ir-L1] obtained from TDDFT with ωPBE (ω_{opt}=0.14 bohr^{-1}). The n'th (spin-conserving) excitation S_n is stated with its energy and oscillator strength. See main text for details.
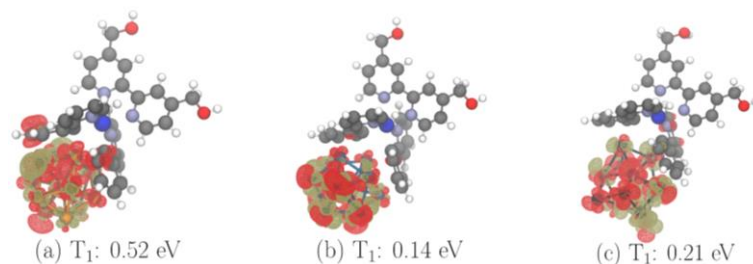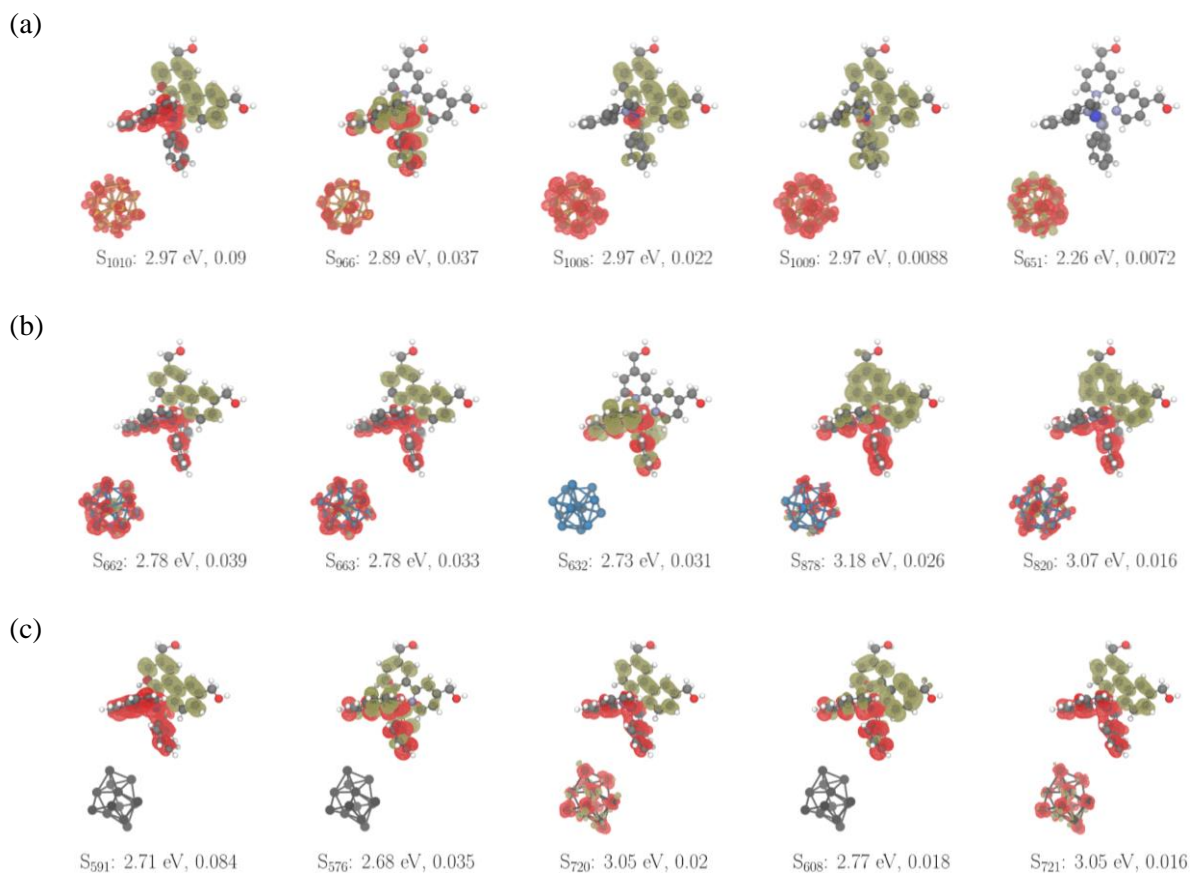
Figure S25. Difference density of optical excitations and the ground state of Pd$_{13}$/[Ir-L1] obtained from TDDFT with ωPBE (ω_{opt}=0.12 bohr^{-1}). The n'th (spin-conserving) excitation S$_n$ is stated with its energy and oscillator strength.

S$_{606}$: 2.78 eV, 0.018 S$_{501}$: 2.51 eV, 0.0095 S$_{559}$: 2.66 eV, 0.0093 S$_{599}$: 2.75 eV, 0.0078 S$_{565}$: 2.68 eV, 0.0073

S$_{669}$: 2.92 eV, 0.0072 S$_{551}$: 2.64 eV, 0.0072 S$_{563}$: 2.67 eV, 0.0072 S$_{451}$: 2.38 eV, 0.0068 S$_{548}$: 2.64 eV, 0.0067

S$_{574}$: 2.7 eV, 0.0067 S$_{730}$: 3.04 eV, 0.006 S$_{510}$: 2.53 eV, 0.0057 S$_{515}$: 2.55 eV, 0.0056 S$_{517}$: 2.55 eV, 0.0051

S$_{794}$: 3.15 eV, 0.0051 S$_{535}$: 2.6 eV, 0.005 S$_{713}$: 3 eV, 0.0048 S$_{568}$: 2.68 eV, 0.0046 S$_{373}$: 2.15 eV, 0.0046

S$_{804}$: 3.17 eV, 0.0043 S$_{798}$: 3.16 eV, 0.0043 S$_{769}$: 3.11 eV, 0.0043 S$_{380}$: 2.17 eV, 0.0041 S$_{382}$: 2.18 eV, 0.0041

S$_{263}$: 1.8 eV, 0.004 S$_{189}$: 1.52 eV, 0.0039 S$_{513}$: 2.54 eV, 0.0039 S$_{582}$: 2.72 eV, 0.0038 S$_{434}$: 2.33 eV, 0.0038

Figure S26. Difference density of optical excitations and the ground state of Pt$_{13}$/[Ir-L1] obtained from TDDFT with ωPBE (ω_{opt}=0.11 bohr^{-1}). The n'th (spin-conserving) excitation S$_n$ is stated with its energy and oscillator strength.

150

(a) T$_1$: 0.52 eV   (b) T$_1$: 0.14 eV   (c) T$_1$: 0.21 eV

Figure S27. Difference density of the lowest spin-flip excitation (labeled T$_1$) of M_{13}/[Ir-L1] with the given energy obtained from TDDFT (TDA) with the optimally tuned ωPBE. Ni$_{13}$/[Ir-L1] (ω_{opt}=0.14 bohr^{-1}) is shown in panel (a), Pd$_{13}$/[Ir-L1] (ω_{opt}=0.12 bohr^{-1}) in panel (b) and Pt$_{13}$/[Ir-L1] (ω_{opt}=0.11 bohr^{-1}) in panel (c). See main text for details.

(a)

S$_{1010}$: 2.97 eV, 0.09   S$_{966}$: 2.89 eV, 0.037   S$_{1008}$: 2.97 eV, 0.022   S$_{1009}$: 2.97 eV, 0.0088   S$_{651}$: 2.26 eV, 0.0072

(b)

S$_{662}$: 2.78 eV, 0.039   S$_{663}$: 2.78 eV, 0.033   S$_{632}$: 2.73 eV, 0.031   S$_{878}$: 3.18 eV, 0.026   S$_{820}$: 3.07 eV, 0.016

(c)

S$_{591}$: 2.71 eV, 0.084   S$_{576}$: 2.68 eV, 0.035   S$_{720}$: 3.05 eV, 0.02   S$_{608}$: 2.77 eV, 0.018   S$_{721}$: 3.05 eV, 0.016

Figure S28. Difference density of optical excitations and the ground state of M_{13}/[Ir-L1] obtained from TDDFT (TDA) with ωPBE. Starting from the equilibrium position, M_{13} was displaced from Ir-L1 by 10 bohr along the line connecting their centers of mass. Ni$_{13}$/[Ir-L1] (ω_{opt}=0.14 bohr^{-1}) is shown in panel (a), Pd$_{13}$/[Ir-L1] (ω_{opt}=0.12 bohr^{-1}) in panel (b) and Pt$_{13}$/[Ir-L1] (ω_{opt}=0.11 bohr^{-1}) in panel (c). The n'th (spin-conserving) excitation S$_n$ is given with energy and oscillator strength. See main text for details.

151

7.6.4 References

[S1] A. Altomare, M. C. Burla, M. Camalli, G.L. Cascarano, C. Giacovazzo, A. Guagliardi, A.G.G. Moliterni, G. Polidoli, R. Spagna, *J. Appl. Cryst.* **1999**, *32*, 115.

[S2] G. M. Sheldrick, *Acta Crystallogr. Sect. C Struct. Chem.* **2015**, *C71*, 3.

[S3] L. J. Farrugia, *J. Appl. Cryst.* **1999**, *32*, 837.

[S4] C. F. Macrae, P. R. Edgington, P. McCabe, E. Pidcock, G. P. Shields, R. Taylor, M. Towler, J. van de Streek, *J. Appl. Crystallogr.* **2006**, *39*, 453.

[S5] A. G. Condie, J. C. Gonzáles-Gómez, C. R. J. Stephenson, *J. Am. Chem. Soc.* **2010**, *132*, 1464.

[S6] Y. K. Hwang, D.-Y. Hong, J.-S. Chang, S. H. Jhung, Y.-K. Seo, J. Kim, A. Vimont, M. Daturi, C. Serre, G. Férey, *Angew. Chem. Int. Ed.* **2008**, *47*, 4144.

[S7] J. Hermannsdörfer, M. Friedrich, N. Miyajima, R. Q. Albuquerque, S. Kümmel, R. Kempe, *Angew. Chem. Int. Ed.* **2012**, *51*, 11473.

[S8] S. Proch, J. Herrmannsdörfer, R. Kempe, C. Kern, A. Jess, L. Seyfarth, J. Senker, *Chem. Eur. J.* **2008**, *14*, 8204.

[S9] F. Neese, *WIREs Comput. Mol. Sci.* **2012**, *2*, 73.

[S10] A. Schäfer, H. Horn. R. Ahlrichs, *J. Chem. Phys.* **1992**, *97*, 2571.

[S11] A. Becke, *Phys. Rev. A* **1988**, *38*, 3098.

[S12] S. Grimme, J. Antony, S. Ehrlich, H. Krieg, *J. Chem. Phys.* **2010**, *132*, 154104; S. Grimme, S. Ehrlich, L. Goerigk, *J. Comput. Chem.* **2011**, *32*, 1456.

[S13] A. Klamt, G. Schüürmann, *J. Chem. Soc. Perkin. Trans. 2* **1993**, 799.

[S14] M. J. Piotrowski, P. Piquini, J. L. Da Silva, *Phys. Rev. B* **2010**, *81*, 155446.

[S15] A. M. Köster, P. Calaminici, E. Orgaz, D. R. Roy, J. U. Reveles, S. N. Khanna, *J. Am. Chem. Soc.* **2011**, *133*, 12192.

[S16] A. S. Chaves, M. J. Piotrowski, J. L. Da Silva, *Chem. Phys.* **2017**, *19*, 15484.

[S17] M. J. Piotrowski, C. G. Ungureanu, P. Tereshchuk, K. E. Batista, A. S. Chaves, D. Guedes-Sobrinho, J. L. Da Silva, *J. Phys. Chem. C* **2016**, *120*, 28844.

[S18] M. Van Den Bossche, *J. Phys. Chem. A* **2019**, *123*, 3038.

[S19] J. P. Perdew, K. Burke, M. Ernzerhof, *Phys. Rev. Lett.* **1996**, *77*, 3865.

[S20] J. P. Perdew, K. Burke, M. Ernzerhof, *Phys. Rev. Lett.* **1997**, *78*, 1396.

[S21] S. Grimme, *J. Comput. Chem.* **2004**, *25*, 1463.

[S22] F. Weigend, R. Ahlrichs, *Phys. Chem. Chem. Phys.* **2005**, *7*, 3297.

[S23] L. Leppert, R. Kempe, S. Kümmel, *Phys. Chem. Chem. Phys.* **2015**, *17*, 26140.

[S24] L. L. Wang, D. D. Johnson, *Phys. Rev. B Condens. Matter* **2007**, *75*, 235405.

[S25] D. Tilgner, M. Klarner, S. Hammon, M. Friedrich, A. Verch, N. de Jonge, S. Kümmel, R. Kempe, *Austr. J. Chem.* **2019**, *72*, 842.

[S26] M. Klarner, S. Hammon, S. Feulner, S. Kümmel, L. Kador, R. Kempe, *ChemCatChem* **2020**, *12*, 4593.

[S27] S. Nosé, *J. Chem. Phys.* **1984**, *81*, 511.

[S28] W.G. Hoover, *Phys. Rev. A* **1985**, *31*, 1695.

[S29] A. Schäfer, H. Horn, R. Ahlrichs, *J. Chem. Phys.* **1992**, *97*, 2571.

[S30] A. Savin, *Theor. Comput. Chem.* **1996**, *4*, 327.

[S31] R. Baer, D. Neuhauser, *Phys. Rev. Lett.* **2005**, *94*, 043002.

[S32] P. M. W. Gill, R. D. Adamson, J. A. Pople, *Mol. Phys.* **1996**, *88*, 1005.

[S33] H. Iikura, T. Tsuneda, T. Yanai, K. Hirao, *J. Chem. Phys.* **2001**, *115*, 3540.

[S34] T. M. Henderson, B. G. Janesko, G. E. Scuseria, *J. Chem. Phys.* **2008**, *128*, 194105.

[S35] M. A. Rohrdanz, J. M. Herbert, *J. Chem. Phys.* **2008**, *129*, 034107.

[S36] Y. Shao, Z. Gan, E. Epifanovsky, A. T. Gilbert, M. Wormit, J. Kussmann, A. W. Lange, A. Behn, J. Deng, X. Feng et al., *Mol. Phys.* **2015**, *113*, 184.

[S37] M. Levy, J. P. Perdew, V. Sahni, *Phys. Rev. A* **1984**, *30*, 2745.

[S38] R. Baer, E. Livshits, U. Salzner, *Annu. Rev. Phys. Chem.* **2010**, *61*, 85.

[S39] M. E. Casida, *Recent Advances in Density Functional Methods* **1995**, 155.

[S40] M. E. Casida, *J. Chem. Phys.* **2005**, *122*, 054111.

[S41] S. Hirata, M. Head-Gordon, *Chem. Phys. Lett.* **1999**, *314*, 291.

[S42] TURBOMOLE V7.4, **2019**.

8   List of Publications

The following publications were published during the work on this thesis:

1.   M. Friedrich, <u>M. Klarner</u>, J. Hermannsdörfer, R. Kempe, *Polyhedron* **2018**, *155*, 441-446.
Nanometer-Scaled Iridium Particles Gas-Phase-Loaded into the Pores of the Metal-Organic Framework MIL-101

2.   D. Tilgner, <u>M. Klarner</u>, S. Hammon, M. Friedrich, A. Verch, N. de Jonge, S. Kümmel, R. Kempe, *Aust. J. Chem.* **2019**, *72*, 842-847.
H_2-Generation from Alcohols by the MOF-Based Noble Metal-Free Photocatalyst $Ni/CdS/TiO_2$@MIL-101

3.   <u>M. Klarner</u>, S. Hammon, S. Feulner, L. Kador, S. Kümmel, R. Kempe, *ChemCatChem* **2020**, *12*, 4593-4599.
Visible Light-driven Dehydrogenation of Benzylamine under Liberation of H_2

4.   <u>M. Klarner</u>, S. Bieger, M. Drechsler, R. Kempe, *Z. Anorg. Allg. Chem.* **2021**, *647*, 2157-2161.
Chemoselective Hydrogenation of Olefins Using a Nanostructured Nickel Catalyst

5.   <u>M. Klarner</u>, P. Blach, H. Wittkämper, N. de Jonge, C. Papp, R. Kempe, *ChemCatChem* **2021**, *13*, 3257-3261.
Key Parameters for the Synthesis of Active and Selective Nanostructured 3d Metal Catalysts Starting from Coordination Compounds – Case Study: Nickel Mediated Reductive Amination

6.   S. Hammon, <u>M. Klarner</u>, G. Hörner, B. Weber, M. Friedrich, J. Senker R. Kempe, T. Branquinho de Queiroz, S. Kümmel, *J. Chem. Phys. C* **2021**, 10.1021/acs.jpcc.1c05756.
Combining Metal Nanoparticles with an Ir(III) Photosensitizer

9 Acknowledgement / Danksagung

9.1 Acknowledgement

I would also like to express my deep gratitude to Prof. Lothar Kador and Werner Reichstein for their continued interest in my samples, their willingness to engage in scientific discussions, and their extremely friendly manner.

I would like to thank my cooperation partners from the INM Leibniz Institute in Saarbrücken, Prof Niels de Jonge and Patricia Blach, as well as from FAU Erlangen, Dr Christian Papp and Haiko Wittkämper, for their constructive collaboration.

For numerous measurements I would like to thank Dr. Markus Drechsler, Birgit Brunner, Florian Puchtler, Hannah Kurz, Tanja Feller, Felix Baier, Dr. Ulrike Lacher, Sabrina Thomä, Dr. Sven Hüttner,

I would like to thank the SFB840 of the German Research Foundation for providing research funds and financing this dissertation. I would like to thank the Elite Network of Bavaria, the Graduate School and the women's support program CoMento of the University of Bayreuth for the financial support of various education courses.

My greatest thanks go to Axel, who has been my strongest emotional support at every moment of the last years.

Finally, and above all, I am endlessly thankful to my family - especially to my parents Astrid & Hans Hugo, my grandparents Gerda & Adam and my sister and at the same time best friend Leoni - for their indescribable support. Thank you for your motivation and love during all the ups and downs in my PhD.

9.2 Danksagung

Mein besonderer Dank gilt meinem akademischen Lehrer Prof. Dr. Rhett Kempe, der mir die Möglichkeit gegeben hat, unter ausgezeichneten Arbeitsbedingungen auf diesem sehr interessanten Thema zu forschen. Ich bedanke mich für die vielen konstruktiven, wissenschaftlichen Diskussionen und nicht zuletzt für das Vertrauen, mir die größtmögliche wissenschaftliche Freiheit während dieser Promotion zu gewähren.

Ich möchte mich herzlich bei Dr. Christine Denner für die reibungslose Integration in ihre Arbeitsgruppe, die ausgezeichnete Betreuung und die freundschaftliche Unterstützung in jeder Phase meiner Promotion bedanken.

Mein großer Dank gilt auch meinen Laborkollegen und -Kolleginnen, die mich (teilweise) während der Doktorarbeit begleitet haben. Dr. Dominic Tilgner, Dr. Christoph Bäumler, Dr. Tobias Schwob, Barbara Klausfelder, Anna-Lena Wolff, Leah Kaiser, Matthias Elfinger, Timon Schönauer, Christof Bauer und Christina Thiersch - ihr habt unsere gemeinsame Zeit durch die kollegiale, unterstützende Arbeitsatmosphäre im Labor, durch zahlreiche wissenschaftliche Diskussionen und nicht zuletzt wegen unseres freundschaftlichen Umgangs miteinander positiv geprägt. Des Weiteren möchte ich mich bei Alexander Goller, Patrick Wolff, Martin Schlagbauer, Tobias Schwarz, Felix Künstler, Fabian Lukas, Johannes Porschke, Hendrik Kempf, Dr. Fabian Kallmeier, Dr. Frederick Freitag, Dr. Gabriela Hahn, Dr. Thomas Dietel, Dr. Andreas Gollwitzer, Dr. Nicklas Deibl, Dr. Torsten Irrgang und Dr. Winfried Kretschmer für die unvergessliche Zeit am Lehrstuhl bedanken. Vor allem das Lehrstuhl-Segeln wird mir nachhaltig in Erinnerung bleiben.

Besondern bedanke ich mich bei meinem Laborkollegen und guten Freund Dr. Martin Friedrich für die schöne gemeinsame Zeit im Labor, die andauernde Diskussionsbereitschaft und die motivationssteigernden Gespräche während der Promotion. Ein besonderer Dank gilt auch meinem Studienkollegen Robin Fertig, der im Laufe der Zeit zu meinem besten Freund innerhalb und außerhalb der Universität geworden ist.

Ich bedanke mich bei all meinen Praktikanten und Praktikantinnen und besonders bei Christoph Maier, Lukas Federer und Sandra Bieger, die mich während ihrer Abschlussarbeiten tatkräftig bei der täglichen Laborarbeit unterstützt haben und neue Impulse gegeben haben.

Ein großes Dankeschön geht an Tina Fell, Heidi Maisel, Anna-Maria Dietel, Sandra Keller und Dana Dopheide, für jegliche technische und organisatorische Hilfe im Promotionsalltag. Besonderes bedanke ich mich bei Marlies Schilling für ihre Hilfsbereitschaft und ihr umwerfendes Organisationsgeschick.

Ich bin dankbar für die großartige Kooperation mit Prof. Stefan Kümmel, Thiago Branquinho de Queiroz und Sebastian Hammon im Rahmen unseres gemeinsamen Projekts im SFB840. Die offene Kommunikation und die Diskussionsbereitschaft habe ich sehr geschätzt, ebenso wie die produktive Arbeitsatmosphäre in Sebastians Büro, wo ich diese Doktorarbeit hauptsächlich verfasst habe.

10 (Eidesstattliche) Versicherungen und Erklärungen

(§ 8 Satz 2 Nr. 3 PromO Fakultät)

Hiermit versichere ich eidesstattlich, dass ich die Arbeit selbstständig verfasst und keine anderen als die von mir angegebenen Quellen und Hilfsmittel benutzt habe (vgl. Art. 64 Abs. 1 Satz 6 BayHSchG).

(§ 8 Satz 2 Nr. 3 PromO Fakultät)

Hiermit erkläre ich, dass ich die Dissertation nicht bereits zur Erlangung eines akademischen Grades eingereicht habe und dass ich nicht bereits diese oder eine gleichartige Doktorprüfung endgültig nicht bestanden habe.

(§ 8 Satz 2 Nr. 4 PromO Fakultät)

Hiermit erkläre ich, dass ich Hilfe von gewerblichen Promotionsberatern bzw. -vermittlern oder ähnlichen Dienstleistern weder bisher in Anspruch genommen habe noch künftig in Anspruch nehmen werde.

(§ 8 Satz 2 Nr. 7 PromO Fakultät)

Hiermit erkläre ich mein Einverständnis, dass die elektronische Fassung der Dissertation unter Wahrung meiner Urheberrechte und des Datenschutzes einer gesonderten Überprüfung unterzogen werden kann.

(§ 8 Satz 2 Nr. 8 PromO Fakultät)

Hiermit erkläre ich mein Einverständnis, dass bei Verdacht wissenschaftlichen Fehlverhaltens Ermittlungen durch universitätsinterne Organe der wissenschaftlichen Selbstkontrolle stattfinden können.

Bayreuth, den 25.06.2021   Mara Klarner